SIMULTENEOUS TRANSMIT AND RECEIVE (STAR) ANTENNAS FOR GEO-SATELLITES AND SHARED-ANTENNA PLATFORMS

by

Elie Germain Tianang

B.S., Yaoundé Advanced School of Engineering, 2007

M.S., University of Colorado, Boulder, 2017

A thesis submitted to the

Faculty of the Graduate School of the

University of Colorado in partial fulfillment

of the requirement for the degree of

Doctor of Philosophy

Department of Electrical, Computer, and Energy Engineering

2019

This thesis entitled:

Simultaneous Transmit and Receive (STAR) Antennas for Geo-Satellites and Shared-Antenna Platforms

written by Elie Germain Tianang

has been approved for the Department of Electrical, Computer, and Energy Engineering

_____

Dejan S. Filipovic

_____

Mohamed A. Elmansouri

Date_____

The final copy of this thesis has been examined by the signatories, and we find that both the content and the form meet acceptable presentation standards of scholarly work in the above mentioned discipline.

Elie Germain Tianang (Ph.D., Electrical, Computer, and Energy Engineering)

Simultaneous Transmit and Receive (STAR) Antennas for Geo-Satellites and Shared-Antenna Platforms

Thesis directed by Professor Dejan S. Filipovic

This thesis presents the analysis, design, and experimental characterization of antenna systems considered for shipborne, airborne, and space platforms. These antennas are innovated to enable Simultaneous Transmit and Receive (STAR) at same time and polarization, either at the same, or duplex frequencies. In airborne and shipborne platforms, developed antenna architectures may enhance the capabilities of modern electronic warfare systems by enabling concurrent electronic attack and electronic support operations. In space, and more precisely at geostationary orbit, designed antennas aim to decrease the complexity of conventional phased array systems, thereby increasing their capabilities and attractiveness. All antennas researched are first designed as a standalone radiator, then as entity of a platform having multiple different antennas.

An ultrawideband, lossless cavity-backed Vivaldi antenna array for flush-mounting applications is first investigated. Eigen-mode analysis is used to analyze antenna-cavity interaction and to show that the entire structure may resonate within the band of interest resulting in a significant degradation of antenna performance. A simple approach based on connecting the array's edge elements in E-plane to the cavity walls is proposed to eliminate the deleterious impact of these cavity resonances. The designed antenna is a 3 × 4 array with 3 elements in E-plane and 4 elements in H-plane, fabricated using stacked all-metal printed circuit board technique. Scan performance of the proposed cavity-backed antenna is investigated in two principal planes and is shown to have similar performance compared to

its free-standing counterpart. A simplified version of this single-polarized antenna, when used for broadside only applications is developed. This antenna, excited with a single coaxial feed is shown to have a smaller aperture than the 3 × 4 array. Isolations between two of these antennas when mounted on a compact shared-antenna platform are investigated through computation and experiments.

To extend the capability of systems relying on these designed antennas, frequency reuse is enabled through dual-polarized functionality. A dual-polarized, flush mounted, Vivaldi antenna, directly integrated with an all-metal cavity is introduced as an alternative to coax-fed quad-ridge horns. An approach based on shaping the side walls of the cavity is used to eliminate the occurrence of resonances. The proposed dual-polarized resonant-free antenna has two orthogonal 2 × 1 arrays with two elements in the E-plane, one element in the H-plane. It is fed using two 2-way power dividers that can be easily designed to maintain low amplitude and phase imbalances. The antenna is fabricated as a single piece and experimentally shows a monotonic gain increase with low cross-polarization over 4:1 bandwidth.

Phased array antennas operating at geostationary orbit are required to scan within Earth's field of view, without any grating lobe appearance. For dual-polarized applications, this requirement has limited the widespread and attractiveness of these systems at frequencies such as X-band. The narrow 150 MHz guard range between transmit and receive bands, leads to impractical diplexers in conventional dual-polarized systems. This research introduces a dual-polarized subarray architecture for X-band phased array systems which enables high isolation between closely separated TX and RX bands. The proposed approach either eliminates the need for diplexers, or significantly decreases their required complexity.

Dedication

To my lovely wife Kevine, our son and daughter

To my mother and sisters

To my father who couldn't wait to see his doctor son

To the memory of my brother

Acknowledgements

I would like to express my sincere gratitude to my advisor, Prof. Dejan Filipovic for his endless support, patience, motivation, and guidance. Reaching this point in my education would not have been possible without his immense contribution. Special appreciation also goes to Dr. Mohamed Elmansouri, who has been deeply involved with my research and always provided his assistance whenever needed.

I would like to thank the members of my thesis committee: Prof. Barton, Prof. Palo, and Dr. Kefauver for their time, comments, encouragements, and efforts to evaluate my research.

I would like to thank all postdoctoral fellows, graduate students, and alumni from the Antenna Research Group and RF Group; especially, Dr. Ignatenko, Dr. Ha, Prof. Lasser, Dr. Jastram, Dr. Altarifi, Dr. Manafi, Dr. Garrido, Dr. Abdelraham, Dr. Pack, Dr. Sanghai, Dr. Rahman, Dr. Walaleprasannakumar, Dr. Hirachandra, Ljubodrag Boskovic, Carlos Hernandez, Aman Samaiyar, Conrad Andrews, Selena Leitner, Merarys Caquias, Karina Hoel, Mauricio Pinto, Abdulaziz Haddab, Laila Marzall, Milica Notoros, Richard Smith, Mattew Arendall, Andrew Kee, Roger Hasse, and Bradley Allen for their fruitful technical conversations.

I would like to thank my funding agencies, especially, Dr. Joel Goodman and Dr. Luciano Boglione from Naval Research Laboratory, Dr. Neill Kefauver and Mr. Thomas Cencich from Lockheed Martin Corporation for supporting these projects which improved my knowledge and understanding of electromagnetics and antennas.

Last, but most importantly, I would like to show my deepest appreciation to my love, family and friends. My wife Kevine Fonkwa, who has always been on my side and provided the support, love, and patience needed to complete this work. Great thanks to my

late fathers and brother, whose, spirits are always there to guide me. My mother, who has dedicated her life to provide me with the best possible education. My parents-in-law for their supports, encouragements and their trust. My friend Dr. Violet Mwaffo for proof reading this thesis and his valuable comments. My longtime friend Lois Kamga, my Cameroonian family here in Colorado for their support during the past five years. I would finally like to thank all my friends and family back home.

Table of Contents

List of Tables

List of Figures

Chapter 1

Introduction

1.1 Motivation

The increased demand for high throughput connectivity in modern wireless communication systems is posing serious challenges to service providers. The high contention of the electromagnetic spectrum and the need to reuse the existing infrastructures as much as possible are forcing service providers to look for systems with higher spectral efficiency. Several techniques are currently being implemented in different wireless systems to increase spectral efficiency. The framework of future 5G networks suggests the use of robust access schemes based on orthogonal frequency division multiplexing (OFDM), phased array antennas, and high order modulations and coding [1]-[3]. In space and commercial satellite services, the burst in high throughput satellites has shifted the focus to spot beam coverage with high gain antennas that can generate higher effective isotropic radiated power (EIRP) and G/T [4]-[5]. In most of these applications, transmit and receive predominantly happen at different times or at different frequencies as shown in Figures 1.1(a)-(b). Allowing these systems to simultaneously transmit and receive at the same frequency, time, and polarization can theoretically double the spectrum efficiency [6]-[9]. This architecture referred to as simultaneous transmit and receive (STAR) (Figure 1.1(c)) is of great interest for future wireless systems. The most difficult problem

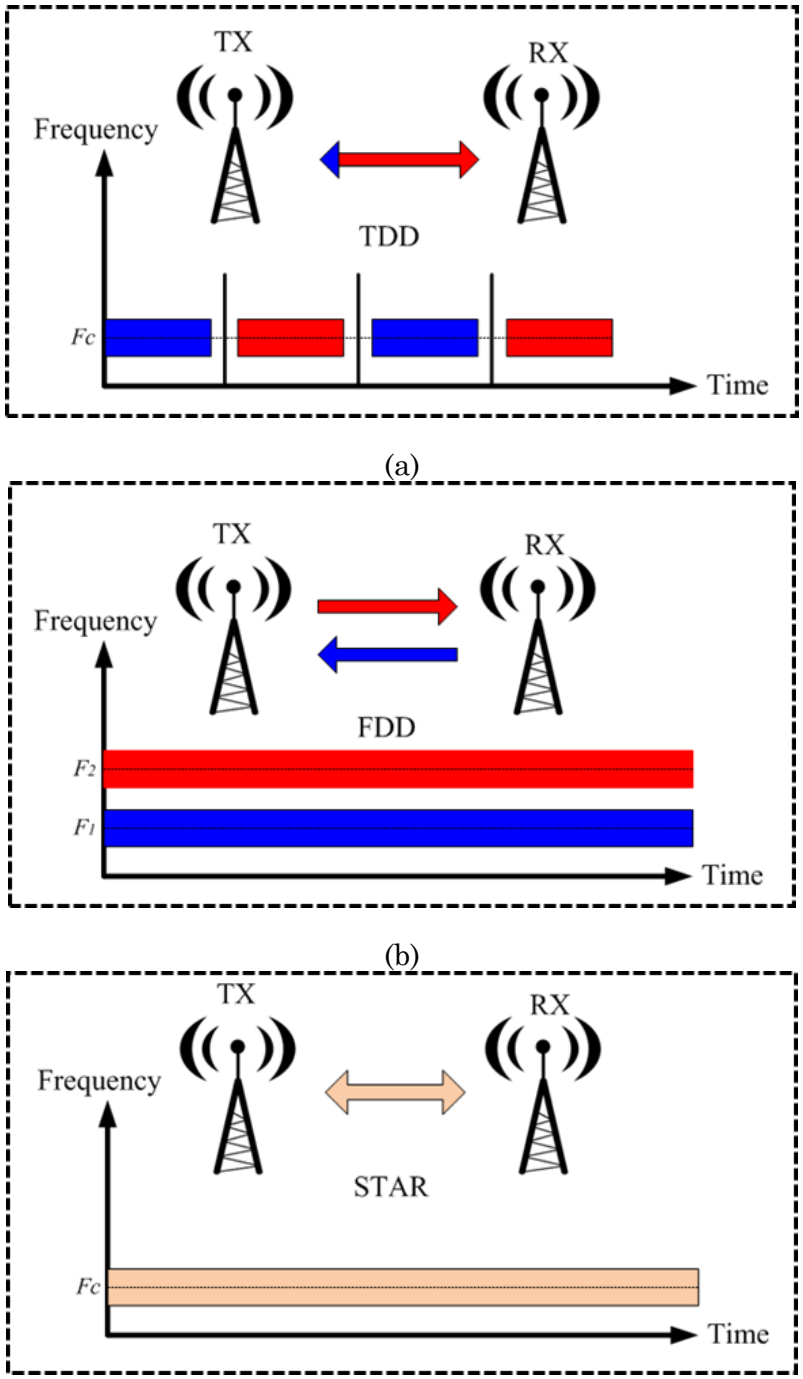

Figure 1.1: Illustration of different duplex transmission techniques: (a) Time Division Duplex (TDD), (b) Frequency Division Duplex (FDD), and (c) Simultaneous Transmit and Receive (STAR).

that has so far limited the widespread implementation of STAR systems is the self-interference from the transmitter. High transmit receive isolation is needed in these systems, not only to prevent increase in receiver noise floor, but also avoid LNA compression. The required level of isolation is application based, and it typically depends on the transmit power, bandwidth, receiver sensitivity, and is often quantified in excess of 100 dB [11]-[13]. To achieve such high isolation, different cancellation layers are combined as illustrated in Figure 1.2. Cancellation at the antenna layer is the first line of defense against self-interference. The level of isolation achievable on subsequent layers strongly depends on the residual power level after antenna cancellation. For illustration, the analog to digital converter (ADC) dynamic range in the digital cancellation layer is the bottleneck of the maximum achievable cancellation in that layer [11]. A strong receive signal will lead to clipping, thereby increasing quantization error. This simple observation highlights the importance of achieving high isolation at the antenna layer. The past few years have shown a significant amount of research efforts aiming to increase the antenna layer isolation of STAR systems [14]-[37]. Researched cancellation techniques, depend on the used STAR aperture approaches. In bi-static STAR systems, separate transmit and receive antennas

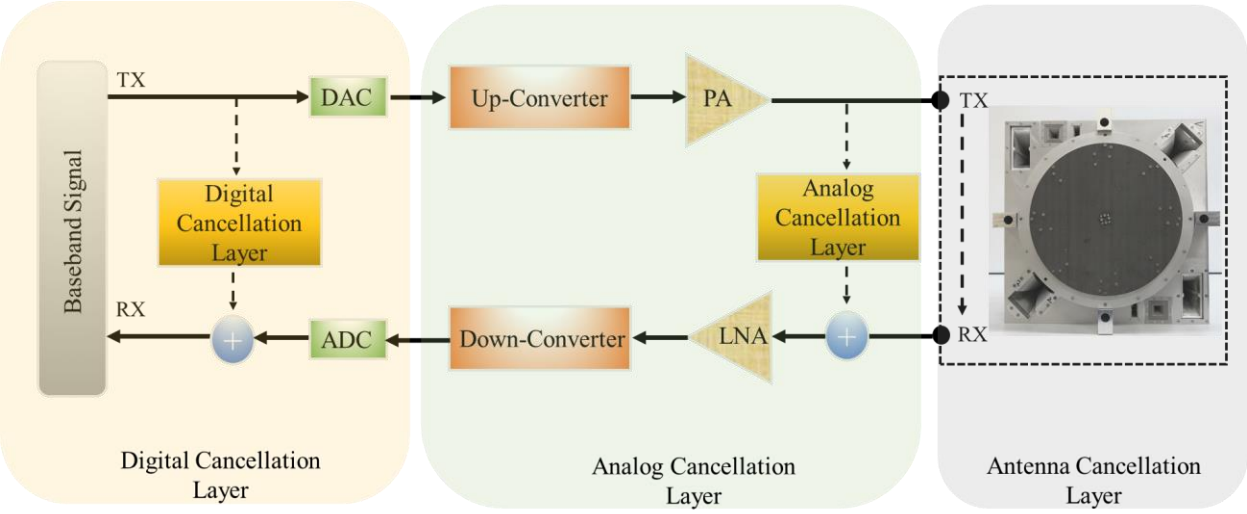

Figure 1.2: Illustration of different cancellation layer needed for functional STAR system

are used. The TX/RX isolation in this case is directly correlated to the physical separation between antennas and nearby scatterers [14]-[24]. In a monostatic STAR topology, a common aperture is used for transmit and receive. Isolation is achieved in this case by some combination of circulators, polarization diversity, and beamforming network configuration [25]-[37]. This topology strongly depends on geometrical symmetry and is therefore more sensitive to environmental effects, such as nearby reflections and imbalances of realistic components.

Beyond the increased spectral efficiency, STAR has the potential to significantly improve the performance of electronic warfare (EW) [38] systems by enabling concurrent electric support and electronic attack operations. STAR can also be built on top of conventional FDD systems to decrease the complexity of these platforms. This is of particular interest in duplex communications with narrow guard band between transmit and receive frequencies. This is illustrated in Figure 1.3, where typical rejection of a filter, needed to isolate the two channels of an FDD system is decreased from 80 dB to 40 dB.

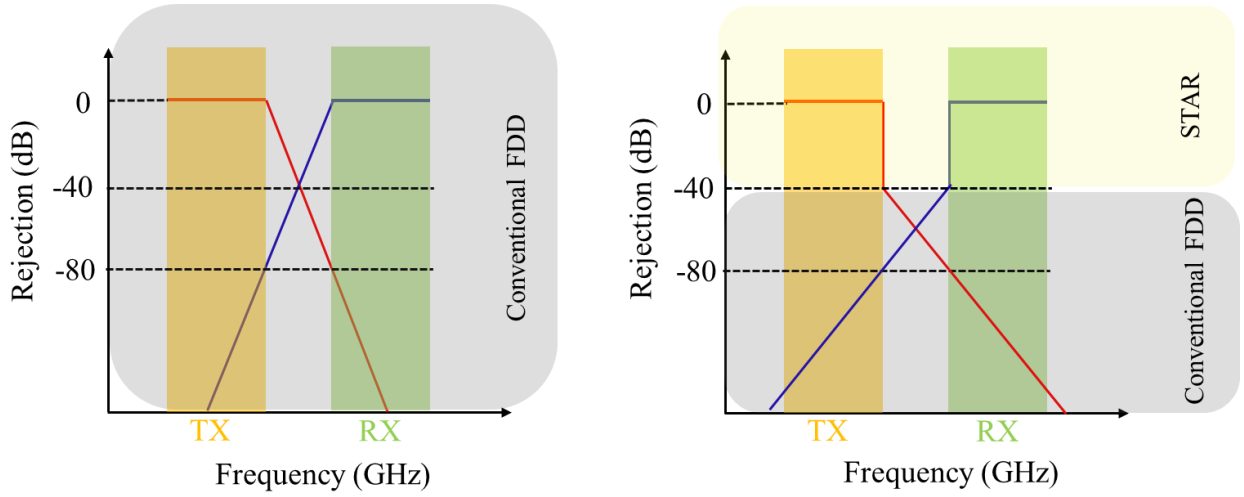

Figure 1.3: Illustration of hybrid STAR/FDD aiming to decrease the complexity of filters used in narrow guard band FDD systems: (a) conventional system, and (b) hybrid STAR/FDD.

This thesis presents the design of ultrawideband and narrowband antennas to be used in STAR systems. The ultrawideband antennas are designed to cover both S- and C-bands and are used in a bi-static compact shared antenna platforms. These antennas are designed for EW STAR systems. The narrow band antennas are designed to operate at X-band and are used in a hybrid STAR/FDD phased array system for a geostationary satellite.

1.2 Elements of EW STAR Systems

1.2.1 EW Antennas on Shipborne and Airborne Platforms

The search for enhanced capabilities of new generations of shipborne and airborne EW systems has resulted into a proliferation of antennas used on these platforms. For example, the number of antennas on a typical 1990-era destroyer is on the order of 80 [39]-[40]. This figure is expected to have significantly increased for present day deployed systems. The consequence of this proliferation of antennas on these platforms leads to numerous problems among which:

- Increase of radar cross section: the highly visible electromagnetic signature increases its vulnerability when platform is in a "silent" mode.
- Increase of co-site interference: interference decreases the signal to noise ratio, thereby leading to slower communication rate or blanking of its own systems.
- Increased mass, and space: which decreases the size and capabilities of the payload.
- Maintenance issues and associated costs: each antenna is unique for its kind and requires a unique set of spares and maintenance personnel.

To mitigate these issues, office of naval research (ONR) Integrate Topside is initiated to integrate several shipboard RF functions into a common aperture [40]-[42]. A demonstration of this system is presented in [22], and relies on a bi-static STAR active electronic scanned array (AESA). In [22], transmit and receive AESAs are heavily loaded

with RF absorbers to decrease electromagnetic coupling. The use of absorbers increases complexity, weight, cost, and may decrease the radiation efficiency of the system. Whereas lower efficiency may be acceptable for the receiver, in the transmit chain, more amplifications are needed to compensate for the drop in gain. The main challenge therefore is, to achieve high isolation with closely separated antennas, without any used of absorbers.

In this research, ultrawideband antennas covering the S- and C-bands are designed and integrated in a compact multi-antenna platform. It is demonstrated herein that these antennas can simultaneously transmit and receive with isolation > 50 dB while maintaining close physical separation between apertures.

1.2.2 EW Antennas for Concurrent S- and C-bands

Ultrawideband (UWB) antennas often used in EW systems must satisfy two equally important design challenges. In the RF domain, it is desired that antennas have wide bandwidth, low loss, high power, high gain, and some scanning ability. Dual-polarization is also researched for enhanced capabilities. From a mechanical perspective, the antennas are required to be compact given the limited space often available, and flush mountable to conform to the aerodynamics of the platform. For operations in S- and C-bands, different classes of radiators are often considered:

- Horn antennas: they are the radiator of choice when easy concealment is needed. They are all metal based with high radiation efficiency and gain. For S- and C-bands, they are typically fed with a coaxial adapter [43]-[44].
- Spiral antennas: they belong to the class of frequency independent antennas and are inherently circularly polarized. To generate a directional beam needed for EW applications, they are typically backed with a metallic cavity [46].
- Tapered slot antenna: this antenna element has intensively been used in UWB array and phased array systems [47]-[51]. It is flared to provide smooth transition from its

feed's impedance (typically 50 Ω) to 377 Ω (i.e. free-space intrinsic impedance). It can be designed for a decade bandwidth with an increase of its longitudinal length [52]-[53]. This large impedance bandwidth is obtained at the expense of degraded off-axis cross-polarization component in the diagonal plane [52]-[53].

Each of the above mentioned antennas are investigated for potential use at S- and C-bands on a shared antenna platform. Dual-polarized coax-fed quad-ridge horns have an asymmetrical response between orthogonal polarizations and degraded cross-polarization due to this feeding mechanism. Cavity-backed spiral antennas are predominantly loaded with RF absorber, thereby decreasing their radiation efficiency. Tapered slot antennas, also known as Vivaldi antennas can be arrayed and phased to scan their radiation to a precise direction; they are mainly backed with a metallic ground plane. Despite these great features when used as a standalone radiator, not much attention has been given to the flush mounted embodiment of these antennas.

In this research, the design of a single and dual-polarized all-metal, resonant-free, and cavity-backed Vivaldi antenna array is studied. Performances of this radiator when used in a STAR shared antenna platform are analyzed.

1.3 X-band Phased Array Antennas for Geo-Satellites

A phased array antenna is composed of groups of radiating elements distributed in linear or two-dimensional spatial configuration as shown in Figure 1.4. The radiating element, often referred to as unit cell can be a single radiator or a small array of radiators (subarray). The amplitude and phase of each unit cell can be independently controlled to scan the beam in a desired direction in space as shown in Figure 1.4. Phased arrays offer multiple advantages over gimbals based mechanical steerable systems. The rapid and accurate beam scanning allows these arrays to meet the small response time needed in applications such as, guided missile or-, radar tracking, just to name a few. In satellite

domain, which is of interest for this research, the difficulty to predict business needs over the 15+ years of a satellite mission, makes phased arrays attractive for a dynamic Earth coverage.

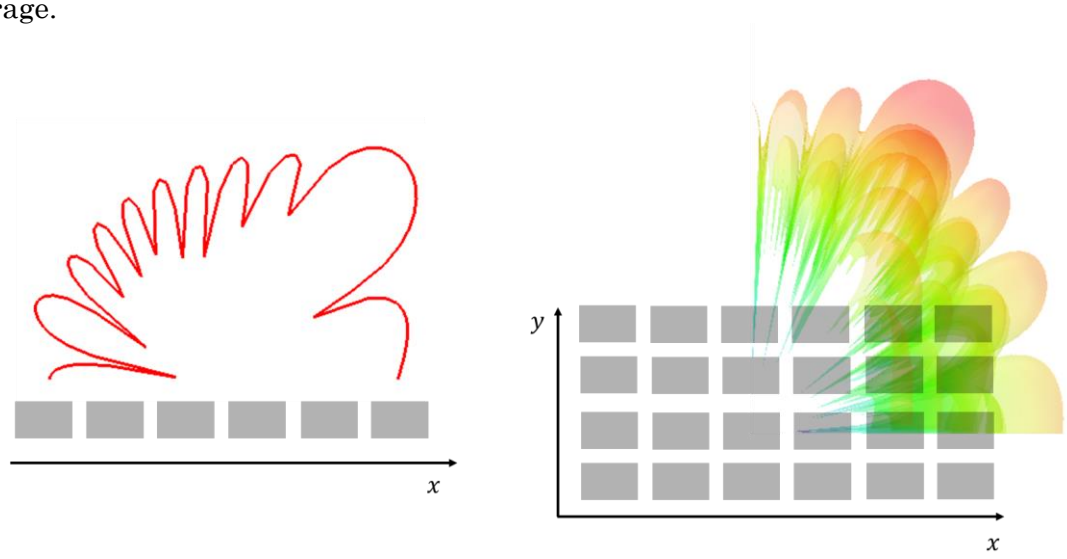

(a) (b)

Figure 1.4: Horn antennas in (a) linear array, (b) planar array.

1.3.1 Scan Array Theory

Elements of phased array are excited typically with varying phase to generate a directed beam in a given direction. This is of particular interest for satellite communications where international regulations may restrict the power density over certain countries [54]. In most implementations of phased arrays, the main requirement is to achieve maximum gain in the scan direction. These types of antennas, also called pencil beam arrays, are obtained by using a linear phase progression between the elements. This research mainly focuses on pencil beam planar phased arrays with array factor expressed as:

$$AF\ (\theta, \phi) = \sum_{n=1}^{n=N} I_n e^{[jk_0 sin\theta\{x_n cos\phi + y_n sin\phi\}]} \tag{1.1}$$

where (x_n, y_n) is the coordinate on the nth element and I_n is its complex excitation. For a general planar grid shown in Figure 1.5, the coordinate of the nth element can be expressed as:

$$x_n = pa + \frac{qb}{tan\alpha} \qquad y_n = qb \tag{1.2}$$

where p and q are two integers indicating that the nth element is located at the pth oblique column and qth oblique row. The unit cell separation in x and y directions are a and b respectively, and α represents the cell angle. One major requirement of phased array systems is to avoid the appearance of grating lobes within the desired field of view. For a square array to scan over $\pm\theta_0$ in all planes without any grating lobe appearance, the following condition must be satisfied [55]:

$$a \leq \frac{\lambda_0}{2sin\theta_0} \tag{1.3}$$

For a satellite located at the geostationary orbit, $\theta_0 = 8.7^\circ$ is needed for visible Earth coverage. This therefore implies that $a \leq 3.3\lambda_0$ (λ_0 is the wavelength in free space at the highest operating frequency).

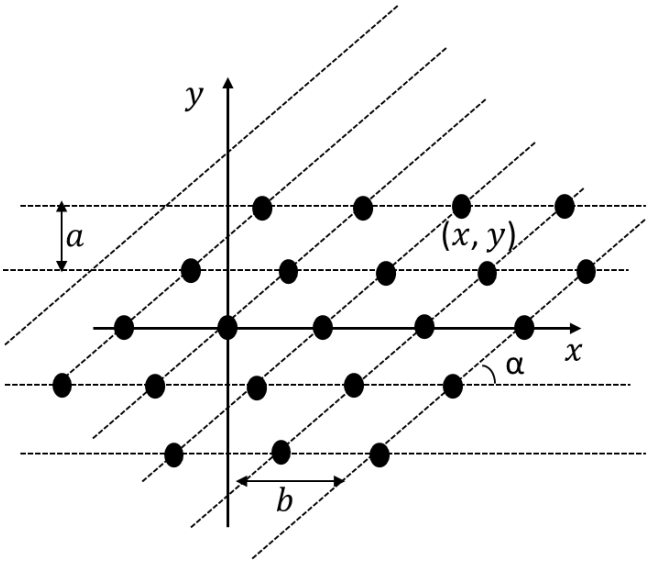

Figure 1.5: General grid representation for planar phased array.

The second important parameter in the design of a phased array system is the scan loss. The maximum acceptable scan loss must meet the edge of coverage (EoC) requirement of the mission. For a uniformly illuminated pencil beam array with spacing between elements given by a, the maximum scan loss for a beam directed at θ_0 off boresight is:

$$Scan\ loss\ at\ \ \theta_0 = 20log\frac{Gain(0,0)}{Gain(\theta_0,0)} \tag{1.4}$$

where $Gain(0,0)$ is the co-polarized boresight gain, and $Gain(\theta_0,0)$ is the co-polarized off axis gain at θ_0 calculated as:

$$Gain(\theta_0,0) = \sqrt{\frac{4\pi a^2}{{\lambda_0}^2}}\frac{sin[k_0 asin\theta_0/2]}{k_0 asin\theta_0/2} \tag{1.5}$$

The scan loss for different unit cell spacing is plotted in Figure 1.6. As seen, decreasing the unit cell spacing decreases the scan loss. Smaller spacing will further increase the grating lobe-free field of view of the array. Larger spacing is however,

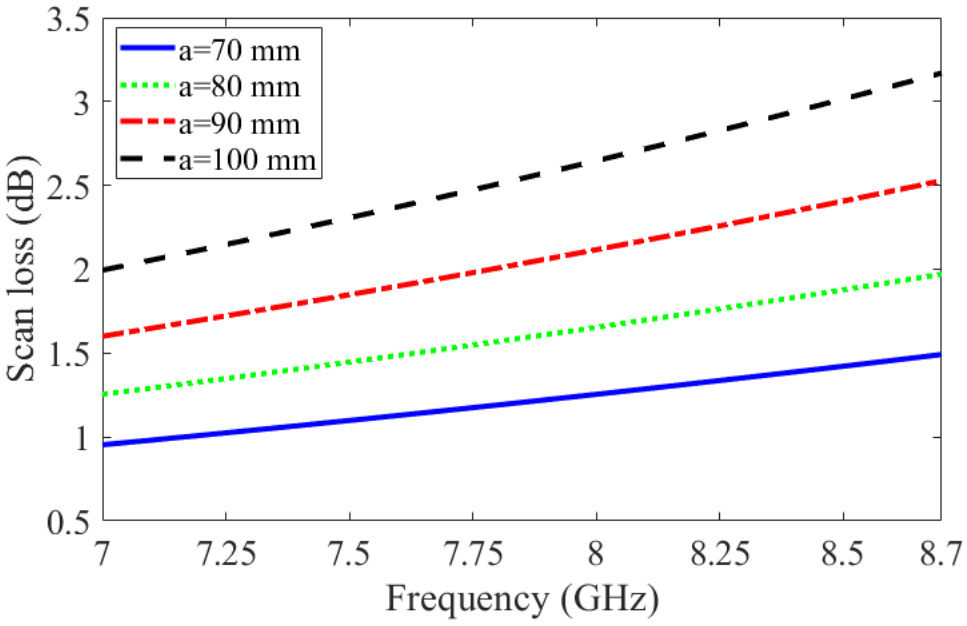

Figure 1.6: Scan loss at 8.7° versus frequency for different array spacing

preferable in order to decrease the number of array elements for a given physical aperture. The highest operating frequency analyzed in this work is 8.4 GHz, $a = 100\,mm = 2.8\lambda_{8.4\,GHz} \leq 3.3\lambda_{8.4\,GHz}$ is therefore chosen. This size allows for some margin with respect to satellite movement within its controlled box.

1.3.2 Transmit-Receive Isolation in FDD systems: Why

The schematic of a 9-element active TX/RX phased array is shown in Figure 1.7. On the transmit side, a phase shifter, power amplifier (PA), and transmit filter are connected to each subarray. Each receiving subarray is attached to a receive filter, LNA, and phase shifter. Depending on the geometry, transmit and receive antennas may share the same aperture. In an ideal frequency division duplex system, no front end filter is required given the non-overlap frequencies. In realistic full duplex systems, spurious out of band emissions from the PA will couple to the receive antenna. This power can be high enough to bring the LNA to compression or increase the receiver noise floor. Transmit and receive filters shown in Figure 1.7 are therefore designed to attenuate these undesired emissions.

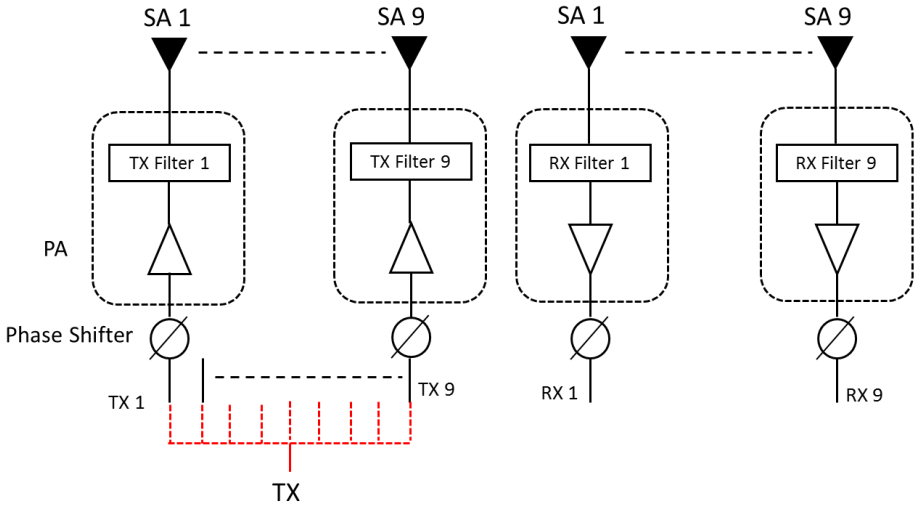

Figure 1.7: Schematic of an active phased array system where the subarray units are separated only for presentation purpose.

The transmit filter should attenuate the following voltages:

- The transmit noise coupling into the receive band: the transmitter noise that falls inside the receive band cannot be filtered out. The transmit filter should therefore provide enough attenuation to bring this noise below the receiver noise floor.
- Inter-modulations (IM) coupling into RX band: odd order IM of the power amplifier can fall inside the receive band and will need to be significantly attenuated by the transmit filter. Even order IM are typically out of the RX band, they however still need to be filtered out by the receive filter to prevent LNA saturation.

The receive filter should attenuate the following signals:

- TX signal coupling into the LNA band: to avoid LNA saturation, the coupled transmit signal which is out of the receiver band should be reduced.
- IM3 obtained from out of band TX coupled signal and in band receive signal: the TX signal coupled to the LNA may be low enough to not be a threat to LNA saturation. It can however combine with the receive signal to create a third order intermodulation in the RX band, thereby increasing the noise floor.

Typically, isolation as high as 140 dB is needed to enable simultaneous transmit and receive operation in an active phased array system.

This research provides alternative techniques to obtain high isolation in an X-band active phased array by either eliminating the filters in the architecture or decreasing their required complexity.

1.4 Thesis Organization

The thesis is organized as follows:

- Chapter 2 introduces the design of a single-polarized cavity-backed Vivaldi array antenna operating over the S- and C-bands. Design techniques to have a 3 × 4 Vivaldi antenna array with a resonance free response when recessed inside a

lossless metallic enclosure are presented. A cost effective fabrication technique based on multi-layer stacked PCB is discussed. Scan performance of this antenna and its comparison with a respective free standing embodiment are also discussed. A more compact and simple single-polarized antenna is proposed based on the developed design concepts for the final use in a compact 12" × 12" shared antenna platform.

- Chapter 3 introduces a dual-polarized configuration of the resonance free 3 × 4 Vivaldi array to demonstrate that the design techniques proposed in Chapter 2 can be extended to dual-polarized operation. A simplified cavity-backed 2-element array is also introduced for the practical implementation on the dual-polarized 12" × 12" platform. A stripline power divider/combiner operating from 1.5 to 8 GHz is designed and integrated with the antenna in a compact form. Techniques to increase transmit receive isolation when two of these antennas are mounted on a ground plane are also discussed.
- Chapter 4 introduces a dual-polarized OMT-free and all-metal subarray to be used as a unit cell of an X-band phased array. The proposed subarray STAR architecture eliminates the need for a diplexer which complexity has so far been one of the limiting factor for dual-polarized functionality. Design of different passive microwave components to be used in the proposed system is described.
- Chapter 5 presents an alternative dual-polarized X-band phased array architecture that relies on a diplexer. The proposed system decreases the complexity of the required diplexer while maintaining high aperture efficiency and a compact footprint. The magneto-electric dipole antenna is used as a radiator and detailed description of its design for improved mechanical robustness is discussed.
- Chapter 6 concludes the thesis, reviews the contributions, and highlights future directions.

Chapter 2

Single-Polarized STAR Antennas

2.1 Overview

Key requirements of EW systems include high power capability needed to blind the enemy; high receiver sensitivity to increase situation awareness; and mechanical robustness. Antennas that meet these key requirements are preferably wideband, all metal to handle high power, and flush mountable to conform to the aerodynamics of the platform. In recent years, tightly coupled arrays have been considered for such demands [56]-[60]. A close separation between elements is used therein to increase scanning bandwidth. Since Munk's used wire array elements to describe the principle of operation of this class of radiators [61], different unit-cell elements have been researched including dipoles [57], bowtie [58], patch [62], and Vivaldi [63]-[65], just to name a few. Despite, all these cited work may satisfy some of the RF requirements, they are not designed to be flush-mounted in a compact way and are usually backed by a large ground plane. While this ground plane may be used to mitigate back radiation, the exposed profile of the antenna is an issue for its practical use when aerodynamic and conceal needs are important.

Design of ultrawideband cavity-backed antennas is challenging given the deleterious impact of high quality factor (Q) cavity resonances on antenna performance. Lossy materials such as absorbers are often placed near the surface of the cavity to dampen these high-Q resonant modes [66]. This; however, can lead to a degradation of antenna efficiency.

Another approach often used is to increase the separation between the antenna and the cavity in order to reduce their respective coupling [67]-[69]. This is done at the expense of an increased overall size; thereby deflating a wider use of these antennas and arrays.

Only few design attempts of a flush-mounted Vivaldi antenna are reported in open literature [70]-[73]. In [70], a Vivaldi element is placed in a cylindrical cavity; yet, the bottom of the cavity is kept open to eliminate cavity modes. However, this approach makes the RF isolation of backend electronics nearly impossible. In [71], the size and the shape of a trapezoidal cavity is increased to mitigate its interaction with the antenna within the operating bandwidth leading to a relatively large, non-compact, flush-mountable structure. In, [72], only the feed region is backed with a cavity leaving the radiating section free-standing. A circular cavity loaded with absorber is presented in [73] for receive-only direction finding. While this antenna may be suitable for receiving applications, the reduction in efficiency is not acceptable for prime power needy RF uses.

In this chapter, a design approach that led to a resonant free 3 × 4 Vivaldi antenna array fully recessed inside a lossless metallic cavity is discussed. A parametric study is performed to evaluate effects of the antenna proximity to the side walls in two principal planes. Eigen-mode analysis is used to study antenna-cavity interaction in both E- and H-planes. The proposed 3 × 4 array is fabricated using a multilayer stacked all-metal circuit board technique [74]. The scan performance of the fabricated array is investigated using measured active element patterns and compared to its free-standing embodiment. The findings on the 3 × 4 array are used to develop a simplified single feed compact antenna. The performances of the two designed antennas when used in a co-polarized STAR platform are investigated; more precisely, simulated and measured TX/RX isolation of the STAR antenna and the impact of nearby scatterers on the antenna performances.

This chapter is organized as follows:

- Section 2.2 shows the analysis and design of a cavity-backed all metal Vivaldi antenna recessed inside a metallic cavity is discussed.
- Section 2.3 presents a single feed and reduced aperture cavity-backed Vivaldi antenna.
- Section 2.4 analyzes the bi-static STAR capabilities of the antenna configurations of Section 2.2 and 2.3. Performances of the antennas when integrated on compact antenna platforms are discussed.
- Section 2.5 summarizes the chapter.

2.2 Single-Polarized 3 × 4 Cavity-Backed Vivaldi Antenna Array

2.2.1 Antenna Analysis and Design

The geometry of the unit-cell of the proposed array and its parameters are shown in Figure 2.1 and Table 2.1. To maintain low side-lobe level (SLL) over the 1.5 – 7.5 GHz bandwidth (chosen to cover S and C bands), the unit-cell width W is chosen to be 18 mm ($\lambda_{8\ GHz}/2$). To enable easy attachment of a coaxial connector, the thickness of the element is chosen to be 6 mm ($\lambda_{1.5\ GHz}/33$). The advantages of a thick Vivaldi antenna have been previously reported in [75]. The feed region of the unit-cell, including the transition from the coax to the slotted section of the element is highlighted in Figure 2.1. Also shown is the slotted section of the unit-cell which is seen to be better assimilated to a parallel plate waveguide given its thickness. The width i between the two plates is chosen for a 50 Ω characteristic impedance. To reduce the discontinuity at the coax to parallel plate transition, a 50 Ω air-filled rectangular coaxial line is implemented [76]. This transition is further improved by equating the plate thickness to the width of the inner conductor of the rectangular coaxial line.

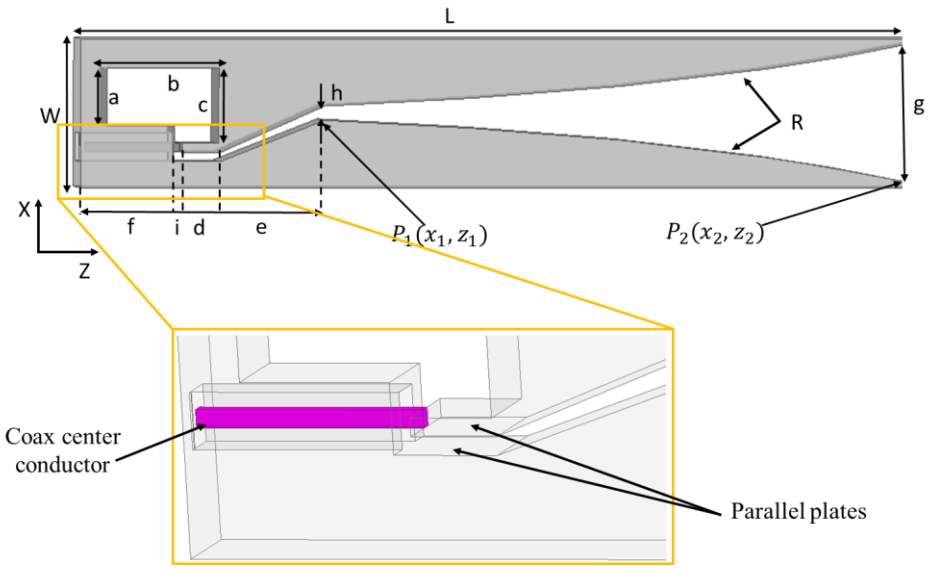

Figure 2.1: Unit-cell of the proposed array with characteristic parameters denoted.

Table 2.1: Design Parameters of Array Unit-Cell (in mm)

Parameter	a	b	c	d	e	f
Value	8	14	11	5.13	13.97	12.54
Parameter	g	h	i	W	L	R
Value	17	1.72	1.1	18	112	0.2

Other parameters are determined based on an infinite array analysis [55] aimed to achieve wideband impedance match at a reduced computational cost. It is found that the main parameters affecting VSWR are the exponential growth rate (R), the length (L), and the open cavity delimited by segment ($a - b - c$) shown in Figure 2.1. The impedance match bandwidth increases with an increase of the length L which is chosen to be ~ $\lambda_{1.5\ GHz}/2$, to keep the overall profile of the array low. An exponential taper is used to describe the flaring section of the aperture with profile equation described as,

$$x = R_1 e^{Rz} + R_2 \tag{2.1}$$

where

$$R_1 = \frac{x_2 - x_1}{e^{Rz_2} - e^{Rz_1}} \tag{2.2}$$

$$R_2 = \frac{x_1 e^{Rz_2} - x_2 e^{Rz_1}}{e^{Rz_2} - e^{Rz_1}} \tag{2.3}$$

The growth rate R is chosen between 0 and 1, with 0 being a linear taper. Values of R close to zero increase gain at lower frequencies. When R = 0, the discontinuity between the feed and the flare section is increased, leading to the degradation in impedance match. Increasing the size of the open cavity improves the match at low frequencies; however, its fundamental resonant frequency is lowered. The size of this cavity is adjusted to have its fundamental resonant frequency above 7.5 GHz.

The active VSWR of a tightly coupled infinite array composed of unit-cells with parameters from Table 2.1 is shown in Figure 2.2. The infinite array response is used to guide the selection of a finite 3 × 4 free-standing array also shown in the same figure. The computed VSWR of this 3 × 4 array fed with ideal 12-way power divider is plotted in Figure 2.2. As seen, VSWR < 2 is obtained above 2.5 GHz therefore verifying the usefulness of parametric studies conducted with infinite array. As expected, the infinite array has better match at lower frequencies. The finite array approaches the infinite array model as the number of elements is increased; however, the 3 × 4 array is chosen as compromise between the size, desired minimum gain of 5 dBi, and desired turn-on frequency around 2 GHz.

Effect of recessing the designed 3 × 4 Vivaldi array in a rectangular metallic enclosure, as illustrated in Figure 2.3, is now analyzed. The bottom side of the array is connected to the cavity base. Offset distances, D_x and D_y, are kept between the array and the cavity side walls in H- and E-plane, respectively. The center-to-center separation between the array elements in H-plane, D_s, is kept equal to the unit-cell width W to maintain low side-lobe levels in the H-plane cut. Cavity height is kept equal to the unit-cell

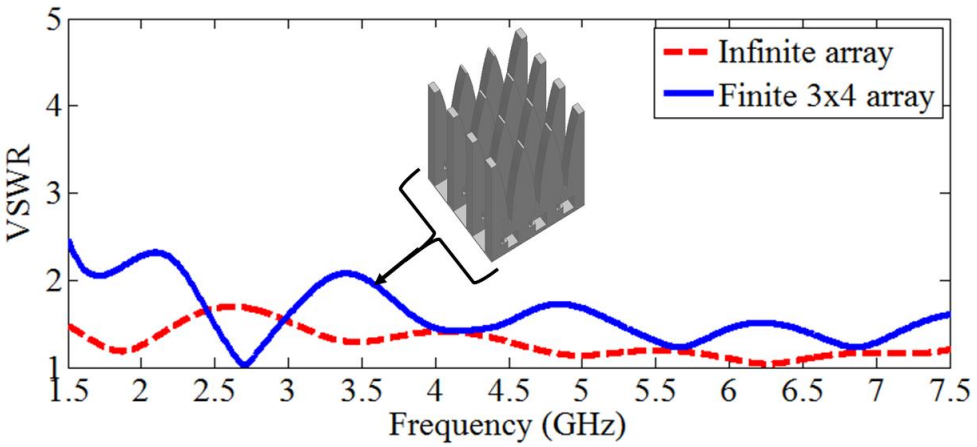

Figure 2.2: Active VSWR of an infinite and finite 3 × 4 Vivaldi arrays. The 3 × 4 array is fed using ideal 12-way power divider in this analysis.

length L. Three elements are connected in E-plane to form a single row of the array. The values of D_x and D_y are varied and the cavity-backed array performance analyzed. Offset distance D_x is set respectively to 0, 1, 5, and 40 mm while keeping $D_y = 20$ mm. A zero offset means a direct connection between the array and the cavity walls, while offset values equal

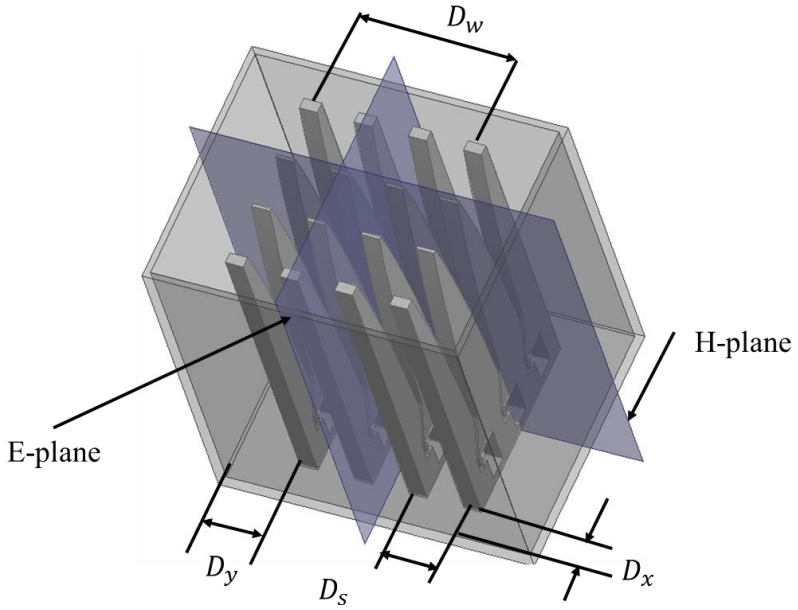

Figure 2.3: Geometrical arrangement of the recessed 3 × 4 array antenna inside a cavity with depicted E- and H-planes.

to 1 mm and 40 mm are used to investigate respectively strong and weak interaction with the cavity. The simulated VSWR and broadside gain of the uniformly excited cavity-backed array are shown in Figure 2.4 for different values of D_x. As seen, periodic dips in broadside gain correlated with spikes in VSWR are observed at specific frequencies for nonzero value of D_x. As D_x keeps increasing the spikes get broader. In this research, our focus is on a compact design where the cavity is brought closer to the antenna.

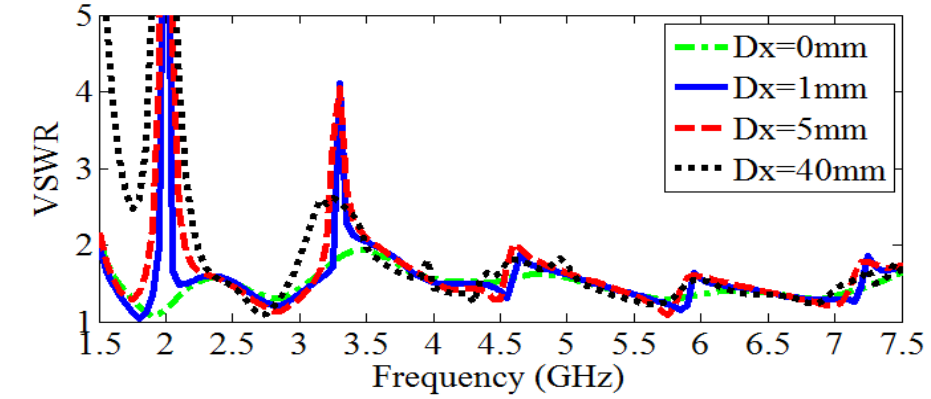

(a)

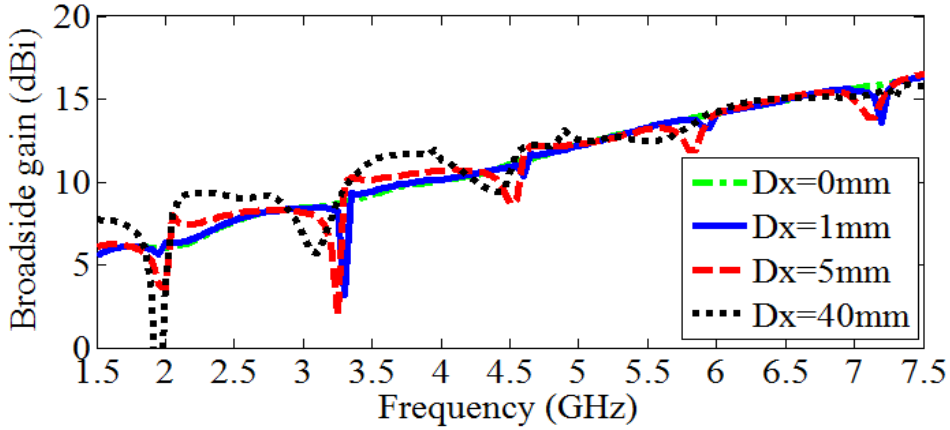

(b)

Figure 2.4: (a) VSWR, and (b) Broadside gain of the 3 × 4 Vivaldi array recessed in a cavity with varying separation between the H-plane wall and the cavity.

To better understand these phenomena, the surface currents on the H-plane cavity wall (cavity wall parallel to array H-plane) are plotted in Figure 2.5(a) at 1.95 GHz, 2.35

GHz, 3.2 GHz, and 4.45 GHz for D_x = 5 mm. As seen, standing waves patterns are clearly formed at 1.95 GHz, 3.2 GHz, and 4.45 GHz. It is observed that the surface current at 2.35 GHz is different and does not reveal a standing wave, suggesting that the spikes observed in the gain and VSWR plots are due to the established standing waves at these frequencies.

To determine the origin of the standing waves at frequencies shown in Figure 2.5(a), Eigen-mode analysis is performed using ANSYS HFSS [77]. It is observed that with perfect magnetic conductor (PMC) boundary placed at the aperture, only a little effect is seen on a driven solution with standing waves described above still present at the same frequencies. The PMC boundary is therefore used to model the cavity aperture in the Eigen-value problem. Setting D_x to 5 mm, the Eigen-mode analysis is shown to reveal several resonant modes in the desired band. The surface currents on the H-plane cavity wall are shown in

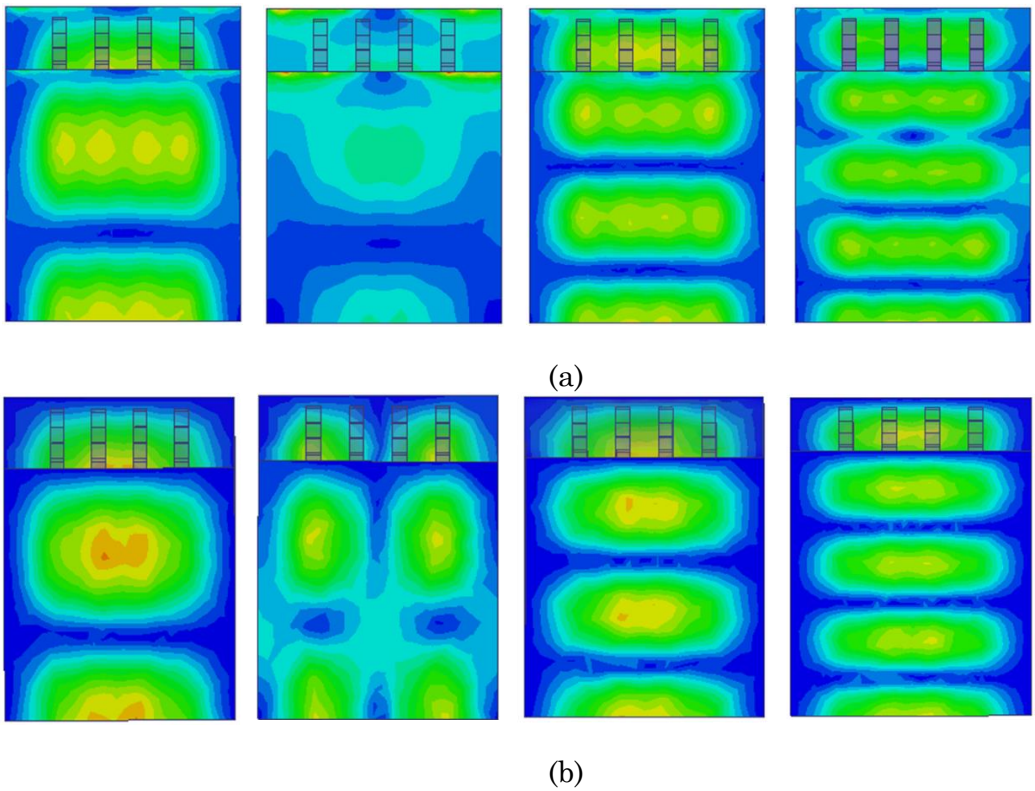

Figure 2.5: Surface currents on the H-plane cavity wall when *Dx*= 5 mm, obtained with (a) driven, and (b) Eigen analysis method.

Figure 2.5(b) for the resonant modes at 1.98 GHz, 3.3 GHz, 2.35 GHz, and 4.64 GHz. As seen, these cavity modes have similar surface current distribution to currents shown in Figure 2.5(a) when the array is uniformly excited. The establishment of the standing waves and thus the gain and VSWR deterioration can therefore be attributed to the excitation of these undesired resonant modes. It can further be seen that the driven mode current distribution at 2.35 GHz is different to the Eigen-current at the same frequency, which implies that this resonant mode is not excited by the array.

The Eigen-mode analysis above is used to confirm the resonance behavior of the antenna at some frequencies but it does not explain why these specific modes are excited. It is found that the cavity E-plane wall, located at D_y = 20 mm for the purpose of this analysis has no impact on the discussed resonance behavior. To demonstrate this, the broadside gain of the open boundary array (E-plane cavity wall removed) is shown in Figure 2.6. As seen, a similar response to Figure 2.4(b) is obtained. It therefore appears that the cavity resonances are excited by another resonating structure. The surface currents at 4.6 GHz for

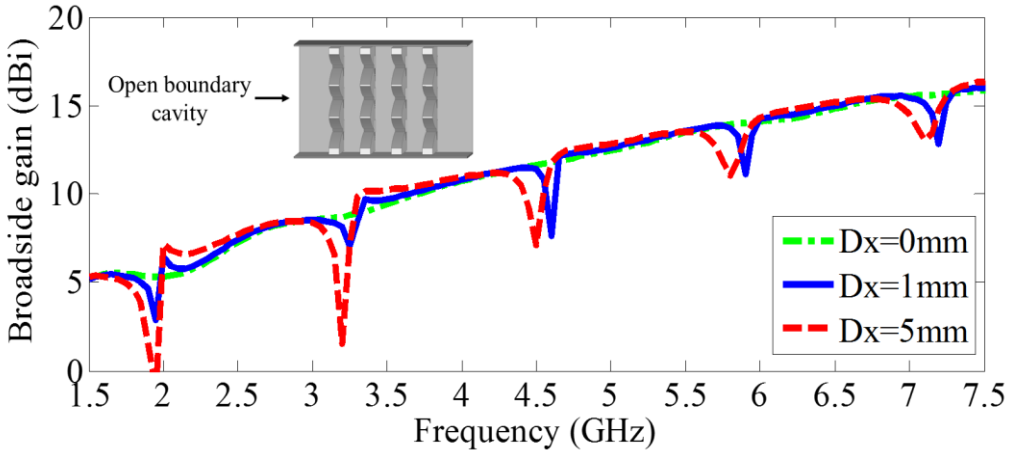

Figure 2.6: Broadside gain of the 3 × 4 Vivaldi array inside an open boundary cavity, as shown in the inset.

this configuration are shown in Figure 2.7. As seen, the standing waves are mainly localized at the edge elements, specifically at the gap between these edge elements and the

H- plane cavity wall. A magnified view of this section of the antenna with a single row represented is shown in Figure 2.8. Given that currents flowing on the edge elements are seen to be localized mainly at the outer boundary, the edge elements can be replaced by a

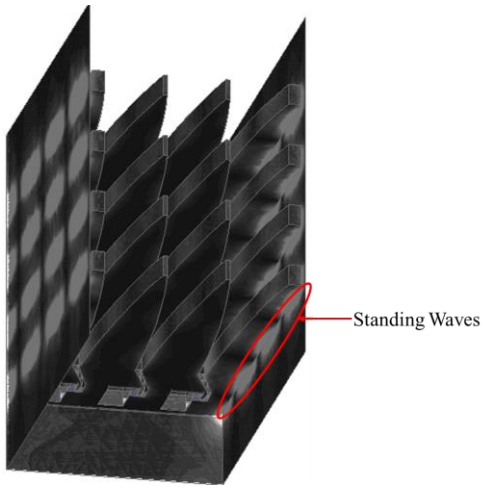

Figure 2.7: Surface currents at 4.6 GHz on the H-plane cavity wall when D_x = 1 mm for the open boundary array.

thin strip without perturbing its current distribution. The combination of this strip, the air gap and the cavity wall forms a quasi-TEM microstrip line; the ground plane being represented by the cavity wall, and an air dielectric materialized by the gap D_x. This line, shorted at the bottom by the cavity base and open at the top, resonates and its resonant frequency can be calculated analytically based on the length of the antenna for different resonant modes as,

$$f_{res} = \frac{(2n+1)c}{4L} \tag{2.4}$$

where c is the speed of light, L is the length of the antenna as denoted in Figure 2.2, and n is the order of the resonance modes.

The resonant frequencies calculated analytically and given in Table 2.2 are seen to be nearly identical to the frequencies at which spikes are occurring.

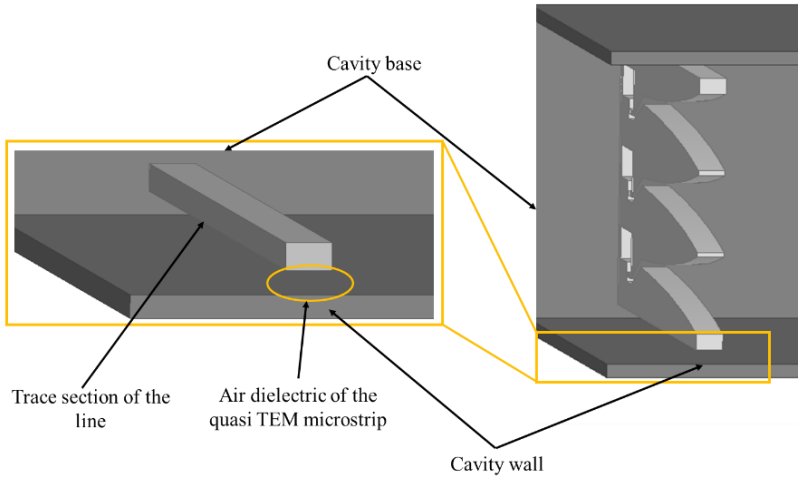

Figure 2.8: Illustration of the interface between array edge elements and the cavity as a quasi TEM microstrip line

Table 2.2: Analytical (Cal.) and full-wave Simulated (Sim.) resonant frequencies (in GHz)

n	0	1	2	3	4
$f_{resonance}$ (Cal.)	0.67	2.08	3.34	4.68	6.02
$f_{resonance}$ (Sim.)		1.95	3.2	4.5	5.9

From this analysis, it can be concluded that the space between the array edge elements and cavity wall provides a transmission line medium for the currents to flow. Resonance occurs as these currents bounce back and forth after seeing an open circuit at the aperture and short circuit at the cavity base. At lower frequencies, currents are weakly radiating before reaching the aperture therefore resulting in a stronger interaction with the cavity. This combination of strong cavity interaction and low radiation results in high Q resonant modes as observed in the VSWR at 1.95 GHz in Figure 2.4(a). At higher frequencies, more currents radiate before reaching the aperture resulting in the reduced Q.

To mitigate the negative impact of these resonances, two approaches are investigated. First, the resonator section of the antenna is resistively loaded. The gain and VSWR are shown in Figure 2.9(a) and Figure 2.9(b) for 50 Ω and 150 Ω respectively. These two values are chosen to assess the effect of low and high resistances. As seen, resonances are eliminated as resistors dissipate part of the reflected currents, thereby contributing to the improved impedance match at low frequencies as seen in Figure 2.9(b). Computed antenna efficiency is 78 % at 2 GHz and over 90 % above 3.5 GHz. While this reduction in efficiency is acceptable for most receiving applications, it is undesired for this research where DC energy resources are scarce.

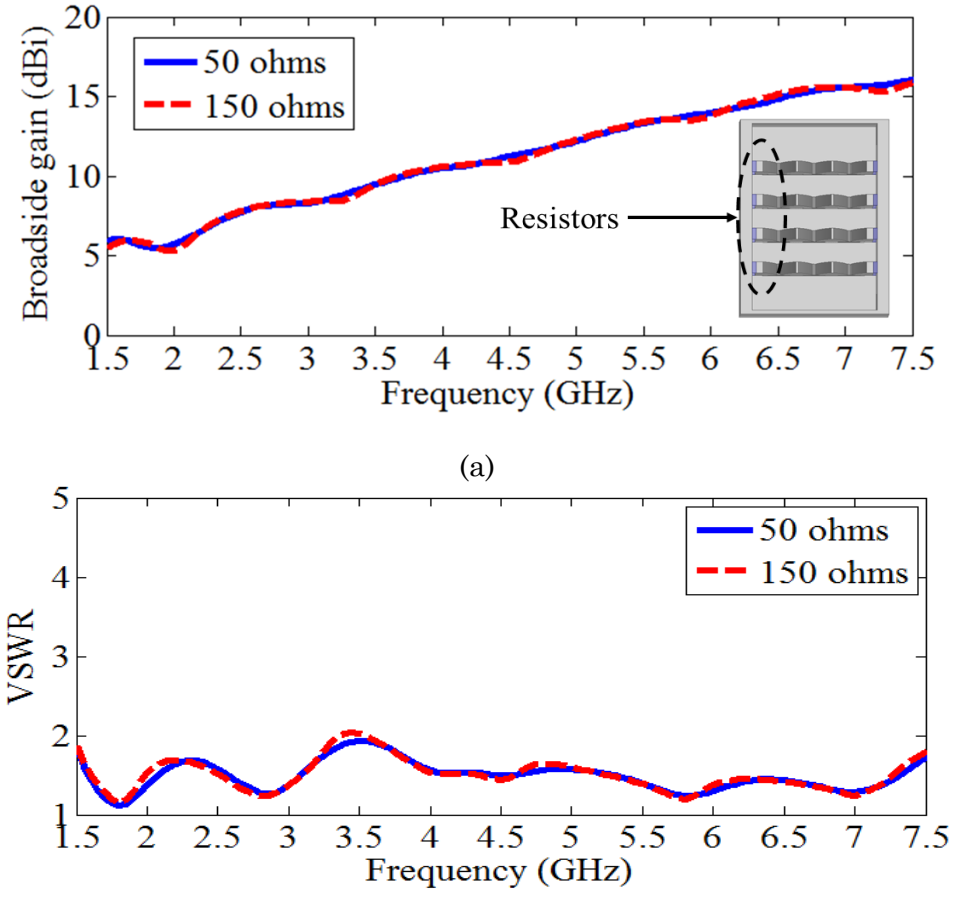

Figure 2.9: Performance of the 3 × 4 cavity-backed Vivaldi array with edge elements terminated with resistors: (a) broadside gain, and (b) VSWR.

The objective of the second approach for mitigating the impact of resonances is to eliminate their topology-related origin. These resonances exist due to the gap between the array edge elements and cavity. This gap is eliminated by shorting the array edge elements to the cavity and therefore, means for establishing standing waves on that cavity wall are eliminated. Interestingly, this approach is the exact opposite of common techniques relying on recessing linearly polarized antenna in a metallic enclosure [67]-[69]. Rather than increasing the separation between the antenna and the cavity, the E-plane wall of the antenna should be shorted to the cavity. The second approach does not need resistive termination and is adopted in this research.

For complete analysis, the interaction with the E-plane cavity wall is investigated next. To do so, D_x is kept at zero as it is shown to yield better response and D_y is swept from 10 to 20 mm with a step of 5 mm. The VSWR and broadside gain response for uniformly excited array are shown in Figure 2.10. As seen, E-plane separation does not reveal any noticeable resonance. Nonetheless, the E-plane separation is critical in determining the turn on frequency as seen in VSWRs of Figure 2.10(a). The separation D_y should be high enough to achieve the desired turn-on frequency and minimum gain, but small enough to mitigate the excitation of high order waveguide modes. To maintain a gain > 5 dBi and a turn on frequency at 1.5 GHz, D_y is set to 20 mm.

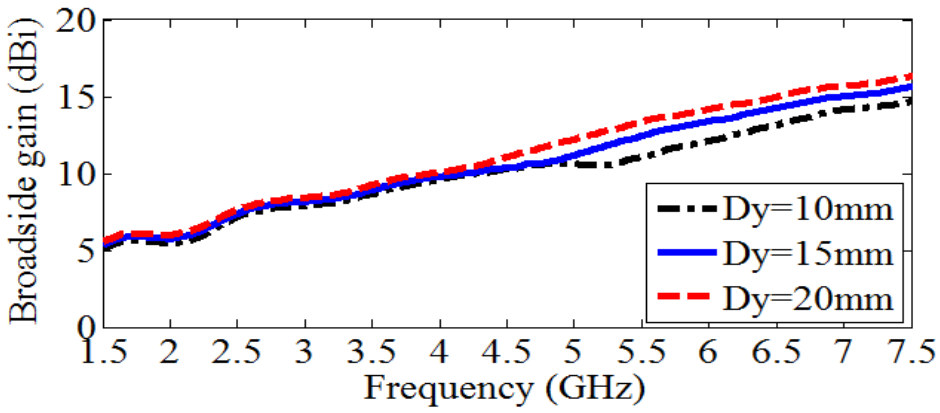

(a)

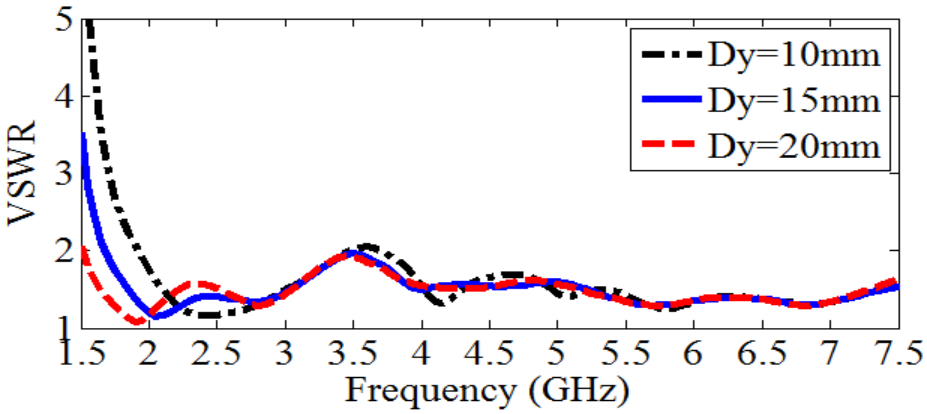

(b)

Figure 2.10: (a) Broadside gain, and (b) VSWR of the 3 × 4 Vivaldi array recessed in a cavity with varying separation between the E-plane wall and the cavity.

2.2.2 Array Fabrication and Measured Performance

The 3 × 4 Vivaldi array and the cavity are fabricated separately using cost-effective manufacturing techniques. Individual rows of the array are assembled by stacking seven printed circuit boards (PCB) to form the thick geometry as shown in Figure 2.11. The utilized PCB stacking process allows the thin inner plate of the coax to parallel plate transition to be easily machined compared to the conventional CNC-machining. When all the 0.85 mm-thick boards are stacked together, the total row thickness is about 6 mm as shown in Table 2.1. Boards 1, 2, 6, and 7 form the bottom and top layers. They are also used to form the bottom and top walls of the rectangular coaxial line, whereas boards 3 and 5 form the side wall. Board 4 is the middle layer and contains the center conductor of the rectangular coax. This central conductor is soldered to the center conductor of a surface mount SMA connector as shown in Figure 2.11. Once the connectors are attached to the antenna, the top 3 layers are added to complete the fabrication of a single row. The seven boards are held together using screws as shown in Figure 2.12(a), where an assembled row is presented. The rectangular cavity shown in Figure 2.12(b) is fabricated using additive manufacturing and plated with a 1.5 oz copper layer. Rectangular holes at the bottom of the

cavity are added to enable mounting of SMA connectors (Figure 2.11). The flush-mountable array is finally obtained by fixing each row into the groove space available in the rectangular cavity, as shown in Figure 2.12(c).

The measured and simulated VSWRs of the prototyped cavity-backed array with uniform excitation is below 2 over 5:1 bandwidth, as seen in Figure 2.13. The ripple in the measured results is due to the coaxial cables not present in the model.

Boards 1, 2, 6, and 7

Boards 3, and 5

Board 4

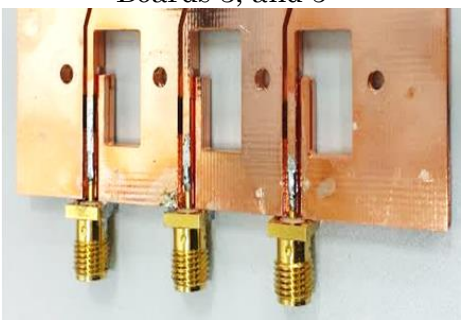

Integration of SMA connectors

Figure 2.11: Illustration of the assembly for the array row: Boards 1, 2, 6, and 7 form the bottom and top layers. Boards 3 and 5 are used to form the sidewall of the rectangular coaxial line. Board 4 is the center layer and is used to solder the inner conductor of the coaxial feed line.

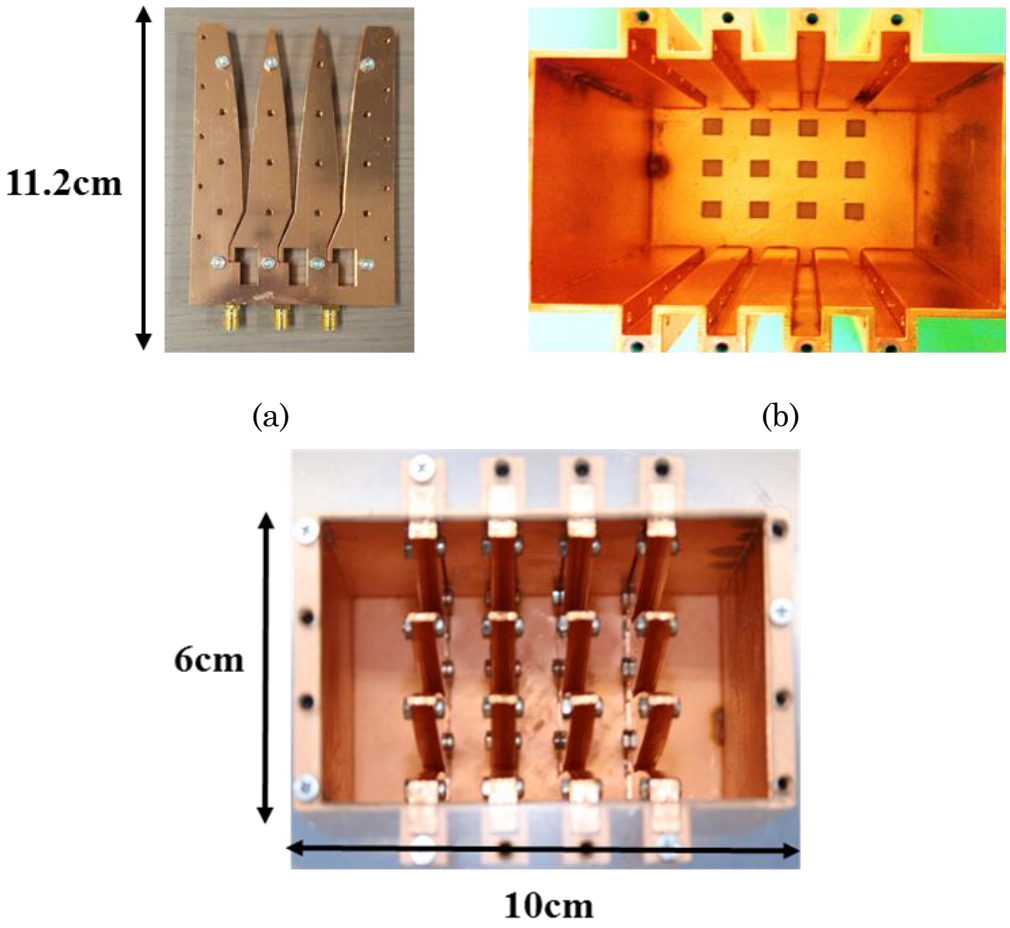

Figure 2.12: Photograph of the prototyped cavity-backed 3 × 4 Vivaldi antenna array: (a) Single row of the array, (b) 3D-printed and copper plated rectangular cavity showing the longitudinal groove reserved for each row of the array, and (c) fully –assembled array recessed in the cavity.

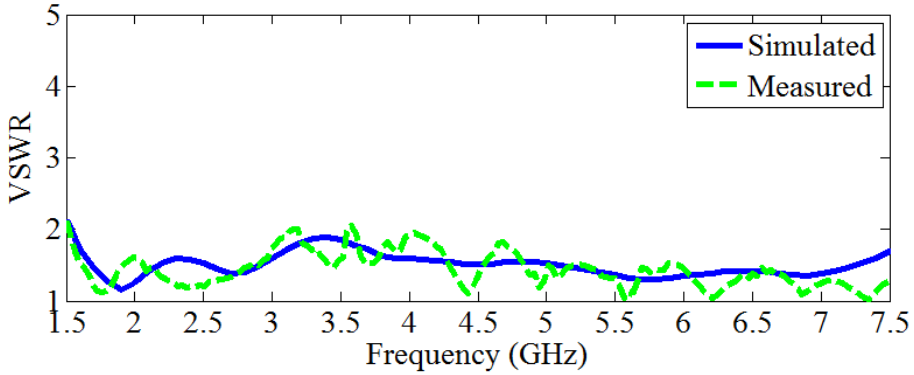

Figure 2.13: Measured and simulated VSWRs of the uniformly excited cavity-backed array.

The measured and simulated broadside gains and the theoretical gain of a uniformly-excited aperture antenna of identical aperture size as the cavity are plotted in Figure 2.14. As seen, measured gain is similar to the gain of the uniformly excited aperture antenna from 2.5 to 7.5 GHz. It can also be observed that the designed array has higher gain than the uniformly-excited aperture at low frequencies. This is due to the fringing fields which contribute to the increased electrical size of the aperture at these frequencies. Gain above 5 dBi is obtained at 1.5 GHz, and its value increases monotonically over the operating band reaching 15 dBi at 7.5 GHz. The aperture efficiency of the developed

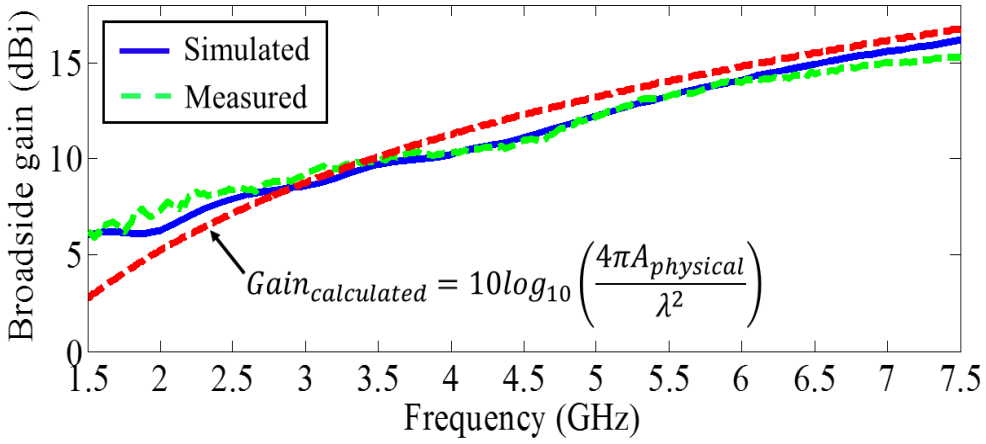

Figure 2.14: Measured and simulated gains of the designed array. The gains are compared to that of a uniformly excited aperture with identical aperture size.

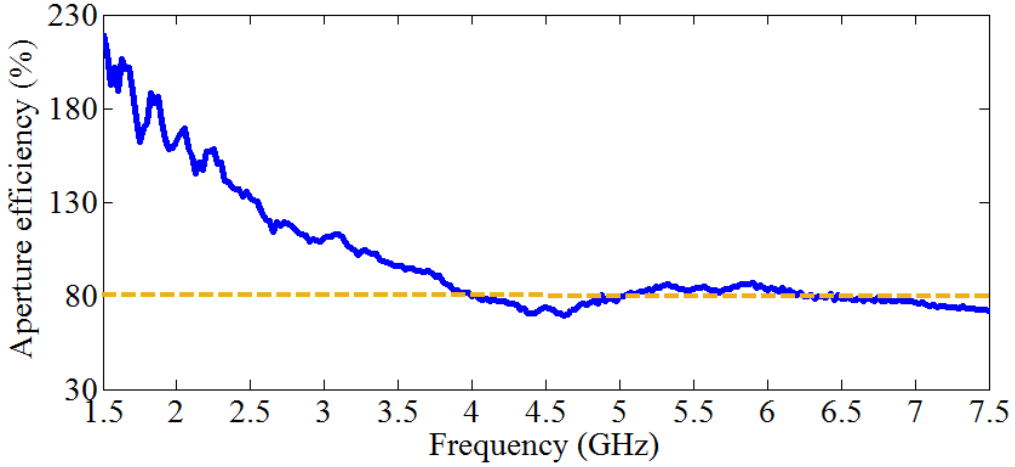

Figure 2.15: Aperture efficiency of the proposed antenna calculated with respect to a physical aperture of 60 × 100 mm².

configuration shown in Figure 2.15 is > 80% over most of the bandwidth. This high aperture efficiency is a result of the combined effect of the tightly-coupled Vivaldi array and the cavity where the proposed arrangement creates a nearly uniform aperture illumination. The aperture efficiency is also seen to be > 100% at lower frequencies due to the fringing fields contributing to increase the electrical size of the aperture.

The measured and simulated E- and H-plane radiation patterns are plotted in Figure 2.16. Patterns are symmetric with SLL < -20dB and low cross polarization characterized with cross polarization discrimination (XPD) of > 25dB over the desired band. The demonstrated agreement between the measurement and simulation indicates the effectiveness and quality of the used low-cost fabrication approach and the robustness of the developed antenna.

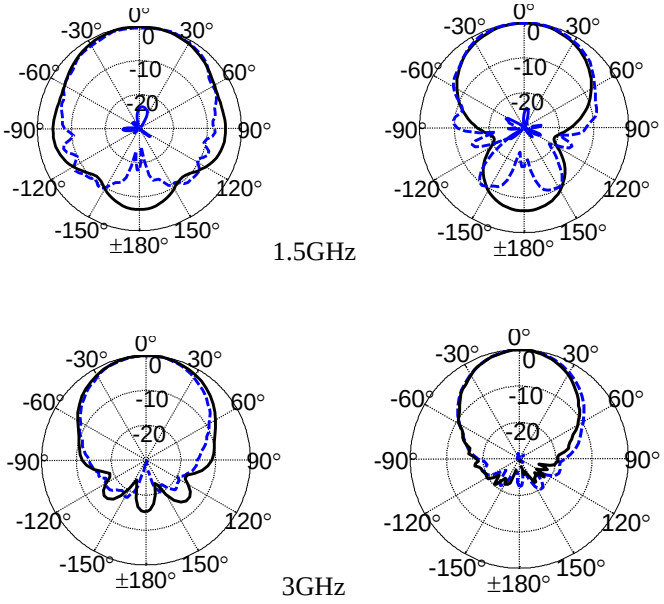

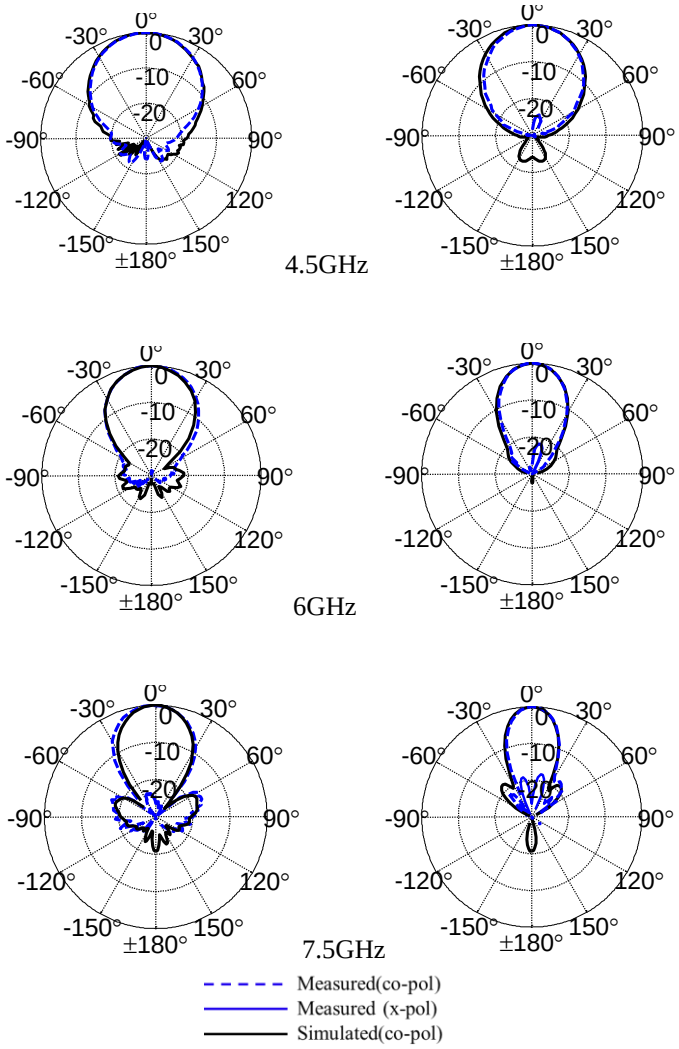

Figure 2.16: Measured and simulated broadside radiation patterns of the 3 × 4 cavity-backed array in (left) E-plane, and (right) H-plane.

2.2.3 Array Scan Performances

The scan performance of the designed cavity-backed antenna is investigated and compared to its free standing embodiment. To perform this analysis, the VSWR and radiation patterns are synthesized from the measured S-parameters and embedded element patterns. Note that the proposed array is designed mainly for non-scanning broadside radiation and its scanning performance can be improved by several approaches, such as

mutual coupling compensation techniques [78]-[80]. For the purpose of simplicity of the proposed analysis, conventional phased tapering is used in this study [80].

The free-standing 3 × 4 Vivaldi array is shown in Figure 2.17 with its center and two H-plane edge elements highlighted. For the purpose of this analysis, the active VSWR at the center element and the input VSWR are compared to the proposed cavity-backed array when scanned at 45° in E-plane. The input VSWR is defined here as the VSWR measured

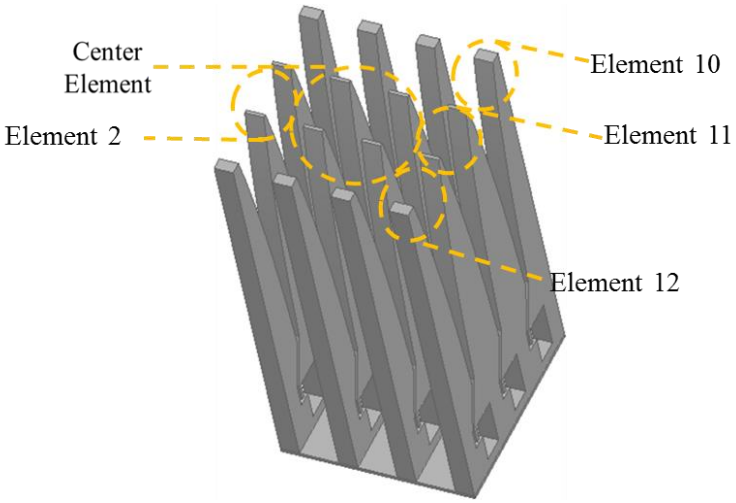

Figure 2.17: Illustration of the free-standing 3 × 4 array with highlighted edge and center elements

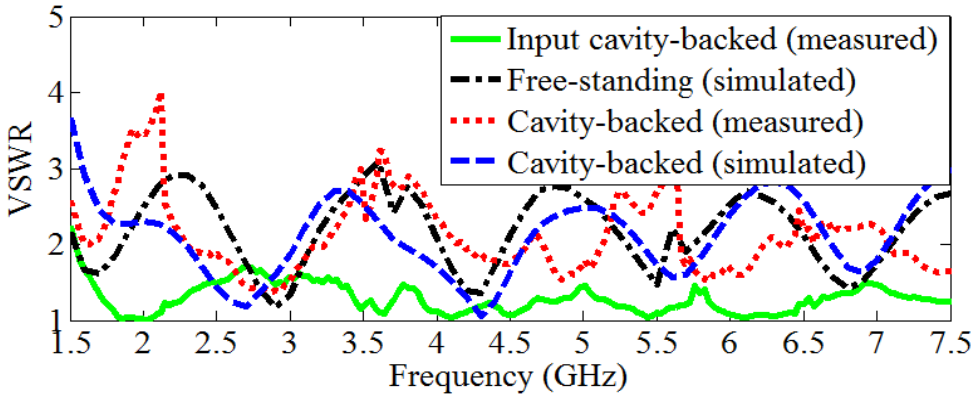

Figure 2.18: Synthesized measured input VSWR, central element active VSWR of the cavity-backed, and free standing arrays when scanned at 45° in E-plane.

at the input of a practical corporate feed network. These VSWRs are shown in Figure 2.18 for 45° scan. As seen, the active VSWR of the cavity-backed array is < 3 over most of the band. The active VSWR of the simulated cavity-backed array is also seen to compare well with free-standing antenna. Some spikes due to experimental non-idealities are observed in the measured active VSWR. Nonetheless, the overall response follows a trend similar to the simulated antenna. The measured input VSWR for 45° scan is also shown to be less than 2 over the entire band. While the active VSWR may be considered high, the input VSWR is seen to be very low. This is due to the active cancellation of the combined S-parameters. In practical realization, this return power will be dissipated inside the feed network or reradiated.

The array mismatch efficiency [80], calculated in (2.5) for N-element array is another figure of merit often used to assess the percentage of power globally accepted by the array. $S_{p,p}$ in (2.5) is the active reflection coefficient of element p.

$$\varepsilon = \left(N - \sum_{p=1}^{p=N} \left| S_{p,p} \right|^2 \right) \Big/ N \tag{2.5}$$

The total mismatch performance of the array for 45° scan in both E- and H-planes is shown in Figure 2.19. The cavity-backed array is seen to have similar mismatch efficiency as the free-standing array for E-plane scanning. The efficiency is > 70% below 4 GHz and remains > 80% for higher frequencies. A similar observation is made for H-plane scanning above 3 GHz. The efficiency is also seen to be more degraded at low frequencies for H-plane scanning (Figure 2.19(b)). This degradation is mainly due to the edge elements. The interaction between these elements and the array is stronger at lower frequencies. Also the inherent broadside radiation of the cavity contributes to the degradation observed in the VSWR response at low frequencies. Nonetheless, the value of mismatch efficiency for 45°

scan is only 10% lower than efficiency obtained for broadside radiation as shown in Figure 2.19(c). It is observed that for broadside radiation, the cavity-backed array has an overall better mismatch efficiency than the free standing array composed of identical number of elements. This improvement in efficiency is attributed to the addition of coherent radiation in broadside direction by the cavity for the uniformly excited array.

The measured and simulated radiation patterns of the free-standing and cavity-backed arrays at 7 GHz when scanned to 45° in both E- and H-plane are shown in Figure 2.20(a) and Figure 2.20(b). As seen, the patterns of the cavity-backed array are similar to those of the free-standing case. This indicates that the scan performance of the array is maintained when the array is recessed and properly integrated with the cavity. It can however be noticed that the first side-lobe of the cavity-backed array is higher than in the free-standing case. This is more pronounced for the H-plane scanning as seen in Figure 2.20(a). The side-lobe level increase is attributed to the cavity interaction which radiates mainly in broadside radiation and does not obey the scan requirement imposed on the array elements. The side lobe level can be reduced by modifying the array excitation; more precisely, the excitation of elements closer to the cavity. To illustrate this, the scan pattern of the cavity-backed array at 45° scan in the H-plane is shown in Figure 2.21(a) with elements 2 and 11 of Figure 2.17 not excited, and in Figure 2.21(b) with elements 10 and 12 not excited. Element 2 and 11 are the two edge elements not connected to the cavity, while elements 10 and 12 are the edge elements directly connected to the cavity. As seen, about 2 to 4.6dB reduction in side lobes is observed for Figure 2.21(a). The side lobe levels are seen to improve by more than 4.5 dB in Figure 2.21(b) when elements 10 and 12 are connected to the cavity. Not exciting these elements modifies the aperture field and reduces the surface currents on the cavity. The low radiation of these currents along with the modified array excitation result in the reduction seen in the side lobe level. This preliminary analysis substantiates the fact that

the scan performance of the proposed cavity-backed array can be further improved by using a non-conventional excitation [79].

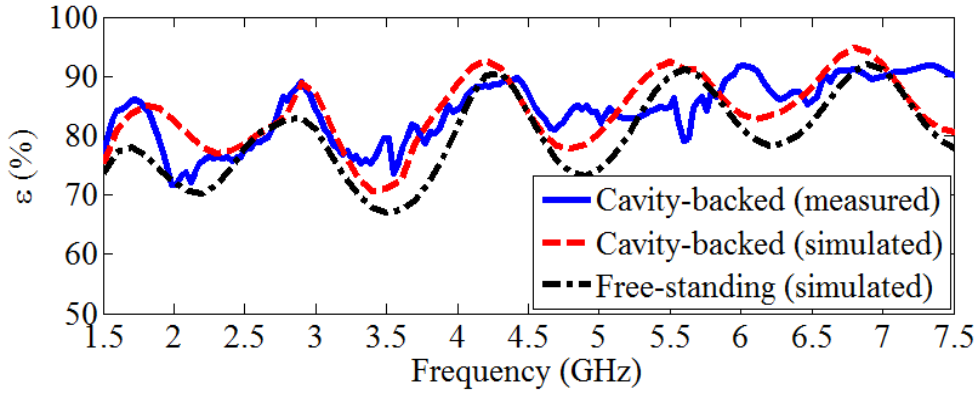

(a)

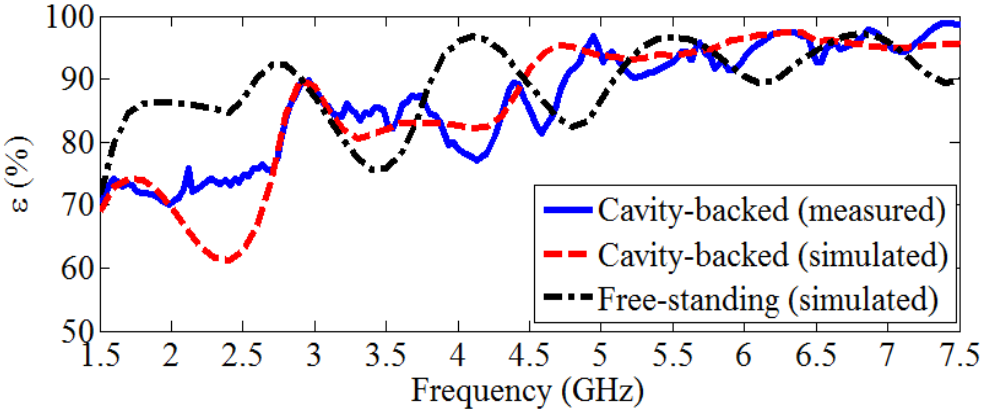

(b)

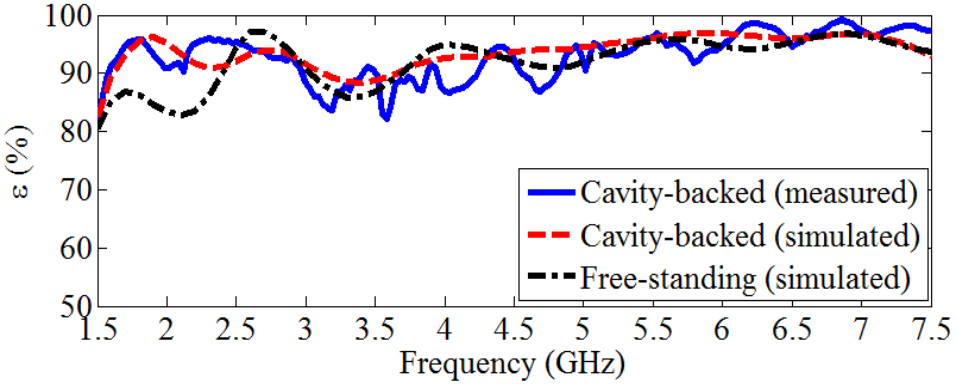

(c)

Figure 2.19: Array mismatch efficiency for (a) 45° scan in E-plane, (b) 45° scan in H-plane, and (c) broadside radiation.

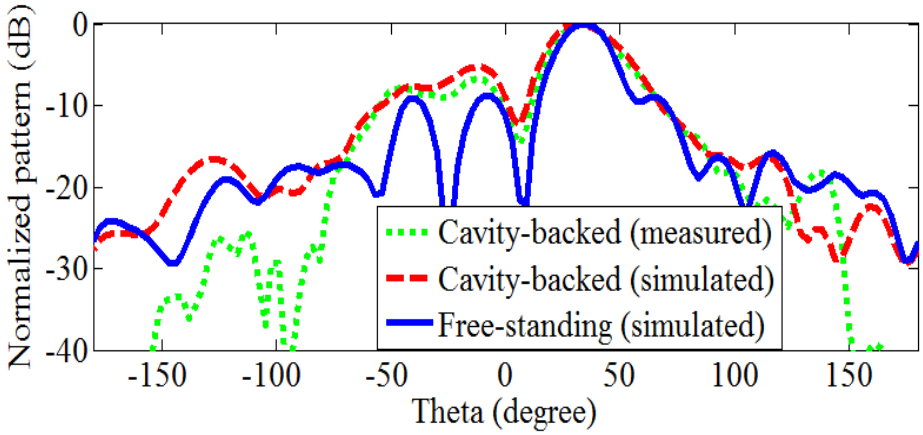

(a)

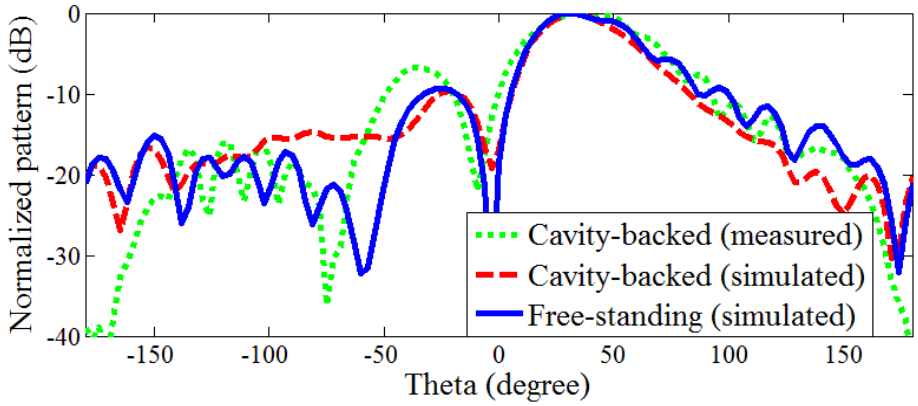

(b)

Figure 2.20: Measured and simulated radiation patterns of the 3×4 free standing and cavity-backed Vivaldi arrays at 7 GHz when scanned at (a) 45° in H-plane, and (b) 45° in E-plane.

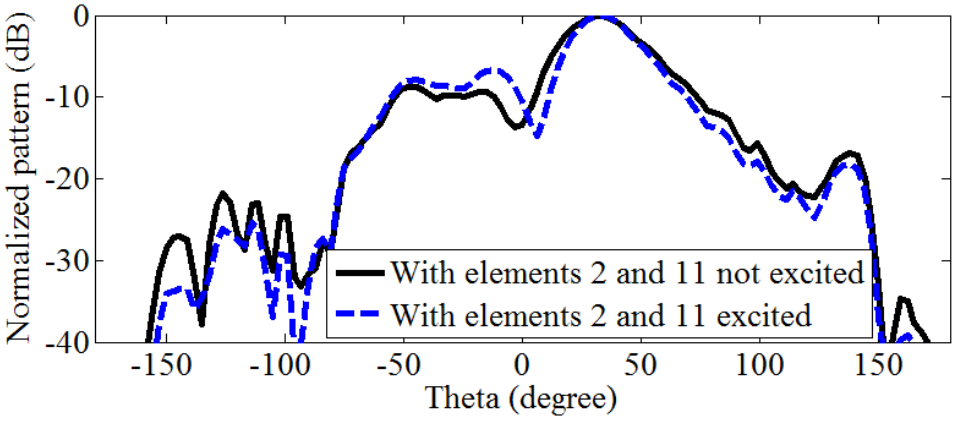

(a)

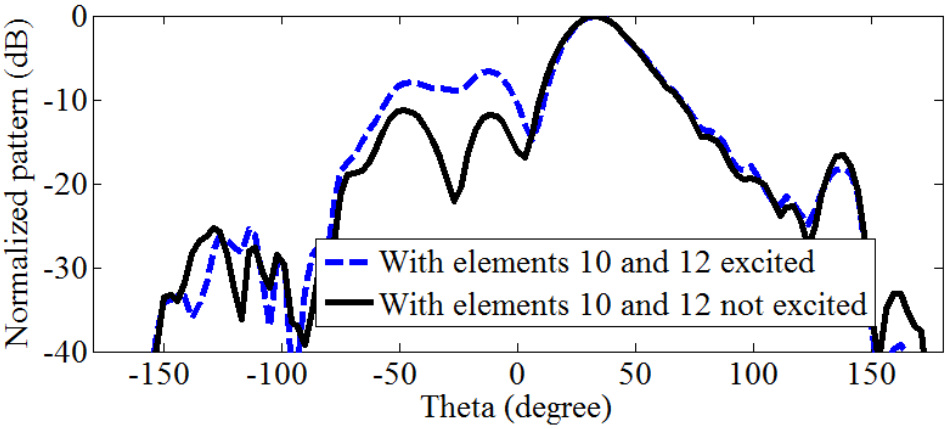

(b)

Figure 2.21: Measured radiation patterns of the 3×4 cavity-backed Vivaldi arrays when scanned to 45° in H-plane at 7 GHz with (a) elements 2 and 11 of Fig. 4.17 not excited, and (b) elements 10 and 12 of Fig. 2.17 not excited.

2.3 Single-Polarized and Single Feed Antenna

The designed, cavity-backed 3 × 4 array of Section 2.2 requires a 12-way power divider, which adds extra loss and complexity for broadside only applications. To decrease the complexity of this antenna, the number of elements is reduced to one and the cavity shape is modified to maintain resonant free response within the 2 – 7 GHz band. The aperture of the antenna is also reduced from 60 × 100 mm^2 of Section 2.2 to 44 × 70 mm^2. This aperture reduction makes this antenna better suited for compact platforms. To improve the impedance match at low frequencies, the Vivaldi element is flared in its transverse plane using a profile similar to TEM horns [81]. The designed antenna is different to the TEM horn as its E-plane is shorted to the cavity to eliminate cavity resonances. The cavity is also flared in H-plane to maintain stable gain response at high frequencies; detailed discussions regarding the proposed cavity shape is presented in Chapter 3. To obtain a design which is resonance free, with turn-on frequency at 2 GHz, the parameters of the newly proposed single polarized antenna, shown in Figure 2.22 are given in Table 2.3.

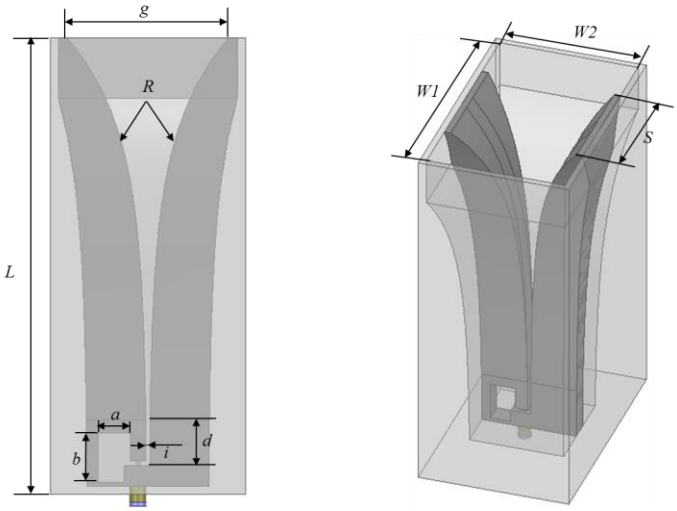

(a) (b)

Figure 2.22: Geometrical parameters of the single-feed and single polarized cavity-backed Vivaldi antenna with (a) front view and (b) isometric view.

Table 2.3: Design Parameters of Single Feed Cavity-Backed Vivaldi Antenna (in mm)

Parameter	*a*	*b*	*i*	*d*	*g*	*L*	*R*	*W1*	*W2*	*S*
Value	8	12	1.1	11.1	40	112	0.45	70	44	36

The designed antenna is fabricated as a single metal block by combining CNC and EDM machining processes. An N-type coaxial launcher is used to feed the antenna, as illustrated in Figure 2.23. The VSWR of the simulated and fabricated antenna are shown in Figure 2.24. As seen, VSWR < 2 is obtained over most of the 2 – 7 GHz band. Measured VSWR is seen to be better than its simulated counterpart at high frequencies, but degrades at low frequencies. This small difference between measured and simulated VSWR is due to the integration of the coaxial launcher. In the fabricated antenna, the inner pin of the coax adapter is press fitted into a cylindrical opening, machined out of one arm of the Vivaldi as shown in Figure 2.25. While good electrical and RF contact are achieved in the simulated

antenna, small gaps between the inner pin and machined hole in the fabricated embodiment add some extra capacitances which affect the input impedance.

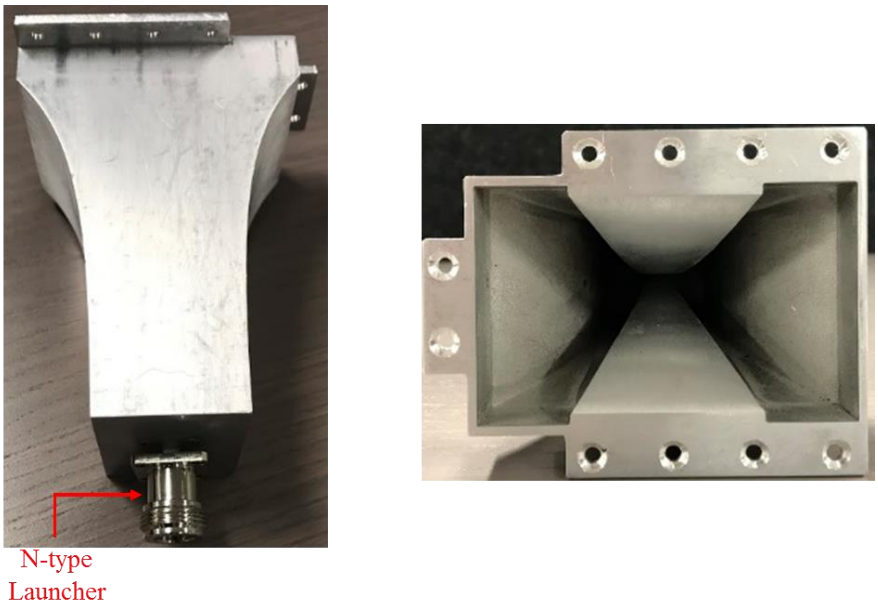

Figure 2.23: Photograph of the fabricated single feed antenna.

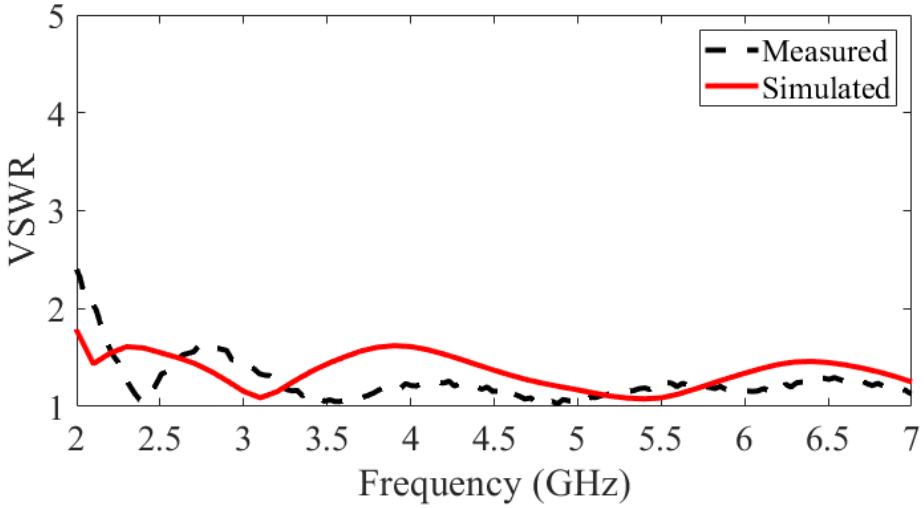

Figure 2.24: Measured and simulated VSWR of the single-feed and single-polarized cavity-backed Vivaldi antenna.

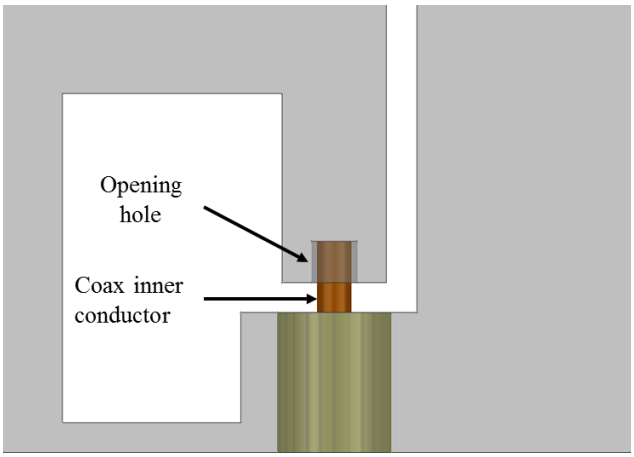

Figure 2.25: Illustrated of the coax to Vivaldi transition.

The measured and simulated broadside gains of this antenna are shown in Figure 2.26. As seen, good agreement is obtained between measured and simulated data. The simulated and measured cross-polarized gains are lower than -30 dB. Co-polarized gain > 5 dBi is obtained at lower frequencies and increases to 12 dBi at 7 GHz. This gain is seen to be lower than that of the 3 × 4 cavity-backed array of Section 2.2, and is due to the combination of smaller aperture size and reduced number of Vivaldi elements. In the tightly coupled 3 × 4 cavity-backed Vivaldi array, the small separation between element leads to quasi-uniform illumination of the aperture. In the single-feed realization of this

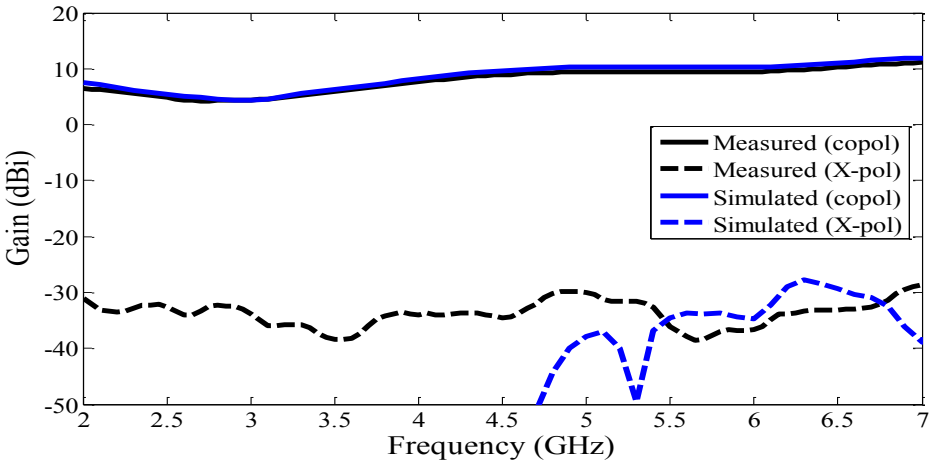

Figure 2.26: Measured and simulated broadside gain of the single feed and single polarized antenna.

section, the aperture field distribution, shown in Figure 2.27 at 5 GHz is closer to that of a TE_{10} mode of a rectangular waveguide. This is known to have a maximum aperture efficiency of 80 %.

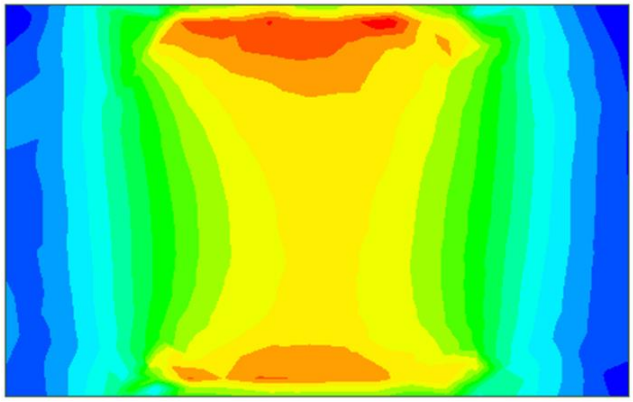

Figure 2.27: Aperture field distributions at 5 GHz of the single feed and single polarized cavity-backed Vivaldi antenna.

The measured and simulated radiation patterns at 2, 4, and 7 GHz are shown in Figure 2.28, for both E-and H-planes. Patterns are seen to be narrower in the H-plane as expected from the wider aperture in that direction. At high frequencies (7 GHz), side lobes start appearing, their levels are seen to be very low. More importantly, the gain near horizon, which is demonstrated in the next section to be very critical for isolation increase, is also very low. Patterns are wider in E-plane with no visible side lobe.

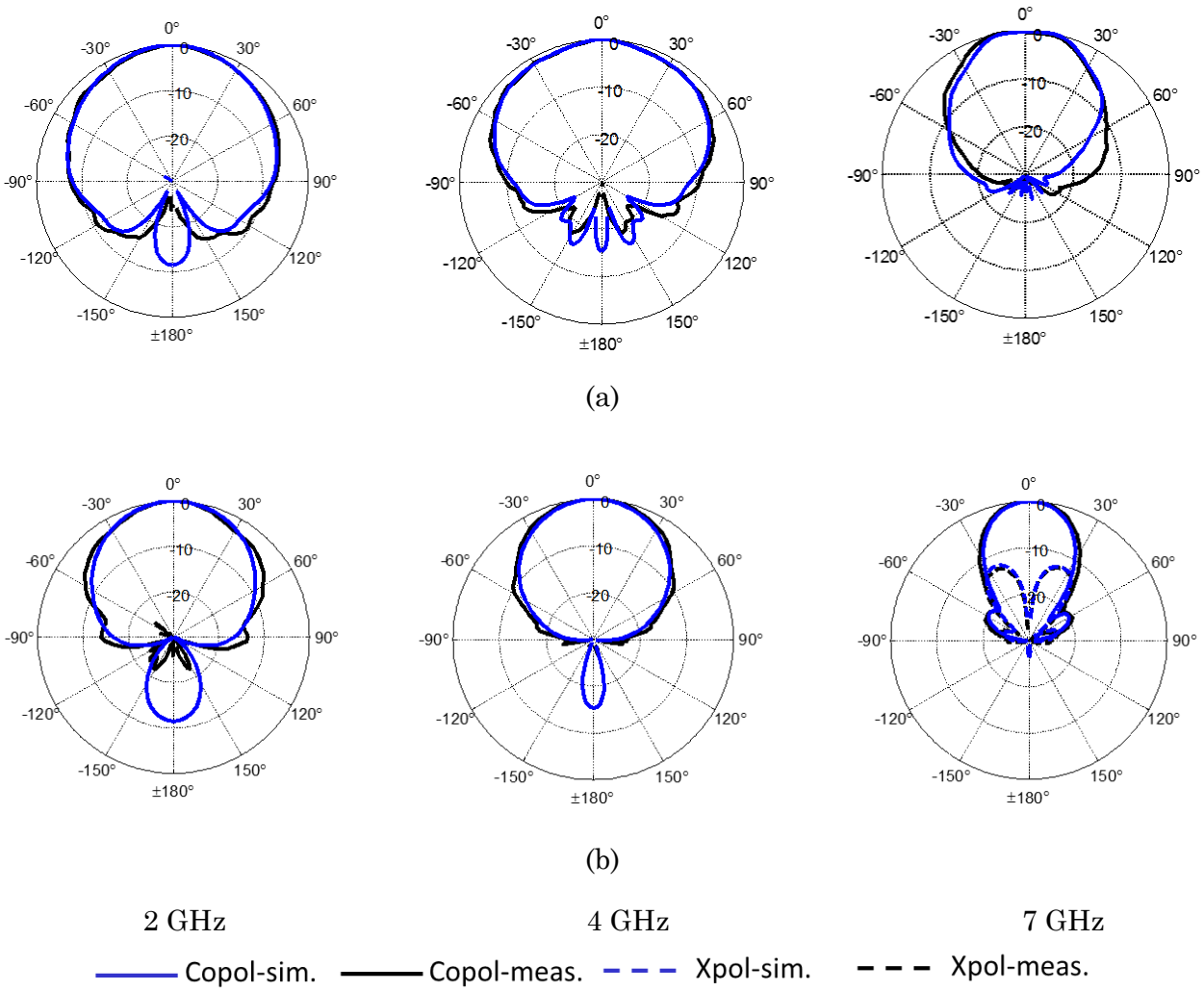

Figure 2.28: Measured and simulated patterns at 2, 4, and 7 GHz of the single polarized and single-fed antenna with (a) E-plane and (b) H-plane.

2.4 Isolation Analysis with Single Polarized Antennas

The last two sections focused on the design of standalone antennas in free space. In this section, isolation, which represents the key performance indicating the suitability of the proposed system for STAR is investigated.

To determine the best orientation of the antennas that are flush-mounted with the ground plane, good understand of the coupling mechanism is first researched. To decrease the computational complexity of the analysis, an open rectangular waveguide antenna,

excited with fundamental TE_{10} mode is used. This antenna has an inherent cavity and is, therefore, flush mountable. Three different orientations of antennas separated by two wavelengths at 2 GHz are analyzed, as shown in Figure 2.29. In Figure 2.29(a), antennas are oriented in their respective E-planes resulting in a TM wave propagation on the ground plane. In Figure 2.29(b), antennas are facing each other in H-plane, which leads to predominant TE wave propagation. In the last configuration shown in Figure 2.29(c), the antennas are oriented in D-plane with hybrid propagation of both TM and TE waves possible. For each of these configurations, the coupling obtained from the full wave simulation is plotted along with calculations based on Friis transmission equation (Figure 2.29). Friis equation uses gain near horizon, specifically at 80° elevation angle in the direction of the opposing antenna. This angle is used to avoid the singularity that may arise at 90°. Analysis of these curves clearly demonstrates that the coupling between transmit and receive antenna is strongly correlated to the gain near horizon. This observation further substantiates the need to maintain low gain near horizon during the design of standalone antennas. It is also seen that Friis calculation diverges from full wave simulations at frequencies below 4.5 GHz. This difference is mainly due to the coupling through surface currents flowing on the ground plane; these are not captured in Friis transmission equation. The surface currents on the ground plane at 2 GHz are also shown in Figure 2.29 with stronger currents observed for E-plane orientation. It is seen that stronger coupling exists when antennas are oriented in E-plane; H-plane facing however provides lower coupling. The H-plane orientation is therefore more appropriate for single-polarized systems and D-plane orientation, more suitable for dual-polarized systems as it provides symmetrical performance between the two polarizations.

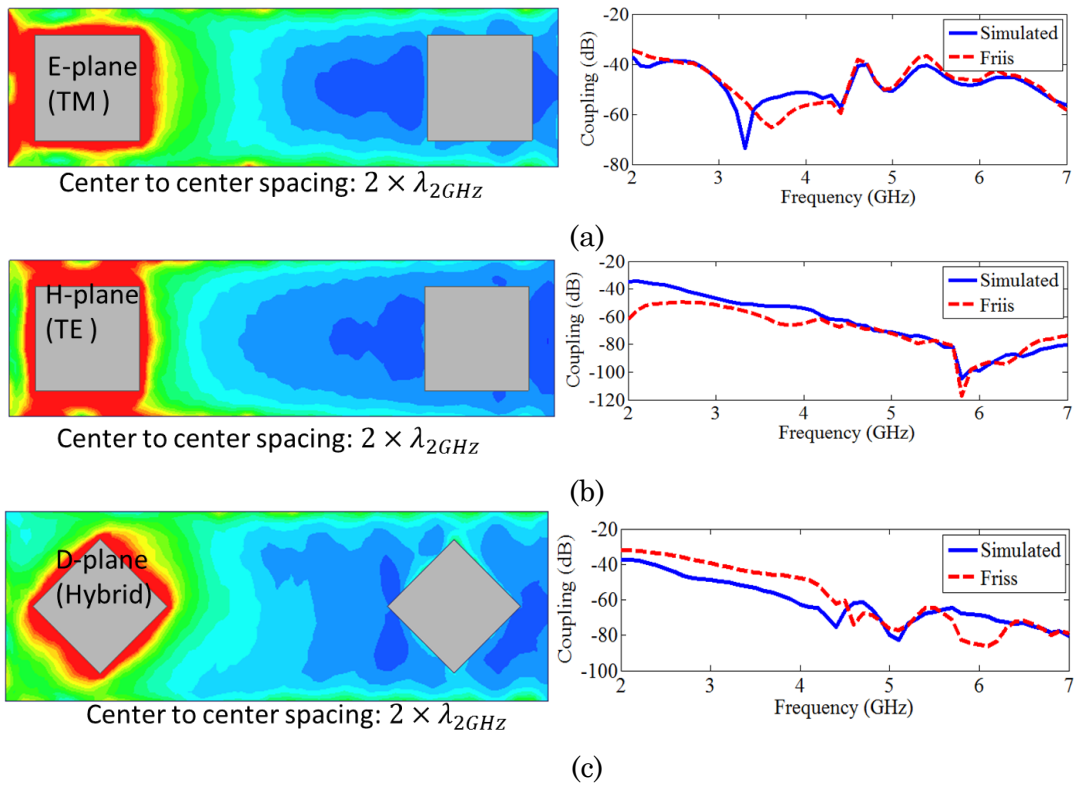

Figure 2.29: Simulated full wave and Friis calculated coupling versus antenna orientation with (a) E-plane, (b) H-plane, and (c) D-plane.

2.4.1 Isolation for 3 × 4 Cavity-Backed Vivaldi Array

It is demonstrated in Section 2.1 that an all-metal Vivaldi antenna can be recessed inside a lossless metallic cavity with resonance free response. Two of the proposed 3 × 4 arrays are mounted on a metallic ground plane as shown in Figure 2.30(a), for isolation analysis. The numbering scheme which describes the different ports of each antenna is illustrated in Figure 2.30(b). The antennas are separated by 25 cm ($\lambda_{2GHz}/6$) and are oriented in H-plane since this is known to have superior isolation performance. The shown separation is chosen for the sake of this analysis to investigate worst case situation of close proximity between antennas. The measured and simulated isolations between the two antennas when all ports are excited are shown in Figure 2.31. The excitation in this case is provided by a 12-way power divider. The isolation is seen to be greater than 60 dB above

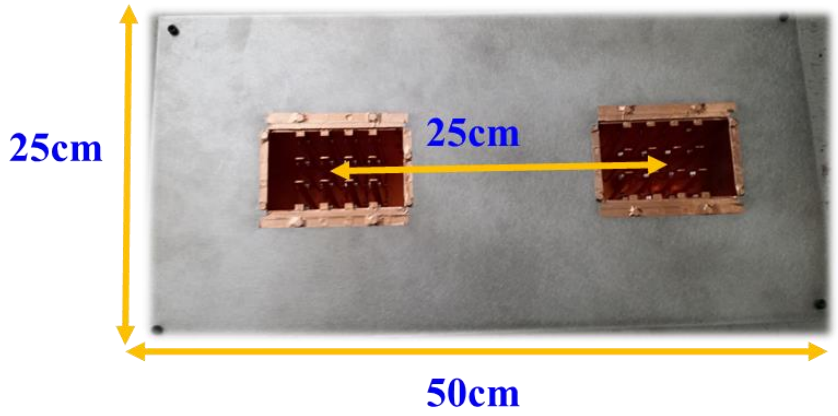

(a)

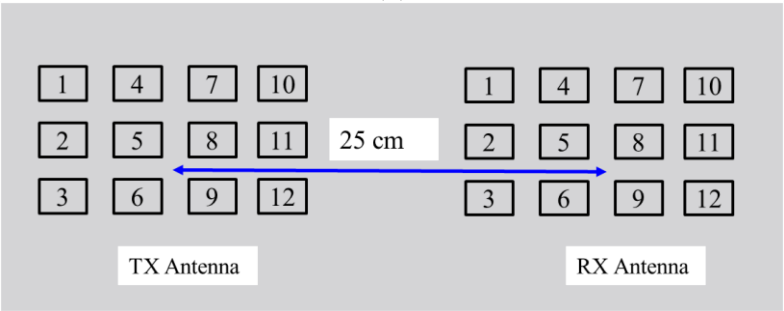

(b)

Figure 2.30: Setup of the cavity-backed 3 × 4 Vivaldi array for isolation analysis with (a) prototyped antenna mounted on a flat 25 × 50 cm^2 ground, and (b) numbering scheme of the different ports of each antenna.

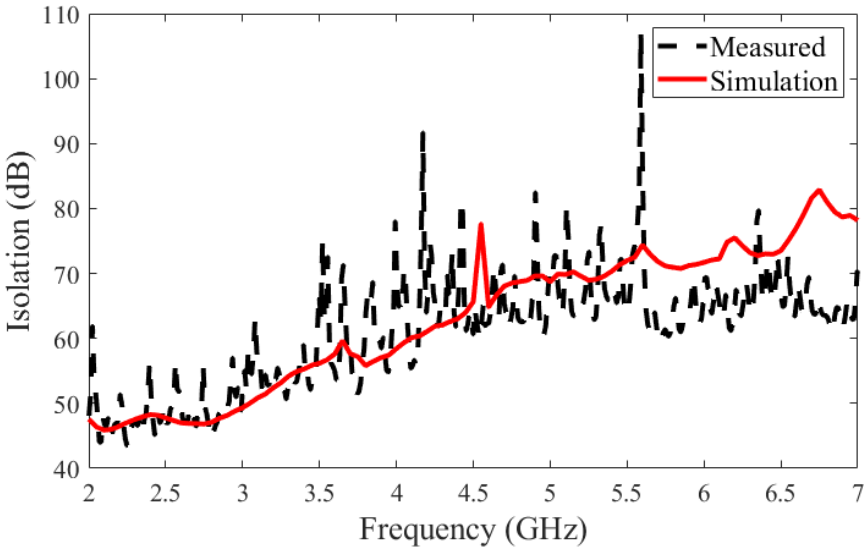

Figure 2.31: Measured and simulated isolation between two closely separated 3 × 4 Vivaldi arrays.

4 GHz and decreases down to 45 dB at 2 GHz. The profiles of the measured and simulated isolation are seen to be in good agreement. The increased beamwidth at low frequencies (high gain near horizon) leads to decrease isolation.

Several techniques are investigated to increase the isolation at low frequencies. The first approach is to decrease the receiver sensitivity by terminating some receive ports of the array with matched loads. This is illustrated in Figure 2.32, where ports 1, 2, 3 and 11 of the receiving antenna are terminated with a 50 Ω load. These elements are selected as a tradeoff between increase in isolation and pattern degradation. Elements 10, 11, and 12 are the closest to the transmit antenna and therefore have stronger coupling to it. Terminating

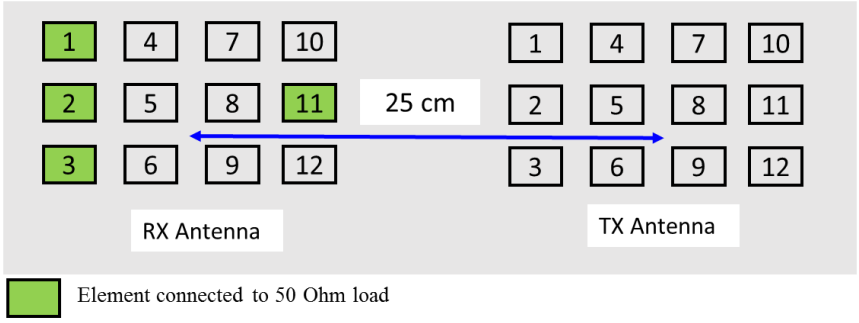

Figure 2.32: Isolation improvement by termination 4 receive antenna ports with matched loads.

these elements will eliminate their coupling contribution. The problem with this option is the beam squint in the direction of the transmit antenna which increases the total coupling. Terminating elements 1, 2, and 3 creates a beam squint in a direction opposite to the transmit antenna. These elements are the farthest from the transmit antenna and have the lowest coupling contribution in the system isolation. To further increase the isolation when 1, 2, and 3 are terminated, element 11, which is closest to the transmit antenna, is also loaded. The measured and simulated isolations for this configuration are shown in Figure 2.33. As seen, isolations are greater than 60 dB above 2.7 GHz and remain above 50 dB for the rest of the band. Impact of this resistive termination on the radiation patterns is shown

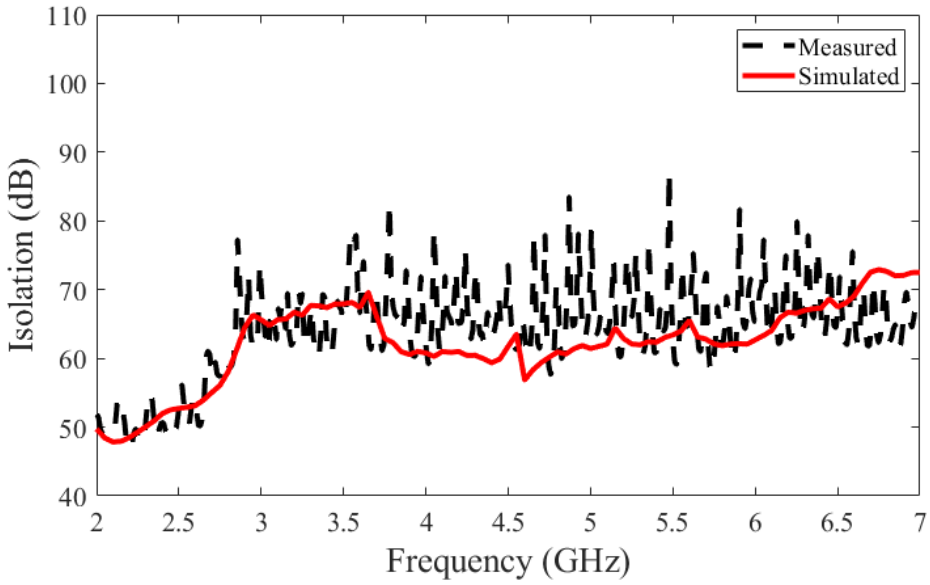

Figure 2.33: Measured and simulated isolation with resistive termination.

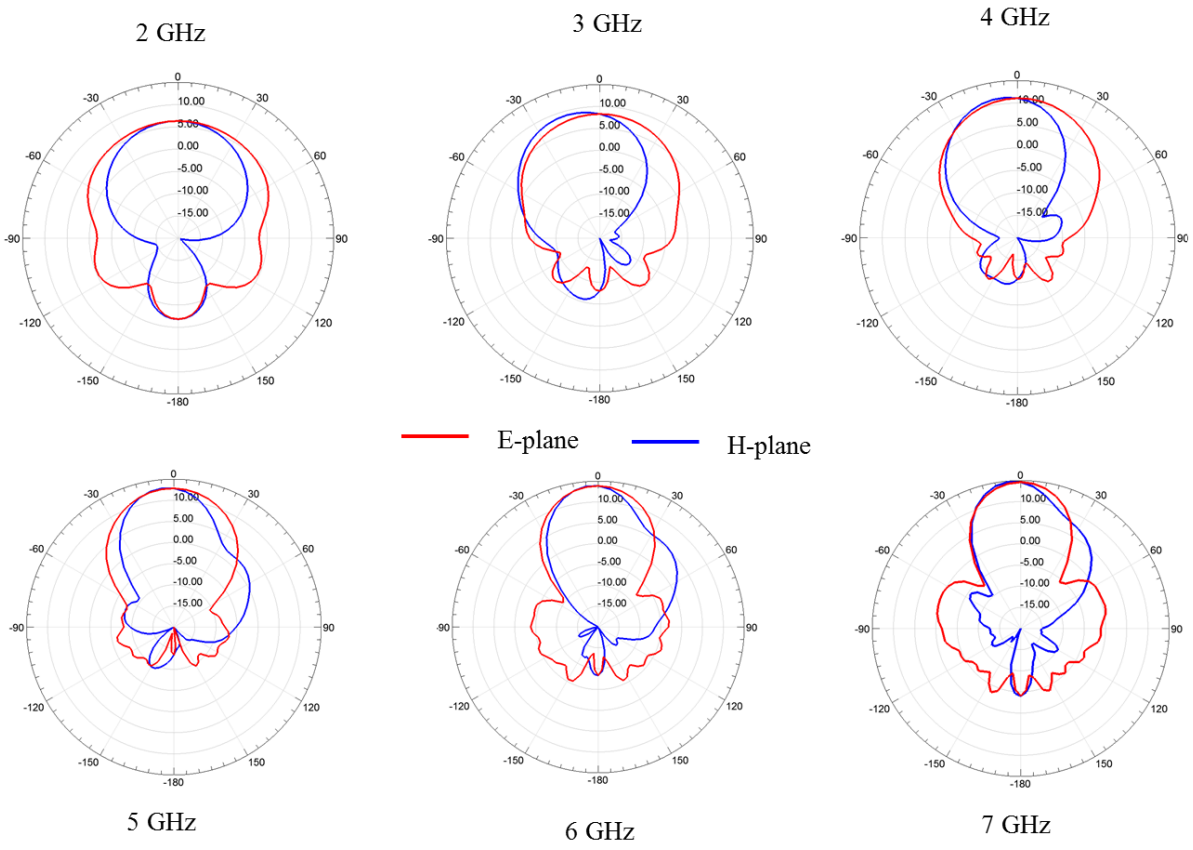

Figure 2.34: Simulated receive patterns when ports 1, 2, 3, and 11 are terminated with matched loads.

in Figure 2.34, where the patterns of the receive antenna are plotted. As seen, marginal degradation in radiation patterns is obtained at frequencies below 4 GHz. Patterns are seen to be squinted 15° away from the transmit antenna in the H-plane. Broadside gain remains > 5 dBi over the band, demonstrating that the resistive termination still guarantees enough gain, needed to close the link budget. The use of the resistors in the demonstrated configuration is also found to have negligible effects on the desirable E-plane patterns.

A well-known technique to increase the isolation between two closely separated antennas is to have them separated by a metallic shield. The main issue with this approach is that; the shield acts as reflector and therefore leads to high beam squint. It is shown from the first approach described above that, terminating elements 10, 11, and 12 will lead to beam squint in the direction of the transmit antenna. It therefore appears that, loading these elements can offset the squint created by a metallic shield. This technique is implemented here by inserting a metallic plate between the two antennas as illustrated in Figure 2.35(a). To partially compensate the squint resulting from this reflector, elements 10, 11, and 12 are terminated on matched loads as shown in Figure 2.35(a). Element 2 is also loaded to further increase the isolation at low frequencies. The metallic plate is experimentally realized by covering a 5 cm thick foam with a copper tape (Figure 2.35 (b)). The isolation of this configuration is shown in Figure 2.36, and is seen to be greater than 60 dB over most of the band. Measured and simulated isolations are also seen to diverge over 5 GHz. Reduction of the measured isolation above that frequency is found to be due to reflection from the absorbing walls of the anechoic chamber [82]. This high isolation is obtained at the expense of pattern squint in H-plane at low frequencies, as shown in Figure 2.37. The squint is more pronounced for the TX antenna where resistive terminations are not used. The location of resistors in the RX antenna helps in mitigating the squint, which is found to be less than 15°.

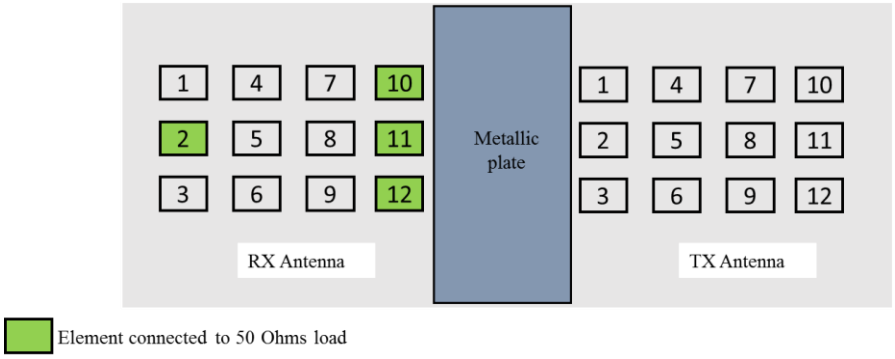

(a)

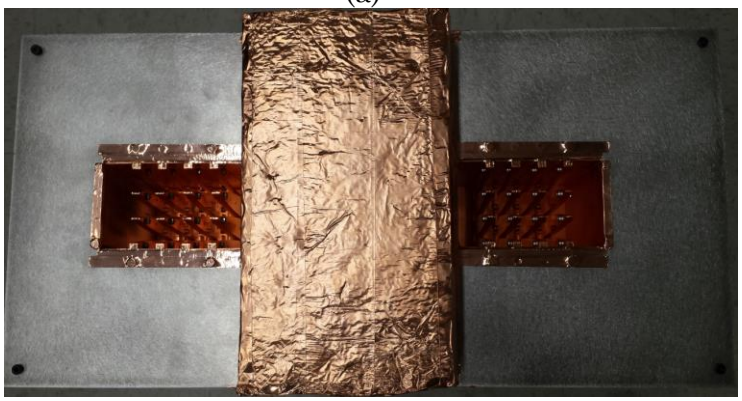

(b)

Figure 2.35: Isolation improvement by termination of 4 receive antenna ports with matched loads and inserting a metallic plate between transmit and receive antennas: (a) layout configuration, (b) measurement setup.

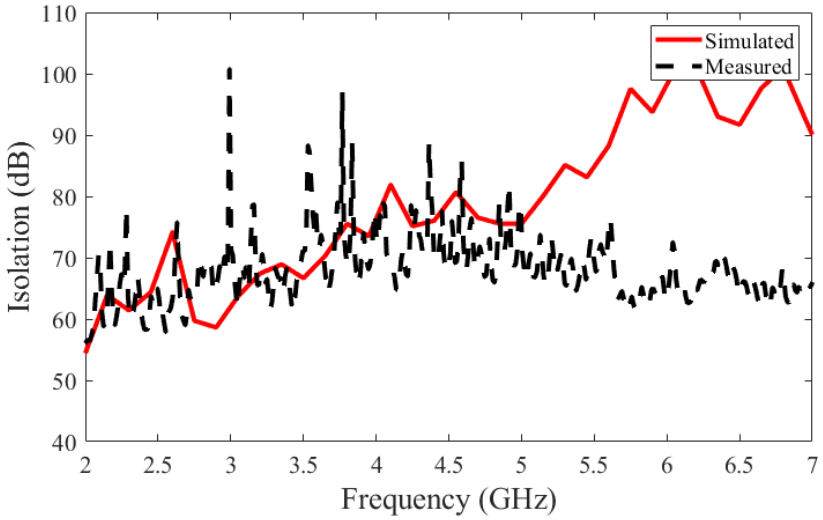

Figure 2.36: Measured and simulated isolation with resistive termination and inserted metallic plate between transmit and receive antennas.

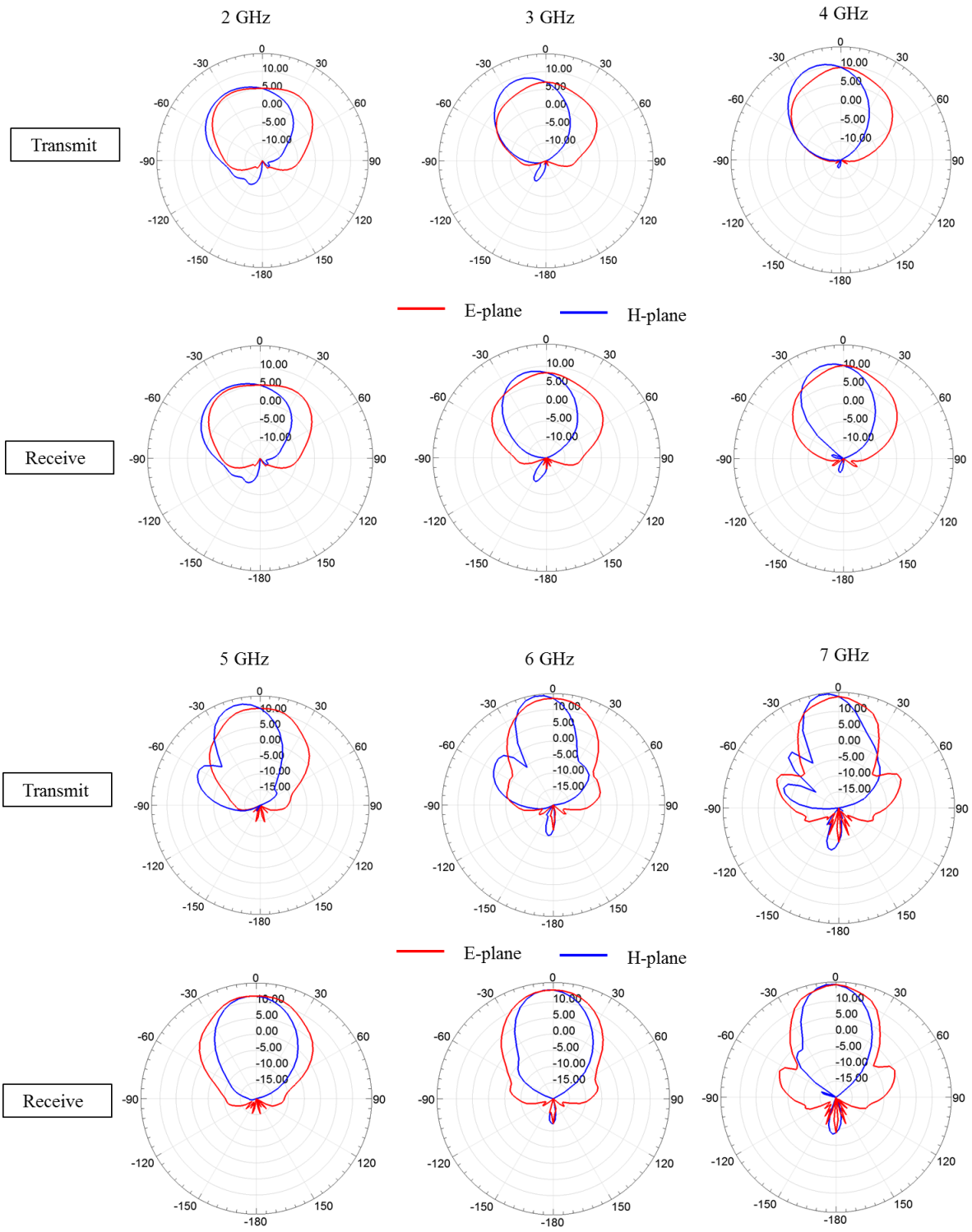

Figure 2.37: Simulated transmit and receive patterns with resistive termination and inserted metallic plate between antennas.

2.4.2 Isolation of the Single Feed Cavity-Backed Element

The second antenna analyzed in this chapter is the single element cavity-backed Vivaldi. Transmit to receive isolation in this case is analyzed on a 12" × 12" (30.6 × 30.6 cm^2) tray designed to incorporate multiple other antennas. The selected platform aims to investigate a more realistic scenario where multiple antennas share the same aperture. The layout of the tray is shown in Figure 2.38. Cavity-backed monostatic spiral based STAR antenna is located in the center of the tray [83]. The antennas of interests in this chapter are the two 2 – 7 GHz portion located in one of the diagonals of the tray. This arrangement increases the electrical path between the antennas. Given the spiral diameter of 8" (20.3 cm), the maximum available aperture for the 2 – 7 GHz antenna is 8 × 8 cm^2. The compact design of the single feed and single polarized antenna is therefore suitable for this available space. The proposed antenna aperture is 4.4 × 7 cm^2 which is smaller than the maximum aperture restriction. In this section, an isolation study is first performed with the abstrac-

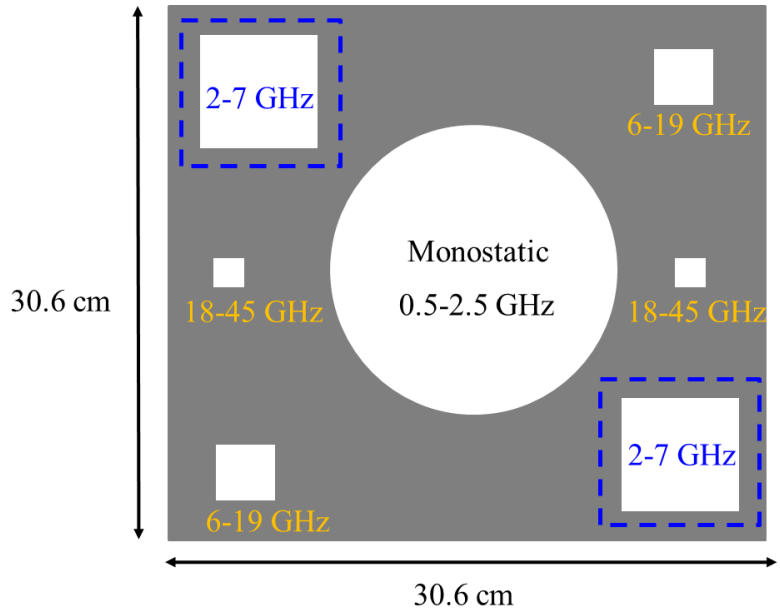

Figure 2.38: Layout arrangement of multiple single polarized antennas on a 12" × 12" tray.

tion of the presence of other antennas. System isolation in the presence of the other antennas is later discussed through experiments, given the complexity of the platform.

As was done for the 3 × 4 cavity-backed Vivaldi array, the two antennas are first placed in their respective H-planes, as illustrated in Figure 2.39, where surface currents at 3 GHz on a flat metallic ground plane are shown. Simulated isolation for this configuration (Conf. 1) between the two antennas is shown in Figure 2.40. As seen, isolation is greater than 60 dB above 4.5 GHz, and decreases to 45 dB at 2 GHz. The reduced isolation at low frequency is due to the surface currents on the ground plane and the high gain near horizon, as previously discussed. The currents are seen to be launched from the E-plane of the antenna and propagate along the edges of the ground plane. To increase the isolation at low frequencies, different approaches aiming to diffract or reflect these currents away from the receiving antenna are investigated.

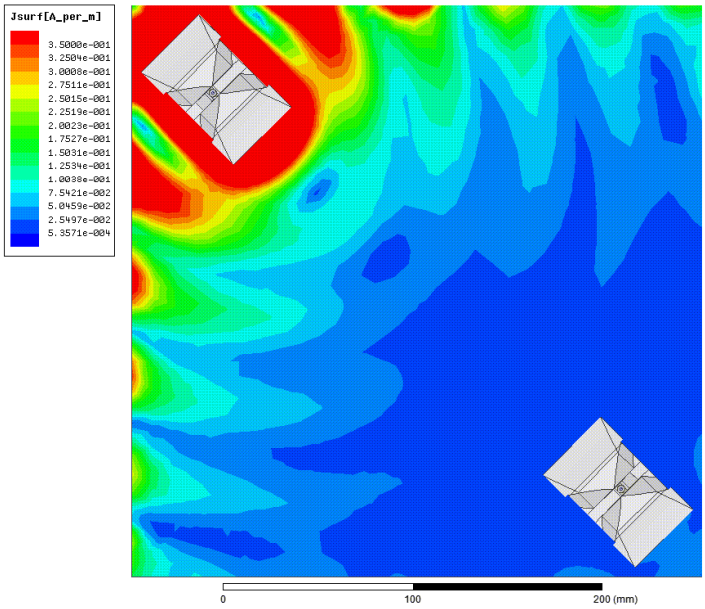

Figure 2.39: Surface currents at 3 GHz for the single polarized antenna on a flat metallic ground plane.

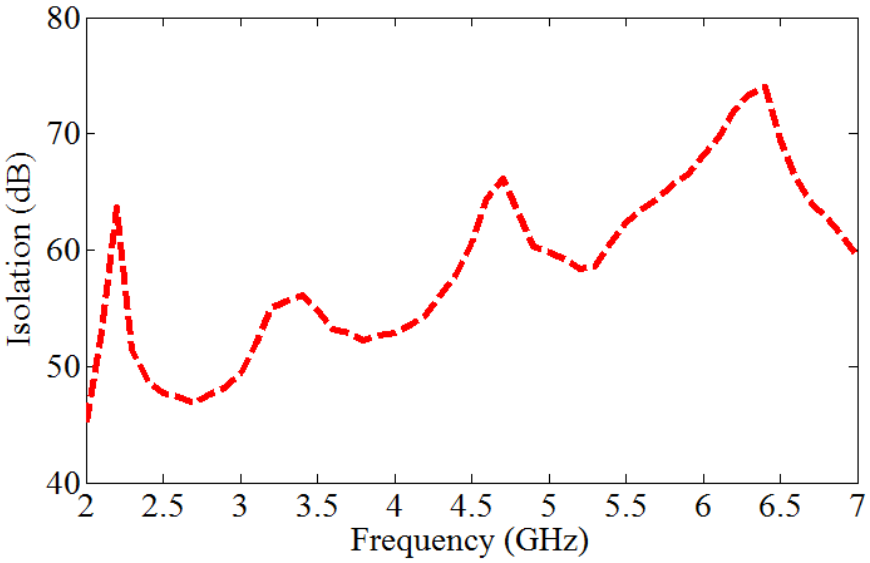

Figure 2.40: Transmit-Receive isolation for Conf. 1 when the two antennas are mounted on a flat metallic ground plane.

We have seen in the 3 × 4 array case that significant improvement in isolation is obtained when a metallic reflector is placed between the two antennas. In the current platform, the reflector cannot be arbitrarily shaped; the presence of other antennas needs to be considered in the design process. Advantage, however, can be taken of the metallic surface of these antennas, if, proper care is taken to control their scattered fields. The center spiral antenna for 0.5 – 2.5 GHz, is recessed inside a cylindrical cavity. Instead of having this cylindrical cavity flushed-mounted, it can be placed above the ground plane to operate as a shield between the two antennas. To assess how this new configuration affects the 2 -7 GHz band, a cylindrical metallic wall with a diameter equal to the spiral cavity is inserted between the two antennas as shown in Figure 2.41, with shown surface currents at 3 GHz. The isolation of this configuration (Conf. 2) is plotted along with that of a flat ground plane (Conf. 1), as shown Figure 2.42. Comparison between these two curves only shows a marginal improvement in isolation. The analysis of the surface currents for Conf. 2 shows low currents flowing in the line of sight direction of the two antennas. Stronger

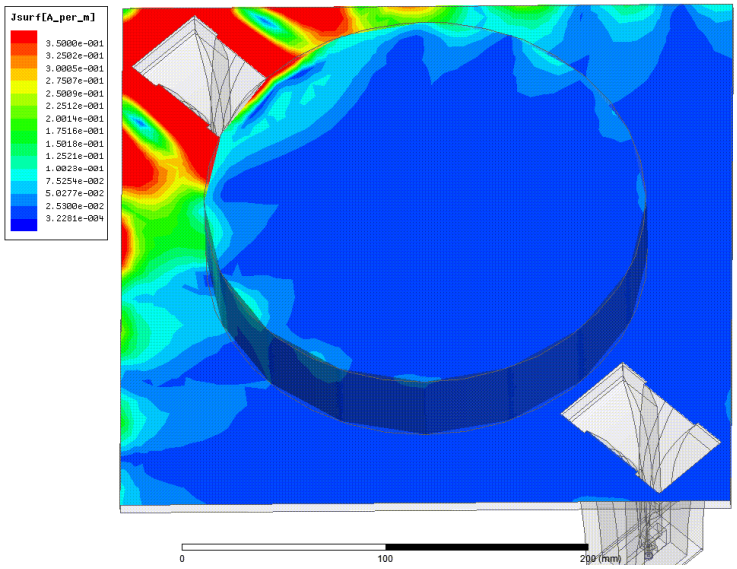

Figure 2.41: Surface currents at 3 GHz for the single polarized antenna mounted on a ground plane with a cylindrical metallic reflector inserted between the antennas.

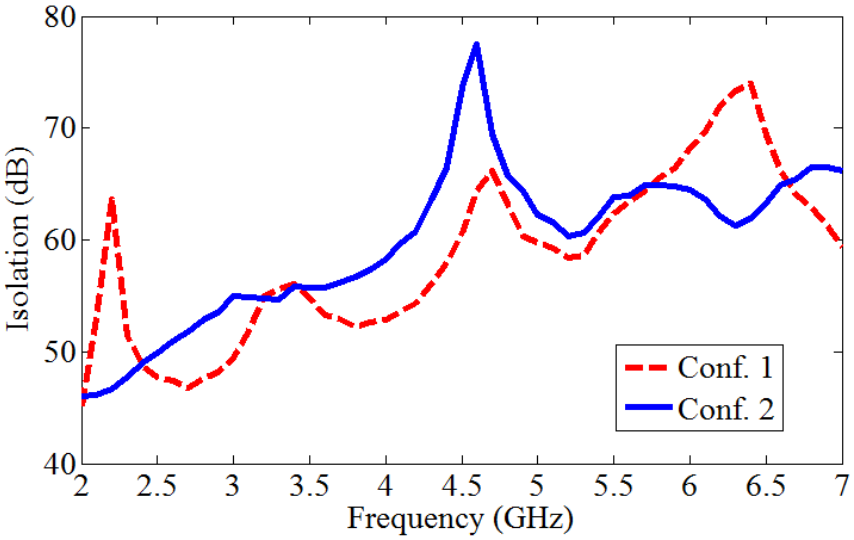

Figure 2.42: Comparison between Conf.1 and Conf.2 isolations.

currents are however still creeping on the edges of the ground plane. The insertion of the cylindrical wall is therefore insufficient to mitigate these edge currents. To further diffract these currents, four pillars, which intend to add extra blockage are inserted as shown in Figure 2.43. These extra metallic reflectors are placed at reasonable distance from the aperture to mitigate beam squint in the E-plane.

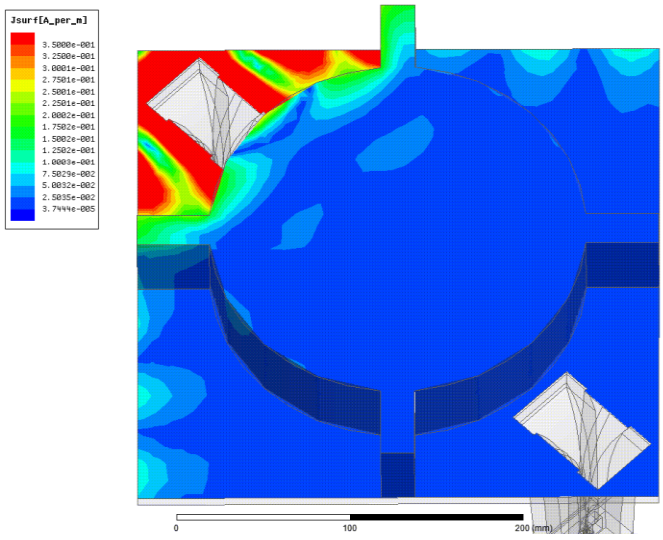

Figure 2.43: Surface currents at 3 GHz for the single-polarized antenna mounted on a ground plane with a cylindrical metallic wall and pillars inserted between the antennas.

Simulated isolation for this configuration (Conf. 3) is compared in Figure 2.44, to that of Conf. 1 and 2. As seen, significant improvement is obtained with isolation greater than 60 dB over most of the frequencies. This high isolation is correlated with the reduction of currents creeping along the edges of the ground plane; strong currents are observed near the transmitting antenna aperture, and their intensity significantly decrease after diffraction and reflection on the pillars and cylindrical wall. As for the case of the 3 × 4

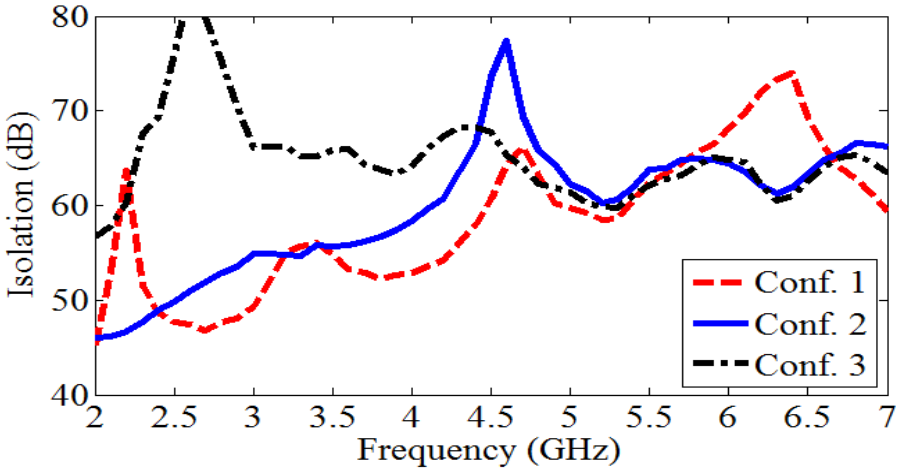

Figure 2.44: Comparison between Conf.1, Conf.2, and Conf. 3 isolations.

antenna, the achieved isolation is obtained at the expense of small beam squint in H-plane patterns.

The analysis of the three configurations discussed so far does not integrated the presence of other antennas on the shared aperture. The impact of these antennas is studied through the built experiment, shown in Figure 2.45. In Figure 2.45, the monostatic STAR antenna based on spiral is located in the center of the tray [83]. Ridge horn antennas are used in 6 -19 GHz, 18 - 45 GHz [14], and 45 – 110 GHz [140] bands. The two fabricated single polarized 2 – 7 GHz antennas are shown flush mounted with the platform. The VSWR and isolation of these two antennas are shown in Figure 2.46. As seen, VSWR < 2 is obtained above 2.5 GHz and isolation > 60 dB above 3.5 GHz. The degraded VSWR below 2.5 GHz is due to the spiral cavity, which strongly interacts with the near field of the antenna at these frequencies. VSWR < 3 is however seen above 2 GHz. The measured isolation is also seen to be lower than Conf. 3 simulated design of Figure 2.44. This degradation is mainly attributed to surface wave propagation enabled by the substrate of the spiral antenna. The E- and H-plane patterns of the antenna when mounted on the platform are compared to its standalone embodiment in Figure 2.47. As seen, no major degradation is observed in E-plane. H-plane patterns are however, squinted 30^{o} off axis at low frequencies. As frequency increases, patterns become more directive and less squint is observed. Broadside gain reduction due to squint is less than 3 dB, thereby maintaining the suitability of the proposed design for multi-antenna STAR platform.

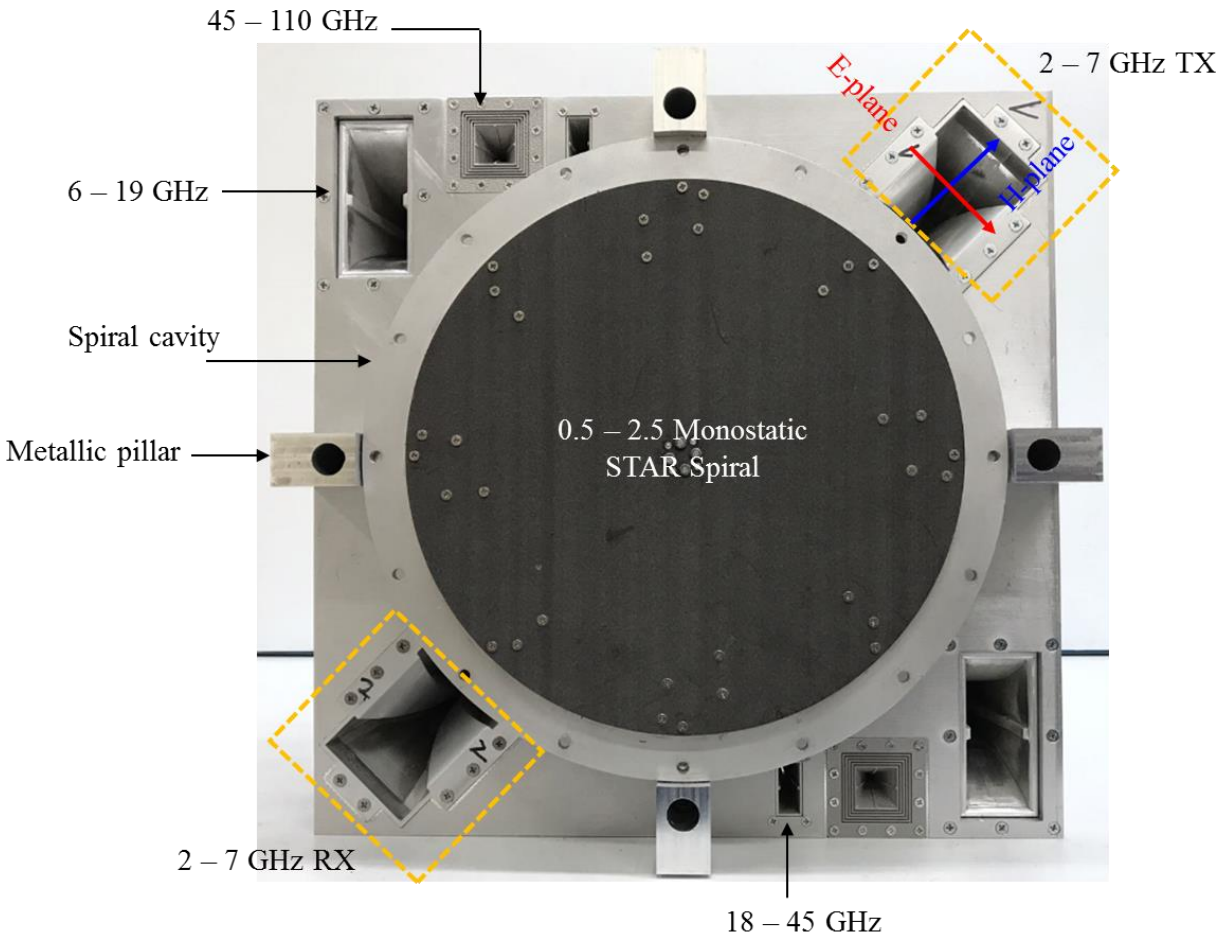

Figure 2.45: Photograph of the 12" × 12 " platform integrating multiple antennas operating from 0.5 to 110 GHz (220: 1 bandwidth).

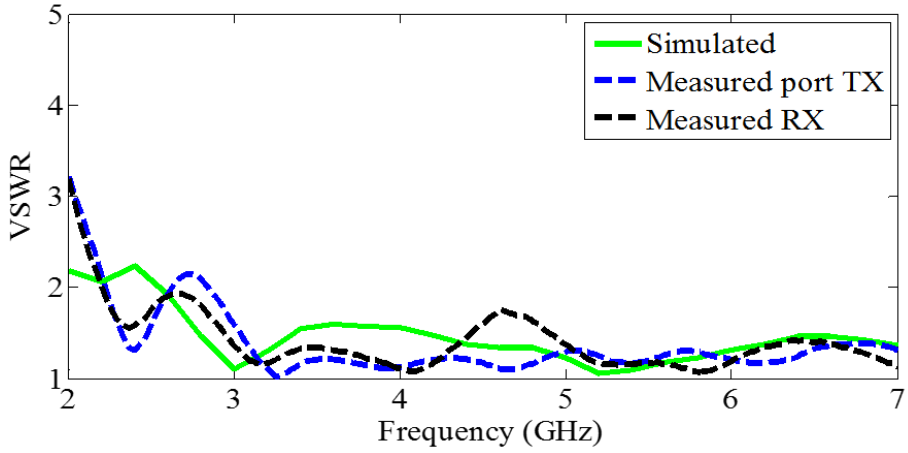

(a)

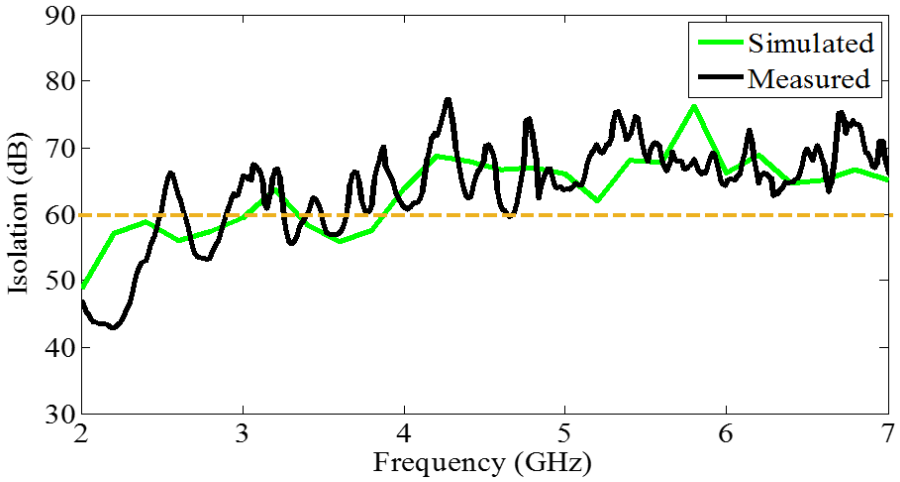

(b)

Figure 2.46: Measured and simulated (a) VSWR, and (b) isolation of the 2 – 7 GHz antenna when mounted on the 12" × 12 "

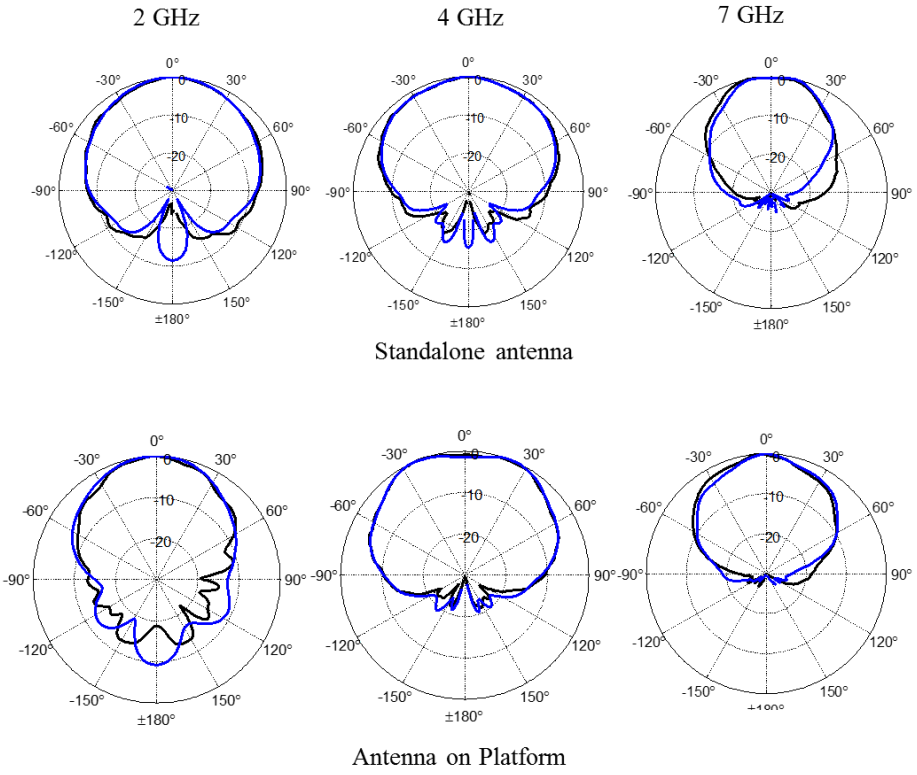

(a)

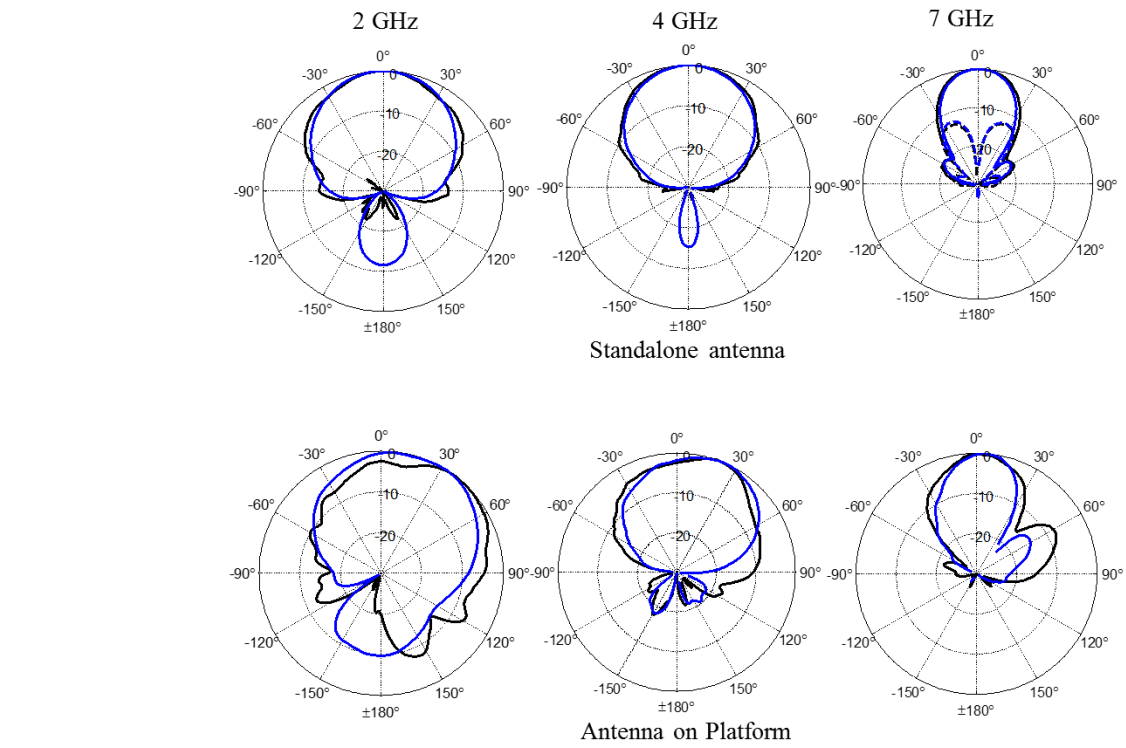

(b)

Figure 2.47: Patterns of the single polarized and single feed antenna in free standing and when mounted on the platform with (a) E-plane, and (b) H-plane.

2.5 Summary

Multi-octave performance of a Vivaldi array is demonstrated after recessing it inside a metallic enclosure. It is seen that if proper care is taken when recessing this radiator inside a cavity, excitation of resonant modes may be avoided. The proposed all-metal antenna does not use absorbing materials and, yet, exhibits resonance-free behavior over 5:1 bandwidth. The cost-effective prototyping has shown to have minor effect on antenna performance. VSWR < 2, gain > 5dBi, and low side lobes with symmetric patterns are demonstrated. Favorable agreement with the theory verifies the robustness of the proposed design. Initial investigation of antenna scan capabilities demonstrates comparable

performance with its free space counterpart. A second embodiment of this radiator, resulting from the decrease of number of array elements to one is proposed. A shaped cavity is used in this case to allow wideband response with monotonic gain increase and low side lobe levels. Designed antennas are used in a bi-static STAR platforms with isolations > 50 dB demonstrated.

Chapter 3

Dual-Polarized STAR Antennas on Share Antenna Platform

3.1 Overview

Chapter 2 focused on single-polarized cavity-backed Vivaldi antennas. In this chapter, a dual-polarized embodiment of this array is investigated. Dual-polarized capability enables frequency reuse and improves the awareness of an EW system. The 3 × 4 single polarized Vivaldi array of the previous chapter has shown promising performances when recessed inside a metallic enclosure. The question that one may ask is how do we obtain a dual-polarized version of that antenna and how does it perform in comparison to its free standing counterpart. Answers to these questions are provided in this chapter. It is shown in this chapter that recessing the dual-polarized Vivaldi array inside a cavity generates different types of resonances that have never been reported in open literature. These resonances can significantly degrade the antenna performances if proper design techniques are not taken to eliminate or mitigate their effects.

This chapter is organized as follows:

- In Section 3.2, analysis and design of a dual-polarized 3 × 4 cavity-backed all metal Vivaldi antenna recessed inside a metallic cavity is discussed.
- Section 3.3 presents a simplified version of the array of Section 3.2 with only two elements in the E-plane and one element in the H-plane. This newly proposed antenna is fed using a 2-way power divider / combiner.

- Section 3.3 introduces a more compact design of a dual-polarized antenna with a smaller aperture and a fully integrated power divider.
- Section 3.4 analyzes the bi-static STAR capabilities of the different designed antennas. Performances of the antennas when integrated on compact antenna platforms are discussed.
- Section 2.5 summarizes the chapter.

3.2 Dual-Polarized 3 × 4 Cavity-Backed Vivaldi Array

Dual-linearly polarized antennas are typically obtained by 90° rotation of their single-polarized embodiment. In the case of this dual-polarized cavity-backed array, the process is not straightforward given the need to maintain resonant free behavior in the presence of the cavity. It is demonstrated in Chapter 2 that a single-polarized Vivaldi antenna can be recessed inside a lossless metallic cavity with resonance free behavior when the E-plane edge elements are directly connected to the cavity. For the dual-polarized embodiment, attempting to short the E-plane edge elements of the two orthogonal ports to the cavity will short the H-plane of the opposite polarization as illustrated in path 1 of Figure 3.1. This configuration provides resonant free behavior as expected but leads to degraded VSWR and reduced gain as seen in Figure 3.2. Attempting to follow path 2 of Figure 3.1, where edge elements are not shorted will generate resonances within the frequency range of interest as expected from the analysis performed in the previous chapter. The question therefore is how can we effectively recess a dual-polarized Vivaldi antenna inside a cavity without significant degradation of its performances? To answer this question, the case of the 3 × 4 Vivaldi recessed inside a 9 × 9 cm^2 cavity is investigated. The size of the cavity is chosen to have 2 cm ($\lambda_{7.5GHz}/2$) separation between the antenna edge elements and the cavity.

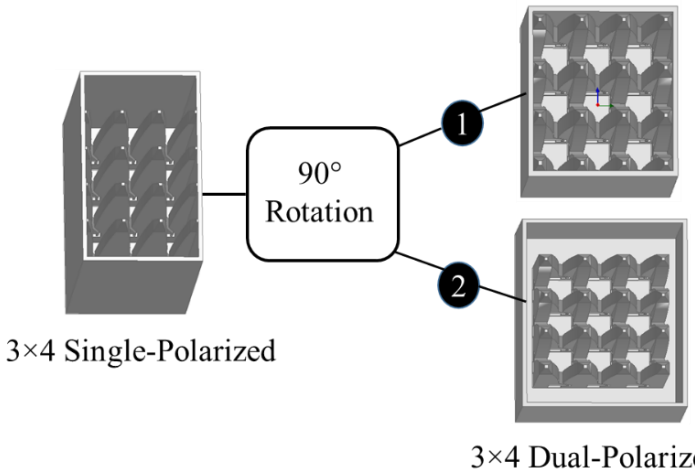

Figure 3.1: Illustration of transition from single to dual-polarized cavity-backed Vivaldi array. Path 1: all edge elements are shorted to the cavity walls. Path 2: none of the edge element is shorted to the cavity walls.

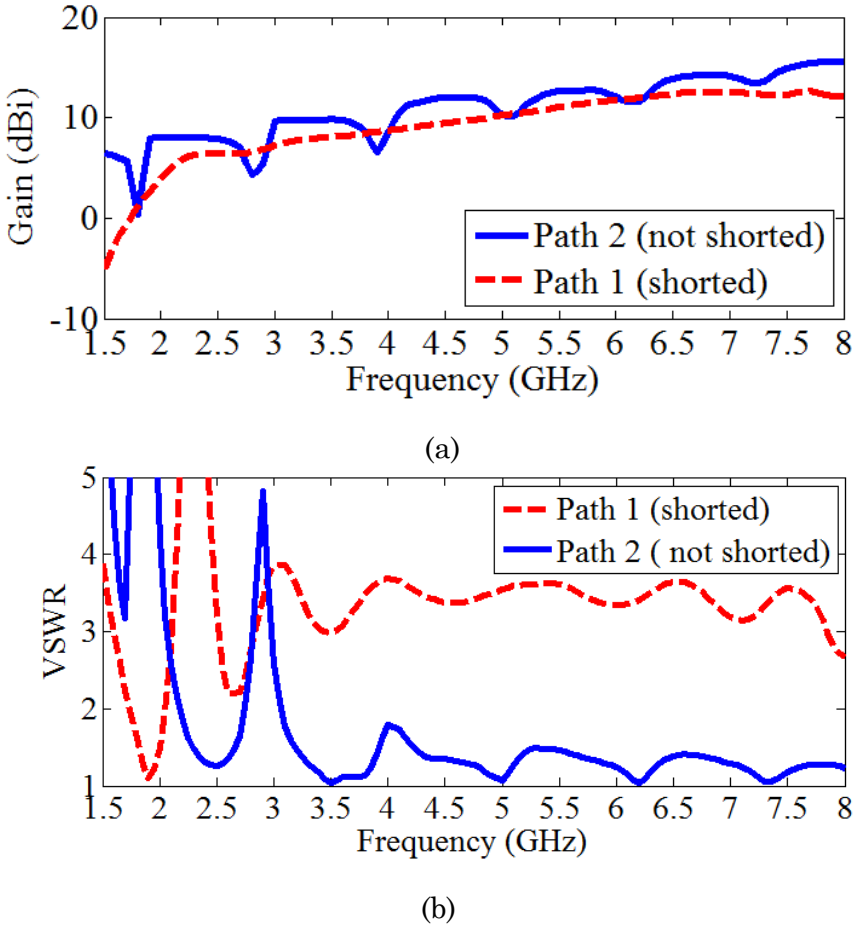

Figure 3.2: (a) Broadside gain and (b) VSWR of the 3 × 4 Vivaldi array recessed in a cavity showing degraded VSWR and resonances respectively when the antenna is shorted and not shorted to the cavity walls.

We have seen that the approach which consists of shorting the E-plane elements to the cavity can suppress all the resonances, at the expense of severe degradation on the VSWR bandwidth and gain. To determine a more efficient mean to suppress the resonances, the surface currents on the recessed array following path 2 of Figure 3.1 are analyzed. These are shown in Figure 3.3, with the cavity hidden for better visualization of the currents. Surface currents are plotted at 2 GHz where a high Q resonance is seen as shown in Figure 3.2. As seen, standing wave patterns can clearly be identified. More importantly, these standing waves are seen to be stronger on the corner elements. This critical observation that is not seen in the singly polarized case is mainly due to the presence of the orthogonal polarization which provides medium for currents to flow. These currents are partially cancelled as they flow on opposite arms of the cross-polarized antenna (balanced-radiation). Currents on corner elements do not see a symmetrical environment needed for cancellation to happen. They are reflected back to the feed, therefore justifying the strong standing waves observed on these elements.

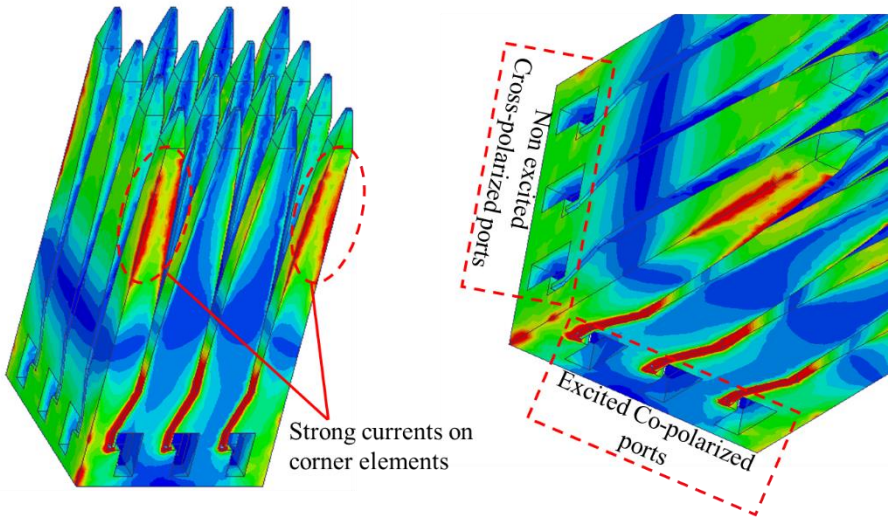

Figure 3.3: Surface currents at 2 GHz on the 3 × 4 dual polarized Vivaldi array recessed in a rectangular enclosure with edge elements not connected to the cavity.

From this analysis, it appears that efficient treatment of corners elements can potentially eliminate or mitigate the negative effect of the seen cavity resonances. The standing waves seen in Figure 3.3 are due to the gap between the corner elements and the cavity. It was demonstrated in Chapter 2 that eliminating any gap at the origin of the resonance behavior is the most effective means to remove its occurrence. This is done in this dual-polarized configuration by shaping the cavity. This newly proposed antenna is obtained by extending the outer boundaries of the corners elements so they can be shorted with the cavity as shown in Figure 3.4. The cavity aperture is also reduced at its corners as illustrated in Figure 3.4, to allow currents to mainly flow on the ground plane.

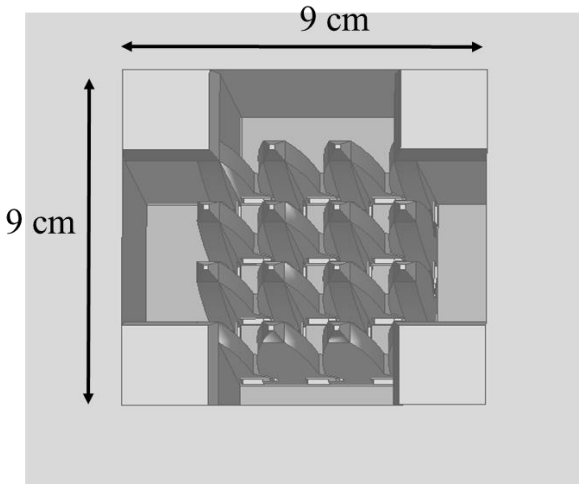

Figure 3.4: Proposed 3 × 4 dual polarized Vivaldi array recessed in a shaped rectangular enclosure with corners elements shorted to the cavity.

To assess the effectiveness of this approach in eliminating the resonances while preserving the performance of the antenna, the broadside gain and VSWR of the designed antenna are shown in Figure 3.5. As seen, the antenna is resonance-free and maintain a VSWR < 2 over more than 3.5:1 bandwidth. The broadside gain of this antenna is compared to that of a uniformly excited aperture of 9 × 9 cm^2. The proposed design is seen to have

lower aperture efficiency. This low aperture efficiency is due to the reduction of the physical aperture needed to suppress resonances within the cavity. Gain is however greater than 5 dBi and monotonically increases over the band of interest (2 – 8 GHz). The broadside radiation patterns are shown in Figure 3.6, and are seen to be symmetric with low cross-polarization (i.e. < 20 dB).

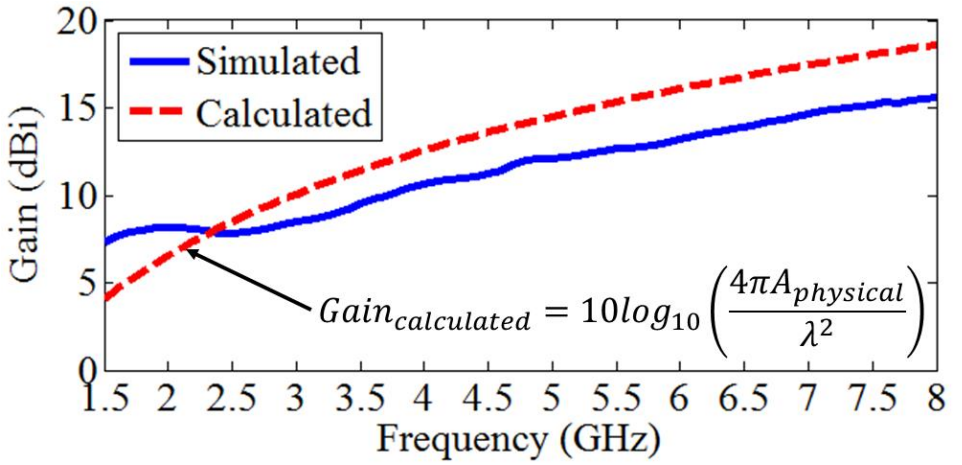

(a)

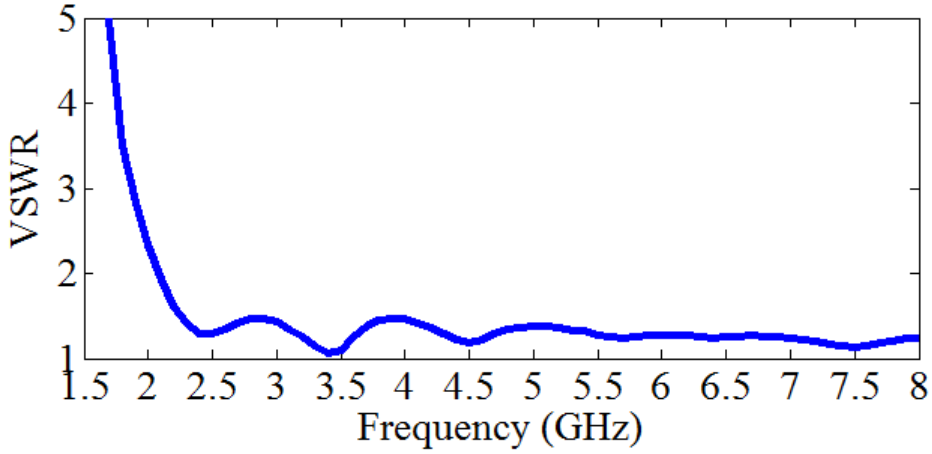

(b)

Figure 3.5: (a) Broadside gain, and (b) VSWR of the proposed 3 × 4 dual polarized Vivaldi array recessed in a lossless cavity showing resonance free response over 4:1 bandwidth.

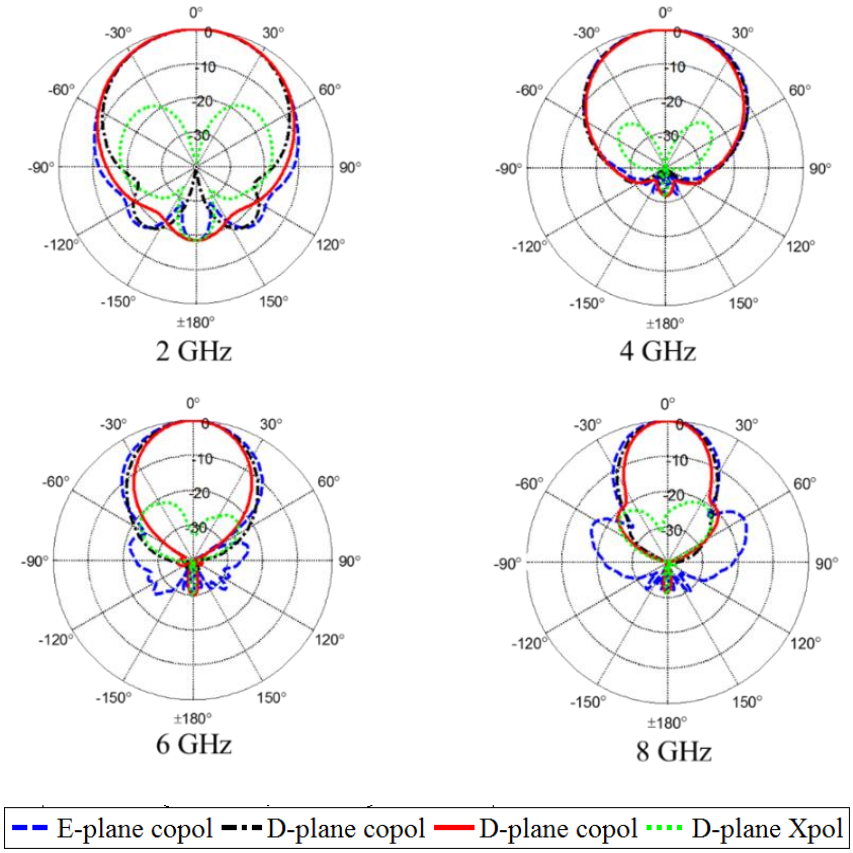

Figure 3.6: Broadside radiation patterns of the dual polarized 3 × 4 cavity-backed array.

3.3 Dual-Polarized 2-Element Cavity-Backed Vivaldi Array

The dual-polarized cavity-backed 3 × 4 array of the preceding section requires a 12-way divider for each polarization. In addition to the complexity of this antenna when only used for broadside radiation, the insertion loss of the power divider may be detrimental for the overall system performance. To decrease the insertion loss and reduce the complexity of the antenna, a 2-element configuration is analyzed. The aperture and profile are similar to parameters used for the 3 × 4 array, the aperture size is 9 cm ($\lambda_{2GHz}/1.66$) and the antenna is 12 cm long ($\lambda_{2GHz}/1.25$). The proposed flush mountable configuration, shown in Figure 3.7, has the shape and the appearance of quad-ridge (QR) waveguide horn antennas, often considered as a prime candidate when dual-polarized operation with easy concealment is

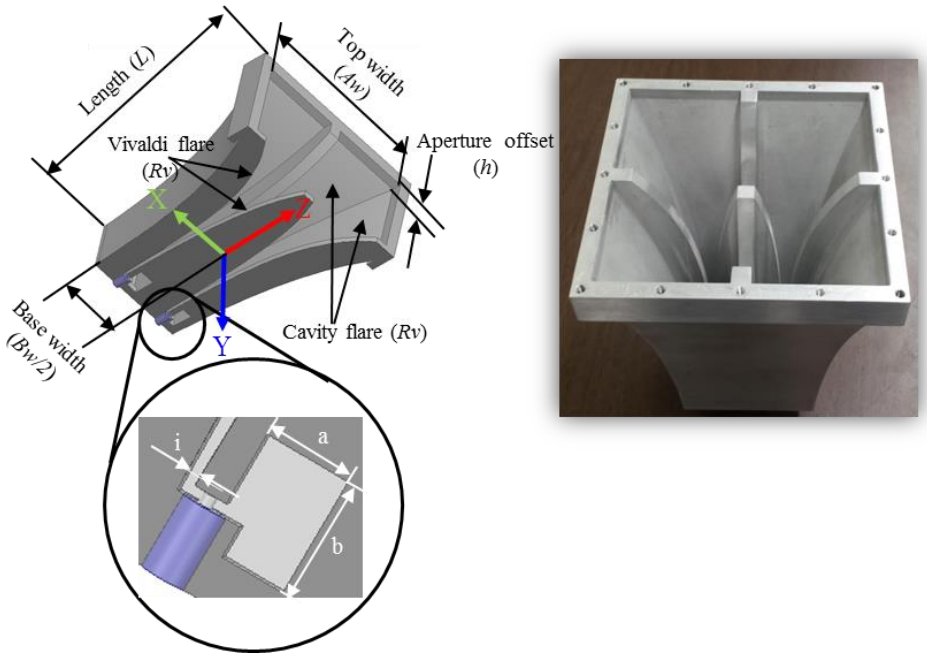

(a) (b)

Figure 3.7: (a) E-plane cut and (b) photograph of the proposed 2-element cavity-backed Vivaldi antenna array.

required [14], [85]-[88]. At high frequencies where feeder losses become significant, horns are typically-fed with ridge waveguides and orthomode transducer (OMT) to combine the two orthogonal polarizations [89]-[94]. At low frequencies (L, S-band), the waveguides are large, and horns are directly fed with coaxial connectors [85]-[88]. The QR horns proposed in [85]-[88] are typically fed with 50 Ω coaxial side connectors where the center conductors of the two orthogonal polarized ports are connected transversely across the ridge gap. This feeding technique creates an asymmetry between the two polarizations since the connectors need to be offset, causing limited polarization isolation and higher cross polarization [86]. For wideband response and high-frequency operation, the offset between the two coax feeds is typically small leading to limited power handling. This antenna is therefore less attractive for applications requiring ultra-wideband response while maintaining

symmetrical response between the two orthogonal ports. Moreover, the separation between ridges is constrained by the thickness of the ridge itself. To provide a smooth transition to a 50 Ω coaxial connector, ridges are chamfered leading to degradation of the VSWR at high frequencies [86].

The herein proposed flush-mountable dual-polarized antenna is designed for the 2 - 8 GHz range. It is resonant free, coax-fed with symmetric performance between orthogonal ports, and therefore achieving high cross-pol isolation over wide bandwidth. The proposed antenna does not rely on differential excitation to achieve high isolation. Instead, a broadband 2-way power divider which is well known for its design simplicity is used per polarized port. In this section, Eigen-mode analysis is used to study the interaction between the antenna and the cavity to enable more intuitive design. A parametric study is performed to assess the impact of some key parameters on the antenna performance. The choice of design parameters for the proposed antenna aims to maintain VSWR < 2, high polarization isolation, low cross-pol, and monotonic gain increase over 2 – 8 GHz band. Comparison between the designed antenna and coax-fed quad-ridge horns is shown in Table 3.1. As seen, none of the reported designs combines high aperture efficiency, and symmetric performance between the two orthogonal polarizations as the configuration herein.

Table 3.1: Comparison between Proposed Antenna and Coax-Fed Quad-Ridge Horns

Ref.	Size ($Area \times H$)	BW (GHz)	Aperture Eff. (%)
This work	$0.36\lambda_{2GHz}^2 \times 0.8\lambda_{2GHz}$	2 - 8	139 - 55
[85]	$0.48\lambda_{2GHz}^2 \times 1.11\lambda_{2GHz}$	2-12	74.4 - 10
[86]	$1.13\lambda_{2GHz}^2 \times \lambda_{2GHz}$	2-26.5	72.2 – 3.8
[87]	$1.13\lambda_{0.75GHz}^2 \times 0.73\lambda_{0.75GHz}$	0.75-3.5	70 – 10.2
[88]	$2.23\lambda_{8GHz}^2 \times 2.05\lambda_{0.75GHz}$	8-18	35 – 44

3.3.1 Antenna Analysis and Design

Photograph of the 2 × 1 dual-polarized array with its two E-plane elements shorted to the cavity is shown in Figure 3.7. Each polarization of the antenna is fed through a 2-way power divider. An exponential flare section with growth rate *Rv* is used for each Vivaldi arm. The inner walls of the cavity are also flared in both, E-, and H-planes following exponential taper with growth rate *Rc*. This inner flare of the cavity is terminated at an offset *h* from the aperture. The values for the parameters shown in Figure 3.7(a) are summarized in Table 3.2.

Table 3.2: Key Design Parameters of The 2-element Cavity-Backed Antenna

Parameter	*a*	*b*	*L*	*h*
Value	8 mm	11 mm	120 mm	5 mm
Parameter	*Rc*	*Rv*	*Aw*	*Bw*
Value	0.2	0.35	90 mm	46 mm

The enlarged view of the feed section, shown in Figure 3.7(a), clearly depicts the transition from the coax to a parallel plate waveguide. A rectangular opening with parameters *a* and *b* is used to create a high impedance near the junction. To enable the use of a 2-way power divider, this transition is engineered to maintain the same polarization of the electric fields in the two Vivaldi elements. This leads to a small asymmetry between the two excited Vivaldi elements needed per polarization. A more symmetric design that further increases the isolation between orthogonal ports would require the use of differential feed. To maintain low amplitude and phase imbalances over the targeted bandwidth, this feed will be rather complex, and therefore a simple modification in antenna design, as described above, is utilized in this research.

To understand the rationale behind the cavity shape, a 2-element Vivaldi antenna recessed inside a rectangular straight cavity is considered. A square 90 × 90 mm^2 cavity is

used, therefore setting turn-on frequency around 2 GHz. The thickness and width of each Vivaldi element are 6 mm and 36 mm (~ $\lambda_{2GHz}/4.2$), as shown in the inset of Figure 3.8. This size is close to $\lambda_{2GHz}/2$ when the apertures of the two Vivaldi elements are combined. The dual-polarized operation is obtained by recessing two 2-element arrays inside the cavity as seen in the inset of Figure 3.8. The edge elements are shorted to the cavity to eliminate resonances in gaps between these elements and the cavity as discussed in Chapter 2. The calculated VSWR and broadside gain using ANSYS HFSS [77] are shown is Figure 3.8.

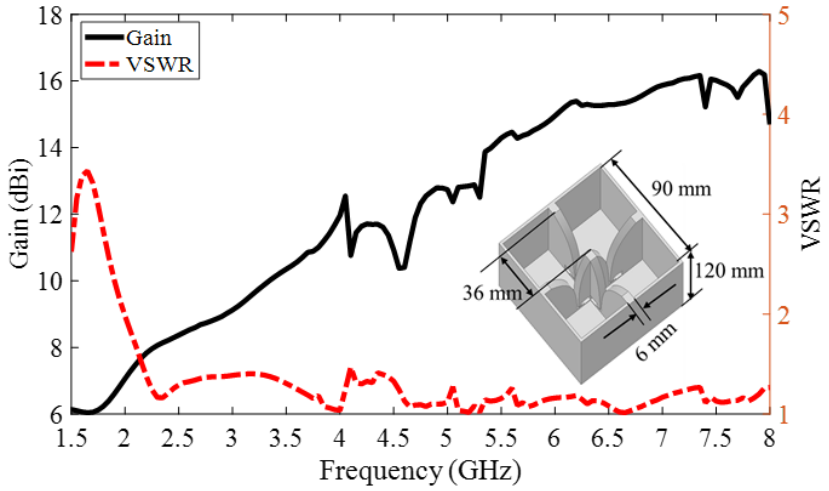

Figure 3.8: VSWR and broadside gain of a 2-element Vivaldi array recessed inside a 90 × 90 mm^2 cavity.

As seen, monotonic gain increase is observed up to 4.1 GHz where a sharp drop in gain is seen. Several dips in gain correlated with small spikes in VSWR are also seen at some specific frequencies above 4.1 GHz.

To understand the origin of the observed phenomena, the surface currents on the cavity walls are plotted in Figure 3.9(a) at 4.1 GHz where the first dip in gain is observed. As seen, standing wave patterns are clearly formed at this frequency suggesting that the spikes are due to the cavity resonance. To provide further validation of the observed phenomena, Eigen-mode analysis is performed using ANSYS HFSS [77]. To have a closed

structure, the cavity aperture is modeled with a perfect magnetic conductor (PMC). Whereas this boundary partially reflects non-tangential fields at the aperture, its impact is found to be insignificant on the observed response and can therefore be used for the Eigen-mode analysis. The Eigen-mode response reveals multiple resonances within the frequency band of interest. The surface currents on the cavity walls for resonant mode at 4.27 GHz is shown in Figure 3.9(b). While some differences can be seen between these currents and the driven mode analysis (Figure 3.9(a)), currents maxima and minima are observed in similar areas, thereby confirming the above claims. The shift in resonant frequency between Eigen and driven mode analysis is due to the use of the PMC boundary. This analysis thereby validates that the dips observed in gain at some frequencies are due to the excitation of cavity resonances in the antenna structure.

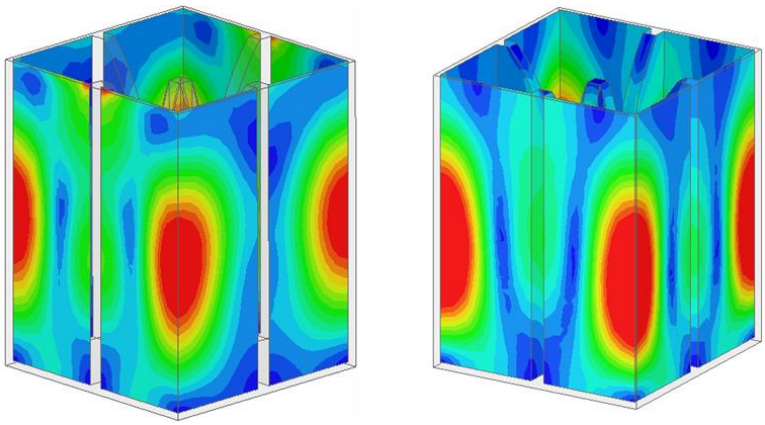

(a) (b)

Figure 3.9: Surface currents on the antenna for a square straight cavity with (a) driven, and (b) Eigen analysis methods.

To suppress this and other resonances and maintain monotonic gain increase over wider bandwidth, their nature and origin must be determined. The Eigen-mode analysis reveals multiple resonances below 4.1 GHz which are not observed in antenna impedance match and radiation patterns. A close observation of the surface currents on the cavity

shows similar standing waves on all four walls of the cavity, suggesting the presence of multiple similar resonances. More precisely, these resonances appear to be generated by four identical resonators. Each resonator is waveguide based and is obtained by the boundary provided by the two sidewalls of the cavity and two cross-polarized Vivaldi antenna elements. This is illustrated in Figure 3.10(a) with an enlarged view showing the detailed dimensions of the resonator.

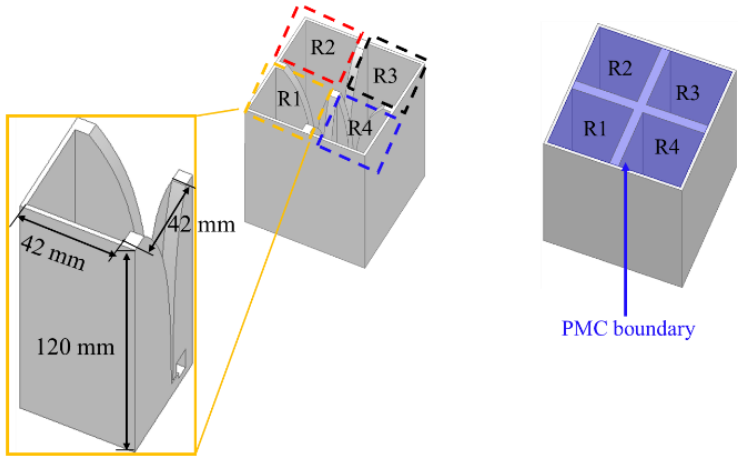

(a) (b)

Figure 3.10: (a) Waveguide resonator obtained by combining boundaries of the cavity and cross-polarized Vivaldi elements, and (b) simplified model.

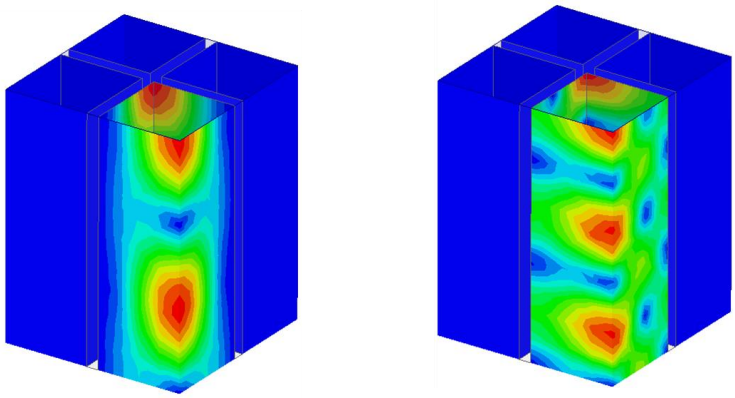

(a) (b)

Figure 3.11: (a) Surface current of waveguide resonant modes terminated on aperture with a PMC (a) TE_{101}, and (b) TE_{102}.

To understand the nature of the resonances, we can replace the Vivaldi elements by metallic walls (Figure 3.10(b)), leading to a simpler model of rectangular waveguide resonator. In this case, the resonator is electrically shorted at one end by the cavity base and magnetically shorted at the other end with the PMC boundary. The surface currents of each resonator at 4.03 GHz (TE_{101}) and 4.74 GHz (TE_{102}) are plotted in Figure 3.11 for resonator R4 of Figure 3.10(b). As seen, TE_{101} resonant mode exhibits similar behavior when compared to the plots of Figure 3.9 for that specific section of the antenna. The main difference is attributed to the model simplification. In a more general sense, for a TE*mn* wave propagating inside the waveguide, the resonant frequency can be calculated as:

$$f_{res} = \frac{c}{2\pi}\sqrt{\left(\frac{m\pi}{d}\right)^2 + \left(\frac{n\pi}{d}\right)^2 + \left(\frac{(2l+1)\pi}{2L}\right)^2} \tag{3.1}$$

where c is the speed of light, L is the length of the antenna as illustrated in Figure 3.7, d (d = 42 mm in Figure 3.10 (a)) is the width of the waveguide, and l is the order of the resonance associated with the longitudinal dimension.

Table 3.3: Calculated and Simulated Resonant Frequencies (In GHz)

Mode	TE_{100}	TE_{101}	TE_{102}	TE_{110}	TE_{111}
$f_{res}(cal)$	3.62	4.03	4.74	5.08	5.38
$f_{res}(sim)$		4.1	4.5	5.05	5.3

The resonant frequencies calculated using (3.1) are given in Table 3.3 and good correlation is obtained between the calculated resonant frequencies and frequencies at which dips are observed in the gain response. The small shift between the calculated and simulated resonances is due to the model simplification, specifically by replacing Vivaldi elements with metallic walls, and using PMC boundary at the aperture. The fundamental

resonant frequency (TE_{100}) of the cavity at 3.62 GHz does not seem to be excited given that no reduction in gain is observed around this frequency. The second mode at 4.03 GHz (TE_{101}) has one standing wave as shown in Figure 3.11. The excitation of this mode therefore explains the sharp drop in gain observed at 4.1 GHz in Figure 3.8. From this analysis, it can be stated that, the seen resonances in the response are due to the presence of TE_{mnl} resonances of resonators obtained from combined cavity walls and cross-polarized Vivaldi arms. These resonant modes are excited at the base of the waveguide at the coax to parallel plate transition discontinuity. Analysis of Table 3.3 shows that the frequency of the dominant excited resonant mode strongly depends on d ($d < L$). Decreasing d is therefore expected to push this first excited resonance to higher frequency. To validate this assertion, the size of the cavity is reduced from 90 mm to 50 mm, thereby reducing d from 42 mm to 22 mm. The resonant frequencies of the TE_{101} and TE_{102} modes in this case are respectively 7.07 GHz and 7.5 GHz. The gain and VSWR of the cavity-backed 2-element Vivaldi antenna in this case are plotted in Figure 3.12. As expected, resonance free response up to 7.3 GHz is achieved. A second resonance is seen at 7.8 GHz. These two resonances are 0.3 GHz shifted from the approximated calculation. The correlation between the responses shown in

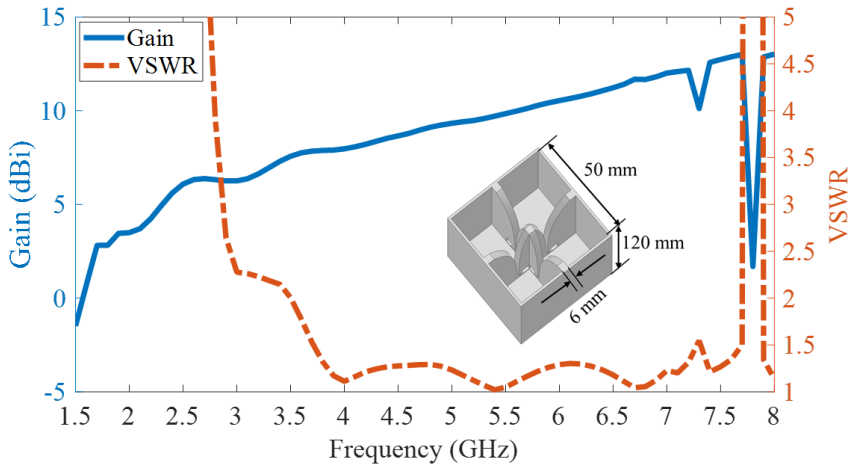

Figure 3.12: VSWR and broadside gain of a 2-element Vivaldi array recessed inside a 50 × 50mm^2 cavity.

Figure 3.12 and theoretical calculation clearly validates that decreasing d is effective in pushing these resonances out of the band of interest. This result also explains why these resonances were not seen in the single-polarized 3 × 4 array. Similar resonances are however observed in the single feed antenna of Section 2.3 if the proposed H-plane shape of the cavity is not inserted. Figure 3.12 shows a clear degradation of VSWR below 3.5 GHz; this is due to the reduced aperture of the antenna. It therefore appears that reducing the cavity width results in pushing the resonances to higher frequencies at the expense of bandwidth reduction.

To obtain a resonant free cavity-backed 2-element dual-polarized Vivaldi antenna over wide bandwidth, the cavity is flared in both, E-, and H-planes. The width of the cavity at its base is Bw = 46 mm, thus eliminating the excitation of TE_{101} mode up to 8.12 GHz. The width of the cavity at the aperture of Aw = 90 mm is chosen to have a turn-on frequency around 2 GHz, as seen in Figure 3.8. An exponential taper shown in the inset of Figure 3.13(b) is used to flare the cavity. With this shaped cavity, no detrimental resonances are expected within the frequency band of interest. The excitation of higher order modes is however expected near the aperture given its larger area. These modes can add constructively or destructively and thereby significantly change the aperture field distribution. To assess the impact of these modes, a parametric study is performed with the cavity flare rate Rc and the aperture offset h. These two parameters are chosen since they are directly correlated to the antenna size near the aperture. In this study, the goal is to achieve gain > 8 dBi at the turn-on frequency with good impedance match and consistently increased directivity (gain) over at least 4:1 bandwidth (2 – 8 GHz).

It is well accepted that a flared inner wall of a circular quad-ridge horn aids in its gain stabilization [85]. Thus, impact of the cavity flare Rc is analyzed first. Rc is varied from 0 to 0.3 with zero representing linear flare as shown in the inset of Figure 3.13(b). The computed broadside gain and VSWR are shown in Figure 3.13 for each parameter. As

seen, the gain starts dropping at 6.5 GHz, 6.9 GHz, 7.3 GHz, and 7.9 GHz for *Rc* 0, 0.1, 0.2, and 0.3, respectively. This is due to the aperture field perturbation caused by the excitation

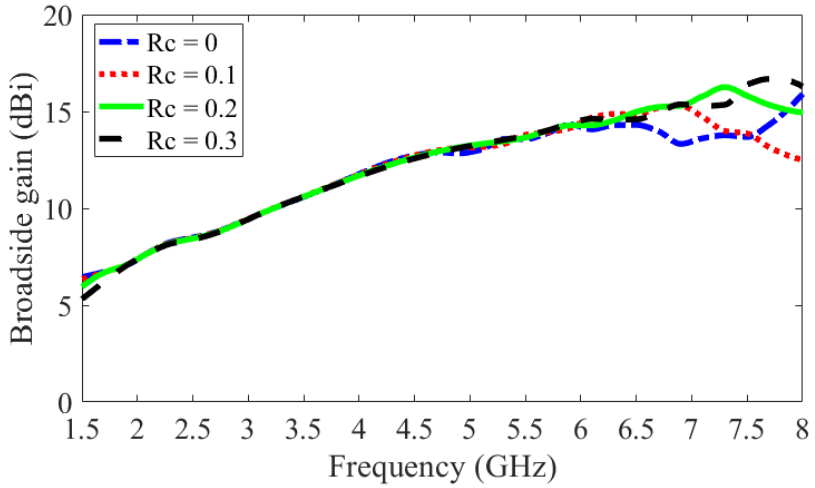

(a)

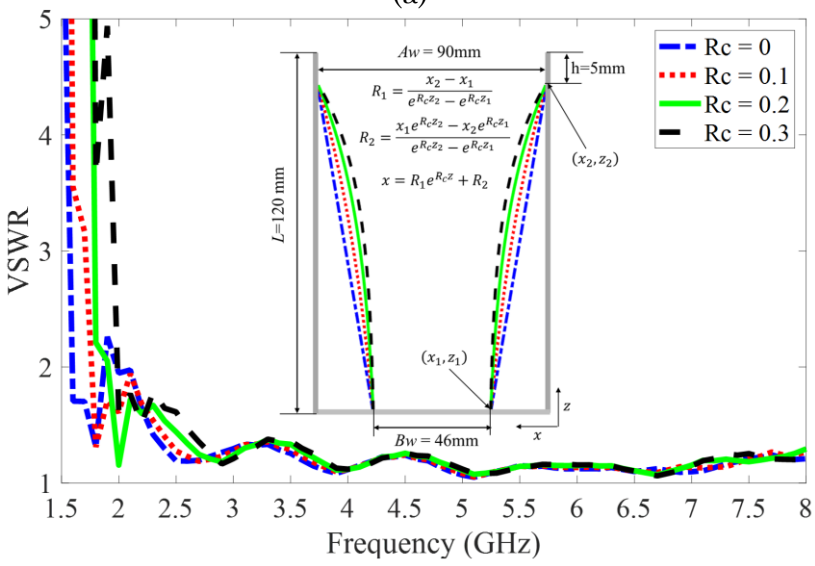

(b)

Figure 3.13: (a) Broadside gain, and (b) VSWR of the cavity-backed 2-element Vivaldi for varying of cavity flare rate *Rc*

of higher-order modes as the cavity size increases near the aperture. A similar trend is seen in VSWR response where the turn-on frequency is shifted to higher frequencies as *Rc*

increases. This degradation of VSWR with increased *Rc* is due to the reduced antenna volume. While larger *Rc* helps mitigate impact of high order modes contribution, the reduced volume of the cavity pushes the stored energies balance to higher frequencies. Based on these results, *Rc* = 0.2 is selected to maintain turn-on frequency of 2 GHz and monotonic gain increase over most of the frequency range of interest.

Since the increase of the volume of an antenna helps decrease its turn-on frequency, the inner walls of the cavity are not flared all the way to the aperture. The offset distance between the aperture and the cavity flare (*h*) is used therefore to lower the turn-on

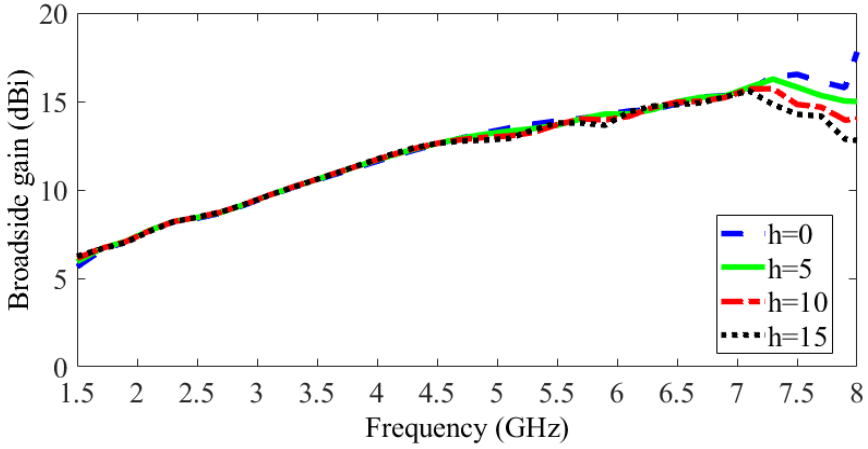

(a)

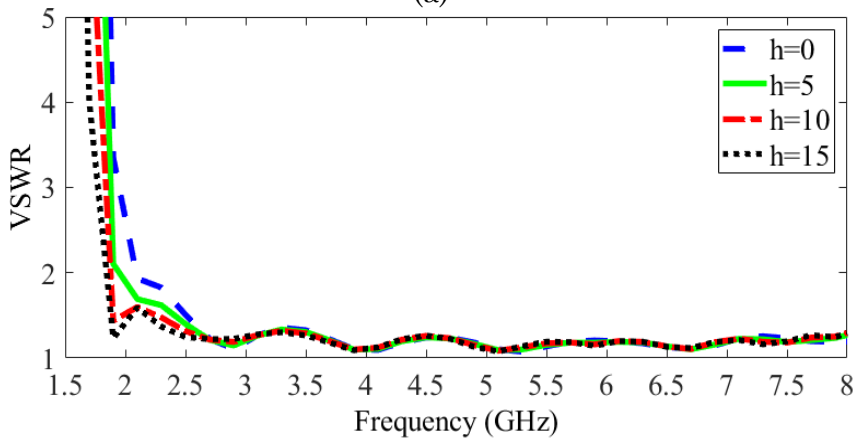

(b)

Figure 3.14: (a) Broadside gain, and (b) VSWR of the cavity-backed 2-element Vivaldi for varying of aperture offset *h*

frequency of the antenna while allowing marginal degradation on its far-field at high frequencies. This offset helps aperture matching, by improving the transition from waveguide to free space. The VSWR and broadside gain are shown in Figure 3.14 for h ranging from 0 to 15 mm. As seen, the turn-on frequency is lowered for higher values of h. The contribution of higher order modes is also seen to be significant with increased h. For h = 0 mm, the monotonic increase in gain is observed over wider bandwidth at the expense of higher degradation of VSWR at low frequencies. For h = 5 mm, the monotonic increase in gain is observed up to 7.2 GHz with maintained turn-on frequency at 2 GHz. This value is therefore selected for the prototype needed to experimentally validate the proposed antenna.

3.3.2 Fabrications and Measurements

The proposed antenna is built as a single aluminum block using combined CNC and EDM machining processes. No split block machining or welding is used during fabrication and assembly. To enable the required excitation, two sellout 2-way power dividers [95] are

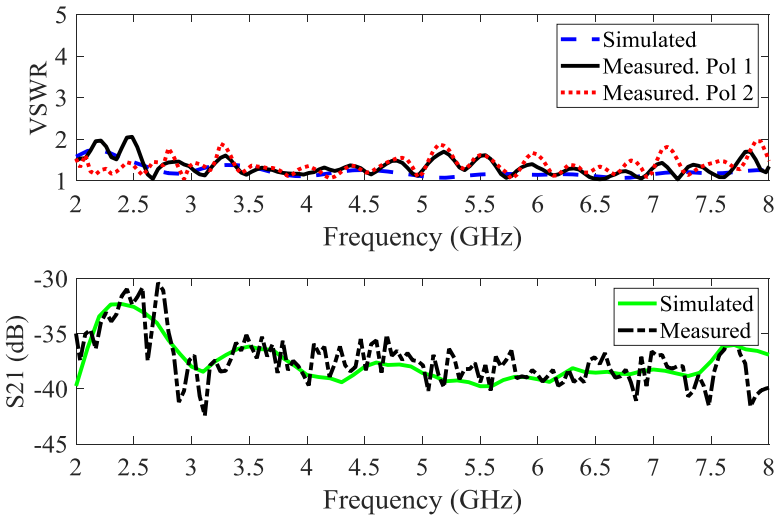

Figure 3.15: Measured and simulated VSWR and coupling of the proposed cavity-backed 2-element Vivaldi array.

used to feed the 2-element array for each polarization. All results in this section are shown from 2 – 8 GHz given that the divider is rated for that frequency range. Obtained VSWR and coupling between the two feeding ports are given in Figure 3.15. The VSWR is seen to be lower than 2 and coupling between the two ports is also seen to be lower than -35 dB over most of the operating bandwidth. The small differences seen in the VSWR measured at the two orthogonal ports are due to the assembly and fabrication imperfections. To emulate the flush mounted performance of the antenna, all far-field measurements are performed with a circular 19 cm diameter ground plane as shown in the inset of Figure 3.16. This ground plane does not have any impact on the VSWR and mainly affects the far-field patterns. The measured and simulated co-polarized broadside gains of the antenna are plotted in Figure 3.16. As seen, gain is > 8 dBi over the band with max of 16 dBi. The measured cross polarization discrimination (XPD) is > 30 dB over the band. This value is lower than the 40 dB limit for the simulated antenna over most of the bandwidth. The degradation in measured cross-pol is due to measurement errors and fabrication tolerances. The theoretical gain based on 100 % aperture efficiency is also calculated and compared to that of the proposed antenna (Figure 3.16). Aperture efficiency greater than 100% is observed at the low frequencies due to the presence of fringing fields at the aperture. At mid and high bands, aperture efficiencies > 80% and > 55%, respectively, are obtained.

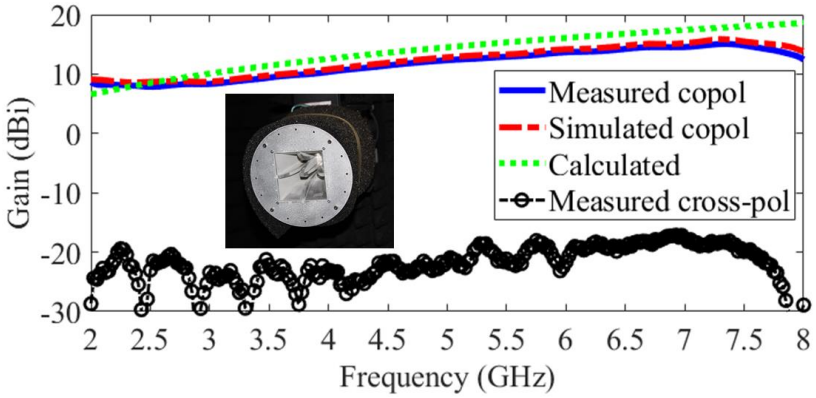

Figure 3.16: Measured and simulated gains of the proposed cavity-backed 2-element Vivaldi array.

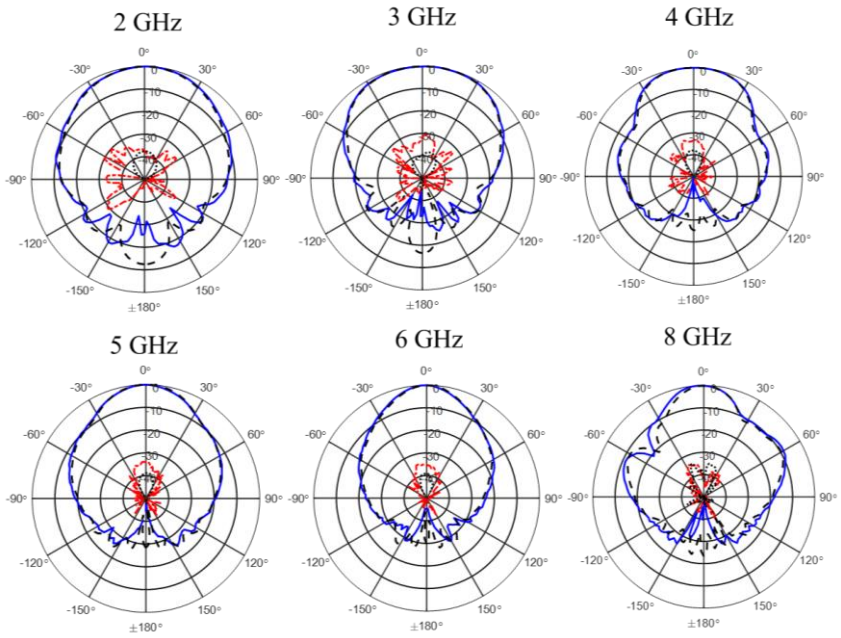

(a)

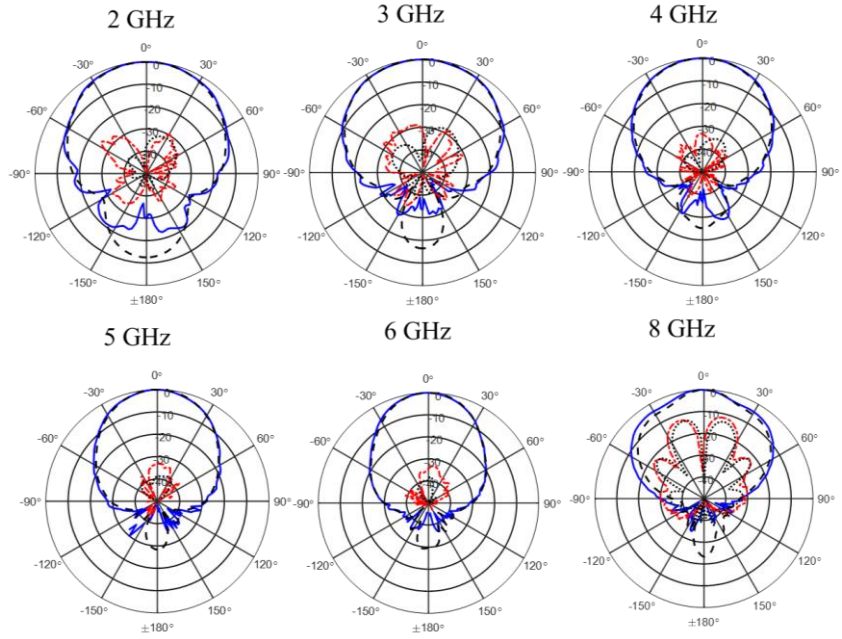

(b)

Measured (co-pol) Simulated (co-pol)
Measured (x-pol) Simulated (x-pol)

Figure 3.17: Measured and simulated radiation patterns of the designed cavity-backed 2-element Vivaldi array.

The measured and simulated patterns at 2 GHz, 3 GHz, 4 GHz, 5 GHz, 6 GHz, and 8 GHz, are shown in Figure 3.17. The obtained patterns are symmetric with low side lobes in both, E-, and H-planes. The other mode of polarization has similar performance as expected from the symmetric configuration and feeding technique. Beam broadening is observed at 8 GHz as a result of the decreased gain and aperture efficiency as described in Section 3.3.1. The H-plane cross-pol is also seen to be higher at this frequency, due to strong contribution of higher order modes.

3.4 Dual-Polarized 2-Element Cavity-Backed Vivaldi Array with Integrated Power Divider

The dual-polarized cavity-backed 2-element Vivaldi antenna discussed in Section 3.3 requires a commercial 2-way power divider per polarized port. The aperture of that antenna is 90 × 90 mm^2, and was chosen for turn on frequency at 2 GHz while maintaining stable patterns at high frequencies. The compact 12" × 12" platform of Section 2.4.1 imposes a maximum antenna aperture of 80 × 80 mm^2 when mounted diagonally on the ground plane for STAR operations. The cavity-backed 2-element Vivaldi of the previous section therefore does not meet the requirements of such platform.

In this section a reduced aperture dual-polarized and cavity-backed 2-element Vivaldi antenna is presented. Knowledge gained from the parametric study of Section. 3.3.1 is combined with proper geometrical modifications of the antenna to obtain a compact 75 × 75 mm^2 aperture with turn on frequency maintained at 2 GHz. The capabilities of this newly introduced antennas are further extended with an integrated power divider / combiner.

3.4.1 Stripline T-junction Power Divider

VSWR of the cavity-backed 2-element Vivaldi is found to be unaffected with the type of power divider used (isolated vs. non-isolated). Wilkinson isolated power dividers require resistive components [96] which limit the power handling capability and increase prototype cost. Non-isolated T-junction dividers are simple and can easily be fabricated in multilayer PCB boards. The proposed T-divider is designed in stripline using two 60 mils Taconic TLY 5 substrates. Thick substrate and resistor-free design enable high power handling capability. The T-junction is realized by exponentially tapering a stripline from 50 Ω at the input to 25 Ω at the junction. Two power dividers (one per polarization) are stacked together, with output ports, aligned with antenna input as shown in Figure 3.18. Ports 1 and 2 of Figure 3.18 are the two input ports, their respective output ports are 3-4 and 5-6. The fabricated dividers are assembled in a modular configuration, allowing them to be tested as standalone components or part of an integrated system. In the standalone configuration (Figure 3.19), the measured and simulated reflection coefficient and power coupled to ports 3 and 4 are plotted in Figure 3.20. While simulation results are only shown up to 8 GHz, measurements are extended up to 10 GHz to demonstrate the wideband response of the fabricated component. As seen, the divider operates over more than 8:1 bandwidth with S11 < -15 dB. The coupling to the two output ports (ports 3 and 4) are seen to be greater than -3.5 dB from 2- 7 GHz which is of interest for this research. Above 7 GHz, insertion loss increases significantly. This high loss is due to leakage between stacked layers as frequency increases.

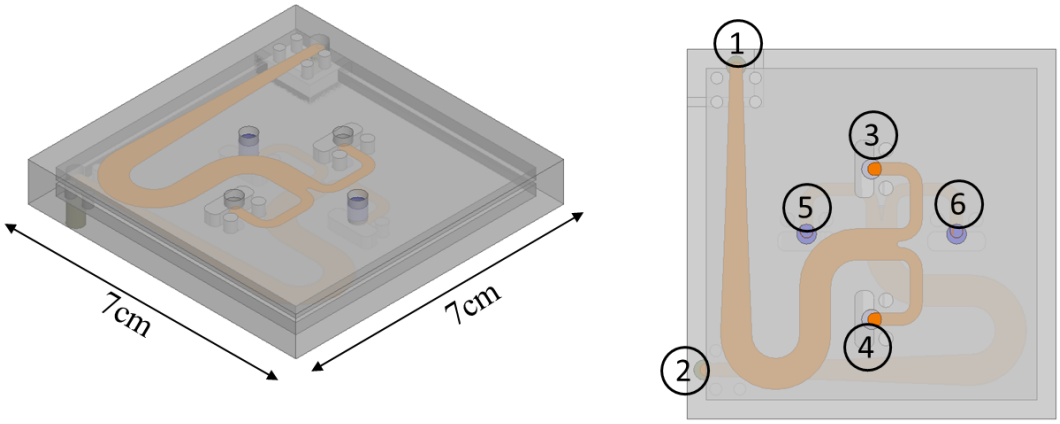

Figure 3.18: Isometric and top view of the proposed integrated T-junction power divider.

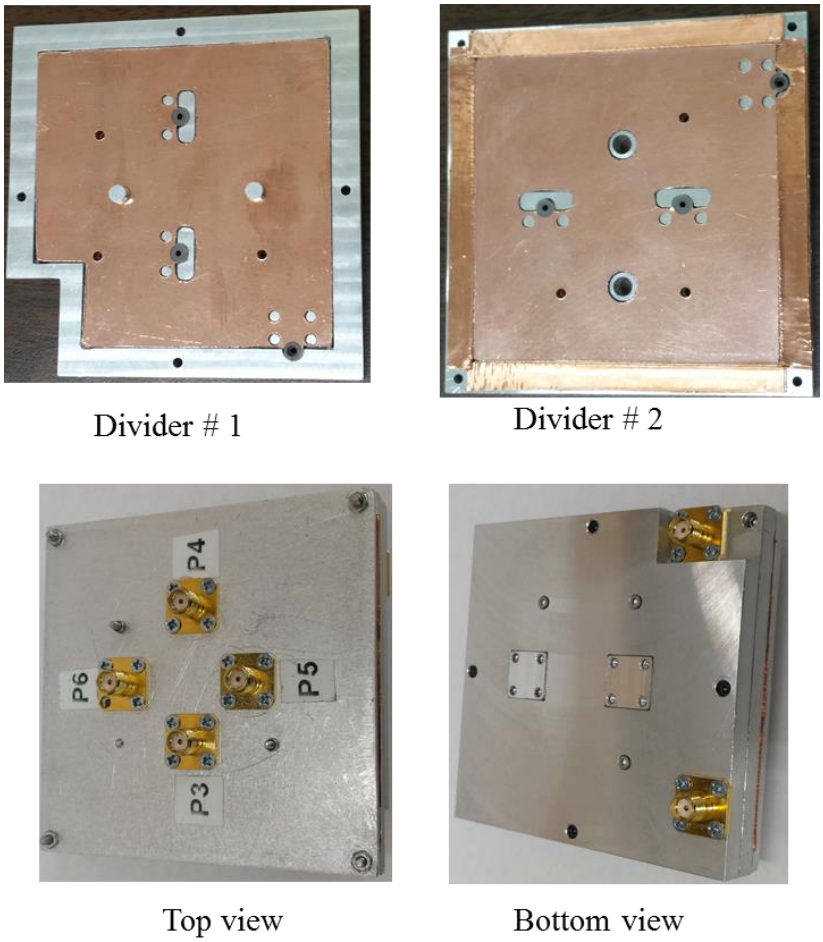

Figure 3.19: Photograph of the fabricated standalone T-junction power dividers.

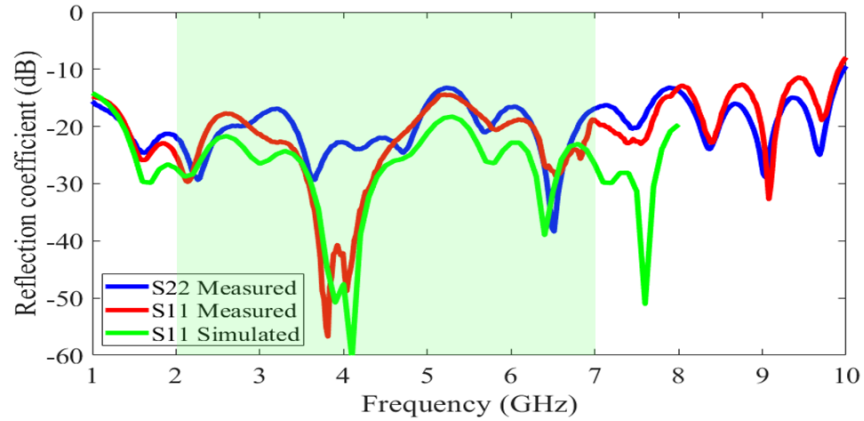

(a)

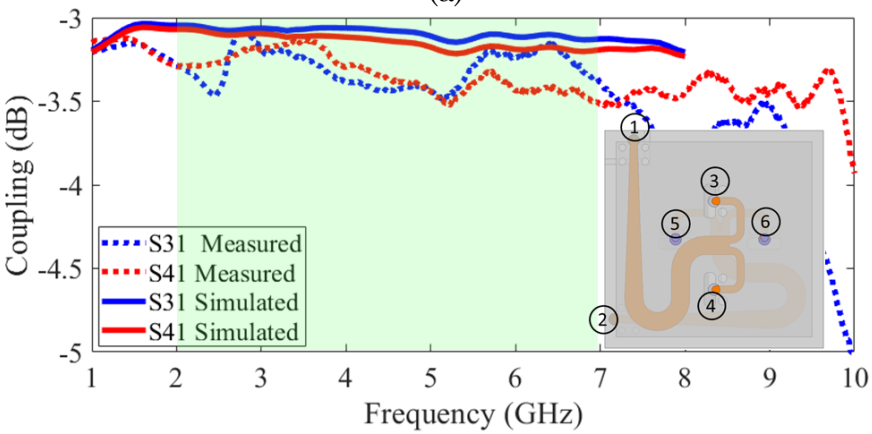

(b)

Figure 3.20: Measured and simulated (a) reflection coefficient and (b) coupling of the standalone T-junction power divider.

3.4.2 Dual-Polarized Antenna with Integrated Divider.

It is shown in Section 3.2.1 that the cavity is not flared all the way up to the aperture, but stop at an offset distance h. This offset from the aperture was seen to have great impact in decreasing the turn on frequency of the antenna. In the case of the 90 × 90 mm^2 aperture, h =5 mm was retained for acceptable far field degradation at high frequencies. Decreasing the aperture size to 75 × 75 mm^2 allows larger values for the parameter h while maintaining good far field pattern at high frequencies. With this reduced aperture, h is set to 20 mm as seen in Figure 3.21(a). The Vivaldi elements are flared in two transverse planes to have the appearance of a TEM horn [81]. This aims to further decrease

the turn on frequency by presenting a larger radiation surface to the low frequency currents. Measured and simulated VSWR of this new dual-polarized configuration are shown in Figure 3.21(b). As seen, VSWR < 2 is achieved over 2 – 7 GHz both, when the

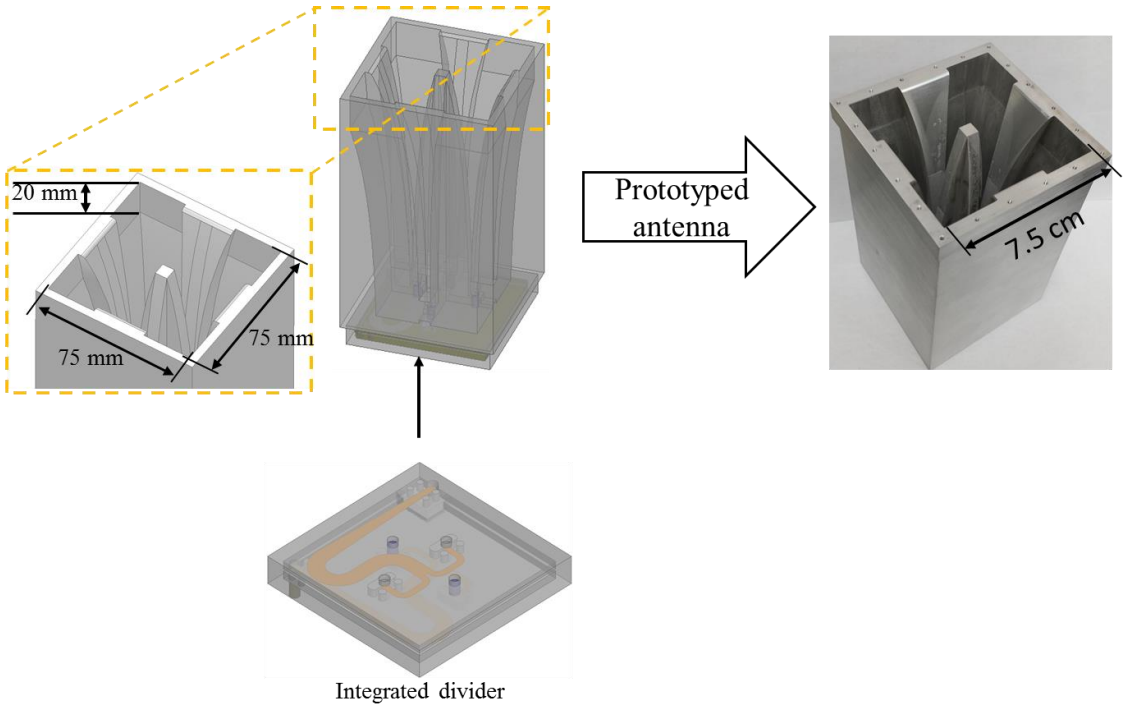

(a)

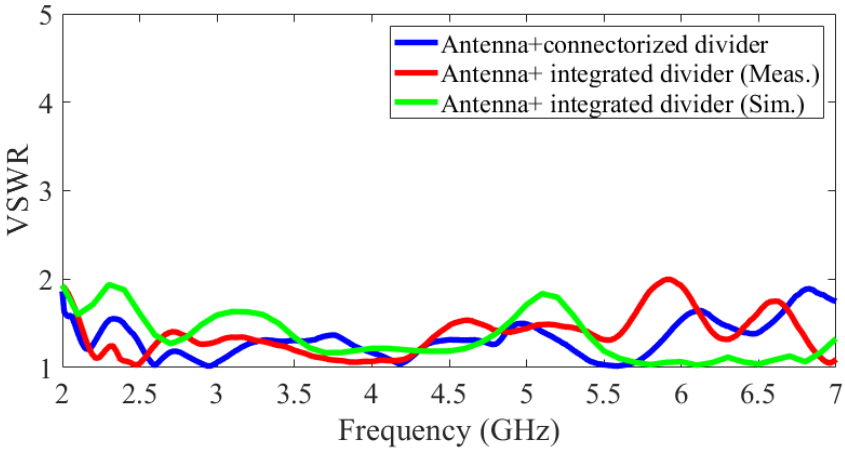

(b)

Figure 3.21: Dual-polarized antenna with integrated divider (a) designed and fabricated antenna (b) measured and simulated VSWR.

antenna is connectorized to the designed divider, and integrated with it. STAR performance of this antenna when mounted on the 12" × 12" platform is discussed in the next section.

3.5 Isolation Analysis with Dual-Polarized Antennas

Section 2.3 presented the isolation performance of single polarized STAR antennas in the 2 – 7 GHz band. In this section a similar study is performed on designed dual-polarized antenna. The study only focuses on the cavity-backed 2 element Vivaldi antenna given its simplicity for broadside radiation. The analysis starts with the 90 × 90 mm^2 aperture which requires a bigger ground plane, transmit receive isolation in this case is investigated on a 17" × 17" platform. The case of the smaller aperture, 75 × 75 mm^2 is later discussed when mounted on a compact 12" × 12" platform.

3.5.1 Isolation with 90 × 90 mm^2 Aperture

To assess the differences between isolations of dual- and single-polarized STAR system, transmit and receive antennas are first mounted on a smaller ground plane shown in Figure 3.22. The size of this ground plane is similar to that of the single polarized system of Section 2.4.1 with the separation between antennas kept equal to 25 cm. The antennas

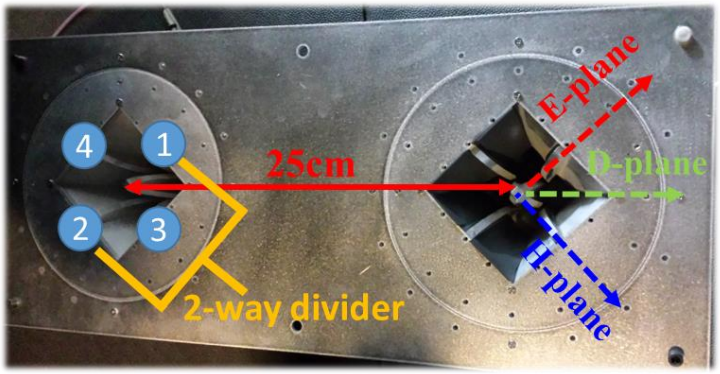

Figure 3.22: Setup of the cavity-backed 2-element Vivaldi array for isolation analysis.

are seen to be oriented in their respective D-plane. The orientations of the E- and H-planes indicated, are given with respect to excitation of ports 1 and 2 using a 2-way power divider. Measured co-polarized isolation is plotted in Figure 3.23(a). As seen, isolation > 60 dB is achieved above 5 GHz. Below this frequency, isolation degrade and reaches 37 dB at 2 GHz This isolation is also seen to be lower than the value obtained for the single polarized case of Figure 2.31. This is due to strong gains near horizon and propagation of TM surface currents when the antennas are oriented in the D-plane. In an attempt to suppress the

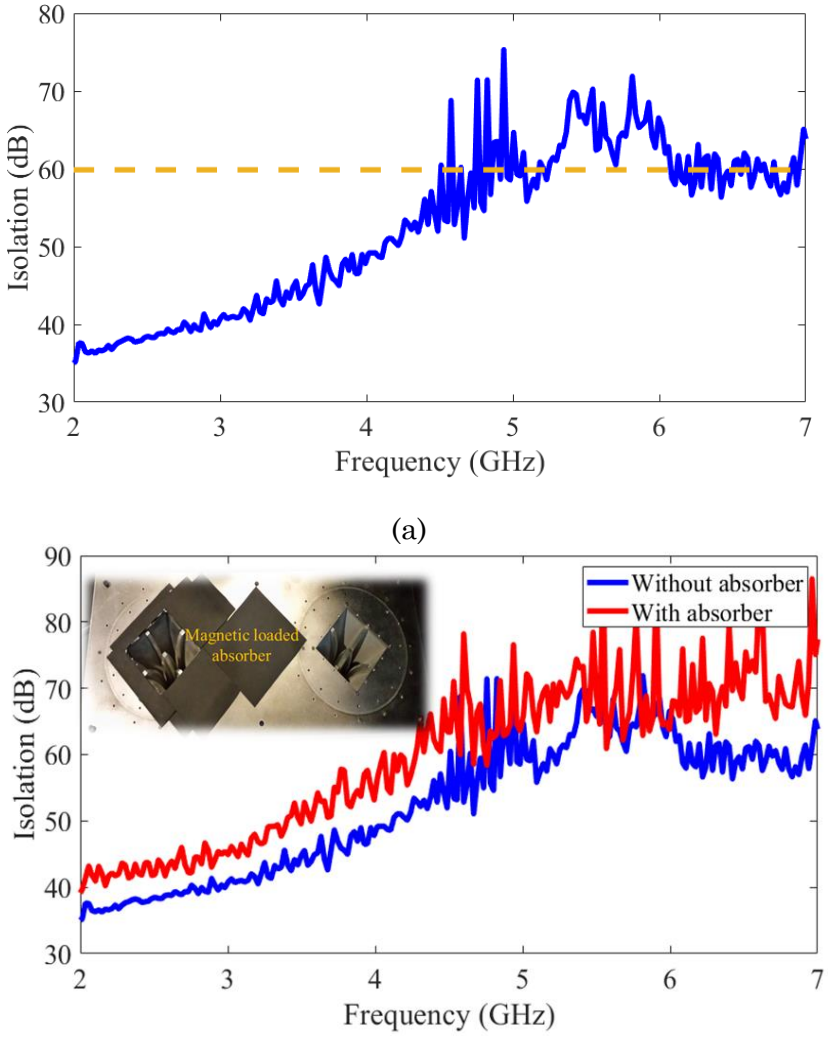

Figure 3.23: Measured co-polarized transmit receive isolation between two designed dual-polarized antennas with (a) flat ground plane, and (b) absorber near the receive antenna.

surface currents on the ground plane, magnetic loaded absorbers [97] are placed near the received antenna as shown in the inset of Figure 3.23(b). The measured isolation with this COTS absorber is shown in Figure 3.23(b). Marginal improvement is seen to the isolation (~5 dB). This small improvement is due to the small thickness of the absorber (1 mm). Better improvement is expected with thicker absorbers, this however, leads to degradation of antenna efficiency when placed closer to the aperture. A different approach that does not rely on absorbers close to the aperture is therefore researched.

It is well accepted that a finite conductive metal ground plane has a surface impedance which is predominantly inductive [98]. Such a ground plane enhances the propagation of TM waves. Capacitive surfaces however prevent these waves from propagating and instead force them to radiate. When antennas are oriented in the D-plane of each other as illustrated in Figure 3.22, TM waves are launched on the ground plane. The propagation of these waves results in the degradation observed in isolation. There are several techniques discussed in [14] that can be used to engineer capacitive surfaces, and thereby mitigate the propagation of TM waves. Among these techniques, use of metallic pins that are periodically arranged to have a capacitive impedance over an octave bandwidth is considered. The surface reactance of a ground plane using double periodic metallic pins is shown in Figure 3.24. As seen, the surface is capacitive from 2 to 4.5 GHz and from 5.8 to 7.5 GHz for a 4 cm pin height ($\lambda_{1.875\ \mathrm{GHz}}/4$). The surface is also seen to be strongly inductive around 5 GHz. To analyze how this response affects the coupling, isolation is simulated for the 4 cm pins configuration. For this analysis, three situations when the pins are not recessed, half, and fully recessed with the ground plane are compared. The setup of these three configurations is shown in Figure 3.25, and the isolation of each setup is plotted in Figure 3.26. Isolation is seen to be higher than the baseline case (no reactive surface) from 2 to 4.5 GHz where the surface is capacitive. It drops around 5 GHz when the surface becomes inductive and increase again above 5.7 GHz when the

surface becomes again capacitive. It is also seen that the improvement in isolation is lower when the pins are recessed with the ground plane. This reduction is due to the low interaction between the surface waves and the impedance surface. The half recessed surface has comparable isolation with the full recessed case and therefore represents the best tradeoff between high isolation and profile reduction.

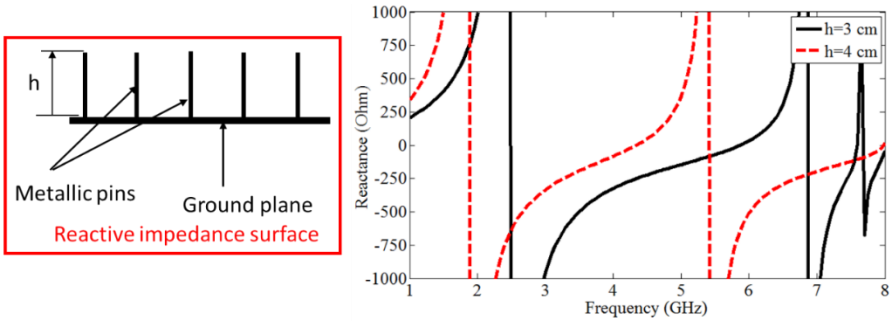

Figure 3.24: Surface reactance of the treated ground plane when loaded with double periodic metallic pins.

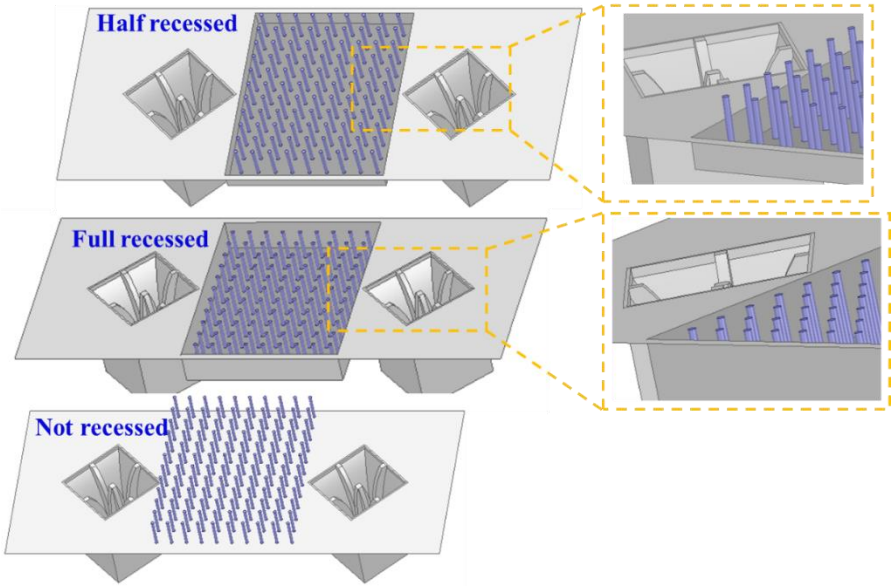

Figure 3.25: Setup for isolation improvement using double periodic reactive impedance.

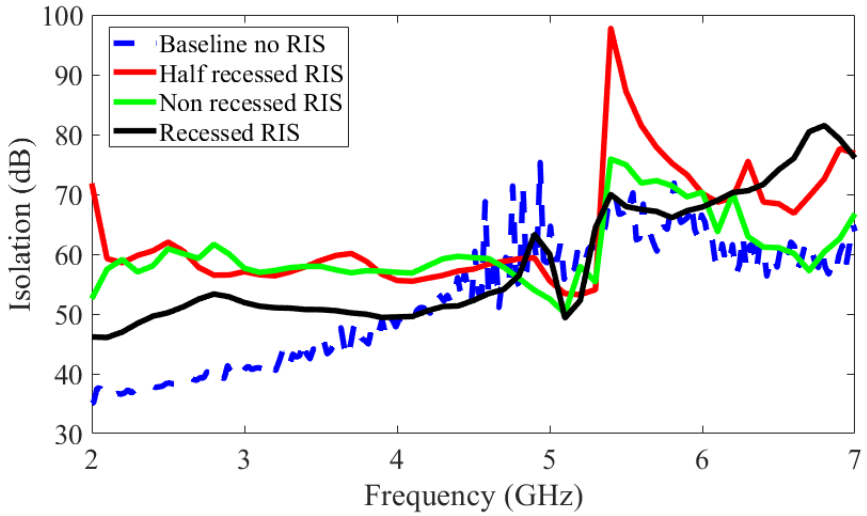

Figure 3.26: Isolation improvement using reactive impedance surfaces (RIS).

The study has so far focused on dual-polarized antennas mounted on a ground planes that do not integrate any other antenna or scatterer. In realistic system as discussed in Chapter 2, the aperture is shared will multiple antennas. To assess the performance of the designed antenna on such a platform, measured and simulated isolations shown in Figure 3.27 are obtained for antennas mounted in the diagonal of a 17" × 17" platform. This platform is illustrated in the inset of Figure 3.27, which shows other flush mounted

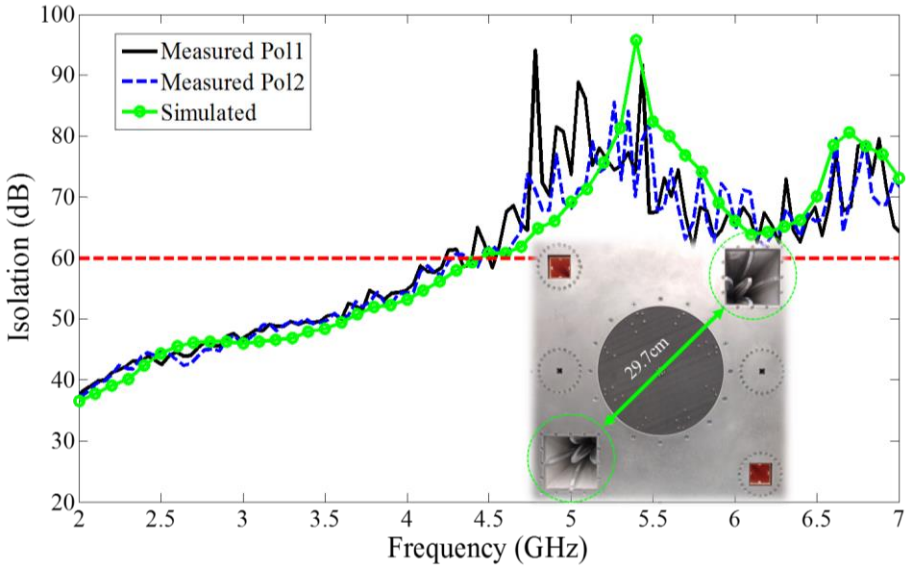

Figure 3.27: Measured and simulated isolation of the dual-polarized 90 × 90 mm² aperture when mounted on a 17" × 17" platform.

antennas. The layout of antennas on the platform is identical to that of Figure 2.38. Good agreement is obtained between measured and simulated isolations. High directivity and increased spacing at higher frequencies results in high isolation above 4.5 GHz. Below this frequency, beam widening and TM wave coupling decrease the isolation.

Having the antennas in the diagonal of the ground plane as shown in the inset of Figure 3.27 is done to obtain the maximum separation distance within the available space. The spiral which is seen between the antennas, occupies the area where reactive surfaces need to be inserted for isolation improvement. It is however seen that having the antennas along the same side provides some room to insert these surfaces. The antenna layout is modified to enable such surfaces as shown in the inset of Figure 3.28, where isolation measurements are shown. Figure 3.28 compared the isolation with and without reactive impedance surface (RIS). As seen, isolation > 45 dB is achieved with RIS which is 10 dB higher than that of a flat ground plane. The improvement in isolation is smaller than the results obtained in Figure 3.26. This is due to the area occupied by the RIS, which is not large enough for efficient operation.

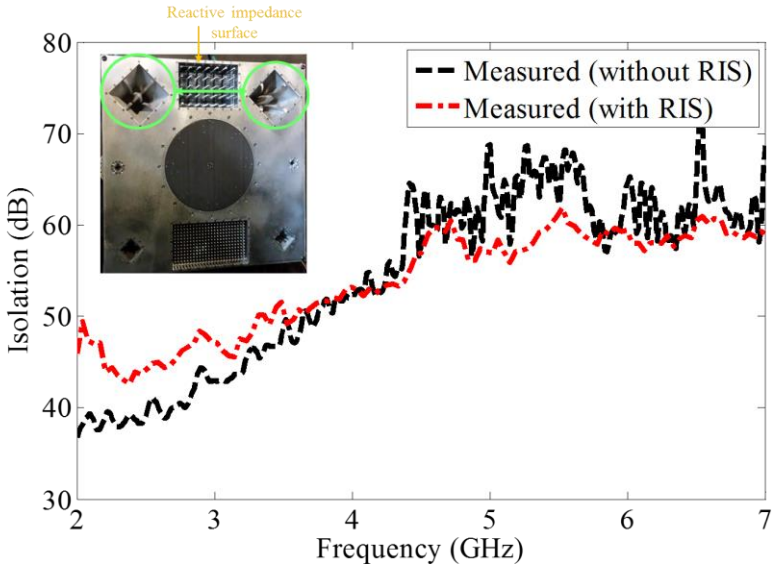

Figure 3.28: Measured isolation of the dual-polarized 90 × 90 mm^2 aperture when mounted on the sides a 17" × 17" platform with RIS in between.

3.5.2 Isolation with 75 × 75 mm² Aperture

Transmit-receive isolation between two dual-polarized antennas mounted on the compact 12" × 12" platform is analyzed in this section. As was demonstrated for the single polarized case, the maximum aperture that can fit in this platform is 8 × 8 cm². The cavity-backed dual polarized 2-element Vivaldi antenna with (7.5 × 7.5 cm²) aperture is therefore used in this study given its smaller aperture. The two antennas are placed in the diagonal of the platform as illustrated in Figure 3.29. Similar to the single polarized case, the analysis will be performed without the presence of other antennas. Same tray setup as shown in Figure 2.38 is used in the final prototype. The antennas are first mounted on a flat ground plane as seen in the inset of Figure 3.29. The measured and simulated isolations of this configuration are shown in Figure 3.29. Good agreement is obtained between experiment and simulation with isolation having similar trends as discussed above. As seen in Figure 3.29, isolation increases with frequency, starting at 37 dB and crossing 60 dB at 6 GHz. Surface currents on the ground plane at 3 GHz are also shown in the inset of Figure 3.29. As seen, strong coupling through these currents contributes to the low isolation at low frequencies. It was shown in the case of the single polarized system of Section 2.4.1 that adding a cylindrical reflector to emulate spiral cavity with four pillars on the sides significantly improve the isolation. A similar approach is done here for the dual-polarized case as seen in Figure 3.30, where surface currents at 3 GHz are also shown. The simulated isolation of this configuration is shown in Figure 3.31. As seen, the isolation is below 60 dB over most of the band, demonstrating that the proposed approach does not have significant impact for the dual polarized case.

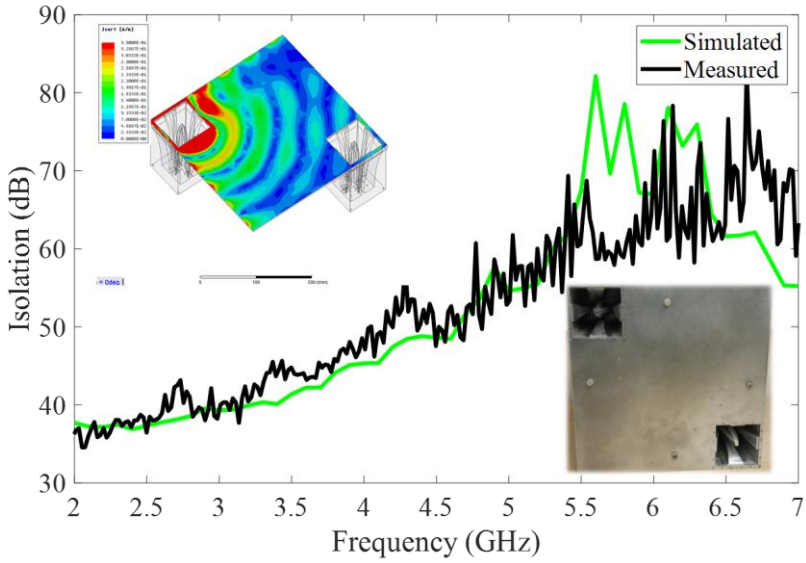

Fig 3.29: Measured and simulated isolation of the dual-polarized antenna mounted on flat 12" × 12" platform.

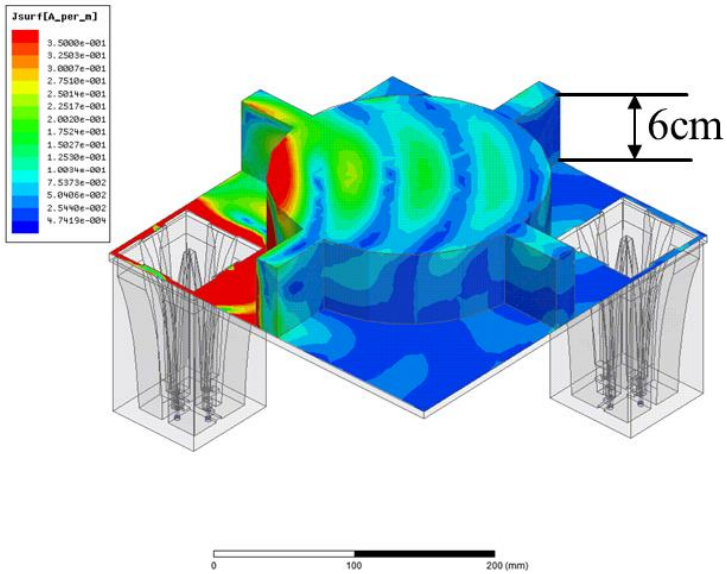

Figure 3.30: Surface currents at 3 GHz for dual-polarized 2 – 7 GHz antennas mounted on a ground plane with a cylindrical metallic wall and pillars inserted between the antennas.

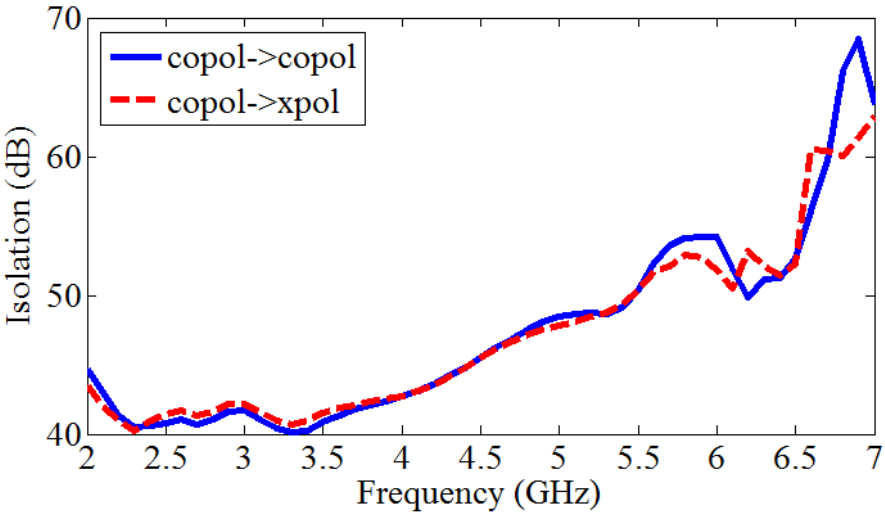

Figure 3.31: Transmit-receive isolation for antennas of Figure 3.30

Analysis of the surface currents at 3 GHz in Figure 3.30 shows strong currents launched in the E-plane of the excited antenna. To prevent these currents from coupling to the receive antenna, the thickness of the pillars is extended and their surface corrugated as illustrated in Figure 3.32. The corrugations do not behave as a reactive surface given the open boundary at the ground plane edges. They are mainly used as means to radiate these currents. These radiated currents can couple back to transmit or receive antennas, leading to increase reflection coefficient and ripple in the patterns. Measured and simulated isolations of this configuration are shown in Figure 3.32. As seen, isolation > 50 dB is achieved over the 2 – 7 GHz band with good agreement between experiment and simulation. Scattered radiation near the aperture may add destructively in the broadside direction, thereby leading to gain nulling. To mitigate this negative effect, each corrugation is loaded with 3.2 mm thick magnetic absorber [99] as seen in the enlarged view of Figure 3.33. The absorbers are not placed near the aperture of the antenna thereby maintaining high radiation efficiency. Broadside gains of the different configurations discussed herein are shown in Figure 3.34(a). As seen, monotonic gain increase is seen for the baseline configuration (flat ground plane) and corrugated loaded absorber case. Gain drop is seen

around 4.6 GHz for the corrugated surface, thereby justifying the use of absorbers. Measured isolations comparing these 3 configurations are shown in Figure 3.34(b). As seen, the isolation is greater than 60 dB over most of the band demonstrating the effectiveness of the proposed technique. To assess the impact on the far field performance, Figure 3.35 shows simulated radiation patterns of the antennas mounted on a flat ground plane along with those of the absorber loaded corrugation of Figure 3.33. As seen, a small squint is observed in the absorber loaded corrugated ground plane. This squint is however seen to be significantly smaller when compared to the single polarized case. This improvement is due to the absorbed which decreases the impact of destructive interference after reflection and diffraction on the corrugated surfaces.

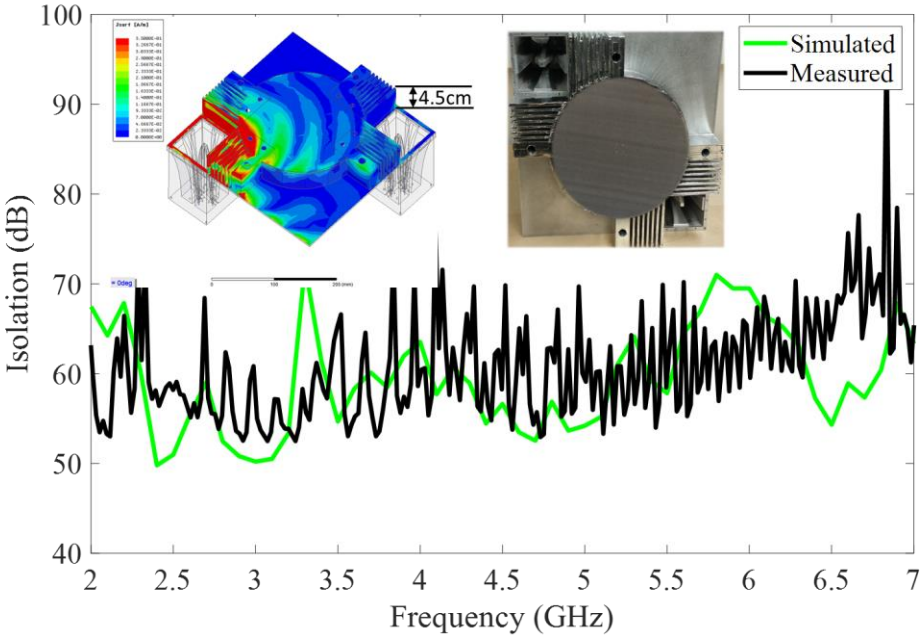

Figure 3.32: Measured and simulated isolation of the dual-polarized 2 – 7 GHz antennas mounted on a ground plane with a cylindrical metallic wall and corrugated pillars placed next to the antennas.

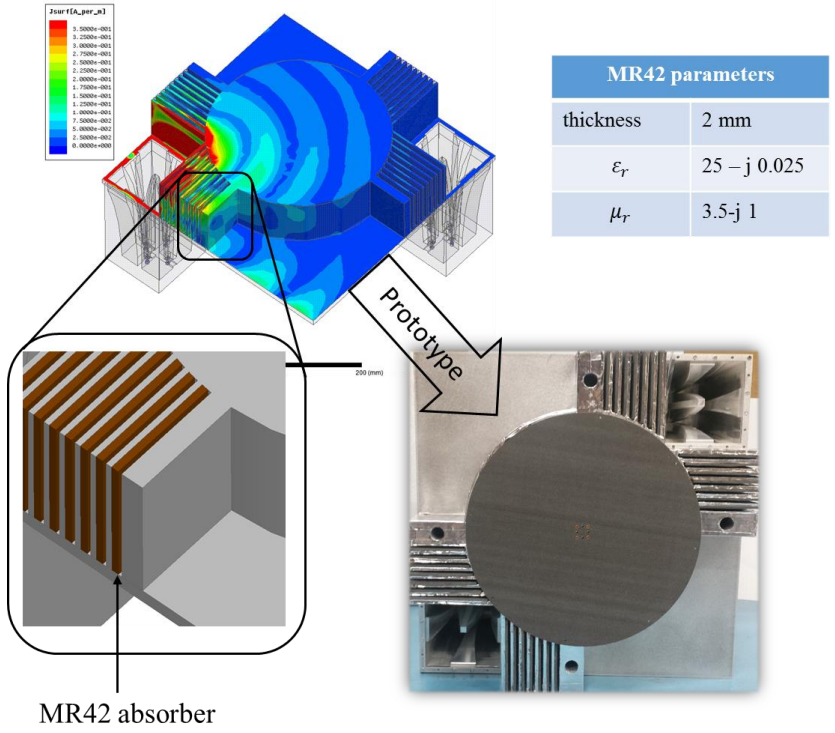

MR42 parameters	
thickness	2 mm
ε_r	25 – j 0.025
μ_r	3.5-j 1

Figure 3.33: Absorber loaded corrugation used to improve transmit receive isolation and gain ripple.

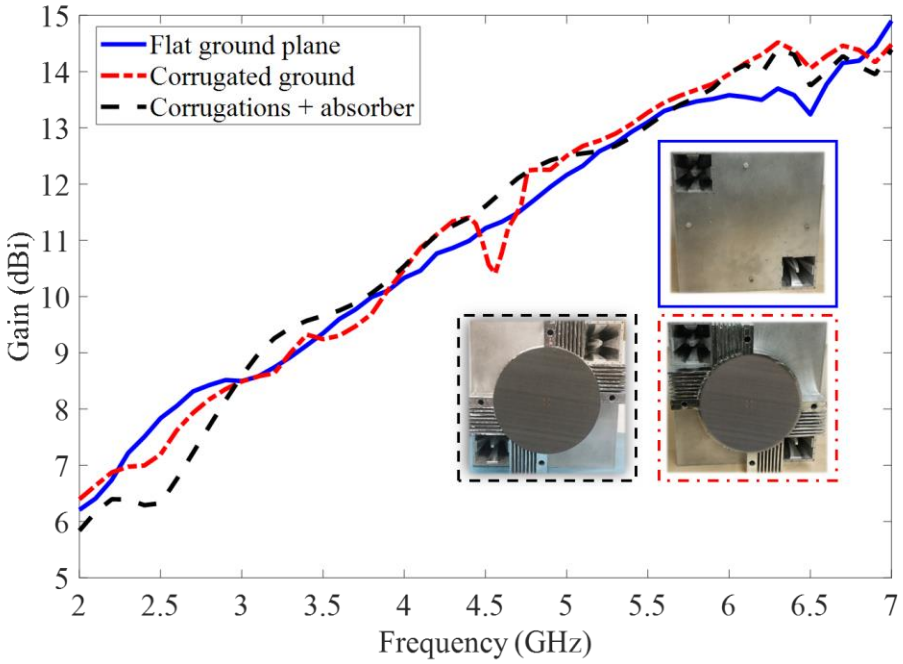

(a)

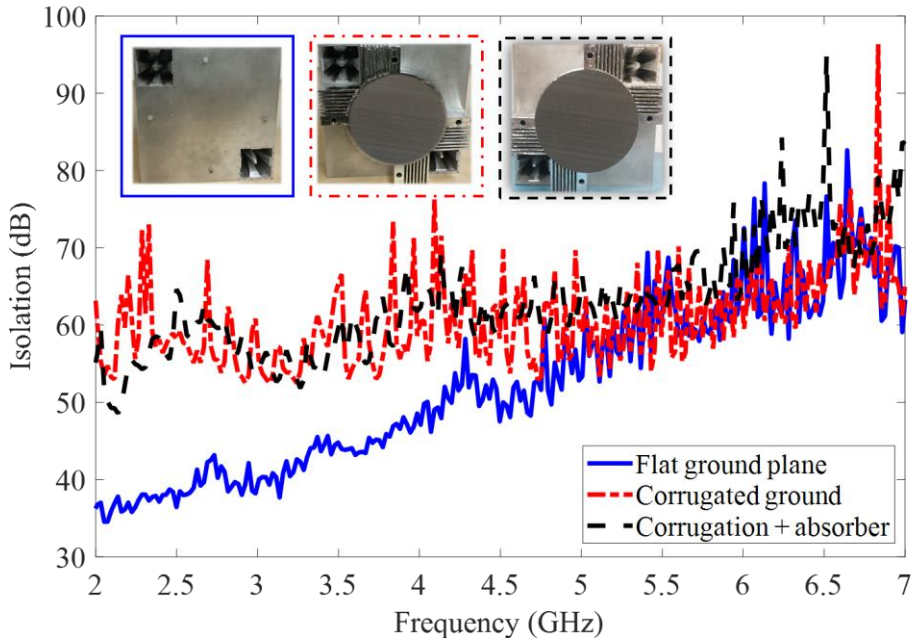

(b)

Figure 3.34: Performance comparison between different configurations of the dual-polarized antennas mounted on the 12" × 12" platform with (a) broadside gain, and (b) isolation.

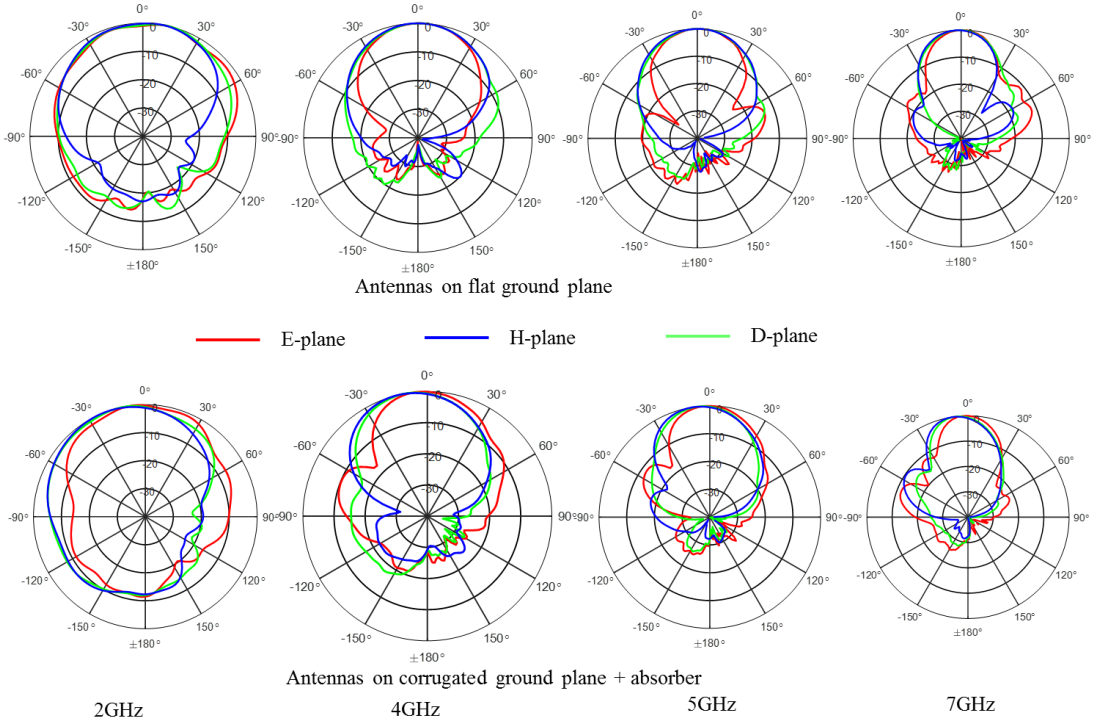

Figure 3.35: Pattern comparison between antennas mounted on the 12" × 12" flat and absorber loaded corrugated ground plane.

3.5 Summary

The design of wideband dual-polarized, all-metal, and cavity-backed Vivaldi array antenna is presented. Simulated results of a 3 × 4 array show a resonant free behavior, thereby demonstrating extended capability of this antenna as an integral part of a shipborne phased array system. A detailed design of a second dual-polarized all-metal antenna comparable to quad-ridge horn antennas is introduced. The antenna is fabricated and demonstrates VSWR < 2, gain > 8dBi, high quality, and symmetric radiation patterns over 4:1 bandwidth. A high power stripline power divider/combiner operating from 1 to 8 GHz is also designed and integrated with the antenna in a compact form, leading to only two feeding points (one per polarization port). Two of the designed antennas are diagonally mounted on a metallic ground plane for bi-static STAR operation. Different techniques aiming to increase transmit-receive isolation are presented. Reactive impedance surfaces are shown to be very effective in that sense when the platform provides enough space for their integration. In space constrained platforms, properly engineered metallic reflective surfaces are shown to be very efficient in decreasing coupling without, significant degradation of the radiation patterns.

Chapter 4

Diplexer-Free X-band FDD Subarray for Geo-Satellites Phased Arrays

4.1 Overview

The previous two chapters are dedicated to STAR antennas for use on airborne and shipborne platforms. More precisely, techniques to increase the isolation of bi-static STAR systems are discussed for antennas mounted on different types of platforms. In this chapter, the focus shifts to monostatic STAR configurations. The main objective is to analyze how monostatic STAR topologies can be combined with conventional Frequency Division Duplex (FDD) systems to decrease their complexity. In this analysis, the platform is a geostationary satellite and interest is on X-band phased array antennas which are gaining popularity in satellite payloads. In the commercial sector, the increase demand for high throughput communication links is pushing most satellite operators to shift their business model from the conventional bend pipe and fixed beam coverage to multi-beam high throughput configurations [100]-[101]. This architecture, which aims to generate more EIRP and G/T is made possible with the use of antenna arrays. The initial deployment of multi-beam systems relied on reflector fed array antennas [102]-[104]. The need to accommodate dynamic earth coverage from geostationary orbit has resulted to a burst of research in phased arrays for space payloads [105]-[110]. These antennas are also of great

importance in defense applications where not only precise shaping of the coverage area, but the ability to create precise null at a designated locations is needed.

Today, advanced satellite payloads use active phased array (APA) as the state of the art technology [111]. Having a power amplifier and LNA per unit cell decreases losses in the RF path. APA also reduces the need for redundant active components; the use of multiple amplifiers and LNAs creates an inherent redundancy in the system. In [105]-[106], a tile based APA is presented where all active components and RF beamforming network (BFN) are stacked, in layers parallel to the subarray aperture. Conventional X-band APA systems based on the tile configuration with TX (7.25 – 7.75 GHz) and RX (7.9 – 8.4 GHz) are predominantly single-polarized [105]-[106]. Polarization diversity is used in these systems to realize frequency division duplex (FDD) communication, leading to inefficient use of the spectrum. To enable dual-polarized operation with co-polarization between transmit and receive, two diplexers are needed per subarray. These diplexers have to provide high rejection over a 150 MHz guard band while being extremely compact to fit under the subarray footprint. This requirement is very challenging given the strong correlation between diplexer size and filter rejection [112]-[114].

In this chapter, a diplexer-free X-band subarray for co-polarized FDD communication systems is presented. The proposed tile subarray enables co-polarized FDD communications using a monostatic STAR architecture. The presented STAR architecture uses a concept proposed in [32] where monostatic subarray for in-band full-duplex communication is demonstrated over a narrow band. The proposed architecture thereby eliminates the need for diplexers. The size of which has limited the development of dual-polarized systems. In this research, the cavity-backed 2-element Vivaldi of Chapter 3 is modified to enable feeding through waveguides. The newly developed all metal antenna, which allows dual-polarization without the need of an orthomode transducer (OMT) is used as the unit cell of the presented subarray.

This chapter is organized as follows:

- Section 4.2 describes the system architecture of the proposed subarray. Design requirements of the different components used in the system are also presented.
- Section 4.3 goes over a detailed design of the different components of the subarray.
- Section 4.4 presents the full characterization of the system. Transmit-receive isolation and far field performance are presented.
- Section 4.5 summarizes the chapter.

4.2 System Architecture and Subarray Description

The schematic of the conventional approach used to realize a dual-CP payload with co-polarized transmit-receive using a single aperture is shown in Figure 4.1(a). Dual-polarization is obtained with two diplexers connected to a dual linearly-polarized (LP) antenna through a quadrature hybrid. The burden is therefore put on the diplexer design, which has to provide the necessary isolation to meet system requirements. This is challenging in phased array systems where size is constrained by the scan requirements.

To overcome this limitation, this research proposes a sequential rotated array (SRA) of dual-polarized linear antennas. This configuration relies on two quadrature hybrids and four balun as shown in Figure 4.1(b). This architecture does not use any diplexer as seen, but instead relies on the beamforming network (BFN) to isolate the receiver. Arrows in Figure 4.1(b) represent the polarization of the electric fields for TX (green arrows) and RX (red arrows). As seen, the subarray (unit cell) is composed of four antenna elements with TX and RX BFNs as illustrated in Figure 4.1(b). Two orthogonally polarized ports in each antenna element are connected to TX and RX paths. The 2 × 2 subarray is obtained by sequential rotation array of the antenna elements with a 90° phase progression as shown in

Figure 4.1(b). TX and RX BFNs are a modified Butler matrix with one 90° hybrid and two 2-way dividers with 180° differential output ports as shown in Figure 4.1(b). The subarray

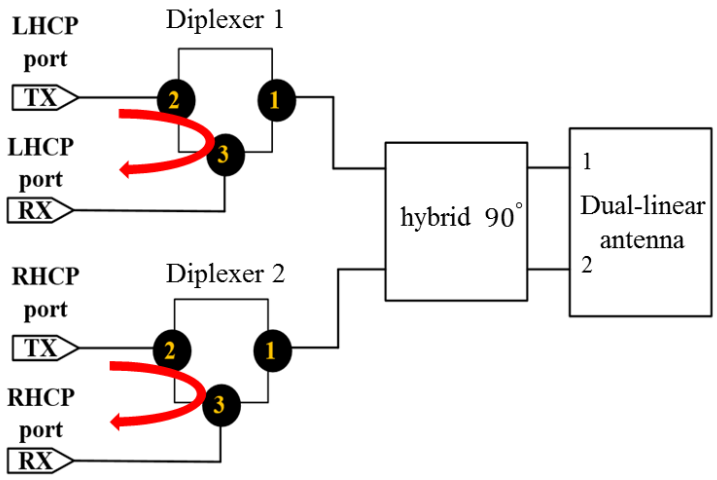

(a)

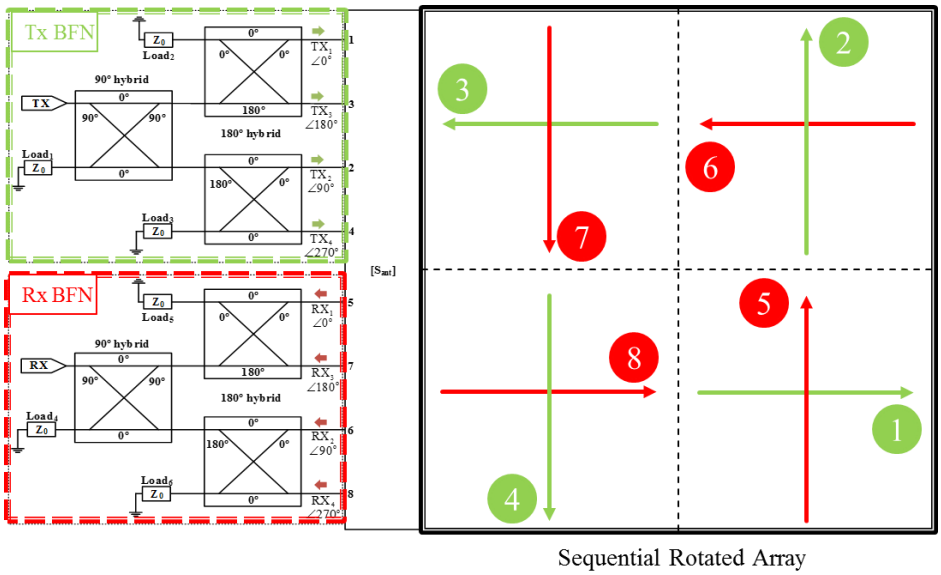

(b)

Figure 4.1: Dual-polarized architecture with co-polarized transmit-receive: (a) conventional approach, and (b) sequentially rotated array architecture.

can operate in left-handed circular-polarization (LHCP) or right-handed circular-polarization (RHCP) with co-polarization between TX and RX. Owing to the symmetry of

the (SRA) and the phase progression, it is demonstrated in [32] that the coupling from TX to RX ports (self-interference) is canceled at the RX port of the BFN. The remaining coupled power is dissipated at the cross-pol. port of the RX 90° hybrid. The proposed architecture can theoretically achieve infinite isolation between the TX and RX port for broadside radiation without diplexer. For practical realizations and when multiple subarrays are phased for beam scanning, the true isolation is finite, due to the imperfection of hybrids, SRA, and non-uniform phase excitation.

The total size of the subarray aperture is set to 100 mm × 100 mm ($2.8\lambda_{8.4GHz}$ × $2.8\lambda_{8.4GHz}$) which is seen to be less than the $3.3\lambda_{8.4GHz} \times 3.3\lambda_{8.4GHz}$ required to maintain grating lobes off the surface of Earth. The different components of the subarray, namely the unit cell antenna and the BFN, are therefore designed to fit under the subarray footprint.

4.3 Subarray Components Analysis and Design

4.3.1 Dual-polarized Unit Element

With the subarray aperture set to $2.8\lambda_{8.4GHz} \times 2.8\lambda_{8.4GHz}$, the maximum element aperture is $1.4\lambda_{8.4GHz} \times 1.4\lambda_{8.4GHz}$. While this size allows higher aperture efficiency at the antenna element, it also leads to higher scan loss and degraded off axis axial ratio. Axial ratio is found to be one of the most critical parameters affecting the element size. To maintain axial ratio below 3 dB in all cuts within 18° beam width, the antenna element size is set to 40 mm × 40 mm ($1.12\lambda_{8.4GHz} \times 1.12\lambda_{8.4GHz}$).

All metal antennas such as horns have mostly been used in space applications to avoid potential electrostatic discharges or outgassing hazards [115]. To obtain dual-polarization with horn antennas, orthomode transducers (OMT), typically designed with either a Bøifot [90] or turnstile junction [89] are used. These two OMT configurations provide high isolation between the two orthogonal polarizations and are therefore widely

used in dual-polarized horn antennas. In an active phased array based on a tile configuration, they have to fit under the antenna footprint. This requirement is difficult to satisfy with Turnstile and Bøifot based OMTs due to the unfolded side arms which increase their profile. A new type of compact dual-polarized all metal antenna therefore needs to be researched to satisfy the tile active phased array requirement. In Chapter 3, a dual-polarized all metal 2-element cavity-backed Vivaldi antenna array was introduced. A coax to parallel plate transition is used to feed each Vivaldi antenna element and a 2-way power divider is used to provide a single input per polarization. While this antenna could be used for the tile phased array, the required external divider and the associated wiring will add losses that may be unacceptable for the intended applications.

To mitigate this problem, a new design of a dual-polarized all metal antenna is introduced. The antenna is based on the dual-polarized cavity-backed 2-element Vivaldi array discussed in Chapter 3. Herein, the coax to parallel plate adapter is replaced with a double ridge to parallel plate transition, and the 2-way power divider is replaced with an inline integrated waveguide bifurcation. A picture of the proposed antenna is shown in Figure 4.2 with a detailed assembly process split into 5 steps. Step 1 shows the design of the proposed inline bifurcation (Y-junction). Each junction is designed as a double ridge waveguide cross section as shown in Figure 4.3. Nonstandard double ridge cross sections are used to fit within the imposed unit cell size. The dimensions of each double ridge cross section are also shown in Figure 4.3. These dimensions are selected to have the cut off frequency of each waveguide below 7 GHz. Also seen in Figure 4.3 is the asymmetry between the two Y-junctions used for each polarized port. Port 2 is attached to a waveguide bend; to provide clear access to this port, the orthogonal port (port 1) is connected to a waveguide section slightly curved using a $\sin^2$ profile. The reflection coefficient at the input of port 1 and 2 of Figure 4.3 are shown in Figure 4.4. As seen, port 1 has a better response and the increase reflection coefficient of port 2 is due to the waveguide bend. The maximum

reflection coefficient is however seen to be less than -25 dB. In step 2 of Figure 4.2, a double ridge to parallel plate transition is designed with return loss >30 dB obtained over the frequency band of interest. This element is needed to provide smooth transition to the 2-element Vivaldi array shown in step 3. The 2-element Vivaldi array is recessed in a metallic cavity to form the element shown in step 4. As discussed in Section 3.4, the two arms of the Vivaldi connected to the cavity are flared in the transverse direction to improve radiation and impedance match at low frequencies. Step 5, which is the final assembly, shows the proposed dual-polarized all metal antenna. As seen, the two orthogonal ports and the associated waveguide paths are under the aperture footprint of 40 mm × 40 mm. The S-parameters of the designed element are shown in Figure 4.5. The reflection coefficients are <-18 dB with coupling between the two orthogonal ports < -60 dB.

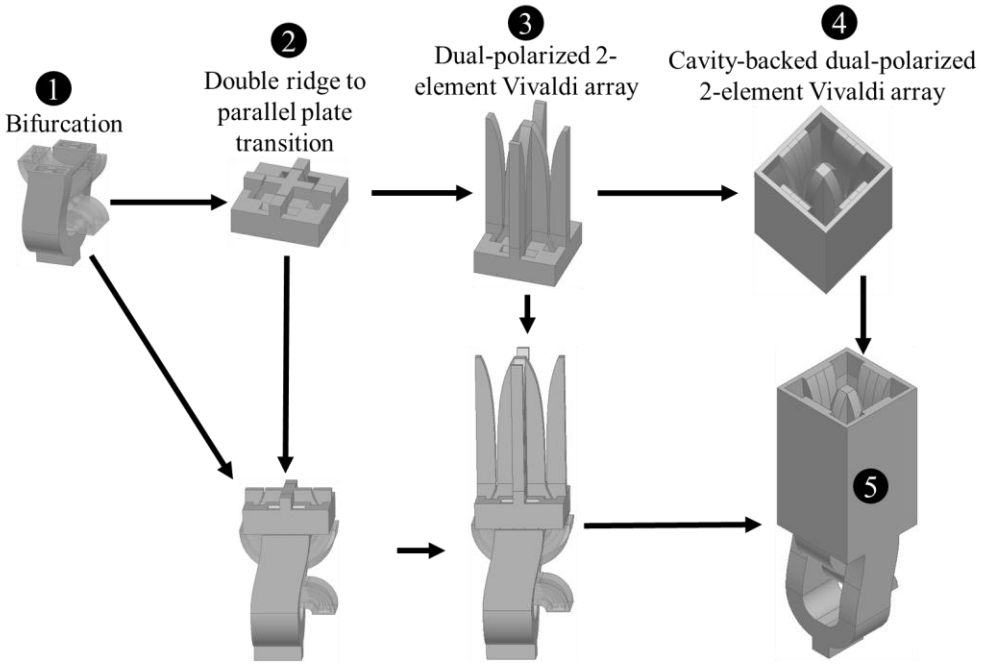

Figure 4.2: Dual-polarized all metal antenna element with the design process shown in greater detail.

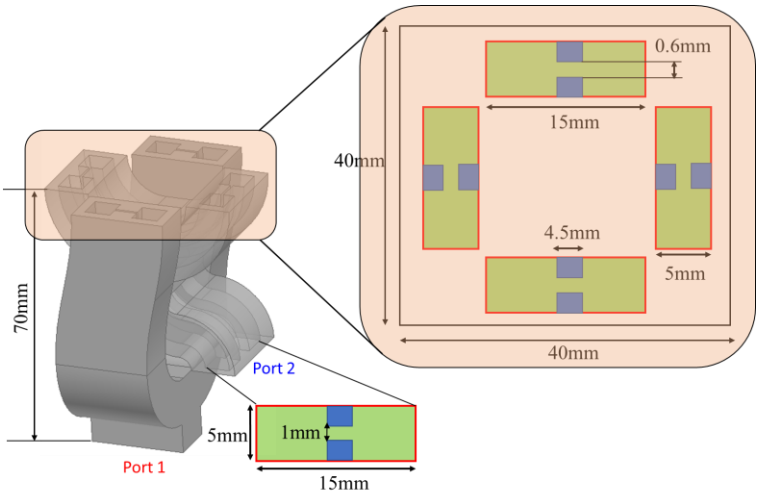

Figure 4.3: Inline bifurcation and design parameters of the double ridge waveguides

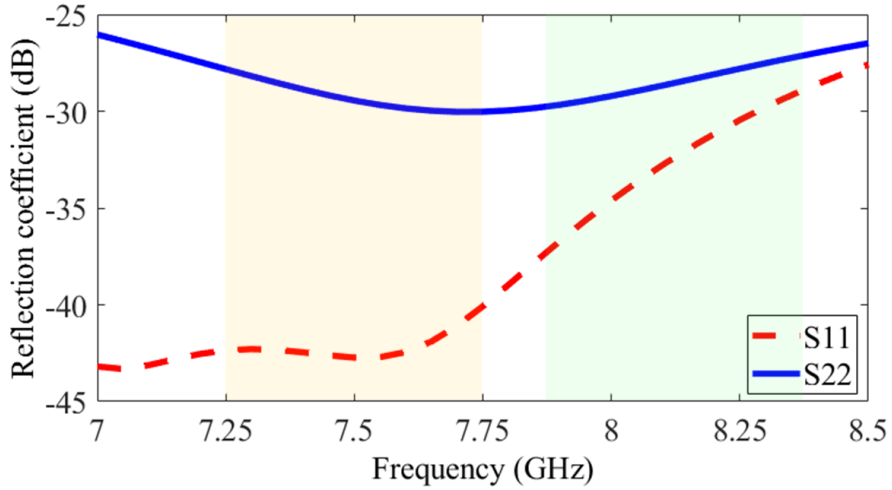

Figure 4.4: Reflection coefficient of the designed Y-junction.

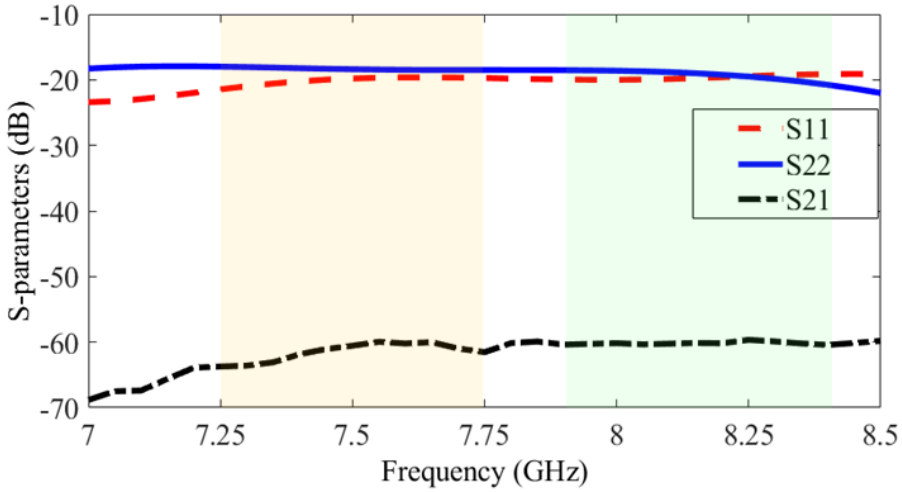

Figure 4.5: S-parameters of the designed dual-polarized unit element.

The far field performances of the unit element are shown in Figure 4.6. Aperture efficiency, which is calculated from simulated directivity is > 70 % over X-band (Figure 4.6 (a)). Broadside gain is plotted along with maximum gain under uniform illumination in Figure 4.6 (a), As seen, obtained gain is 1 dB lower than its maximum. Radiation patterns in E-, H-, and D-planes are shown in Figure 4.5(b). While the shown performances are only demonstrated in X-band, the designed antenna can operate over more than a 3:1 impedance bandwidth.

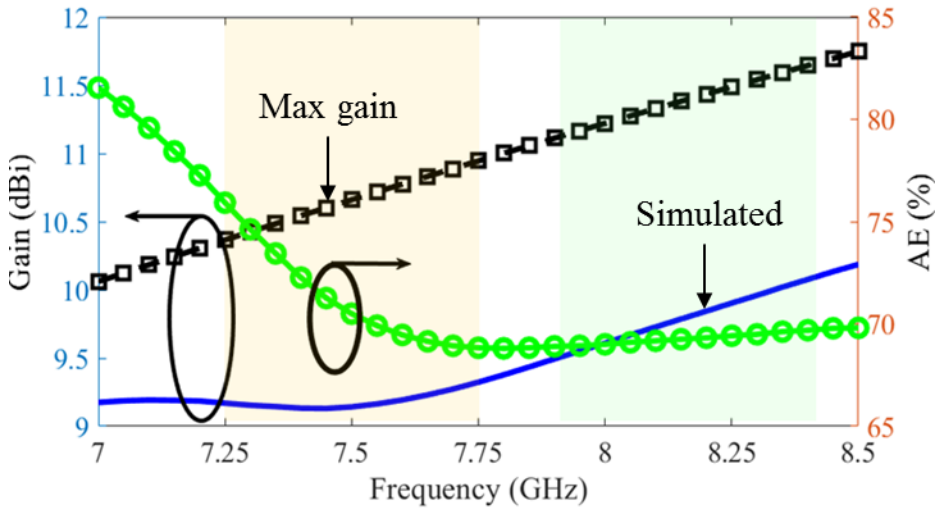

(a)

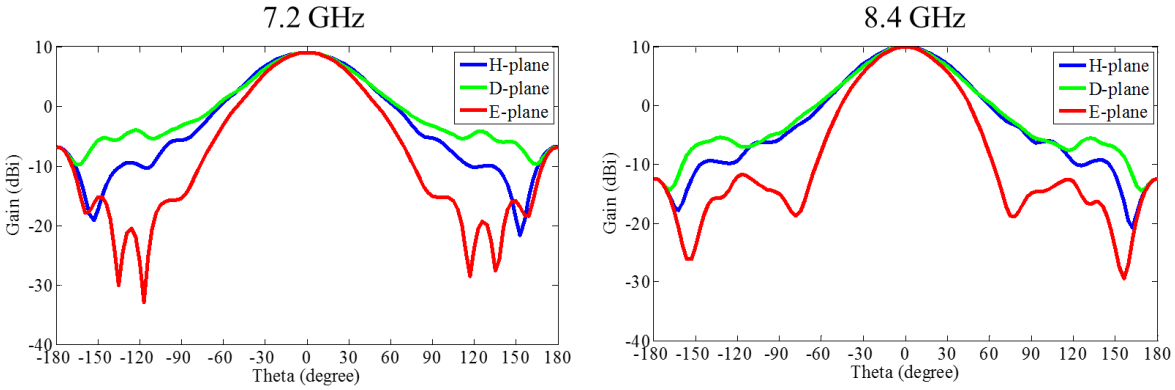

(b)

Figure 4.6: Far field performances of the designed dual-polarized unit element. (a) gain and aperture efficiency, and (b) radiation patterns at 7.2 GHz and 8.4 GHz.

4.3.2 Modified 2 × 4 Butler Matrix

In the full duplex communication discussed in [32], the butler matrix is made by cascading 90° and 180° hybrids. It is also demonstrated in [32] that the achieved isolation is extremely sensitive to the BFN's imbalances, particularly phase imbalances. To provide further simplification of this matrix, the 180° hybrid which is known to have high phase imbalance is replaced with a 2-way power divider with 180° differential output as shown in Figure 4.7. To minimize losses inside the BFN, all components are designed in waveguide technology. The first element is the 2-way power divider with 180° differential output. One possible way to realize this element is to design a Y-junction and attach a 180° phase shifter to one of its output ports. This approach leads to increased complexity, given the need for a 180° phase shifter with low phase imbalance. The approach proposed herein is to use the transition from TE_{10} mode in double ridge waveguide to TEM mode in coaxial line to obtain the 2-way divider with differential output. A schematic of the design principle is shown in Figure 4.7. To obtain 180° phase difference between the output ports, the inner pin of the coax is connected to identical ridge arms. The symmetry of the double ridge cross section leads to theoretically zero amplitude and phase imbalances between the output ports. Also seen in Figure 4.7 is the inline connection of the coax, thereby requiring the design of an inline coax to double ridge transition. A compact inline coax to double ridge transition is designed with the picture shown in the inset of Figure 4.8. The coax is first transition to a single ridge waveguide and a $\sin^2$ profile is used to provide smooth transition from single to double ridge. The reflection coefficient of the transition is shown in Figure 4.8 to be less than -26 dB within the frequency of interest.

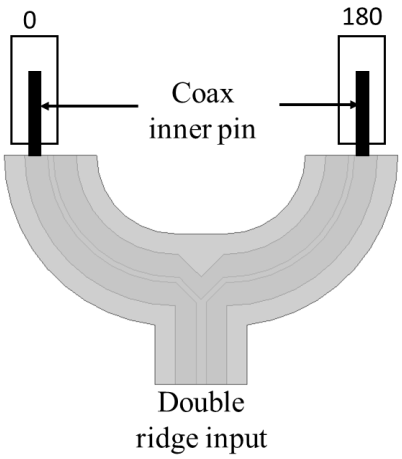

Figure 4.7: Architecture of the 2-way power divider with 180° differential output ports.

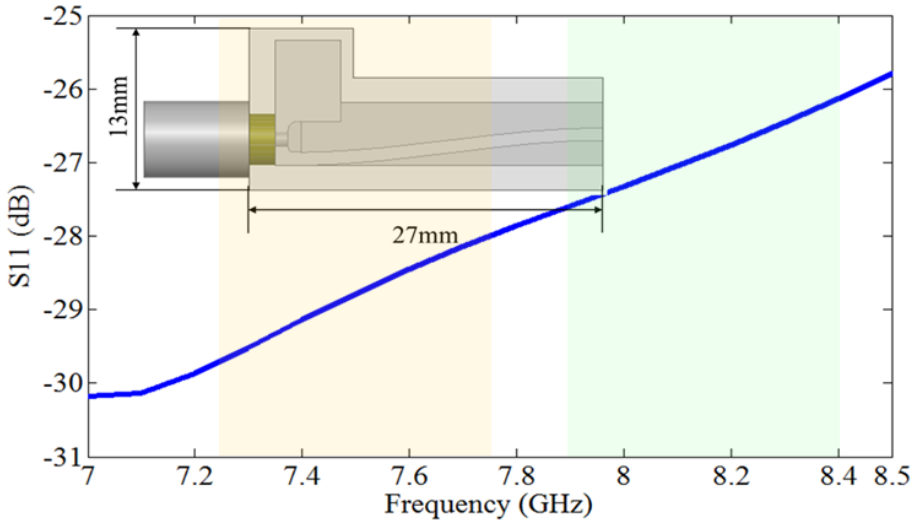

Figure 4.8: Reflection coefficient of the inline coax to double ridge transition.

The second element in the BFN is the 90° hybrid. Given that each output port of this hybrid will be connected to the double ridge input of the 2-way divider (Figure 4.7), it becomes appealing to design the hybrid in double ridge. It is challenging to design 90° hybrids in double ridge waveguides given the rapid change of propagation constant with respect to cross section. The design is instead performed using single ridge sections, a single to double ridge transition is used to obtain double ridge outputs. The hybrid is a three branch waveguide coupler using the concept presented in [116]. While the propagation constant of rectangular waveguide used in [116] remains constant with cross section

variation in E-plane, this is not the case for ridge waveguides. The design parameters presented in [116] are tuned for minimum phase imbalance within the frequency of interest. The designed 90° hybrid is shown in the inset Figure 4.9. The phase difference between the two output ports is seen to have a maximum imbalance of 1° as shown in Figure 4.9(a). The S-parameters of the hybrid are shown in Figure 4.9(b). As seen, the maximum amplitude imbalance is 0.4 dB, the input return loss and isolation are > 18dB.

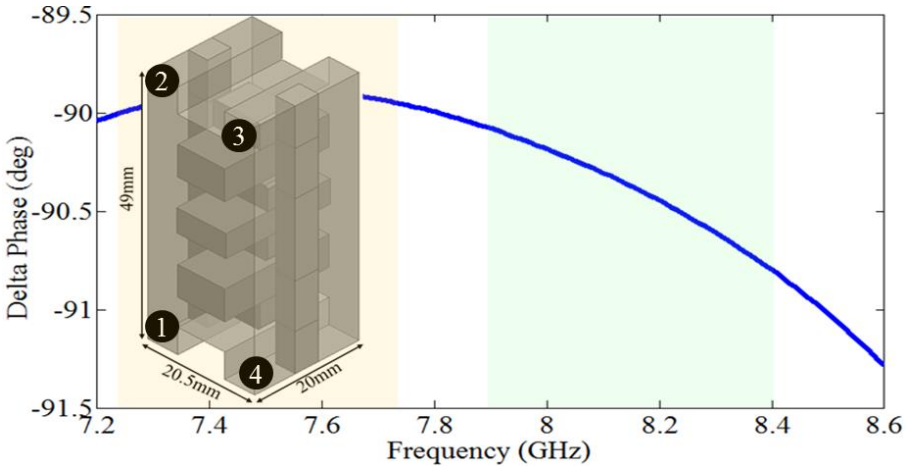

(a)

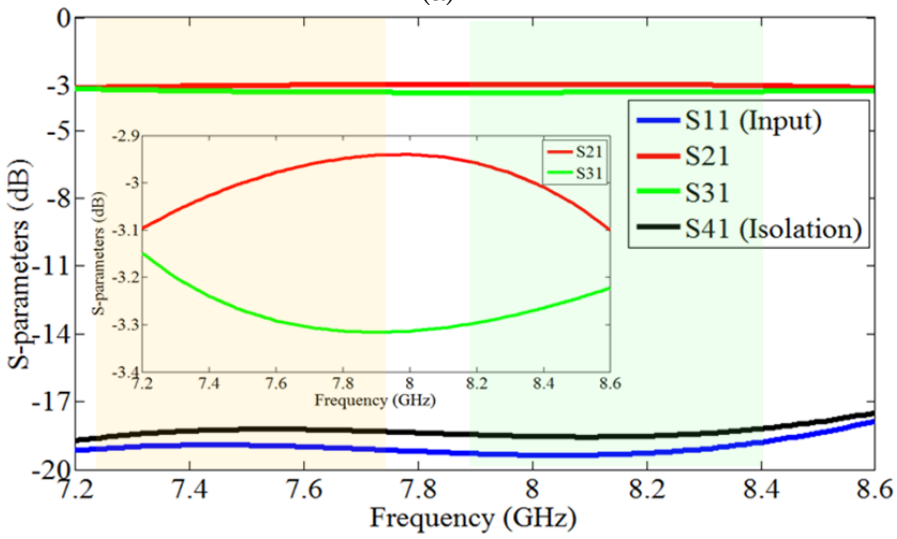

(b)

Figure 4.9: Performances of the ridge waveguide quadrature hybrid with (a) phase difference between the two output ports, and (b) S-parameters.

The BFN is obtained by combining the designed 90° hybrid of Figure 4.9, and the 2-way power divider of Figure 4.7. A picture of the designed 2 × 4 modified Butler BFN is shown in Figure 4.10 with output ports labeled from 2 to 5. Ports 1 and 6 are the input ports and can be respectively used to generate LHCP and RHCP polarizations. A coax to double ridge adapter is also used in this design at the input ports to support the attachment of coaxial cable. This adapter could be replaced by a transition to standard waveguide cross section such as WR112 if needed. The S-parameters of the designed BFN are shown in Figure 4.11. The maximum simulated amplitude imbalance is 0.5 dB and is mainly dominated by the imbalance of the 90° hybrid.

The BFN is fabricated using a split block CNC machining process as shown in Figure 4.12, where the cover is removed to highlight internal features. S-parameters of the fabricated BFN are shown in Figure 4.13. In Figure 4.13 (a), reflection coefficient and isolation are plotted, coupling to the four outputs when port 1 is excited are plotted in Figure 4.13 (b). As seen, the reflection coefficient at the two input ports is below -10 dB and

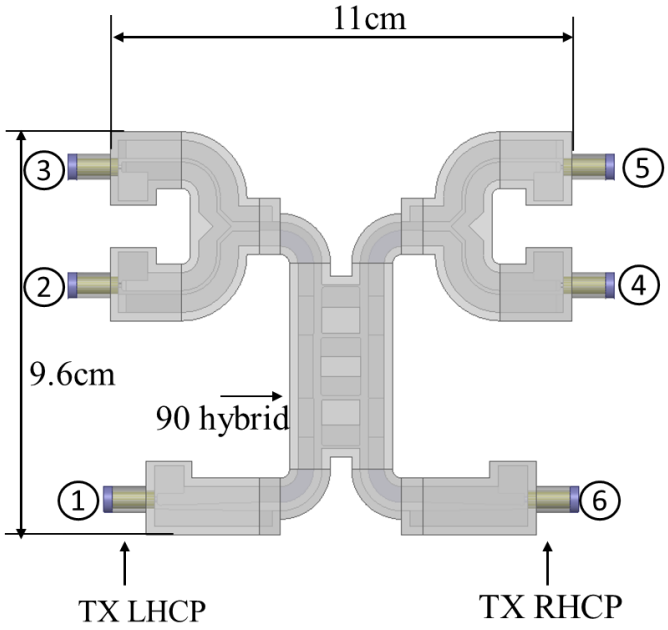

Figure 4.10: Designed 2 × 4 modified Butler BFN combining one 90° and two 2-way power dividers with differential output.

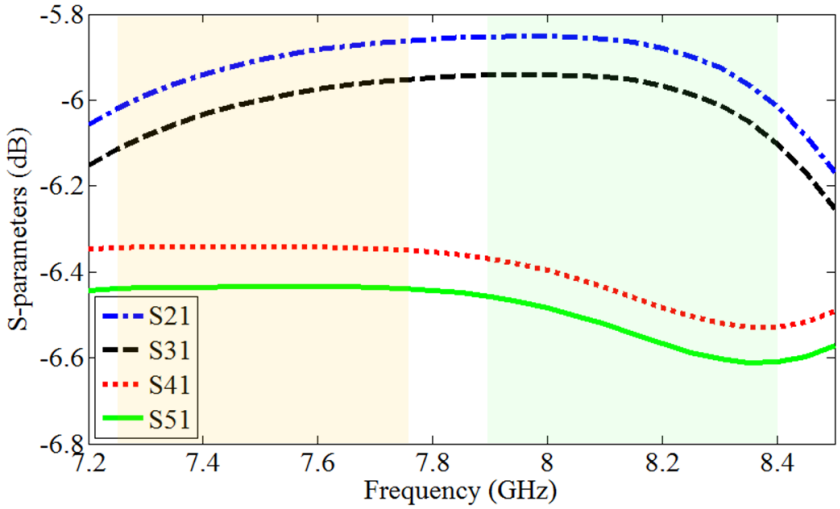

Figure 4.11: S-parameter of the designed BFN

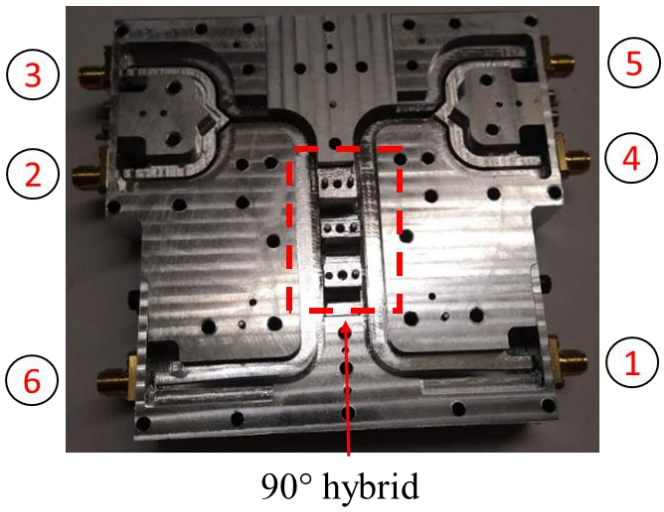

Figure 4.12: Fabricated 2 × 4 modified Butler BFN using split block machining process.

the isolation between these ports is less than -20 dB. Coupling to output ports shown in Figure 4.13(b) is seen to be different than simulated data of Figure 4.11. These differences between simulation and experiment are due to the fabrication imperfections. The total insertion loss is however less than 0.4 dB, amplitude and phase imbalances are < 1.3 dB and 8 degree, respectively. Impact of these imbalances on system performance is discussed next.

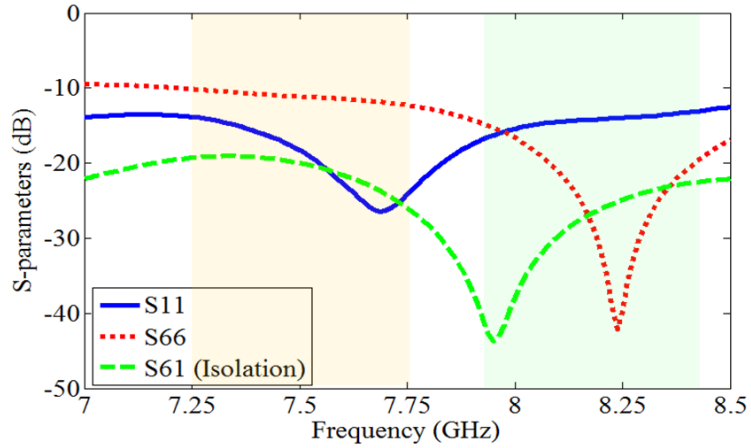

(a)

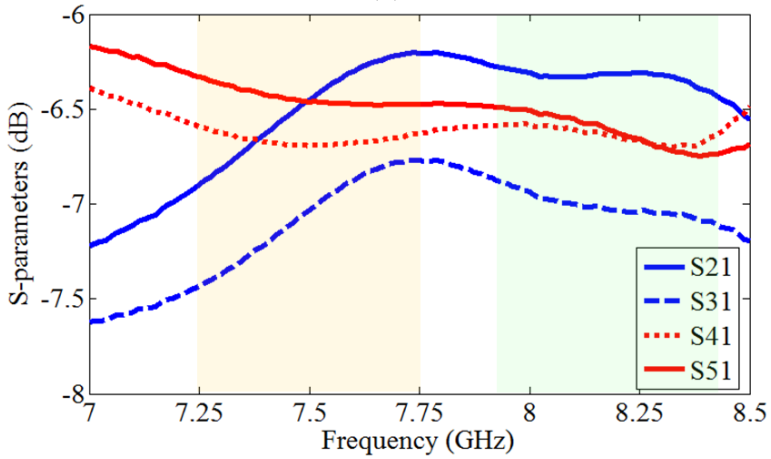

(b)

Figure 4.13: Measured S-parameters of the BFN with (a), reflection coefficients and isolation, and (b) coupling to output ports.

4.4 Subarray Performance Analysis

The designed antenna element in Figure 4.2 is sequentially rotated to obtain the subarray of Figure 4.14 (a). Ports 1 to 4 and 5 to 8 in Figure 4.14 are respectively transmit and receive antenna ports. The arrows represent the polarization of each radiating element and the orientation of the electric field at the aperture when all elements are excited with uniform phase. The subarray is also seen to be flushed with a finite ground plane, the size of the ground plane is chosen such that center to center separation between adjacent

subarrays is less than 100 mm ($2.8\lambda_{8.4GHz}$). The passive S-parameters between port 1 and the remaining ports in Figure 4.14 (a) are shown in Figure 4.15 (a). As seen, the highest coupling is between port 1 and 6 indicating strong E-plane coupling around -25 dB. It is demonstrated in [32] that this mutual coupling is directly correlated to the power loss in the cross-polarized port. Also, for simultaneous dual-polarization operation, the maximum achievable isolation is limited by the highest mutual coupling. To further reduce the coupling, two quarter wave chokes are inserted in the unit element. The first choke is designed at 8 GHz and is applied on the arms of the Vivaldi connected to cavity. The second is a concentric ring choke designed at 7.5 GHz as shown in Figure 4.14(b). The passive S-parameters for this configuration are shown in Figure 4.15(b). As seen, E-plane coupling between port 1 and 6 is reduced in excess of 25 dB and the overall coupling is reduced by more than 10 dB. The subarray of Figure 4.14(b) is retained is this study and will be used for the remaining of the chapter given its superiority. The axial ratio of the designed subarray is shown in Figure 4.16, and is seen to be less than 3 dB over the scan volume. The off axis axial ratio is seen to be worst in the diagonal plane as expected for sequentially rotated arrays [117]. Aperture efficiency of the designed subarray is shown in Figure 4.17. As seen, aperture efficiency < 50 % is obtained over the frequency range of interest. This low aperture efficiency results from the cascade of two contributions. First, aperture efficiency of the unit element shown in Figure 4.6(a) is less than 80 %, thereby setting the first limit in the subarray. Secondly, it is demonstrated in [118] that the maximum aperture efficiency of sequentially rotated arrays of dual-linear polarized element is limited to 50 % when the elements are separated by more than one-half wavelength as used here. The combination of these two effects therefore explains the low aperture efficiency. A design architecture aiming to improve the aperture efficiency is discussed in Chapter 5.

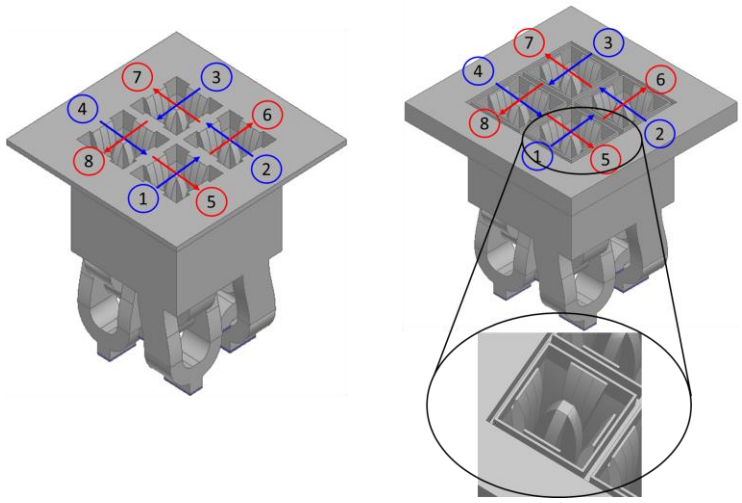

Figure 4.14: Subarray obtained by sequential rotation of unit element of Figure 4.2. (a) subarray without mutual coupling mitigation, (b) subarray with quarter wave chokes for mutual coupling reduction.

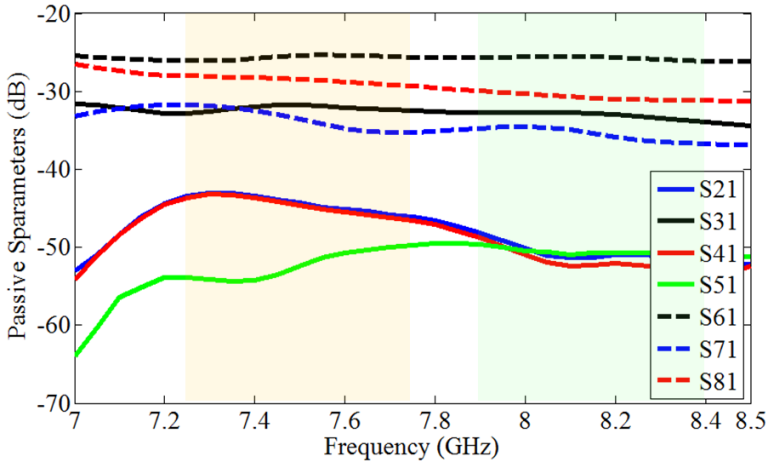

(a)

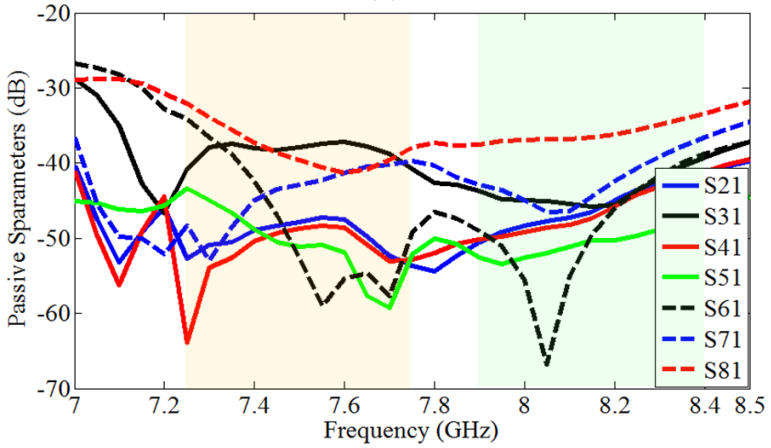

(b)

Figure 4.15: Subarray passive S-parameters (a) without chokes, and (b) with chokes.

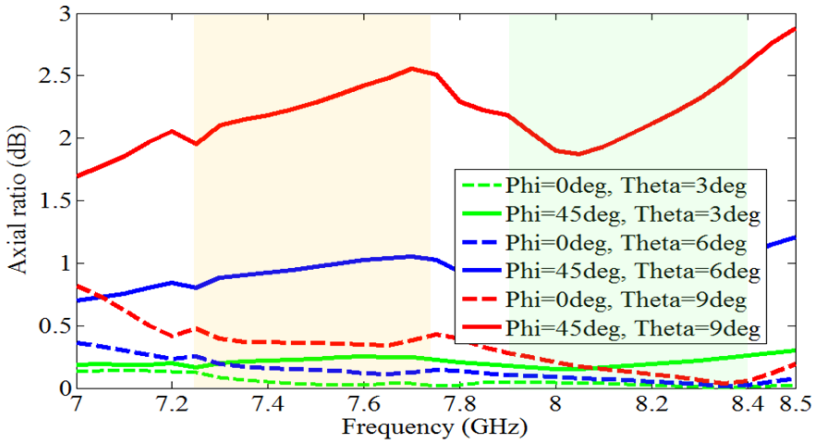

Figure 4.16: Axial ratio of the subarray. Worst axial ratio is in the diagonal plane.

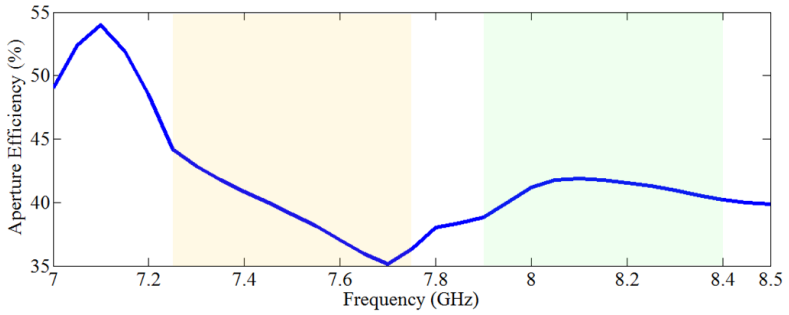

Figure 4.17: Aperture efficiency of the designed subarray, aperture efficiency is calculated with respect to maximum directivity.

The designed subarray is fabricated using combined split block and 3D printing technology as illustrated in Figure 4.18. The aperture part of the array (cavity-backed Vivaldi elements) is 3D printed and copper plated as a single block. Y-junctions are CNC and assembled from multiple blocks.

Measured isolations of the fabricated antenna shown in Figure 4.19 are performed using the fabricated BFN and commercial hybrids [119]. Phase matched cables are used to connect the antenna with the BFN. Both co-polarized isolation are seen to be greater than 44 dB over most of the 7.25 -8.4 GHz band. Isolation obtained using COTS components are seen to be comparable to that of the fabricated BFN. Theoretical isolation from this sequential rotated array configuration is infinite, the finite level obtained in Figure 4.19 is due to the imbalances of the BFNs used.

Measured far field performance of the subarray are obtained using 2 approaches. First, directivity and radiation patterns are measured when the fabricated BFNs are connected with the antenna. In the second approach, measured embedded element patterns are used to synthesize the combined patterns and directivity. Radiation patterns and directivity of the fabricated subarray are shown in Figure 4.20. Some differences are seen between measurement and simulations. These differences are associated with the imbalances of the BFNs and asymmetry between the antenna elements. As seen, synthesized performances, which do not include any imbalance from the BFN still show some deviations from simulation. Cross-pol of the antenna with the fabricated BFN is seen to be worse than the synthesized case as expected given the measured imbalances.

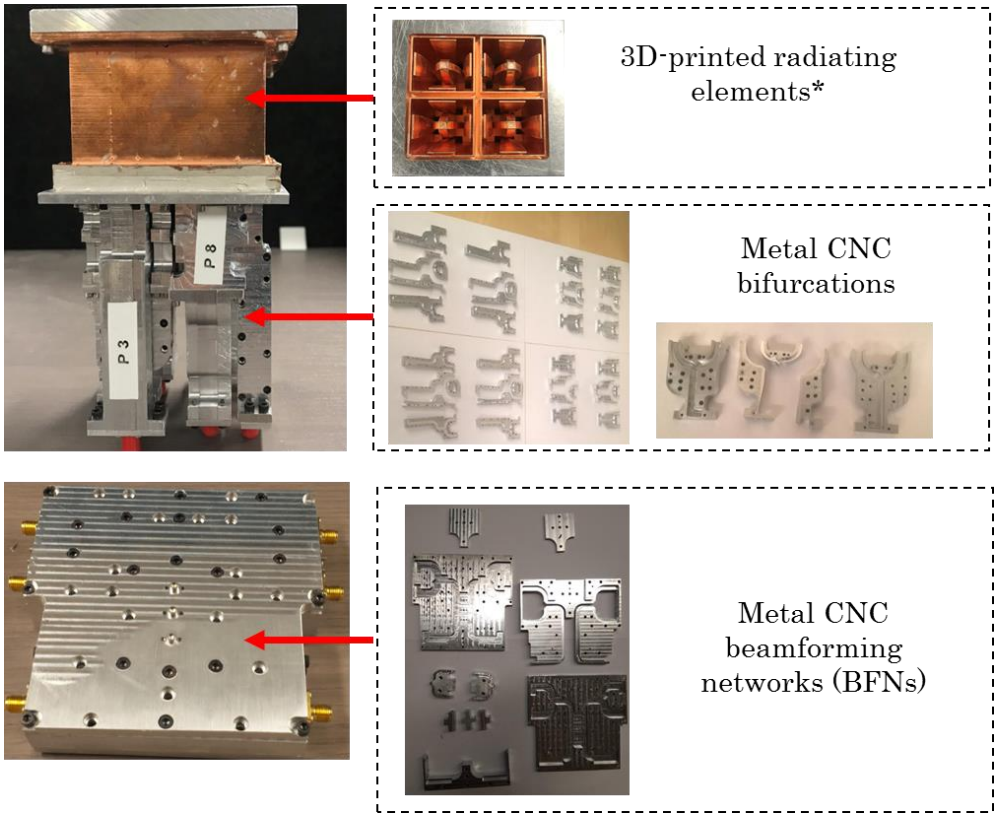

Figure 4.18: Photograph of the prototyped subarray combining CNC machining 3D printing techniques.

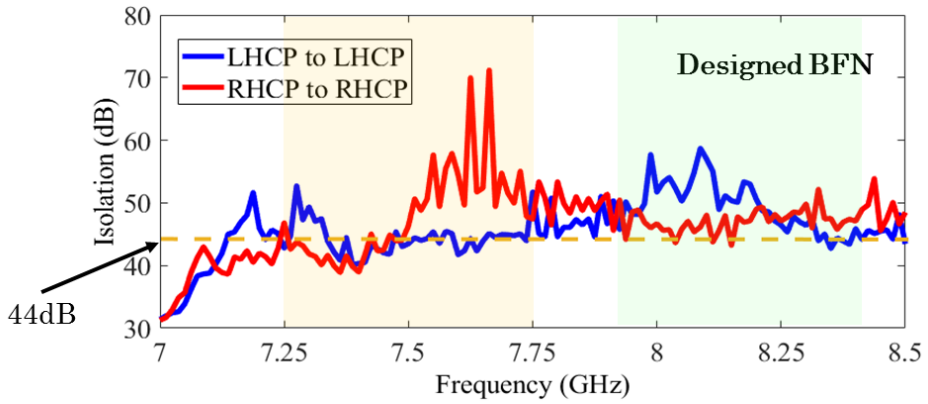

(a)

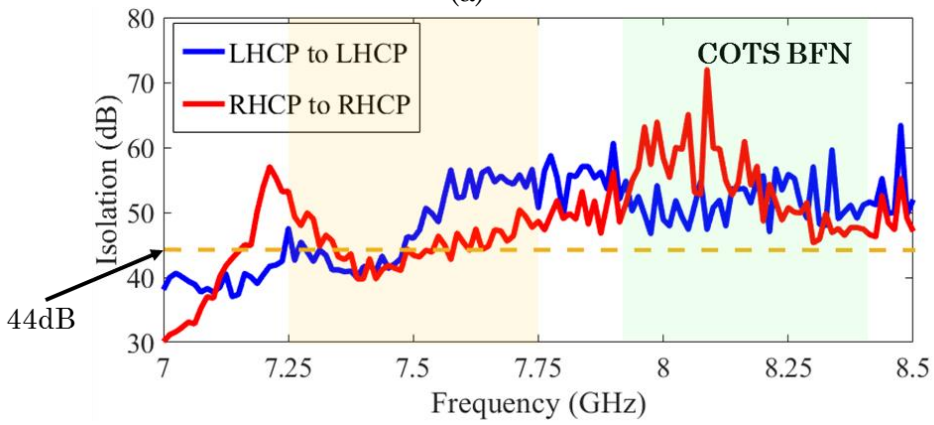

(b)

Figure 4.19: Measured co-polarized transmit receive isolation with (a) using fabrication BFN, and (b) using commercial hybrids.

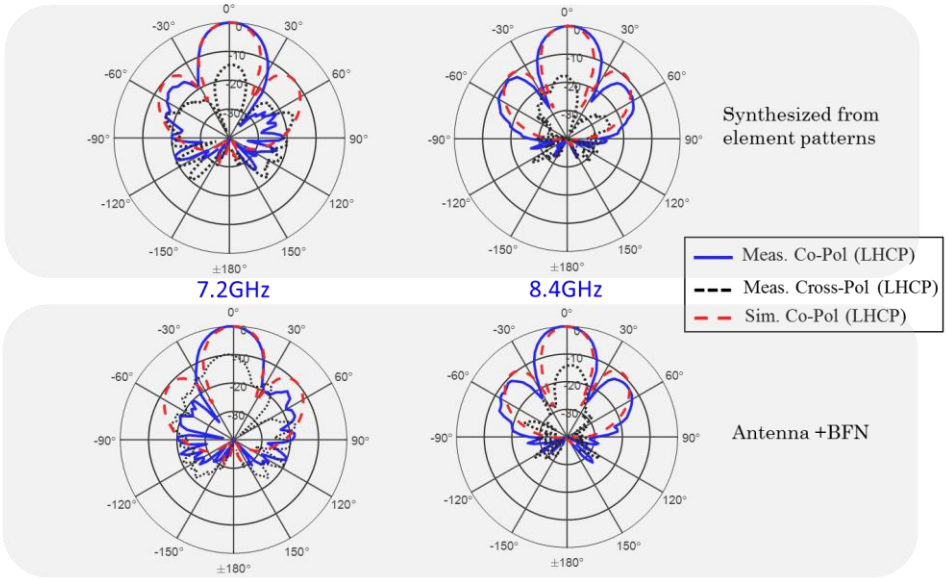

(a)

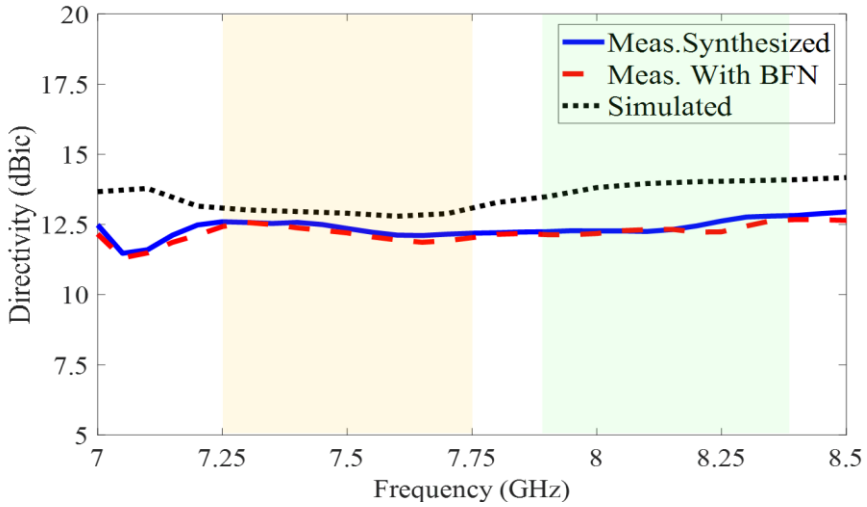

(b)

Figure 4.20: Measured far-field performance (a) measured and simulated patterns,(b) Directivity.

4.5 Summary

An X-band full-duplex subarray, used as the unit cell of a dual-polarized active phased array is designed and fabricated. The proposed architecture enables co-polarized transmit and receive with theoretically infinite isolation. The proposed architecture does not rely on diplexers or circulators, often required for full duplex communication. Measured isolation > 44 dB is demonstrated. The finite achieved isolation is found to be due to imbalances and asymmetry in fabricated components. Detailed design guidelines of each component of the subarray is described. A novel dual-polarized all metal antenna is introduced as a candidate for space capable antennas. This newly introduced antenna is excited with double-ridge waveguides and does not rely on an OMT to realize dual-polarization with simulated cross-pol isolation > 60 dB.

Chapter 5

Balanced-Diplexer FDD Subarray for X-Band Phased Arrays

5.1 Overview

In Chapter 4, we proposed a diplexer-less dual CP X-band subarray with high TX/RX isolation. However, this design is based on a sequentially-rotated array with maximum aperture efficiency limited to 50%, and a high profile which decreases its attractiveness for the targeted application. In this chapter, a different subarray architecture aiming to simplify the diplexer's complexity is proposed. It enables co-polarized FDD communication using an integrated balanced-diplexer network with demonstrated aperture efficiency close to 100%. The balanced-diplexer architecture allows high transmit/receive isolation without major increase in size or complexity of diplexers. Similar concepts are presented in [120]-[121] where a balanced-circulator is used to increase the isolation of a common carrier communication system. Herein, the proposed balanced-diplexer configuration is for the first time reported for use in a phased array system. Unit cell (subarray) of this phased array consists of a 4 × 4 array of dual-polarized magneto-electric (ME) dipoles [122] chosen for their low profile, wide bandwidth, and symmetric E- and H- plane patterns over a wide field of view. The total subarray size is 100 mm × 100 mm which is chosen to have grating lobes off the Earth's surface when scanned at 9^{o} off boresight.

This chapter is organized as follows:

- Section 5.2 describes the architecture of the proposed balanced-diplexer system. Signal flow analysis is used herein to determine the maximum achievable isolation. Sensitivity of this isolation to imbalances of realistic components is presented.
- Section 5.3 presents a detailed design of the different components used in the proposed system; namely, the antenna element, beamforming network, diplexers, and quadrature hybrids.
- Section 5.4 presents a full characterization of the subarray when integrating all designed components. Total system isolation and far-field performances are presented.
- Section 5.5 concludes the chapter.

5.2 Balanced Diplexer Antenna System Description

In Figure 4.1(a), the conventional approach used to realize dual CP payload with co-polarized transmit-receive using a single aperture is shown. As discussed in Chapter 4, the isolation of the diplexer dictates the overall capabilities of such system. To enable high power transmission, the diplexer needs to provide significantly high rejection. This is challenging in a phased array system where size is constrained by the scan requirements. To overcome this limitation without increased complexity in the diplexer design, the balanced-diplexer shown in Figure 5.1 is proposed in this work. The proposed configuration relies on two quadrature hybrids and two diplexers arranged as shown to cancel the leaked signals from the TX to RX paths and vice versa.

To determine the maximum theoretical isolation achievable with the proposed architecture, signal flow analysis is used as shown in Figure 5.1. The case of co-polarized LHCP signal is illustrated. For an incident power wave “a” within the TX range, the

received power "b" is the summation of signals coming from different paths. To calculate the ratio "b/a" which represents the coupling between co-polarized transmit and receive

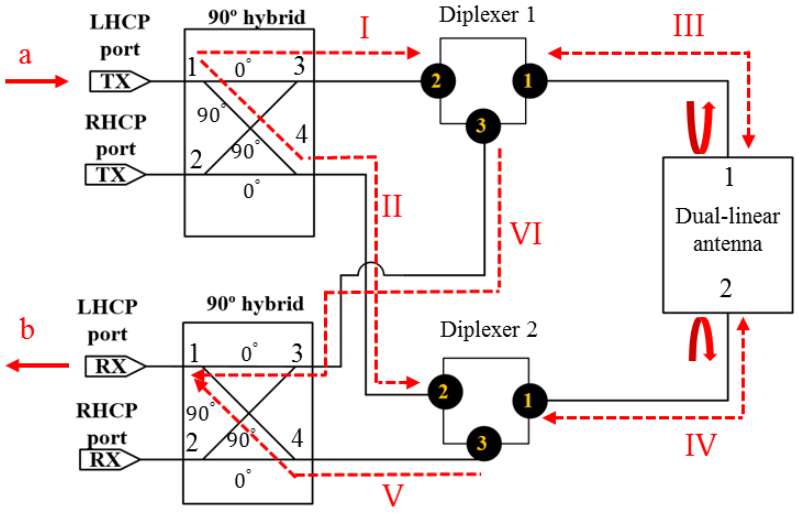

Figure 5.1: Signal flow of the proposed balanced-diplexer architecture with co-polarized transmit-receive.

ports, the summation of power through the different coupling paths is performed. Three pairs of paths are identified as discussed next. Paths 1 and 2 account for coupling through the antenna. Paths 3 and 4 only consider coupling through the hybrids and diplexers. Paths 5 and 6 integrate the reflection at the two input ports of the antenna. Using superscript "A", "D", "H" to identify the S-parameters of the antenna, diplexer, and hybrid respectively, the direction of the six paths are:

$$\text{P1: } S_{31}^{H} \rightarrow I \rightarrow S_{12}^{D} \rightarrow III \rightarrow S_{21}^{A} \rightarrow IV \rightarrow S_{31}^{D} \rightarrow V \rightarrow S_{14}^{H}$$

$$\text{P2: } S_{41}^{H} \rightarrow II \rightarrow S_{12}^{D} \rightarrow IV \rightarrow S_{12}^{A} \rightarrow III \rightarrow S_{31}^{D} \rightarrow VI \rightarrow S_{13}^{H}$$

$$\text{P3: } S_{31}^{H} \rightarrow I \rightarrow S_{32}^{D} \rightarrow VI \rightarrow S_{13}^{H}$$

$$\text{P4: } S_{41}^{H} \rightarrow II \rightarrow S_{32}^{D} \rightarrow V \rightarrow S_{14}^{H}$$

$$\text{P5: } S_{31}^{H} \rightarrow I \rightarrow S_{12}^{D} \rightarrow III \rightarrow S_{11}^{A} \rightarrow III \rightarrow S_{31}^{D} \rightarrow VI \rightarrow S_{13}^{H}$$

$$\text{P6: } S_{41}^{H} \rightarrow II \rightarrow S_{12}^{D} \rightarrow IV \rightarrow S_{22}^{A} \rightarrow IV \rightarrow S_{31}^{D} \rightarrow V \rightarrow S_{14}^{H}$$

Assuming that the two quadrature hybrids and diplexers are identical with symmetric response between the two antenna ports, the power coupled from each path is calculated as:

$$b_1 = aS_{31}^H S_{12}^D S_{21}^A S_{31}^D S_{14}^H e^{j(\frac{\pi}{2}+\varphi_1)} \tag{5.1}$$

$$b_2 = aS_{41}^H S_{12}^D S_{12}^A S_{31}^D S_{13}^H e^{j(\frac{\pi}{2}+\varphi_1)} \tag{5.2}$$

$$b_3 = aS_{31}^H S_{32}^D S_{13}^H e^{j(\varphi_2)} \tag{5.3}$$

$$b_4 = aS_{41}^H S_{32}^D S_{14}^H e^{j(\pi+\varphi_2)} \tag{5.4}$$

$$b_5 = aS_{31}^H S_{12}^D S_{11}^A S_{31}^D S_{13}^H e^{j(\varphi_3)} \tag{5.5}$$

$$b_6 = aS_{41}^H S_{12}^D S_{22}^A S_{31}^D S_{14}^H e^{j(\pi+\varphi_3)} \tag{5.6}$$

$$b = b_1 + b_2 + b_3 + b_4 + b_5 + b_6 \tag{5.7}$$

In (5.1) to (5.6), φ_i represents the phase delay in the diplexer and the antenna for a given path. Owing to the symmetry of the network and the use of reciprocal components, b_1 and b_2 have same magnitude and phase, and coherently add at the co-polarized receive port. Power waves b_3 and b_4 have same amplitude with opposite phase, their contributions are therefore cancelled at the co-polarized received port. Similar results are obtained for b_5 and b_6 which, contributions are mutually cancelled at the co-polarized received port; a similar analysis can be done for cross-pol coupling. It can be demonstrated in this case that b_1 and b_2 mutually cancel at the cross-polarized port while b_3, b_4, b_5 and b_6 all add coherently at the same port. The maximum theoretical TX/RX isolation at the co-polarized receive port for a lossless system is thereby:

$$I_{copol1} = -20log\left|\frac{(b_1 + b_2)}{a}\right| = -20log\left|S_{21}^A S_{31}^D\right| \tag{5.8}$$

Seeing as, the network of Figure 5.1 is reciprocal, transmit and receive can be interchanged. It can be shown that when transmission emanates from RX band ($S_{12}^{D} \neq 0$, $S_{31}^{D} = 1$) and TX port used for reception, the maximum isolation is given by:

$$I_{copol2} = -20log\left|S_{21}^{A}S_{21}^{D}\right| \tag{5.9}$$

It can be concluded from (5.8) and (5.9) that the maximum achievable isolation is a summation of diplexer rejection and port to port (i.e. cross-polarization) isolation of the antenna. The system isolation can therefore be increased without added complexity for the diplexers by having antennas with high port to port isolation.

To validate these findings, a circuit simulation of Figure 5.1 is performed. Two identical and ideal 90o hybrids are used in the model. Two identical diplexers, designed for X-band with a response shown in Figure 5.2 are used. The design of this diplexer, which has 30 dB rejection at the lower end of the RX band, is described in Section 5.3. The proposed response is used here for the sole purpose of this proof of concept. Any X-band diplexer that allows proper routing of power, could be used for this analysis.

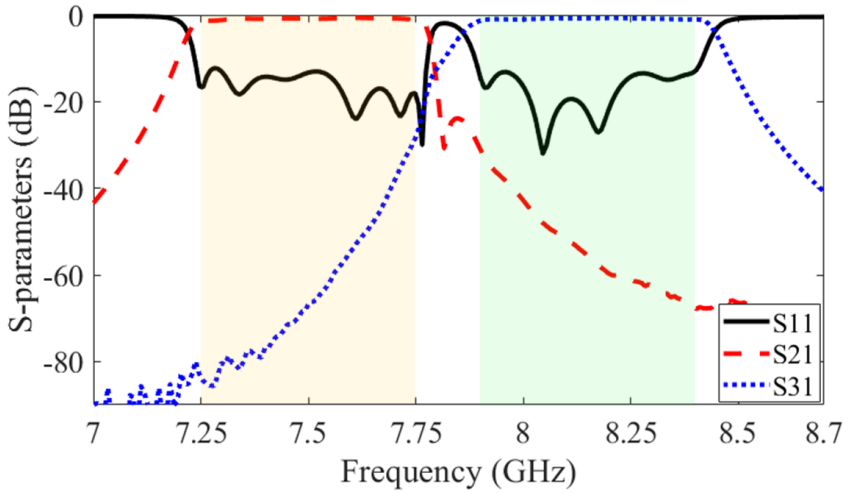

Figure 5.2: Measured S-parameters of a designed X-band diplexer used for proof of concept.

The reflection coefficient and port to port isolation of a dual-polarized antenna used in the analysis is shown in Figure 5.3(a). Detailed description of the design of this antenna is presented in Section 5.3. To demonstrate the impact of antenna port to port isolation on the overall system isolation, the S21 of the antenna is modified by adding 20 and 40 dB attenuation as seen in Figure 5.3(a). The co-polarized system isolation is shown in Figure 5.3(b). As seen, the total simulated co-polarized transmit-receive isolation is the summation

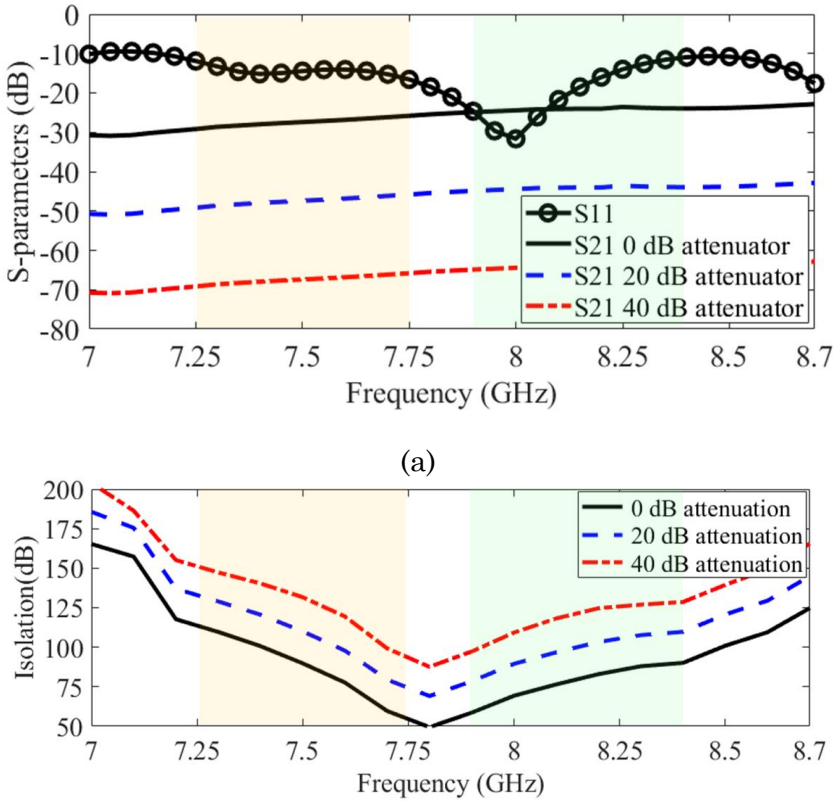

Figure 5.3: (a) S11 and S21 of a dual-polarized antenna with varying S21 using different attenuation settings, and (b) isolation of the proposed balanced-diplexer with different sets of attenuations.

of diplexer and antenna port to port isolation as demonstrated in (5.8) and (5.9). A linear correlation is also seen between isolation and S21 of the antenna. At the start of RX band (7.9 GHz) where diplexer isolation is 30 dB, the system isolation in the 20 dB attenuation case (S21= 46 dB) is seen equal to 76 dB. Designing a diplexer to have 76 dB at band edge is

challenging given the narrow guard band. Whenever such a diplexer design is made possible, it can still be used in the proposed architecture to further increase the system isolation.

The analysis presented so far is based on ideal 90° hybrids and assumes perfect symmetry between different components of the system. In a practical and more realistic environment, amplitude and phase imbalances are expected from all these components. To assess the impact of these imbalances on isolation, random amplitude and phase imbalances are added to one of the hybrids. Amplitude imbalance is synthesized with the insertion of a variable attenuator ranging from to 0 to 6 dB with 0.25 dB step. Phase imbalance is generated with a variable phase shifter ranging from 0 to 8 degree with 0.5 degree step. The selected range is guided by the cascade of realistic imbalances that can emanate from different components. The contour plot in Figure 5.4 shows isolation sensitivity for a given amplitude and phase imbalances at 7.9 GHz. As seen, isolation is at theoretical maximum of 58 dB with zero imbalance and drops below 45 dB for high imbalances. This contour plot also shows a greater sensitivity to phase imbalances than

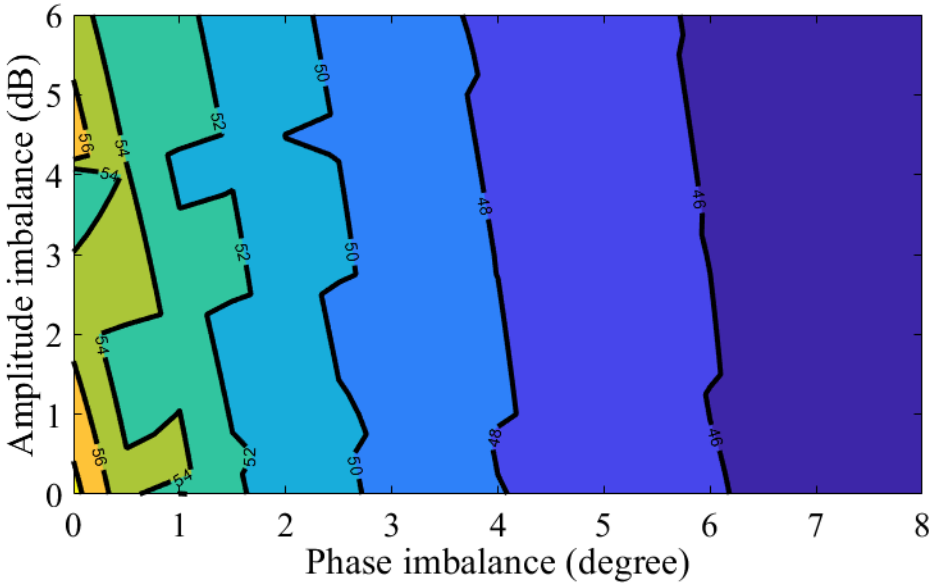

Figure 5.4: Isolation sensitivity analysis at 7.9 GHz with varying amplitude and phase imbalances.

amplitude imbalances. This observation was made on similar work that relies on symmetry for isolation improvement [32], [83]. It can, however, be seen that significantly high isolation (> 50 dB) can be maintained even with moderate imbalances (amplitude and phase imbalances < 3 dB or degree respectively).

5.3 Subarray Components Design and Performance

5.3.1 Dual-linearly Polarized Unit element

The unit element of the subarray is required to be dual-polarized, low profile, and wide impedance bandwidth that covers the designated X-band while fitting within a 25 × 25 mm^2 footprint. High isolation between orthogonal ports is also researched, since this is demonstrated to be directly correlated to the overall system isolation. Dual-polarized patch antennas [123]-[126] are often the prime candidate when low profile and moderate bandwidths are required. Most of these antennas rely on aperture coupling and multilayered stacked configuration for bandwidth improvement; leading to increased feed complexity, decreased radiation efficiency, and increased back radiation.

Magneto-electric (ME) dipoles have recently emerged as a potential candidate for low profile applications requiring symmetric E- and H-plane patterns over wide field of view [127]-[131]. In all implementations of this class of radiator, the underlying principle is the equal excitation of dipole and loop modes to broaden the antenna bandwidth and decrease back radiation. The work proposed in [128] introduced a simplified feed mechanism for this antenna with good impedance match and high port to port isolation over wide bandwidth. The proposed feeding architecture, while being simple, lacks the mechanical robustness required for space applications.

In this work, a compact, dual-polarized, X-band ME dipole is developed as a unit cell for the proposed subarray. The antenna feed is designed for stronger mechanical stability

and better resistance to mechanical stress. The geometrical arrangement of the proposed unit cell is shown in Figure 5.5. The element consists of 4 metallic patches that are grounded using 4 rectangular posts (Figure 5.5(a)). Two gamma probes, seen in the right of Figure 5.5(a), supported by a Teflon plug are used to excite the two orthogonal polarizations of the antenna. To decrease the axial ratio when this antenna is fed for circular polarization, the gamma probes are curved in opposite directions at the junction area while maintaining identical physical length. The element is recessed inside a square metallic cavity to decrease back radiation and coupling to nearby elements in the array environment. Top and side views of the antenna are shown in Figure 5.5(b) and the geometrical parameters of the unit cell reported in Table 5.1. These values are obtained from an infinite array analysis aiming to achieve a VSWR < 2 for the two polarized ports and port to port isolation greater than 20 dB over the frequency range of interest. Simulated VSWR of the proposed unit cell based on an infinite array analysis is shown in Figure 5.6(a). As seen, VSWR < 2 is demonstrated over the frequency range of interest. The proposed unit cell is prototyped for initial validation before inclusion to the subarray. The four patches, metallic posts, and the cavity are fabricated in aluminum using CNC machining process. An extra 45 mm^2 ground plane is added to accommodate the two SMA connectors as shown in the inset of Figure 5.6(b). Two transmission lines are used to connect the gamma probes and the SMA connectors. The VSWR of the fabricated unit cell is plotted along with its simulated counterpart in Figure 5.6(b). As seen, VSWR < 2 is achieved over most of the band. VSWR is also seen to be different than the infinite array simulation of Figure 5.6(a). These differences are expected since the antenna is designed for an array environment. The measured and simulated E- and H-planes patterns of the standalone ME dipole at 7.5 GHz and 8.1 GHz are shown in Figure 5.7. As seen, patterns are symmetric with low back radiation and cross-pol below -20 dB over a wide field of view.

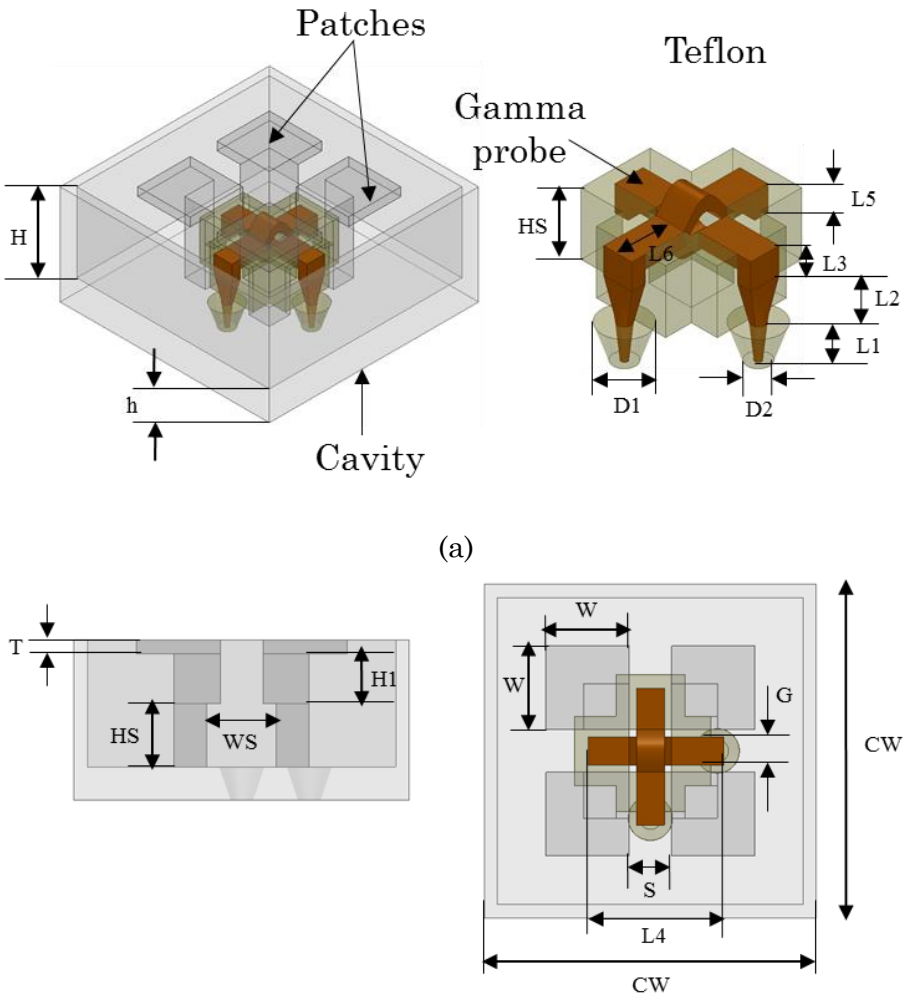

Figure 5.5: Geometrical arrangement and parameters of the dual-polarized magneto-electric dipole; (a) isometric view, and (b) side and top views.

Table 5.1: Geometrical Parameters of the dual-Polarized ME Dipole

Parameters	H	HS	h	H1	W	WS
Values (mm)	9.4	4.7	2.5	3.7	6.26	5.2
Parameters	L1	L2	L3	L4	L5	L6
Values (mm)	2.5	2.7	1.9	10.2	1.9	3.9
Parameters	T	S	G	D1	D2	CW
Values (mm)	1	3.2	2.1	3.4	1.7	25

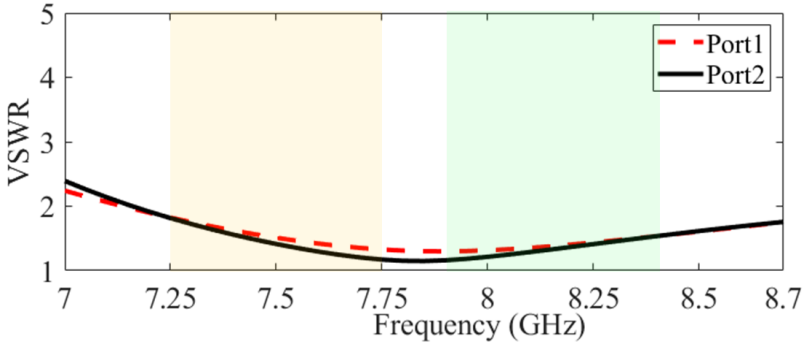

(a)

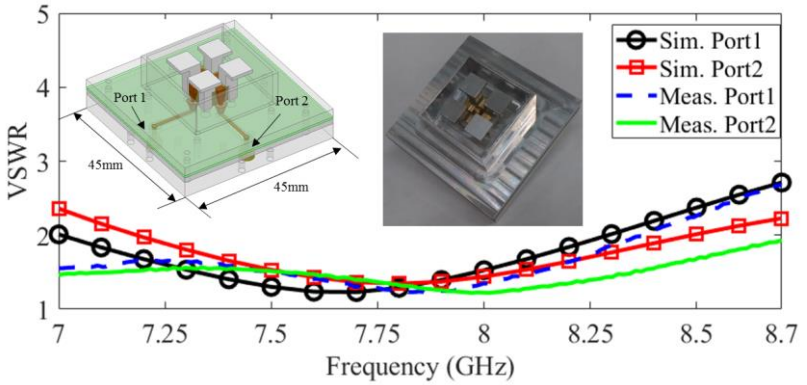

(b)

Figure 5.6: VSWR of the magneto-electric dipole unit cell: (a) infinite array, and (b) standalone element.

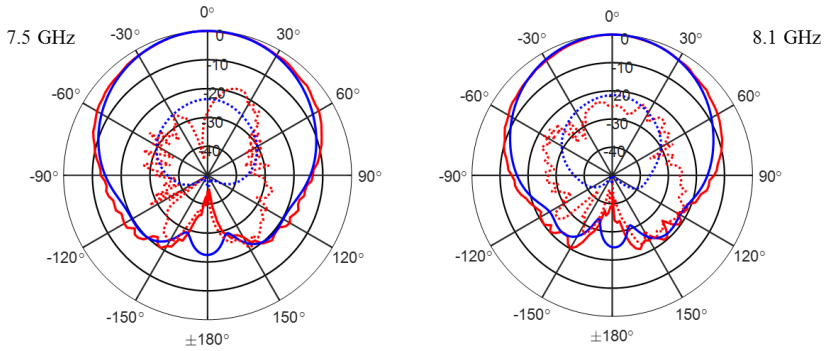

(a)

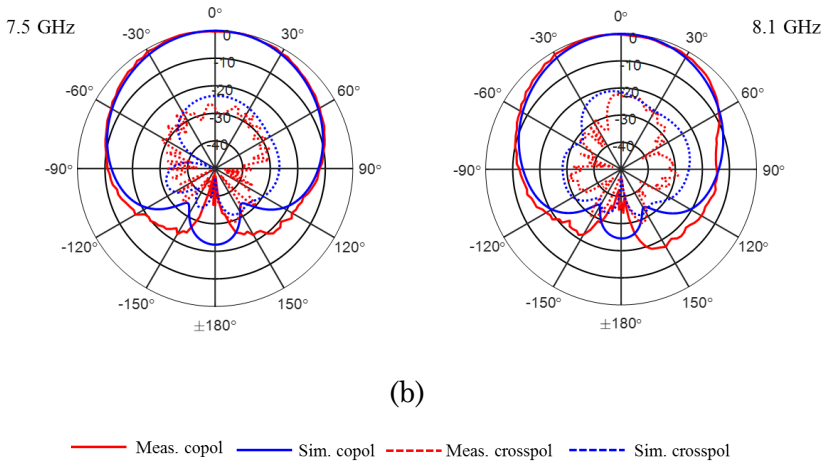

Figure 5.7: (a) E-plane, and (b) H-plane patterns of the standalone unit cell at 7.5 GHz and 8.1 GHz.

5.3.2 Dual-linearly Polarized Subarray and Feed Network

The designed unit cell (Figure 5.5) is arranged in 4 × 4 topology to realize the proposed subarray as shown in Figure 5.8. To maintain symmetric response between the two input VSWRs of the subarray, the gamma probes are interleaved between adjacent cells as shown in the enlarged view of Figure 5.8.

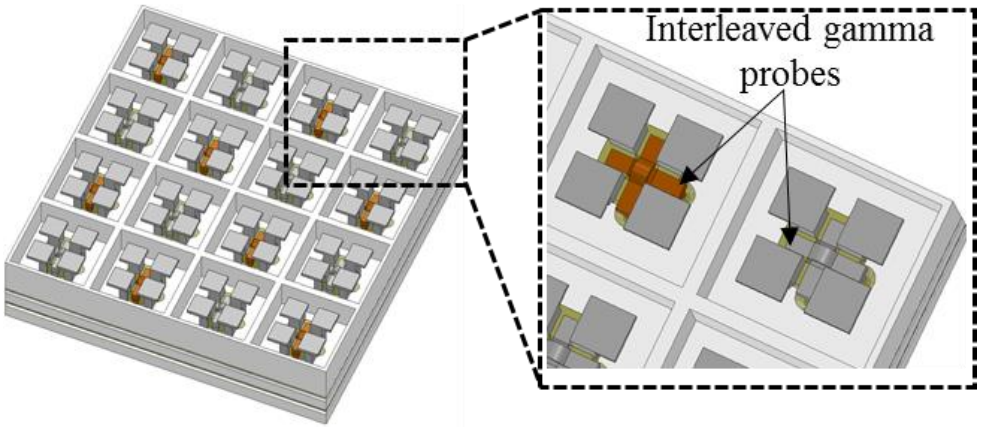

Figure 5.8: Proposed subarray obtained as a 4 × 4 array of unit cells in Figure 5.5.

The beamforming network (BFN) is an important part of the subarray system. The routing paths are engineered to minimize physical length and a low-loss transmission line

approach is utilized. Specifically, a TEM transmission line is used based on a hybrid integration of grounded coplanar waveguide and air-coax shown in Figure 5.9(a). The proposed transmission line approach aims to reduce the insertion loss and manufacturing cost given the use of a single layer PCB board. The PCB portion of the transmission line is realized on a 20 mils Taconic RF 30 board. The upper and lower ground planes are connected through 0.5 mm diameter vias. The separation between adjacent vias is 0.7 mm. To uniformly excite the 4 × 4 array, four 4-way power dividers/combiners are used per polarization as shown in Figure 5.9(b). The inputs of these power dividers are further combined using a second set of 4-way power dividers constructed on the upper layer. The transition between layers is through a Teflon filled 50 Ω coaxial line as shown in Figure 5.9(b). The cascade connection of the 4-way dividers in the two layers leads to the dual-linearly polarized subarray.

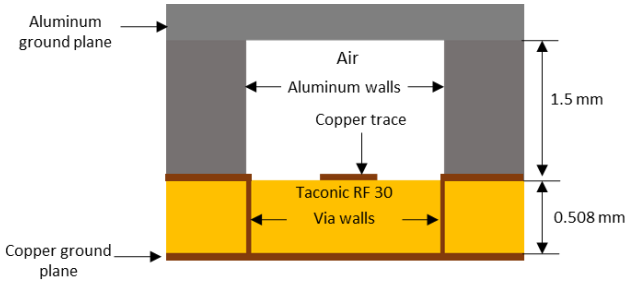

(a)

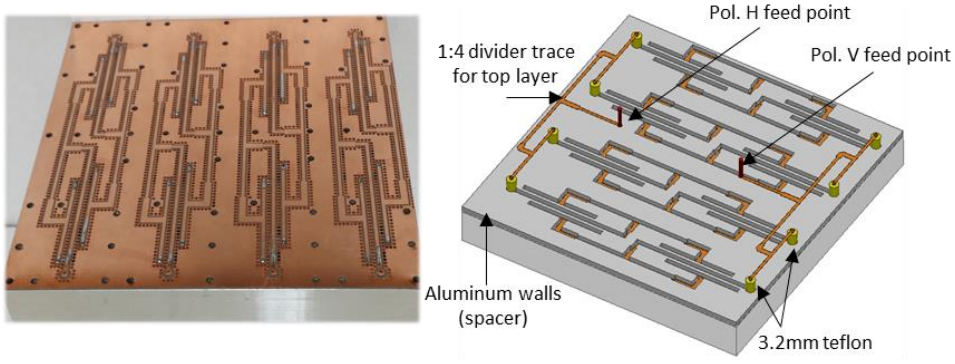

(b)

Figure 5.9: (a) Cross section of the proposed hybrid transmission line, and (b) 16-way corporate feed network.

The dual-linearly polarized antenna is fabricated as shown in the inset of Figure 5.10 with the corresponding VSWR and S21 of the prototyped subarray. As seen, VSWR < 2 is demonstrated both through simulation and measurements. Measured VSWRs at the two polarized ports are very similar, the small difference observed is attributed to imperfect symmetry of soldering during the assembly process. Good agreement is also observed between measured and simulated coupling between the two ports. This coupling is lower than -25 dB over most of the band, thereby setting the limit of the maximum achievable isolation when combined with the diplexer. The measured realized gain and aperture efficiency of the dual-linearly polarized subarray are shown in Figure 5.11. The measured realized gain is found to be about 1.5 dB lower than simulation. Lower aperture efficiency is also observed. This reduction in measured realized gain and aperture efficiency suggests uncharacterized mismatch losses as well as higher imbalances in the fabricated BFN. This is most likely due to the misalignment of the aluminum spacer used to realize the TEM transmission line. The E- and H-plane normalized patterns at 7.5 GHz and 8.15 GHz of the

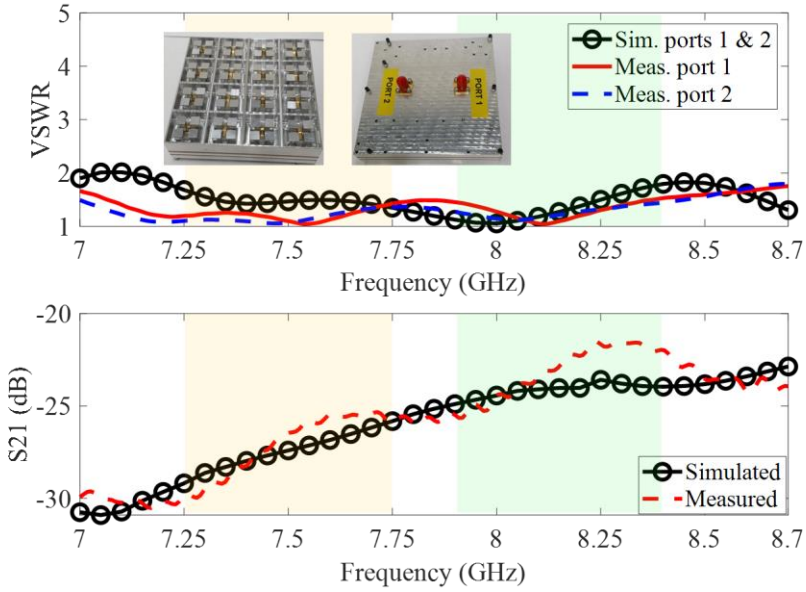

Figure 5.10: Measured, simulated VSWR, and S21 of the dual-linear polarized subarray.

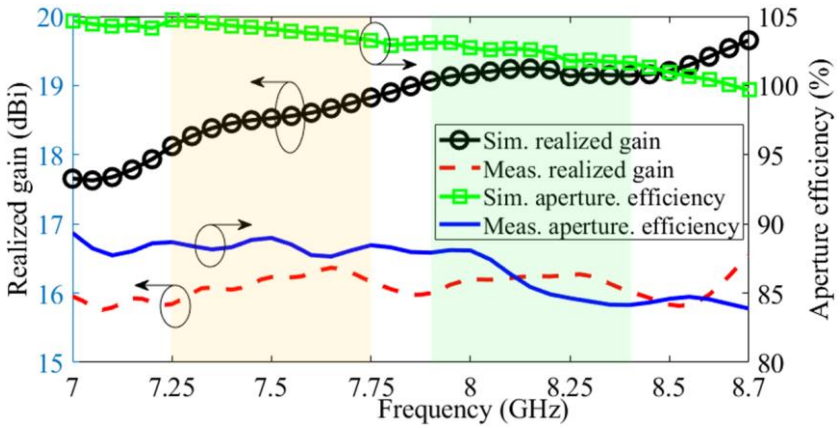

Figure 5.11: Measured and simulated realized gains and aperture efficiency of the dual-linear subarray.

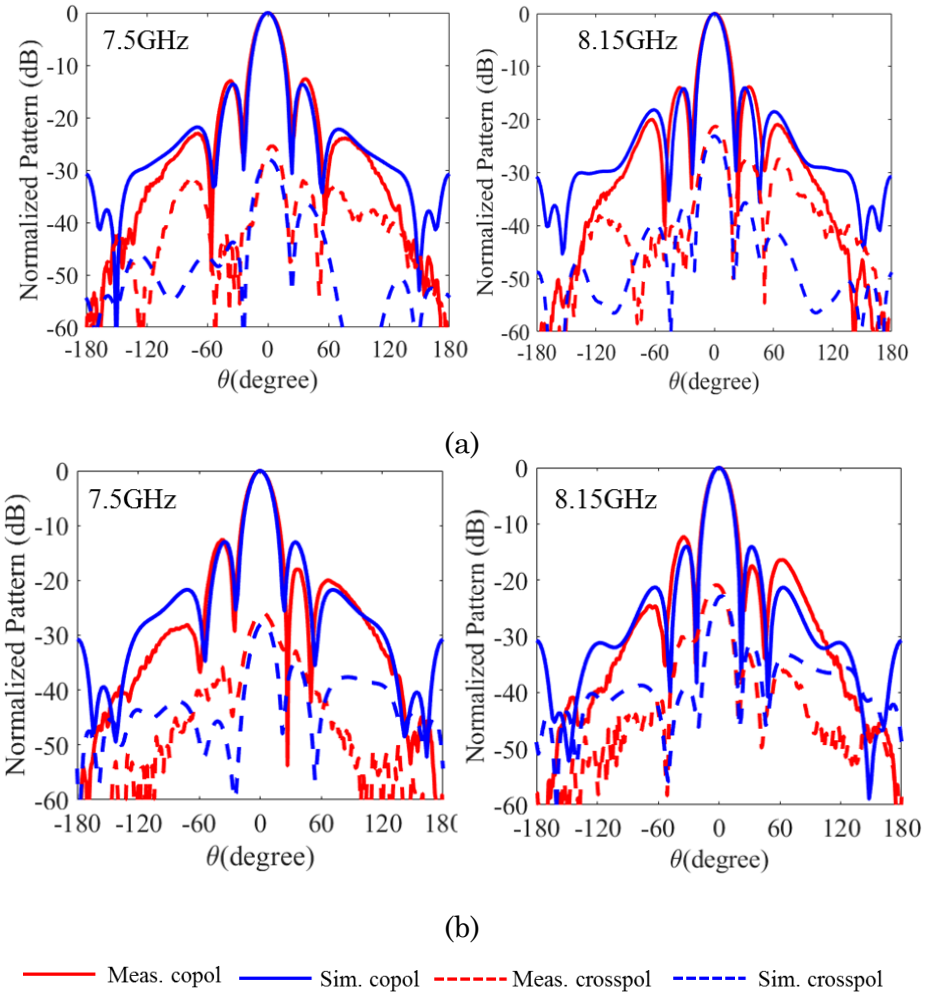

Figure 5.12: (a) E-plane, and (b) H-plane normalized patterns of the dual-linear polarized subarray at 7.5 GHz and 8.15 GHz.

dual-linear subarray are shown in Figure 5.12. As seen, symmetric patterns are obtained with cross-polarized component, 20 dB below the principal plane.

5.3.3 Quadrature Hybrids

The sensitivity analysis of Section 5.3.1 demonstrated that amplitude and phase imbalances can severely degrade the total isolation of the system. The conventional one section 90° hybrid [132] is known to be balanced at the single designed frequency. Multiple branch hybrids can be used to increase the bandwidth, over which, low imbalances are observed; however, they require extra area which is not compatible with the desired compact integration. Herein, a modified version of the single branch hybrid with open circuit stubs is used to flatten the amplitude and decrease phase imbalances over the band of interest [133]. The designed hybrid is realized using transmission line approach

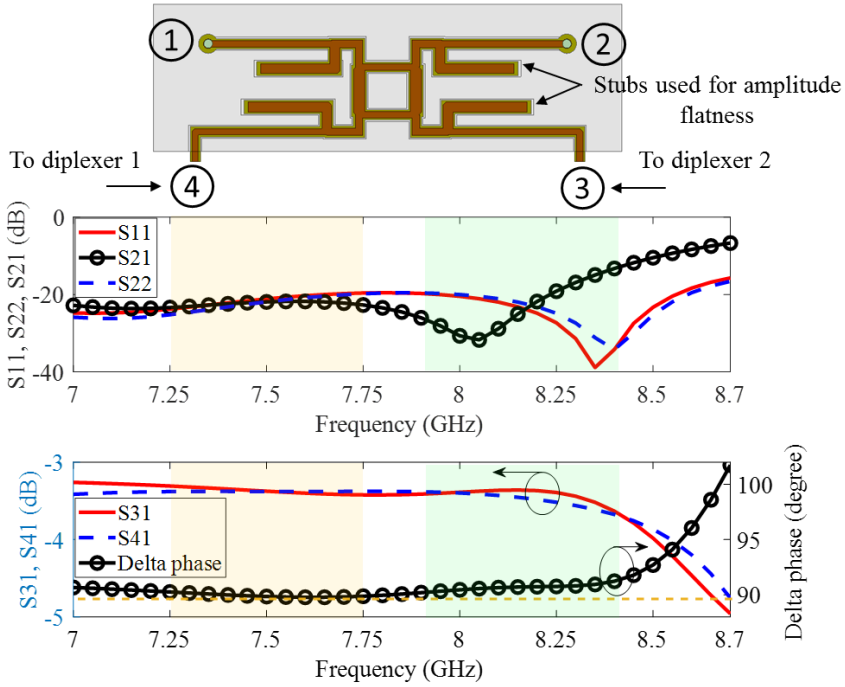

Figure 5.13: S-parameters of the stub loaded single-section quadrature hybrid with flat amplitude and phase over wide bandwidth.

described above. Ports 1 and 2 are the input ports; they can either be used for transmit or receive. Ports 3 and 4 are the two output ports connected to the diplexer to realize the balanced configuration. The S-parameters and schematic of the designed hybrid are shown in Figure 5.13. As seen, the reflection coefficient and coupling to the isolated port are lower than -17 dB over X-band. Flat amplitude between the two output ports is also observed over wide band. Flat phase response is also observed over the range of interest with the maximum phase imbalance less than 2 degrees.

5.3.4 Diplexer Technology

Filter implementations based on planar PCB resonators are well known for their attractiveness for low profile applications. Unfortunately, they have low unloaded Q (200~500) [134]. Waveguide components in contrary are known to have low insertion loss; yet, they are bulky and not attractive for the intended applications [112]-[113]. As compromise between insertion loss and size, a diplexer design based on coaxial cavity resonators is proposed [135]-[137]. The diplexer is designed by combining two 6th order Chebyshev bandpass filters centered at the TX and RX bands respectively. The layout of the two filters is shown in Figure 5.14(a) highlighting a total of 12 resonators. The diplexer is formed by combining the input of the two filters using a transmission line transformer. The lengths of this 3-port transformer are optimized in AWR circuit simulator [138] to achieve the proper diplexer response. The 3-port junction is shown in Figure 5.14(b) for the fabricated diplexer. Square coaxial cavity resonators are used with width w = 10 mm, height h = 10 mm, and coax inner conductor diameter D = 2.5 mm as shown in Figure 5.14(a). With these chosen dimensions, the calculated unloaded Q using Ansys HFSS [77] is 4000 using aluminum as base material. Coupling between resonators is illustrated with the dash lines shown in Figure 5.14(a). This coupling being predominantly inductive, metallic

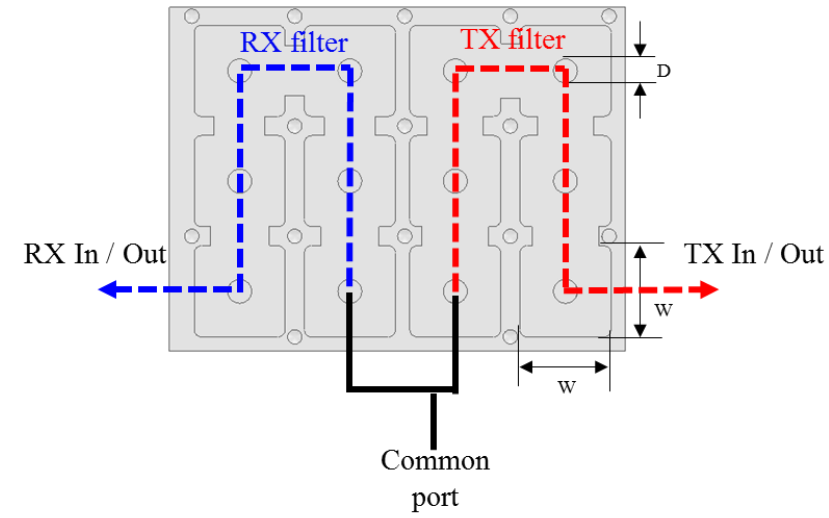

(a)

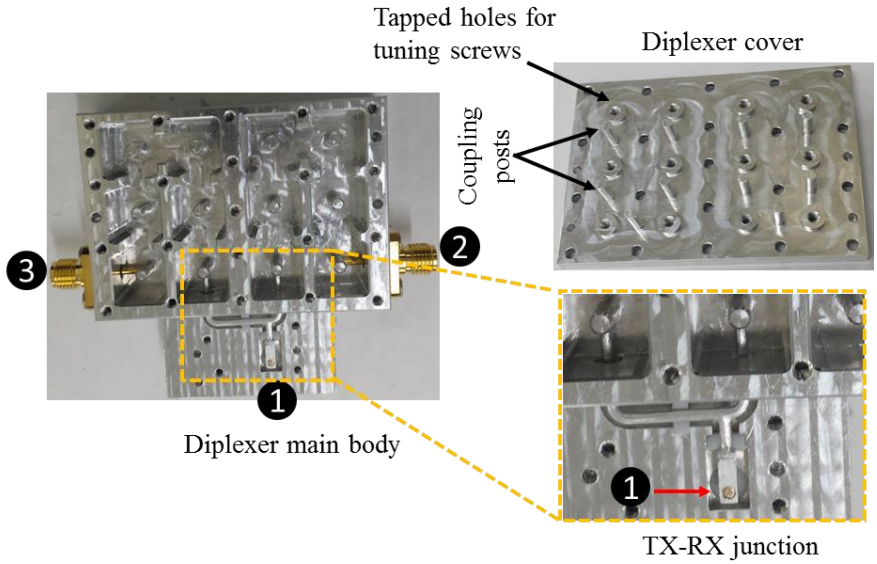

(b)

Figure 5.14: (a) Layout of the designed coaxial cavity diplexer, and (b) fabricated split block diplexer.

posts are inserted at the center of these irises to increase coupling while keeping the iris width within machining tolerances. The diplexer is assembled in two main parts. The bottom (body part) contains the cavity resonators and the associated coaxial connectors for power excitation. The inner conductor of the coax connectors is directly connected to edge resonators through circular trenches machined in the center conductor of the coaxial

cavities. The top part (cover) contains the coupling post and holes for post fabrication tuning screws. These tuning screws are needed to compensate the fabrication imperfections given the high unloaded Q of the resonators. Schematic of the prototyped diplexer is shown in Figure 5.14(b). Its scattering parameters are plotted in Figure 5.2. As seen, reflection coefficient at the common port is less than -13 dB and isolation at 7.9 GHz (RX band edge) is 30 dB. Measured insertion loss of the prototyped diplexer is less than 1 dB, justifying the usefulness of this type of filter technology.

5.4 Full System Characterization

The diplexer designed in the last section is a connectorized standalone component fabricated to demonstrate the practical feasibility of the proposed design in a compact form. In the balanced diplexer configuration, two identical diplexers are placed back to back as shown in Figure 5.15. The SMA connectors of Figure 5.14(b) are removed, and the output ports of the diplexers (ports 2 and 3 in Figure 5.14(a)) are directly connected to the 90^{o} hybrids. The common port of the diplexer is designed in this case for 25 Ω characteristic impedance instead of 50 Ω, as in Section 5.3.4. This port is attached to a 4-way power divider/combiner. Designing the diplexer for 25 Ω impedance eliminates the need for extra transmission line length needed for impedance transformation. The layout of the fully integrated, and proposed balanced diplexer is shown in Figure 5.15. The diplexer's cover and the aluminum spacer of the different transmission lines are hidden for better visibility in the figure.

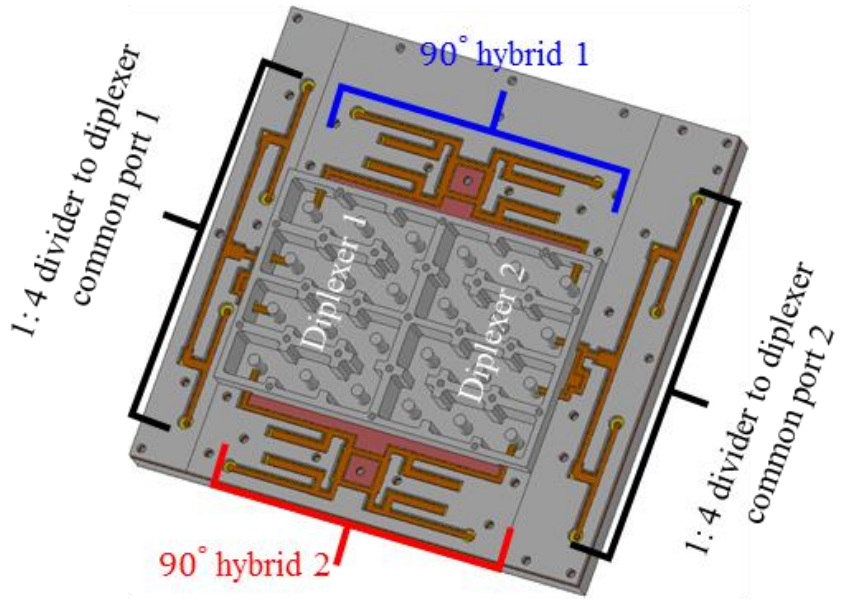

Figure 5.15: Layout of the balanced-diplexer with clearly visible compact integration of two diplexers, two quadrature hybrids, and two 1:4 power dividers/combiners.

As seen, two 4-way power dividers/combiners, two 90° hybrids, and two diplexers are compactly integrated in a 100 mm × 100 mm footprint. To tune the diplexer in this balanced configuration, eight SMA connectors are temporary attached to the output of the two 4-way power dividers. Two COTS 4-way power combiners [139] are then connected to the diplexer using four sets of phase matched cables as shown in the inset of Figure 5.16. The input of the COTS power combiner, therefore served as the common port of the diplexer. In this tuning arrangement, the measured insertion loss combined both diplexer and hybrids losses. The tuned diplexer response measured from the input of the hybrids is shown in Figure 5.16. As seen, common port reflection coefficient is less than -12 dB over TX and RX bands. The S21 in the TX and RX pass bands is -5 dB, thereby indicating total 2 dB insertion loss in the diplexers and 90° hybrids. Diplexer transmit filter rejection at 7.9 GHz is 25 dB. This is 5 dB lower than values obtained in the standalone diplexer. This difference is due to the post-fabrication tuning which was aimed at increasing the similarity

between the two diplexer responses, rather than decreasing its filter roll-off. This work aims to demonstrate paths towards dual-polarized phased array systems when transmit receive isolation does not rely on diplexers only.

The commercial power dividers, phase matched cables, and connectors are removed after post fabrication tuning. The balanced diplexer is then integrated with the dual-linear antenna to realize the compact dual CP subarray shown in Figure 5.17(b). An exploded view of this antenna, shown in Figure 5.17(a) highlights the integration of all the components described herein.

The measured co-polarized transmit-receive isolation of the proposed balanced architecture is shown in Figure 5.18. As seen, isolation > 50 dB is obtained over the band for the co-polarized RHCP case. The isolation for co-polarized LHCP is greater than 40 dB over the band. The reduction of isolation for LHCP polarization is due to higher imbalances of the diplexer responses for this polarization after tuning. The measured RHCP isolation is seen to be more than 15 dB higher than the standalone diplexer of Figure 5.2. The cross-polarized isolation is equivalent to the diplexer rejection of Figure 5.16, as demonstrated in

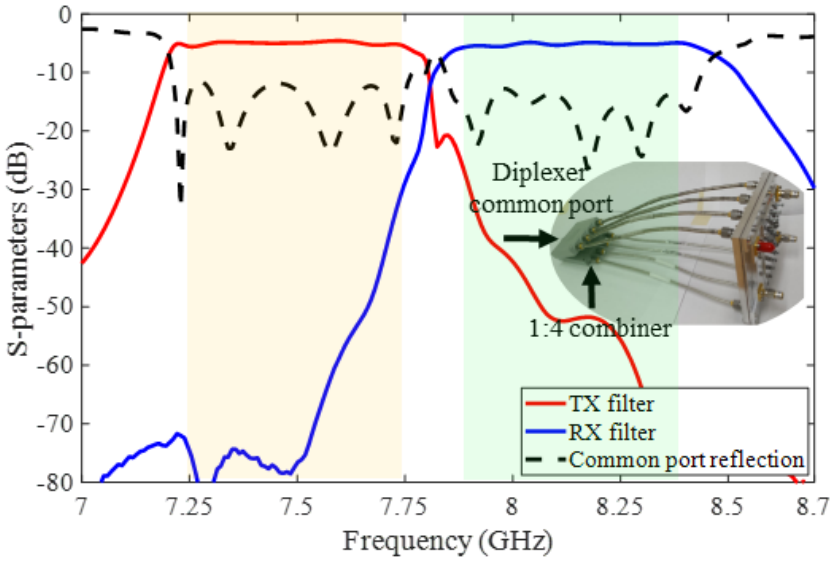

Figure 5.16: S-parameters of the tuned diplexer in the balanced configuration.

Section 5.2. These promising results demonstrate real potential for isolation improvement with better controlled assembly and fabrication process.

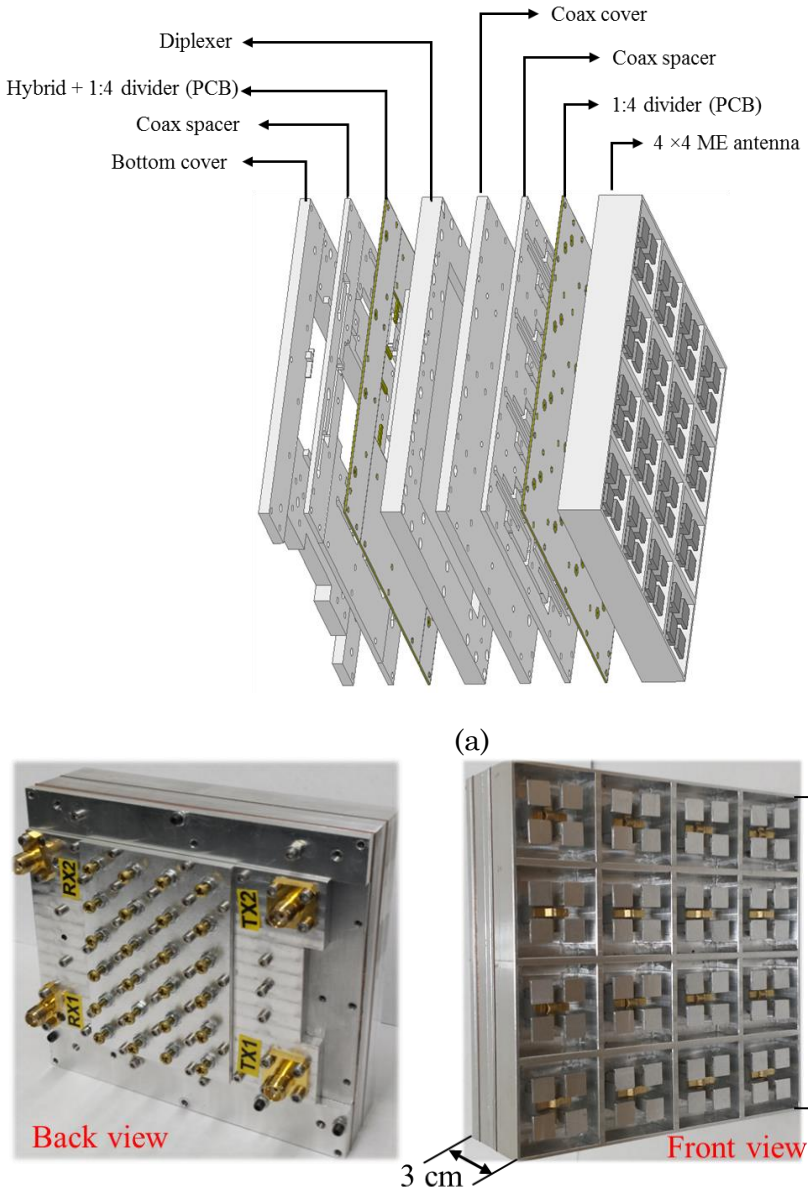

Figure 5.17: Layout and photograph of the prototyped X-band subarray: (a) exploded view highlighting the integration of the different components of the antenna, (b) front and back views of the fully integrated array with brass screws used to tune the diplexers.

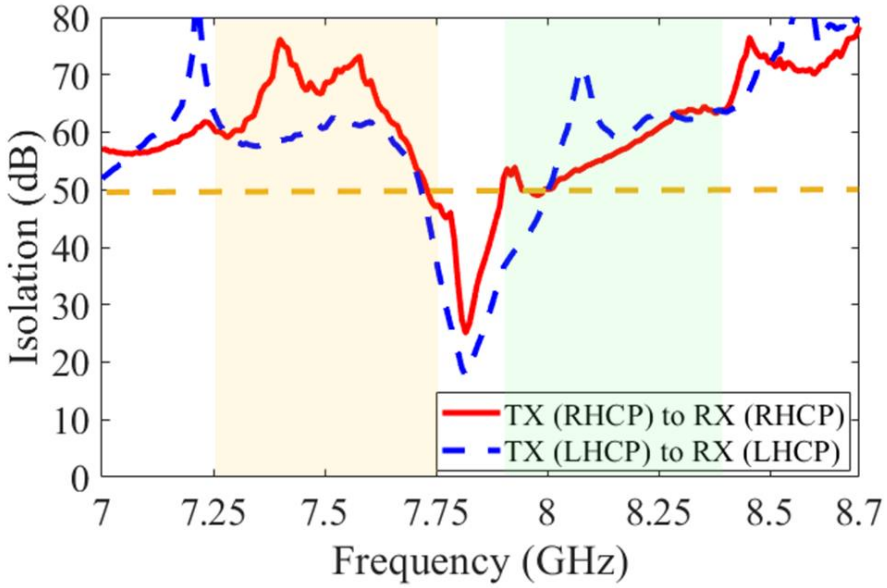

Figure 5.18: Measured co-polarized isolation of the proposed balanced-diplexer subarray.

The measured and simulated co- and cross-polarized realized gains of the subarray are shown in Figure 5.19, with visible roll-off due to the diplexer response. As seen, measured realized gain is seen to be greater than 15 dBic, and its cross-polarized component lower than -5 dB (axial ratio < 2 dB). Measured radiation patterns at 7.6 GHz and 8.2 GHz are shown in Figure 5.20. Symmetric patterns are obtained and low cross-polarization is seen over more than 18° field of view needed for visible Earth.

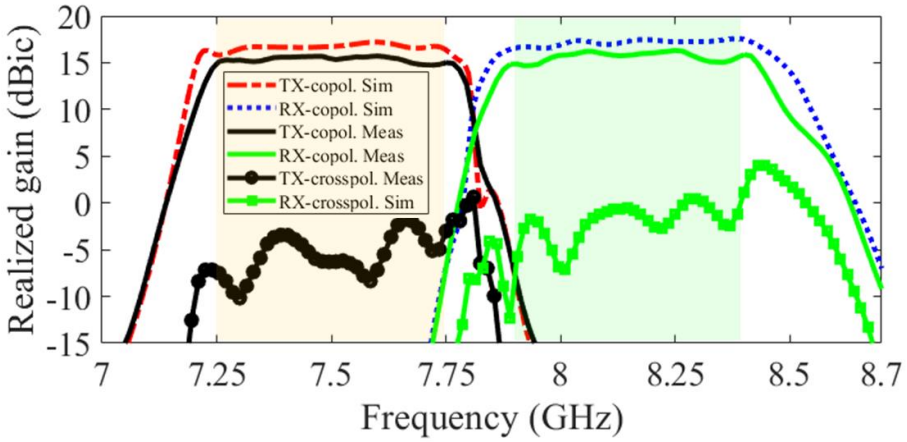

Figure 5.19: Measured and simulated co- and –cross-polarized realized gains of the fabricated subarray with seen roll-off indicating the diplexer response.

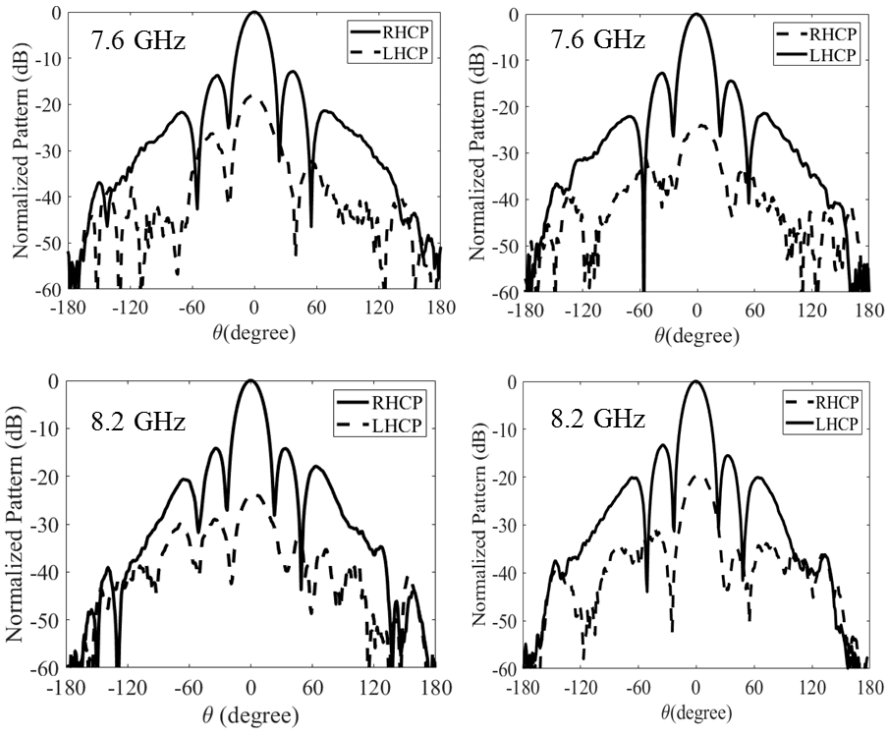

Figure 5.20: Measured CP radiation patterns of the balanced-diplexer subarray at 7.6 GHz and 8.2 GHz.

5.5 Summary

A low profile, robust, and dual-circularly polarized FDD subarray with high isolation and good far-field performance is demonstrated. It is shown, herein, that the complexity of higher order filters needed to generate sharp rejection over narrow guard band can be decreased with the proposed architecture. The maximum achievable isolation is demonstrated through calculation and experiments. It is demonstrated, through sensitivity analysis, that if proper care is taken in the design of different components of the system, achieved isolation can approach its maximum theoretical limit. The design of the different components of the proposed architecture is described both as standalone radiators and as part of an integrated system. VSWR < 2, axial ratio < 2 dB, realized gain > 15 dBic, symmetric, and co-polarized transmit receive isolation > 50dB are demonstrated for the

fully integrated dual-circularly polarized subarray. The obtained isolation can be further enhanced at the band edge by improving the port to port isolation of the used element.

Chapter 6

Conclusion and Future Work

6.1 Summary

In this thesis, the analysis, design, and prototyping of different antennas and antenna systems for possible use in airborne, shipborne, and space platforms are researched. For airborne and shipborne applications, designed antennas are all metal, flush mountable, and have low side lobes, thereby making them attractive for bi-static simultaneous transmit and receive (STAR). In space platforms, novel antennas and systems have been designed and fabricated with promising results which anticipate interesting new capabilities.

This research demonstrated that the ultrawideband response of Vivaldi antennas, which has made them popular in phased array systems, can be maintained when recessed inside a metallic enclosure. The conventional approach which seeks to increase the separation between the antenna and the cavity in order to decrease their mutual interaction is found to be ineffective. This was shown in the studied single polarized 3 × 4 array to have numerous issues with resonances excited inside the cavity. These high Q resonances significantly affect the performance of this antenna, with multiple gain nulls appearing over the frequency range. The nature and origin of these resonances are described in great detail. An efficient technique that does not rely on any lossy material is proposed to suppress these resonances. In contrary to most conventional cavity-backed

antennas, the proposed approach relies on antennas, in which, the E-plane edge elements of the array are shorted to cavity. This cavity backed 3 × 4 is fabricated using a cost effective manufacturing technique combining 3D printing and stacked multi-layer PCB. Measured ultrawideband, resonance-free response, is observed over more than 5:1 bandwidth with VSWR < 2. The proposed antenna when used for broadside only radiation has a very interesting feature at low frequencies; its aperture efficiency is seen to be greater than 100%. The tightly coupled Vivaldi elements, when recessed inside a metallic enclosure have strong fringing fields at low frequencies, leading to a bigger effective aperture. Initial investigations of the antenna's scan capabilities demonstrate comparable performance with its free standing counterpart. For broadside only applications, a more compact embodiment of this antenna with single feed is proposed. Isolation analysis in a bi-static STAR system based on developed antennas is presented. Different techniques are proposed to increase transmit-receive isolation. In one case, termination of some specific array elements with match loads has resulted in isolation improvement of more than 15 dB. In other scenarios, when antennas are mounted on shared platforms, antenna placement and the use of reflective surfaces are demonstrated to increase the isolation value to > 55 dB.

Dual-polarized, cavity-backed Vivaldi antenna elements have revealed new challenges not encountered in the single-polarized embodiment. The approach which aims to short the E-plane edge elements to the cavity is found to be insufficient for a resonance – free response. Instead, different types of resonances, confirmed with Eigen-mode analysis are observed inside the cavity. In the 2-element, cavity-backed antenna designed for broadside radiation, resonances are found to be formed by the boundaries provided by the cross-polarized Vivaldi arms and cavity walls. To suppress their occurrence within the frequency range of interest, the cavity is shaped in the form of a quad-ridge horn antenna. The proposed dual-polarized antenna has a symmetrical response between orthogonal polarizations which has so far been a limitation for ultrawideband coax-fed quad-ridge

horns. The designed cavity-backed 3 × 4 and 2-element Vivaldi are mounted in different types of platforms for isolation analysis. Different techniques to increase TX-RX isolation are presented. Use of reactive impedance surfaces (RIS) between antennas demonstrate improvement in isolation in excess of 15 dB. Absorber loaded, corrugated metallic reflectors are used to improve the isolation between closely separated antennas when mounted on a shared-antenna platform.

A monostatic STAR antenna subarray is proposed at X-band to enable dual-polarized capability in a phased array system at geostationary orbit. The presented architecture is based on sequentially rotated arrays (SRA) of dual-linearly polarized antenna elements. The proposed architecture relies on a modified Butler matrix beamforming network (BFN) which is carefully engineered such that all leaked signals from the transmitter are cancelled at the co-polarized receive port. The proposed architecture does not rely on any diplexer which, until now has limited these arrays to a single polarization. An all metal design philosophy, more suitable for space environment is used. The radiating element is a newly proposed dual-polarized waveguide based antenna that does not rely on an orthomode transducer. The BFN is all waveguide based to decrease insertion loss. A novel waveguide balun with theoretically zero amplitude and phase imbalances is introduced. Measured isolation of the proposed subarray is > 44 dB using designed components.

Additional approach that enables high isolation in a dual-polarized X-band phased array is proposed. In this configuration, instead of removing the diplexer, their complexity is decreased while maintaining high isolation. The approach is based on a balanced-diplexer architecture; it utilizes two 90^{o} hybrids which are connectorized such that all leaked transmit signals are partially cancelled at the co-polarized received port. Total system isolation is demonstrated to be equal to the combined isolation of diplexer and antenna cross-polarization. The proposed architecture has an aperture efficiency close to 100%. As a

proof of concept, a low profile, robust, and dual-circularly polarized subarray is designed and fabricated. Design of the different components of the proposed architecture is described both as standalone radiators and as part of an integrated system. VSWR < 2, axial ratio < 2 dB, realized gain > 15 dBic, symmetric, and co-polarized transmit receive isolation > 50dB are demonstrated.

6.2 Contributions

The major contributions to this research are as follows:

- It is demonstrated for the first time that a Vivaldi antenna array can be recessed inside a metallic cavity while maintaining ultrawideband performance. The newly developed antenna is all metal, with high aperture efficiency (>100% at low frequencies), and low turn on frequency. These features are of great importance in electronic warfare applications.
- A compact single feed and single-polarized Vivaldi recessed inside a cavity is demonstrated. The proposed cavity shape allows operation over a 2 -7 GHz band with very low side lobe levels (<-20 dB from boresight). This performance decreases its susceptibility to jamming and makes it very suitable for space constraint platforms.
- Design of a dual-polarized cavity-backed 2-element Vivaldi antenna is demonstrated as an alternative to conventional coax-fed quad-ridge horns. The proposed antenna enables symmetrical responses between orthogonal ports, high cross-polarization isolation (>35 dB), and stable radiation patterns over 4:1 bandwidth from 2 to 8 GHz.
- Designed 2 – 7 GHz antennas are used in shared-aperture platforms with demonstrated high TX/RX isolations. Techniques to increase the isolation for closely separated antennas are developed.

- A newly developed X-band, dual-polarized subarray, which allows diplexer-free operation while maintaining high TX/RX isolation in a monostatic STAR system is introduced. Proposed STAR architecture can theoretically achieve infinite isolation between co-polarized transmit and receive ports.
- A new dual-polarized all metal antenna with double ridge waveguide excitation is introduced. High cross-polarization isolation (> 60dB) is demonstrated with the proposed architecture without any use of an orthomode transducer.
- An all metal, waveguide based, beamforming network (BFN) that integrates a 90^{o} hybrid and a balun is demonstrated. The proposed BFN has a low insertion loss, and low amplitude and phase imbalances over X-band. It is therefore very attractive for applications requiring high power.
- A novel balanced-diplexer subarray is proposed to enable dual-CP at X-band with co-polarization between transmit and receive. This architecture decreases the complexity of diplexers used in X-band phased array systems with a narrow guard band between TX and RX.
- Design of a mechanically robust X-band magneto-electric dipole is demonstrated.
- The design of a fully assembled and low profile X-band subarray, which conforms to a compact $10 \times 10 \times 3$ cm^3 volume, and, integrates two coaxial cavity diplexers, two branch line hybrids, two 4-way power dividers, and a 4×4 array of magneto-electric dipoles, is demonstrated.

6.3 Future Work

In the discussed balanced-diplexer approach, the maximum achievable isolation is limited by the cross-pol isolation of the constitutive antenna element. To remove this limitation, use of dual-CP elements is proposed. Each dual-circularly polarized antenna element is sequentially rotated and fed in a balanced configuration (Figure 6.1). A separate

BFN is used between the two orthogonal polarizations of the array, thereby eliminating the cross-pol contribution in the total co-polarized isolation. All reflections and leakages are cancelled in a similar fashion as the balanced diplexer. When circularly-polarized elements are used in the unit cell of the subarray, very high aperture efficiency can be achieved even in a large array [118]. With this approach, we can achieve high isolation with high aperture

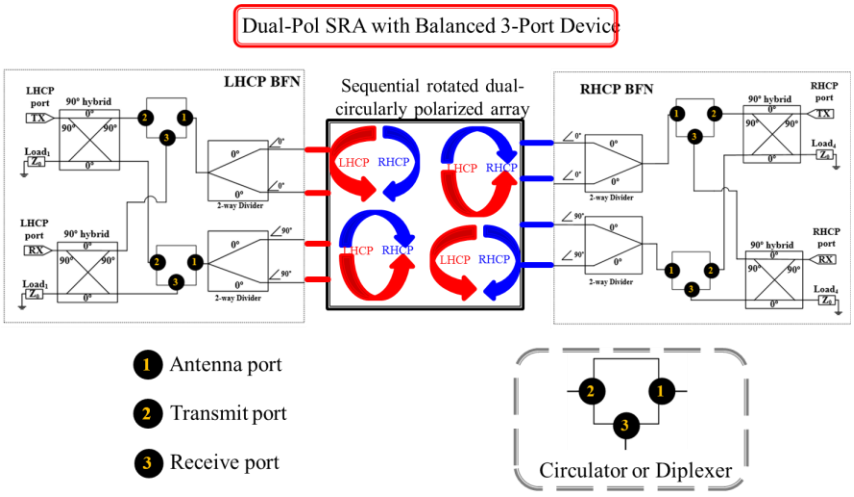

Figure 6.1: Architecture of combined sequential rotated array and balanced diplexer.

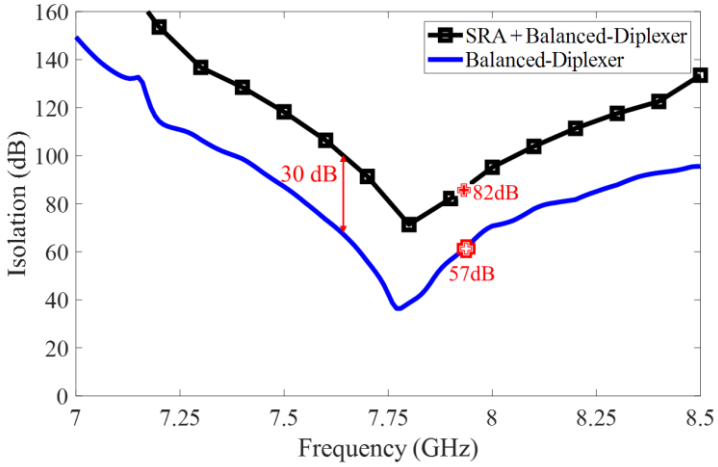

Figure 6.2: Simulated isolation showing isolation improvement with balanced diplexer.

efficiency at the cost of increased complexity. Simulated isolation of the previous SRA with balanced diplexer is plotted along with balanced diplexer proposed herein (black curve in Figure 6.2). As seen, 30 dB improvement in isolation is achieved while using identical dual-polarized linear elements.

BIBLIOGRAPHY

[1] S. Venkatesan and R. A. Valenzuela, "OFDM for 5G: Cyclic prefix versus zero postfix, and filtering versus windowing," *2016 IEEE International Conference on Communications (ICC)*, Kuala Lumpur, 2016, pp. 1-5.R.

[2] B. Farhang-Boroujeny and H. Moradi, "OFDM Inspired Waveforms for 5G," *in IEEE Communications Surveys & Tutorials*, vol. 18, no. 4, pp. 2474-2492, Fourthquarter 2016.

[3] T. Xu and I. Darwazeh, "Spectrally efficient FDM: Spectrum saving technique for 5G?," *1st International Conference on 5G for Ubiquitous Connectivity*, Akaslompolo, 2014, pp. 273-278.

[4] B. Palacin et al., "Multibeam antennas for very high throughput satellites in Europe: Technologies and trends," *2017 11th European Conference on Antennas and Propagation (EUCAP),* Paris, 2017, pp. 2413-2417.

[5] E. A. Candreva, R. Suffritti and M. Dervin, "Increasing the feeder link efficiency in broadband satellite systems," *2014 7th Advanced Satellite Multimedia Systems Conference and the 13th Signal Processing for Space Communications Workshop (ASMS/SPSC),* Livorno, 2014, pp. 300-305.

[6] H. Ju, X. Shang, H. V. Poor and D. Hong, "Bi-directional use of spatial resources and effects of spatial correlation," *in IEEE Transactions on Wireless Communications*, vol. 10, no. 10, pp. 3368-3379, October 2011.

[7] H. Ju, D. Kim, H. V. Poor and D. Hong, "Bi-directional beamforming and its capacity scaling in Pairwise Two-Way Communications," *in IEEE Transactions on Wireless Communications*, vol. 11, no. 1, pp. 346-357, January 2012.

[8] D. Kim, S. Park, H. Ju and D. Hong, "Transmission capacity of full-duplex-based two-way Ad Hoc networks with ARQ protocol," *in IEEE Transactions on Vehicular Technology*, vol. 63, no. 7, pp. 3167-3183, September 2014.

[9] I. Randrianantenaina, H. Elsawy and M. Alouini, "Limits on the Capacity of In-Band Full Duplex Communication in Uplink Cellular Networks," 2015 IEEE Globecom Workshops (GC Wkshps), San Diego, CA, 2015, pp. 1-6.

[10] N. V. Shende, Ö. Gürbüz and E. Erkip, "Half-duplex or full-duplex communications: Degrees of freedom analysis under self-interference," *in IEEE Transactions on Wireless Communications*, vol. 17, no. 2, pp. 1081-1093, February 2018.

[11] A. Sabharwal, P. Schniter, D. Guo, D. W. Bliss, S. Rangarajan and R. Wichman, "In-Band Full-Duplex Wireless: Challenges and Opportunities," *in IEEE Journal on Selected Areas in Communications*, vol. 32, no. 9, pp. 1637-1652, Sept. 2014.

[12] Z. Zhang, K. Long, A. V. Vasilakos and L. Hanzo, "Full-Duplex Wireless Communications: Challenges, Solutions, and Future Research Directions," *in Proceedings of the IEEE*, vol. 104, no. 7, pp. 1369-1409, July 2016.

[13] J. Zhou et al., "Integrated full duplex radios," *in IEEE Communications Magazine,* vol. 55, no. 4, pp. 142-151, April 2017.

[14] P. V. Prasannakumar, M. A. Elmansouri and D. S. Filipovic, "Wideband Decoupling Techniques for Dual-Polarized Bi-Static Simultaneous Transmit and Receive Antenna Subsystem*," in IEEE Transactions on Antennas and Propagation, vol.* 65, no. 10, pp. 4991-5001, Oct. 2017.

[15] J. A. M. Lyon, C. J. Digenis, W. W. Parker, and M. A. H. Ibrahim. (Jun. 1968). "Electromagnetic coupling reduction techniques," Dept. Electr. Eng., Univ.

Michigan, Ann Arbor, MI, USA, Tech. Rep. AFAL-TR-68-132. [Online]. Available: https://deepblue.lib.umich.edu/handle/ 2027.42/6402
[16] D. Shrekenhamer et al., “Cascaded metasurfaces for broadband antenna isolation,” *Proc. SPIE*, vol. 9544, p. 954424, Sep. 2015, doi: 10.1117/12.2188413.
[17] X. Yang, Y. Liu, Y. X. Xu and S. x. Gong, "Isolation enhancement in patch antenna array with fractal UC-EBG structure and cross slot," *in IEEE Antennas and Wireless Propagation Letters*, vol. 16, pp. 2175-2178, May 2017.
[18] H. Qi, X. Yin, L. Liu, Y. Rong and H. Qian, "Improving isolation between closely spaced patch antennas using interdigital lines," *in IEEE Antennas and Wireless Propagation Letters*, vol. 15, pp. 286-289, June 2016.
[19] H. Qi, L. Liu, X. Yin, H. Zhao and W. J. Kulesza, "Mutual coupling suppression between two closely spaced microstrip antennas with an asymmetrical coplanar strip wall," *in IEEE Antennas and Wireless Propagation Letters*, vol. 15, pp. 191-194, June 2016.
[20] M. A. Khojastepour, K. Sundaresan, S. Rangarajan, X. Zhang, and S. Barghi, “The case for antenna cancellation for scalable full-duplex wireless communications,” *In Proc*. 10th ACM Workshop Hot Topics Network, 2011, pp. 1-6.
[21] E. Everett, A. Sahai and A. Sabharwal, "Passive Self-Interference Suppression for Full-Duplex Infrastructure Nodes," *in IEEE Transactions on Wireless Communications*, vol. 13, no. 2, pp. 680-694, February 2014.
[22] R. Cacciola, E. Holzman, L. Carpenter and S. Gagnon, "Impact of transmit interference on receive sensitivity in a bi-static active array system," *2016 IEEE International Symposium on Phased Array Systems and Technology (PAST)*, Waltham, MA, 2016, pp. 1-5.
[23] E. G. Tianang and D. S. Filipovic, "A dipole antenna system for simultaneous transmit and receive," *2015 IEEE International Symposium on Antennas and Propagation & USNC/URSI National Radio Science Meeting*, Vancouver, BC, 2015, pp. 428-429.
[24] M. A. Elmansouri and D. S. Filipovic, "Realization of ultra-wideband bistatic simultaneous transmit and receive antenna system," *2016 IEEE International Symposium on Antennas and Propagation (APSURSI)*, Fajardo, 2016, pp. 2115-2116.
[25] G. Makar, N. Tran and T. Karacolak, "A High-Isolation Monopole Array With Ring Hybrid Feeding Structure for In-Band Full-Duplex Systems*," in IEEE Antennas and Wireless Propagation Letters*, vol. 16, pp. 356-359, 2017.
[26] K. E. Kolodziej, P. T. Hurst, A. J. Fenn and L. I. Parad, "Ring array antenna with optimized beamformer for Simultaneous Transmit And Receive*," Proceedings of the 2012 IEEE International Symposium on Antennas and Propagation*, Chicago, IL, 2012, pp. 1-2.
[27] J. Wu, M. Li and N. Behdad, "A Wideband, Unidirectional Circularly Polarized Antenna for Full-Duplex Applications," *in IEEE Transactions on Antennas and Propagation*, vol. 66, no. 3, pp. 1559-1563, March 2018.
[28] K. E. Kolodziej, S. Ycgnanarayanan and B. T. Perry, "Wideband Antenna-Isolation Improvement using Photonics for STAR Applications," *2018 IEEE International Symposium on Antennas and Propagation & USNC/URSI National Radio Science Meeting*, Boston, MA, 2018, pp. 1533-1534.
[29] W. F. Moulder, B. T. Perry and J. S. Herd, "Wideband antenna array for Simultaneous Transmit and Receive (STAR) applications," *2014 IEEE Antennas*

and Propagation Society International Symposium (APSURSI), Memphis, TN, 2014, pp. 243-244.
[30] M. A. Elmansouri, A. J. Kee and D. S. Filipovic, "Wideband Antenna Array for Simultaneous Transmit and Receive (STAR) Applications," *in IEEE Antennas and Wireless Propagation Letters,* vol. 16, pp. 1277-1280, 2017.
[31] R. Lian, T. Shih, Y. Yin and N. Behdad, "A High-Isolation, Ultra-Wideband Simultaneous Transmit and Receive Antenna With Monopole-Like Radiation Characteristics," *in IEEE Transactions on Antennas and Propagation*, vol. 66, no. 2, pp. 1002-1007, Feb. 2018.
[32] J. Ha, M. A. Elmansouri, P. Valale Prasannakumar and D. S. Filipovic, "Monostatic Co-Polarized Full-Duplex Antenna With Left- or Right-Hand Circular Polarization," *in IEEE Transactions on Antennas and Propagation*, vol. 65, no. 10, pp. 5103-5111, Oct. 2017.
[33] E. A. Etellisi, M. A. Elmansouri and D. S. Filipović, "Wideband Multimode Monostatic Spiral Antenna STAR Subsystem," *in IEEE Transactions on Antennas and Propagation*, vol. 65, no. 4, pp. 1845-1854, April 2017.
[34] M. A. Elmansouri and D. S. Filipovic, "Realization of ultra-wideband bistatic simultaneous transmit and receive antenna system," *2016 IEEE International Symposium on Antennas and Propagation (APSURSI)*, Fajardo, 2016, pp. 2115-2116.
[35] T. Snow, C. Fulton and W. J. Chappell, "Multi-antenna near field cancellation duplexing for concurrent transmit and receive," *2011 IEEE MTT-S International Microwave Symposium*, Baltimore, MD, 2011, pp. 1-4.
[36] T. Snow, C. Fulton and W. J. Chappell, "Transmit–Receive Duplexing Using Digital Beamforming System to Cancel Self-Interference," *in IEEE Transactions on Microwave Theory and Techniques*, vol. 59, no. 12, pp. 3494-3503, Dec. 2011.
[37] L. Laughlin, M. A. Beach, K. A. Morris and J. L. Haine, "Optimum Single Antenna Full Duplex Using Hybrid Junctions," *in IEEE Journal on Selected Areas in Communications*, vol. 32, no. 9, pp. 1653-1661, Sept. 2014
[38] A. E. Spezio, "Electronic warfare systems," *in IEEE Transactions on Microwave Theory and Techniques*, vol. 50, no. 3, pp. 633-644, March 2002.
[39] J. W. Rockway, S. T. Li, L. C. Russel, C. W. Manry, J. B. Mcgee, J. H. Meloling. "EM Design Technology for Topside Antenna System Integration," [Online]. Available:https://onlinelibrary.wiley.com/doi/pdf/10.1111/j.1559-3584.2001.tb00009.x
[40] G. C. Tavik et al., "The advanced multifunction RF concept," *in IEEE Transactions on Microwave Theory and Techniques*, vol. 53, no. 3, pp. 1009-1020, March 2005.
[41] G. V. Trunk et al., "Advanced multifunction RF system (AMRFS) preliminary design considerations," *NRL*, Washington, DC, Formal Rep.5300-01-9914, Dec. 10, 2001.
[42] G. C. Tavik, J. Y. Choe, and P. K. Hughes, "Advanced multifunction radio frequency (AMRF) concept testbed overview," *in Government Microcircuit Application Conf. Dig*., San Antonio, TX, Mar. 2001, pp. 100–102.
[43] H. Schantz, The Art and Science of Ultra–Wideband Antennas. Reading, MA: Artech House, 2005.
[44] A. D. Olver, P. J. Clarricoats, A. A. Kishk, L. Shafai, Microwave Horns and Feeds, *IEE Electromagnetic wave series* , vol 39.

[45] D. S. Filipovic and T. P. Cencich Sr., “Frequency Independent Antennas,” *in Antenna Engineering Handbook*, 4th Ed. New York: Mc–Graw Hill, 2007, chapter 13.
[46] M. C. Buck and D. S. Filipovic, "Unidirectional spiral antenna with improved gain and WoW," *2005 IEEE Antennas and Propagation Society International Symposium*, Washington, DC, 2005, pp. 541-544 vol. 3A
[47] P.S. Kooi, T.S. Yeo, and M.S. Leong, “Parametric Studies of the Linearly Tapered Slot Antenna (LTSA),” *in Microwave and Optical Technology Letters*, Vol. 4, No. 5, April 1991, pp. 200–206.
[48] R.N. Simons and R.Q. Lee, “Linearly Tapered Slot Antenna Impedance Characteristics,” *1995 IEEE AP–S International Symposium Digest*, Vol. 1, 1995, pp. 170–173.
[49] R. Q. Lee, “Noth Antennas.,” Glenn Research Center, NASA Tech Memorandum, NASA TM-2004-213057,
[50] P. J. Gibson, "The Vivaldi Aerial," *1979 9th European Microwave Conference*, Brighton, UK, 1979, pp. 101-105.
[51] J. Shin, and D. H. Schaubert, "A parameter study of stripline-fed Vivaldi notch-antenna arrays," *in IEEE Transactions on Antennas and Propagation*, vol. 47, no. 5, pp. 879-886, May 1999.
[52] J. T. Logan, R. W. Kindt and M. N. Vouvakis, "Low Cross-Polarization Vivaldi Arrays," *in IEEE Transactions on Antennas and Propagation*, vol. 66, no. 4, pp. 1827-1837, April 2018.
[53] R. Kindt and D. Taylor, "Polarization correction in dual-polarized phased arrays of flared notches*," 2011 IEEE International Symposium on Antennas and Propagation (APSURSI)*, Spokane, WA, 2011, pp. 1961-1964.
[54] Internation Telecommunications Union (ITU), Radio regulations (RR). [Online]. Available: https://www.itu.int/pub/R-REG-RR
[55] A. K. Bhattacharyya, “Phased Array Antennas, Floquet analysis, synthesis, BFNs, and active array systems,” John Willey & Sons, Inc. Hoboken, New Jersey, 2006.
[56] M. Jones and J. Rawnick, "A New Approach to Broadband Array Design using Tightly Coupled Elements," *MILCOM 2007 - IEEE Military Communications Conference*, Orlando, FL, USA, 2007, pp. 1-7.
[57] J. P. Doane, K. Sertel and J. L. Volakis, "A Wideband, Wide Scanning Tightly Coupled Dipole Array With Integrated Balun (TCDA-IB)," *in IEEE Transactions on Antennas and Propagation*, vol. 61, no. 9, pp. 4538-4548, Sept. 2013.
[58] W. F. Moulder, K. Sertel and J. L. Volakis, "Superstrate-Enhanced Ultrawideband Tightly Coupled Array With Resistive FSS," *in IEEE Transactions on Antennas and Propagation*, vol. 60, no. 9, pp. 4166-4172, Sept. 2012.
[59] S. S. Holland, D. H. Schaubert and M. N. Vouvakis, "A 7–21 GHz Dual-Polarized Planar Ultrawideband Modular Antenna (PUMA) Array," *in IEEE Transactions on Antennas and Propagation*, vol. 60, no. 10, pp. 4589-4600, Oct. 2012.
[60] M. Y. Lee, R. W. Kindt and M. N. Vouvakis, "Planar ultrawideband modular antenna (PUMA) wavelength-scaled array," *2016 IEEE International Symposium on Antennas and Propagation (APSURSI)*, Fajardo, 2016, pp. 435-436.
[61] B. A. Munk, Finite Antenna Arrays and FSS. New York, NY, USA:Wiley, 2003.
[62] E. Irci, K. Sertel and J. L. Volakis, "Bandwidth enhancement of low-profile microstrip antennas using tightly coupled patch arrays," *2011 IEEE International*

Symposium on Antennas and Propagation (APSURSI), Spokane, WA, 2011, pp. 1044-1047.
[63] D. H. Schaubert, S. Kasturi, A. O. Boryssenko and W. M. Elsallal, "Vivaldi Antenna Arrays for Wide Bandwidth and Electronic Scanning," *The Second European Conference on Antennas and Propagation, EuCAP 2007*, Edinburgh, 2007, pp. 1-6.
[64] R. W. Kindt and W. R. Pickles, "Ultrawideband All-Metal Flared-Notch Array Radiator," *in IEEE Transactions on Antennas and Propagation*, vol. 58, no. 11, pp. 3568-3575, Nov. 2010.
[65] J. D. S. Langley, P. S. Hall and P. Newham, "Novel ultrawide-bandwidth Vivaldi antenna with low crosspolarisation," *in Electronics Letters*, vol. 29, no. 23, pp. 2004-2005, 11 Nov. 1993.
[66] P. Dixon, "Cavity-resonance dampening*," IEEE Microwave Magazine*., vol. 6, no. 2, pp. 74–84, Jun. 2005.
[67] S. Qu, J. Li, Q. Xue and C. H. Chan, "Wideband Cavity-Backed Bowtie Antenna With Pattern Improvement," *in IEEE Transactions on Antennas and Propagation*, vol. 56, no. 12, pp. 3850-3854, Dec. 2008.
[68] R. A. Moody and S. K. Sharma, "Ultrawide Bandwidth (UWB) Planar Monopole Antenna Backed by Novel Pyramidal-Shaped Cavity Providing Directional Radiation Patterns," *in IEEE Antennas and Wireless Propagation Letters*, vol. 10, pp. 1469-1472, 2011.
[69] D. Awan, S. Bashir and W. Whittow, "High gain cavity backed UWB antenna with and without band notch feature," *2013 Loughborough Antennas & Propagation Conference (LAPC)*, Loughborough, 2013, pp. 299-302.
[70] M. OstadRahimi, L. Shafai, and J. Lovetri, "Analysis of a doubled-layered Vivaldi antenna inside a metallic enclosure", *Progress in Electromagnetic Research*., vol. 143, pp. 503–518, Nov. 2013.
[71] M. Abbak, M. Cayoren and I. Akduman, "Microwave breast phantom measurements with a cavity-backed Vivaldi antenna," *in IET Microwaves, Antennas & Propagation*, vol. 8, no. 13, pp. 1127-1133, 21 October 2014.
[72] A. Tibaldi, et al., "Design considerations for a low frequency Vivaldi array element," *in PIERS Proceeding*, Stockholm, Sweeden, pp. 240–244, Aug. 2013.
[73] D. G. Lopez and D. S. Filipovic, "Flush mountable K/Ka band amplitude only direction finding system," *2016 IEEE International Symposium on Antennas and Propagation (APSURSI)*, Fajardo, 2016, pp. 507-508.
[74] N. Jastram and D. S. Filipović, "Wideband Millimeter-Wave Surface Micromachined Tapered Slot Antenna," *in IEEE Antennas and Wireless Propagation Letters*, vol. 13, pp. 285-288, 2014.
[75] B. T. McWhirter, S. K. Panaretos, J. Fraschilla, L.R. Walker, and J. L. Edie, "Thick flared notch radiator array," *U.S. patent 5 659 326*, Aug. 19, 1997.
[76] M. Lukic, S. Rondineau, Z. Popovic and S. Filipovic, "Modeling of realistic rectangular μ-coaxial lines," *in IEEE Transactions on Microwave Theory and Techniques*, vol. 54, no. 5, pp. 2068-2076, May 2006.
[77] ANSYS High Frequency Structure Simulation (HFSS), Version 15.0.0.
[78] P. Darwood, P. N. Fletcher and G. S. Hilton, "Mutual coupling compensation in small planar array antennas," *in IEE Proceedings - Microwaves, Antennas and Propagation*, vol. 145, no. 1, pp. 1-6, Feb. 1998.
[79] R. C. Hansen, Phased Array Antennas, New York; Wiley-Interscience, 1998.

[80] R. W. Kindt and M. N. Vouvakis, "Analysis of a Wavelength-Scaled Array (WSA) Architecture," *in IEEE Transactions on Antennas and Propagation*, vol. 58, no. 9, pp. 2866-2874, Sept. 2010.
[81] M. A. Elmansouri and D. S. Filipovic, "Ultrawideband Flush-Mounted Antenna," *in IEEE Antennas and Wireless Propagation Letters*, vol. 16, pp. 1973-1976, 2017.
[82] Allen, Brad Frank, "Isolation Enhancement for Cylindrical Structure Millimeter-Wave Repeaters" (2018). *Electrical, Computer & Energy Engineering Graduate Theses & Dissertations.* 158.
[83] E. A. Etellisi, M. A. Elmansouri and D. S. Filipovic, "Wideband Monostatic Simultaneous Transmit and Receive (STAR) Antenna," *in IEEE Transactions on Antennas and Propagation*, vol. 64, no. 1, pp. 6-15, Jan. 2016.
[84] S. Manafi, M. Al-Tarifi and D. S. Filipovic, "45–110 GHz Quad-Ridge Horn With Stable Gain and Symmetric Beam," *in IEEE Transactions on Antennas and Propagation*, vol. 65, no. 9, pp. 4858-4863, Sept. 2017.
[85] A. Akgiray, S. Weinreb, W. A. Imbriale and C. Beaudoin, "Circular Quadruple-Ridged Flared Horn Achieving Near-Constant Beamwidth Over Multioctave Bandwidth: Design and Measurements," *in IEEE Transactions on Antennas and Propagation*, vol. 61, no. 3, pp. 1099-1108, March 2013.
[86] Z. Shen, and C. Feng, "A new dual-polarized broadband horn antenna," *in IEEE Antennas and Wireless Propagation Letters*, vol. 4, pp. 270-273, 2005.
[87] O. B. Jacobs, J. W. Odendaal and J. Joubert, "Quad-Ridge Horn Antenna With Elliptically Shaped Sidewalls," *in IEEE Transactions on Antennas and Propagation*, vol. 61, no. 6, pp. 2948-2955, June 2013.
[88] A.R.Mallahzadeh, A.A.Dastranj, S.Akhlaghi, "Quadruple-ridged conical horn antenna for wideband applications", *International Journal of RF and Microwave CAE.*, vol. 19, pp. 519-528, 2009.
[89] A. Navarrini and R. L. Plambeck, "A turnstile junction waveguide orthomode transducer," *in IEEE Transactions on Microwave Theory and Techniques*, vol. 54, no. 1, pp. 272-277, Jan. 2006.
[90] A. M. Boifot, E. Lier and T. Schaug-Pettersen, "Simple and broadband orthomode transducer (antenna feed)," *in IEE Proceedings H - Microwaves, Antennas and Propagation*, vol. 137, no. 6, pp. 396-400, Dec. 1990.
[91] G. Pisano et al., "A Broadband WR10 Turnstile Junction Orthomode Transducer," *in IEEE Microwave and Wireless Components Letters*, vol. 17, no. 4, pp. 286-288, April 2007.
[92] A. Tribak, J. L. Cano, A. Mediavilla and M. Boussouis, "Octave Bandwidth Compact Turnstile-Based Orthomode Transducer," *in IEEE Microwave and Wireless Components Letters*, vol. 20, no. 10, pp. 539-541, Oct. 2010.
[93] Y. Aramaki, N. Yoneda, M. Miyazaki and T. Horie, "Ultra-thin broadband OMT with turnstile junction," *IEEE MTT-S International Microwave Symposium Digest, 2003*, Philadelphia, PA, USA, 2003, pp. 47-50 vol.1.
[94] N. Jastram, "Passive front-ends for wideband millimeter wave electronic warfare," Ph.D. dissertation, Dept. Elect. Comput. Energy Eng., Univ. Colorado, Boulder, CO, USA, 2014.
[95] RF-LAMBDA, CA, USA. Model RFLT2W2G08G [online]. Available: http://www.rflambda.com/pdf/medpowercombinersplitter/RFLT2W2G08G.pdf. [Accessed: November 11, 2018]

[96] E. J. Wilkinson, "An N-Way Hybrid Power Divider," *in IRE Transactions on Microwave Theory and Techniques*, vol. 8, no. 1, pp. 116-118, January 1960.
[97] Laird, MCS/SS6M absorber [online]. Available: http://www.eccosorb.com/products-eccosorb-mcs.htm
[98] D. Sievenpiper, L. Zhang, R. F. J. Broas, N. G. Alexopolus, and E. Yablonovitch, "High-impedance electromagnetic surfaces with a forbidden frequency band," *IEEE Transaction. Microwave Theory Techniques*., vol. 47, pp. 2059–2074, Nov. 1999.
[99] MAST Technologies, MR42-007-20 absorber [online]. Available: http://www.masttechnologies.com/products/rf-absorbers/mr42-0007-20-with-psa-backing/
[100] R. Swinford, B. Grau, M. Bousquet, "High throughput satellites: delivering future capacity needs," [online]. Available: http://www.adlittle.com/sites/default/files/viewpoints/ADL_High_Throughput_Satellites-Viewpoint.pdf.
[101] O. Vidal, G. Verelst, J. Lacan, E. Alberty, J. Radzik and M. Bousquet, "Next generation High Throughput Satellite system," *2012 IEEE First AESS European Conference on Satellite Telecommunications (ESTEL)*, Rome, 2012, pp. 1-7.
[102] B. Palacin et al., "Multibeam antennas for very high throughput satellites in Europe: Technologies and trends," *2017 11th European Conference on Antennas and Propagation (EUCAP)*, Paris, 2017, pp. 2413-2417.
[103] M. Cooley, "Phased Array Fed Reflector (PAFR) antenna architectures for space-based sensors," *2015 IEEE Aerospace Conference*, Big Sky, MT, 2015, pp. 1-11.
[104] L. A. Greda, A. Winterstein, A. Dreher, S. A. Figur, B. Schonlinner, V. Ziegler, M. Haubold, and M. W. Brueck, "A Satellite Multiple-Beam Antenna for High-Rate Data Relays," *Progress In Electromagnetics Research*, Vol. 149, 133-145, 2014.
[105] A. Jacomb-Hood and E. Lier, "Multibeam active phased arrays for communications satellites," *in IEEE Microwave Magazine*, vol. 1, no. 4, pp. 40-47, Dec. 2000.
[106] E. Lier and R. Melcher, "A Modular and Lightweight Multibeam Active Phased Receiving Array for Satellite Applications: Design and Ground Testing," *in IEEE Antennas and Propagation Magazine*, vol. 51, no. 1, pp. 80-90, Feb. 2009.
[107] A. I. Zaghloul, R. K. Gupta, E. C. Kohls and O. Kilic, "Design and performance assessment of active phased arrays for communications satellites," *Proceedings 2000 IEEE International Conference on Phased Array Systems and Technology (Cat. No.00TH8510)*, Dana Point, CA, 2000, pp. 197-201.
[108] J. Warshowsky, C. Kulisan and D. Vail, "20 GHz phased array antenna for GEO satellite communications," *MILCOM 2000 Proceedings. 21st Century Military Communications. Architectures and Technologies for Information Superiority (Cat. No.00CH37155)*, Los Angeles, CA, 2000, pp. 1187-1191 vol.2.
[109] N. Seong, C. Pyo, J. Chae and C. Kim, "Ka-band satellite active phased array multi-beam antenna," *2004 IEEE 59th Vehicular Technology Conference. VTC 2004-Spring (IEEE Cat. No.04CH37514)*, Milan, 2004, pp. 2807-2810 Vol.5.
[110] G. Toso, P. Angeletti and C. Mangenot, "Multibeam antennas based on phased arrays: An overview on recent ESA developments," *The 8th European Conference on Antennas and Propagation (EuCAP 2014)*, The Hague, 2014, pp. 178-181.
[111] S. K. Rao, "Advanced Antenna Technologies for Satellite Communications Payloads," *in IEEE Transactions on Antennas and Propagation*, vol. 63, no. 4, pp. 1205-1217, April 2015.

[112] F. Teberio et al., "Compact broadband waveguide diplexer for satellite applications," *2016 IEEE MTT-S International Microwave Symposium (IMS)*, San Francisco, CA, 2016, pp. 1-4.
[113] F. Teberio, I. Arregui, P. Soto, M. A. G. Laso, V. E. Boria and M. Guglielmi, "High-Performance Compact Diplexers for Ku/K-Band Satellite Applications," *in IEEE Transactions on Microwave Theory and Techniques*, vol. 65, no. 10, pp. 3866-3876, Oct. 2017.
[114] U. Rosenberg, A. Bradt, M. Perelshtein and P. Bourbonnais, "Extreme broadband waveguide diplexer design for high performance antenna feed systems," *The 40th European Microwave Conference*, Paris, 2010, pp. 1249-1252.
[115] A. Bogorad, C. Bowman, J. Loman, R. Bouknight, J. Armenti and T. Lloyd, "Relation between electrostatic discharge rate and outgassing rate," *in IEEE Transactions on Nuclear Science*, vol. 36, no. 6, pp. 2021-2026, Dec. 1989.
[116] J. Reed, "The Multiple Branch Waveguide Coupler," *in IRE Transactions on Microwave Theory and Techniques*, vol. 6, no. 4, pp. 398-403, October 1958.
[117] J. Huang, "A technique for an array to generate circular polarization with linearly polarized elements," *in IEEE Transactions on Antennas and Propagation*, vol. 34, no. 9, pp. 1113-1124, September 1986.
[118] A. K. Bhattacharyya, "Comparison Between Arrays of Rotating Linearly Polarized Elements and Circularly Polarized Elements," *in IEEE Transactions on Antennas and Propagation*, vol. 56, no. 9, pp. 2949-2954, Sept. 2008.
[119] PULSAR Microwave Corporation, QS2-06-463/2S [online]. Available: https://www.pulsarmicrowave.com/product/90_degree_hybrid/QS2-06-463-2S
[120] M. E. Knox, "Single antenna full duplex communications using a common carrier," *WAMICON 2012 IEEE Wireless & Microwave Technology Conference*, Cocoa Beach, FL, 2012, pp. 1-6.
[121] P. Valale Prasannakumar, M. A. Elmansouri and D. S. Filipovic, "Broadband Reflector Antenna With High Isolation Feed for Full-Duplex Applications," *in IEEE Transactions on Antennas and Propagation*, vol. 66, no. 5, pp. 2281-2290, May 2018.
[122] K. Luk and B. Wu, "The Magnetoelectric Dipole—A Wideband Antenna for Base Stations in Mobile Communications," *in Proceedings of the IEEE*, vol. 100, no. 7, pp. 2297-2307, July 2012.
[123] B. Li, Y. Yin, W. Hu, Y. Ding and Y. Zhao, "Wideband Dual-Polarized Patch Antenna With Low Cross Polarization and High Isolation," *in IEEE Antennas and Wireless Propagation Letters*, vol. 11, pp. 427-430, 2012.
[124] K. L. Wong, H. C. Tung and T. W. Chiou, "Broadband dual-polarized aperture-coupled patch antennas with modified H-shaped coupling slots," *in IEEE Transactions on Antennas and Propagation*, vol. 50, no. 2, pp. 188-191, Feb. 2002.
[125] M. Barba, "A high-isolation, wideband and dual-linear polarization patch antenna," *in IEEE Transactions on Antennas and Propagation*, vol. AP-56, no. 5, pp. 1472–1476, May. 2008.
[126] K. Ghorbani and R. B. Waterhouse, "Dual polarized wide-band aperture stacked patch antennas," *in IEEE Transactions on Antennas and Propagation*, vol. AP-52, no. 8, pp. 2171–2174, Aug. 2004.
[127] M. Li and K. Luk, "Wideband Magnetoelectric Dipole Antennas With Dual Polarization and Circular Polarization," *in IEEE Antennas and Propagation Magazine*, vol. 57, no. 1, pp. 110-119, Feb. 2015.

[128] B. Q. Wu and K. Luk, "A Broadband Dual-Polarized Magneto-Electric Dipole Antenna With Simple Feeds," *in IEEE Antennas and Wireless Propagation Letters*, vol. 8, pp. 60-63, 2009.
[129] L. Siu, H. Wong, and K. Luk, "A dual-polarized magneto-electric dipole with dielectric loading," *in IEEE Transactions on Antennas and Propagation*., vol. 57, no. 3, pp. 616-623, Mar. 2009.
[130] A. Kaddour, S. Bories, C. Delaveaud and A. Bellion, "Wideband dual-polarized magneto-electric miniaturization using capacitive loading," *2017 IEEE International Symposium on Antennas and Propagation & USNC/URSI National Radio Science Meeting*, San Diego, CA, 2017, pp. 545-546.
[131] Q. Xue, S. W. Liao and J. H. Xu, "A Differentially-driven dual-polarized magneto-electric dipole antenna," *in IEEE Transactions on Antennas and Propagation*., vol. 61, no. 1, pp. 425-430, Jan. 2013.
[132] D. M. Pozar, Microwave Engineering, 3rd ed. New York: Wiley, 2005,pp. 333–336.
[133] G. P. Riblet, "A Directional Coupler with Very Flat Coupling," *in IEEE Transactions on Microwave Theory and Techniques*, vol. 26, no. 2, pp. 70-74, Feb. 1978.
[134] A. Naji and P. Warr, "Independence of the unloaded of a planar electromagnetic resonator from its shape," *in IEEE Transactions on Microwave Theory and Techniques*., vol. 60, no. 8, pp. 2370-2377, Aug. 2012.
[135] J. B. Thomas, "Cross-coupling in coaxial cavity filters - A tutorial overview," *in IEEE Transactions on Microwave Theory and Techniques*., vol. 51, no. 4, pp.1368 – 1376, Apr. 2003.
[136] E. Doumanis, S. Bulja and D. Kozlov, "Compact Coaxial Filters for BTS Applications," *in IEEE Microwave and Wireless Components Letters*., vol. 27, no. 12, pp. 1077-1079, Dec. 2017.
[137] ANATECH ELECTRONICS INC. NJ, USA. Model AD7500-8150D445 [online]. Available: https://www.anatechelectronics.com/7250-7750-mhz-7900-8400-mhz-cavity-duplexer.html. [Accessed: February 26, 2019]
[138] National Instruments Company, AWR, Version 12.03r Rev 1
[139] RF-LAMBDA, CA, USA. Model RFLT4W2G08G [online]. Available: http://www.rflambda.com/pdf/medpowercombinersplitter/RFLT4W2G08G.pdf. [Accessed: February 26, 2019]
[140] S. Manafi, M. Al-Tarifi and D. S. Filipovic, "45–110 GHz Quad-Ridge Horn With Stable Gain and Symmetric Beam," *in IEEE Transactions on Antennas and Propagation*, vol. 65, no. 9, pp. 4858-4863, Sept. 2017.